ISSN 0915-6348

NATIONAL INSTITUTE FOR FUSION SCIENCE

Structures in Confined Plasmas — Proceedings of Workshop of US-Japan Joint Institute for Fusion Theory Program —

(Received – Feb. 6, 1990)

NIFS-PROC-2 Mar. 1990

RESEARCH REPORT
NIFS-PROC Series

NAGOYA, JAPAN

Structures in Confined Plasmas

—— Proceedings of Workshop of US-Japan

Joint Institute for Fusion Theory Program ——

PREFACE

A workshop on " Structures in Confined Plasmas " was held at Institute of Plasma Physics, Nagoya University on the 13th - 16th of March, 1989. Participating in the workshop were 8 US participants (W. Horton, A. M. Dimits, R. Dominguez, F. Driscoll, T. S. Hahm, A. Hasegawa, P. Lyster and P. J. Morrison), Assc. Prof. J. Liu from Peoples Republic of China and 18 Japanese speaker-participants with 12 additional Japanese participants. The present workshop is the seventh workshop on a series of workshops on statistical physics problem in fusion plasmas, organized by the JIFT program since 1981.

The specific topics of the present workshop was the mechanisms by which the selforganization into coherent structures through nonlinear interactions. The contributions to the workshop proceedings are divided into seven sections : I - Vortex Structures in Two-Fluid Plasmas ; II- Temperature Gradient Modes ; III - Structures in One-Fluid Plasmas ; IV - Structures in Vlasov Plasmas ; V - Vortex Structures in Fluids ; VI - Hybrid Code-Particle Electron and Fluid Ion ; VII - Basic Theories.

We are greatly indebted to Profess W. Horton of the University of Texas at Austin for serving as a US coordinator of the workshop, and would like to thank the staff of Institute of Plasma Physics, especially Professor Y. H. Ichikawa and Professor T. Kamimura.

Tadatsugu Hatori

CONTENTS

IV. Structures in Vlasov Plasmas

V. Vortex Structures in Fluids

VI. Hybrid Code-Particle Electron and Fluid Ion

VII. Basic Theories

US Participants

1. A. M. Dimits (Maryland U.)
   Temperature Gradient Modes, Steamers and Anomalous Transport
2. Reme Dominguez (GA Tech.)
   Nonlinear Wave Coupling and Clumps in Drift Wave Turbulence Theory
3. Fred Driscoll (UCSD)
   Growth and Decay of Vortex Structures in Pure Electron Plasmas
4. T. S. Hahm (PPPL)
   Theory of Ion Anomalous Transport in Improved Confinement Regime
5. Akira Hasegawa (Bell Lab.)
   A D-He^3 Fusion Reactor Based on Dipole Magnetic Field
6. Wendel Horton (IFS, UT)
   Drift Wave Vortices and Anomalous Transport
7. P. Lyster (IFS, UT)
   Two-Dimensional k-Space Structure of Shearless Drift Waves, Hybrid Code Simulations
8. P. J. Morrison (IFS,UT)
   A Model for the Effects of Temperature Gradients and Magnetic shear on the Drift Wave Monopole Solutions

Observer

9. Jixing Liu (Inst. Theor. Phys. China)
   Dipolar Vortex Structures in Magnetized Rotating Plasma

Japanese speakers

1. N. Bekki (Nihon U.)
   The Kolmogorov's Spectrum in the η_e-turbulence
2. T. Hatori (IPP, Nagoya U.)
   Formation of a Current-Bubble in a Coupling Process of Tearing Modes
3. S. Horihata (Nihon U.)
   Stationary Drift-Rossy Vortices in Shear Flows
4. H. Irie (Nihon U.)
   Two-Dimensional Vortex-Type BGK Solution
5. K. Kitahara (Tokyo Inst. of Tech.)
   A Computationary Exact Method of Dawson's Model for Hole Dynamics of One-Dimensional Plasma
6. K. Mima (ILE, Osaka U.)
   Some Nonlinear Processes in Free Electron Laser
7. H. Mori (Kyushu U.)
   Long-Time Correlation and Expansion-Rate Spectra of Chaos in Hamiltonian Systems
8. S. Murakami (IFT, Hiroshima U.)
   Non-Adiabatie Behavior of the Magnetic Moment in a Dipole-Field in the Presence of a Low Frequency Electrostatic Wave
9. Y. Nagayama (Dept. Phys., U. Of Tokyo)
   Soft X-Ray Tomography of Sawtooth Oscillation and Disruption
10. T. Nakano (Phys., Chuo, U.)
    Multifractal Distribution in Turbulence
11. M. Nambu (Kyushu U.)
    Chaotic Behavior due to Wave-Wave Interactions in a Modulated Ion Beam-Plasma System
12. K. Saeki (Shizuoka U.)
    Drift Wave Solutions in an Inhomogeneous Magnetized Plasma
13. H. Sakagami (ISR)
    Vortex Associated with the Rayleigh Taylor Instability in Cylindrically Stagnating Targets
14. H. Sugama (PPL, Kyoto U.)
    Anomalous Transport of Resistive Interchange Turbulence

15. M. Wakatani (PPL, Kyoto U.)
    Pressure-Driven Internal Disruption in Heliotron E
16. Z. Yoshida (Dept. of NE, U. of Tokyo)
    Characteristic Method in Dissipative Structure Theory
17. M. Yagi (PPL, Kyoto U.)
    Magnetohydrodynamic Transport Code (MHDT-Code)

Other participants

1. Y. H. Ichikawa (IPP, Nagoya U.)
2. T. Kamimura (IPP, Nagoya U.)
3. M. Kono (Kyushu U.)
4. A. Nishiguchi (ILE, Osaka U.)
5. K. Nishihara (ILE, Osaka U.)
6. H. Sanuki (IPP, Nagoya U.)
7. M. Sato (Nihon U.)
8. Y. Takada (Tokyo I. Tech.)
9. R. Takagi (Tokyo U. Ag. and Tech.)
10. T. Takeda (JAERI)
11. M. Tanaka (IFT, Hiroshima U.)
12. K. Tanno (Tokyo I. Tech.)

Workshop on Structures in Confined Plasmas (March 13-16, 1989), Institute of Plasma Physics, Nagoya University, conference room on the 8th floor.

	13 (M.)	14 (Tu.)	15 (W.)	16 (Th.)
9:00		(Chairman W.Horton)	(Chairman M.Wakatani)	(Chairman T.Hatori)
		P.Morrison (50)	R.Dominguez (60)	Discussion session
		S.Horihata (30)	K.Kitahara (30)	Concluding remark
		K.Saeki (30)	H.Irie (30)	
		F.Driscoll (50)	K.Mima (30)	
			M.Nambu (30)	
13:30	(Chairman Y.H.Ichikawa)	(Chairman K.Mima)	(Chairman P.Morrison)	
	Opening	A.Dimits (50)	A.Hasegawa,	
	W.Horton (50min.)	N.Bekki (30)	M.Yagi (50)	
	H.Mori (50)	T.Hahm (50)	Z.Yoshida (30)	
	J.Liu (50)	H.Sakagami (30)	Y.Nagayama (30)	
	T.Nakano (50)	S.Murakami (30)	M.Wakatani (30)	
			N.Sugama (30)	
		Banquet(18:00~)	T.Hatori (30)	
			P.Lyster (30)	

I. Vortex Structures in Two-Fluid Plasmas

Drift Wave Vortices and Anomalous Transport

W. Horton
Institute for Fusion Studies
The University of Texas at Austin
Austin, Texas 78712

In view of the fact that many plasma equations, including those for drift waves, shear Alfvén waves, flute modes in rotating plasmas, and the Kelvin-Helmholtz modes, possess vortex solutions it is important to consider the transport associated with vortex structures and their mutual interactions.

Vortex structures occur when the amplitude of the fluctuation $\Phi_{\mathbf{k}}$ is sufficient to trap and circulate plasma around the vortex of size $1/k_x, 1/k_y$ in one wave period.[1] For electrostatic $\mathbf{E} = -\nabla\Phi$ vortices, the $\mathbf{E} \times \mathbf{B}$ circulation frequency $\Omega_E(\mathbf{k})$ and drift wave frequency $\omega_{\mathbf{k}}$ are

$$\Omega_E(\mathbf{k}) = \frac{ck_x\, k_y}{B}\,\Phi_{\mathbf{k}} \qquad \omega_{\mathbf{k}} = \frac{k_y\, v_d}{1 + (k_x^2 + k_y^2)\rho_s^2} \tag{1}$$

where $v_d = (cT_e/eB\, r_n)$, $r_n^{-1} = -d\ell n\, N/dr$ and $\rho_s = c(m_i\, T_e)^{1/2}/eB$. The trapping condition is that

$$\Omega_E(\mathbf{k}) > |\omega_{\mathbf{k}}| \tag{2}$$

which for $k_\perp \rho < 1$ is satisfied for

$$\frac{e\Phi_k}{T_e} \simeq \frac{1}{k_x r_n} \simeq \frac{r_0}{r_n} \tag{3}$$

where we use for vortex of radius r_0 the dominant wavenumber $k_x \simeq 1/r_0$ in the k_x spectrum.

For the dipole vortex Meiss and Horton[2] work out the trapping amplitudes in detail. For the dipole vortex the result is $e\Phi_{\rm crit}/T_e = 1.28\, r_0 v_{de}$ in the case where the vortex speed $\dot{y} = u \lesssim v_{de}$.

Numerical simulations[1,3] show that the vortices trap and convect particles, temperature or any other passive thermodynamic field and they are convected until interrupted by a vortex-vortex collision or dissipated by magnetic shear. Study of the vortex collisions shows that the maximum transfer of trapped material across the magnetic field occurs for the offset collisions with the impact parameter b of order the radius r_0 of the vortex. Here we calculate the vortex contribution of the diffusion of the passively convected scalar field $f(x,y,t)$ given by

$$\frac{\partial f}{\partial t} + \frac{\partial \varphi}{\partial x}\frac{\partial f}{\partial y} - \frac{\partial \varphi}{\partial y}\frac{\partial f}{\partial x} - D\nabla^2 f = 0 \tag{4}$$

where φ evolves by the nonlinear drift wave-Rossby wave equation[4]

$$(1-\nabla^2)\frac{\partial \varphi}{\partial t} + v_d \frac{\partial \varphi}{\partial y} - \left[\varphi, \nabla^2\varphi\right] + \mu\nabla^4\varphi = 0\ . \tag{5}$$

From the numerical solutions of Eqs. (4) and (5) we find that the field can be represented by the superposition of vortices and wave fluctuation components

$$\varphi = \sum_{i=1}^{N_v} \varphi^v(x, y - y_i - u_i t) + \sum_{\mathbf{k}} \varphi^w_{\mathbf{k}}(t) e^{i\mathbf{k}\cdot\mathbf{x}}\ . \tag{6}$$

After making this decomposition we assume that the vortices and waves are weakly correlated except during the vortex-vortex collisions which we describe by the cross-section $\sigma(b)$ for inelastic collisions at impact parameter b. The numerical experiments suggest that $d\sigma(b) = db\exp(-b/r_0)$ is a reasonable approximation for the differential cross-section.

The mass per area $m = (L_x L_y)^{-1}\int dx\, dy\, \varphi = \varphi_{\mathbf{k}=0}$ is a constant of the motion given by

$$m = \frac{N_v}{L_x L_y}\int dx\, dy\, \varphi^v + \varphi^w_{\mathbf{k}=0} = \frac{N_v \pi r_0^2 \overline{A}}{L_x L_y} = f_p \overline{A} \tag{7}$$

where f_p is the packing fraction

$$f_p = N_v \pi r_0^2 / L_x L_y = n_v \pi r_0^2 \tag{8}$$

and $\overline{A}$ is the mean amplitude of the vortices. The waves have zero mass since $\varphi^w_{\mathbf{k}} = 0$ by definition. The energy density w in the field is given by

$$w = f_p \overline{A^2} \left(1 + \frac{2\rho_s^2}{r_0^2}\right) + \sum_{\mathbf{k}} \left(1 + k_\perp^2 \rho_s^2\right) [\varphi^w_{\mathbf{k}}]^2 \tag{9}$$

in units of $w_f = n_e T_e L_c (\rho_s/r_n)^2$ where L_c is the effective length of the system (connection length in toroidal plasmas). Similarly, the enstrophy density is

$$u = f_p \frac{\overline{A^2}\,\rho_s^2}{r_0^2} \left(1 + \frac{4\rho_s^2}{r_0^2}\right) + \sum_{\mathbf{k}} k_\perp^2 \rho_s^2 \left(1 + k_\perp^2 \rho_s^2\right) [\varphi^w_{\mathbf{k}}]^2 \tag{10}$$

in the same units. In writing Eqs. (9) and (10) the interaction energies $\sum_{i<j} E(r_{ij})$ and enstrophies are neglected. From Eq. (A5) of Ref. 1 the interaction energy is $E(r_{ij}) = A_i A_j r_0^2 \left(1 + 2\rho_s^2/r_0^2 - \rho_s^2 r_{ij}^2/r_0^4\right) \exp(-r_{ij}^2/r_0^2)$ which is small provided $\left\langle r_{ij}^2 \right\rangle = 1/\pi n_v \gg r_0^2$, that is for small packing fraction f_p. For a dense vortex gas $f_p \lesssim 1$ the interaction energies become strong and the vortices become strongly correlated.

Splitting the fields as in Eq. (6) allows the description of a strongly skewed S and non-gaussian kurtosis K even in the limit of weakly correlated waves and vortices. General formulas for $S = \langle\varphi^3\rangle \,/\, \langle\varphi^2\rangle^{3/2}$ and $K = \langle\varphi^4\rangle \,/\, \langle\varphi^2\rangle^2$ are complicated, but neglecting correlations yields the reduced formulas

$$S = \frac{f_p \overline{A}\,\tilde{\varphi}^2}{\left(f_p \overline{A^2} + \tilde{\varphi}^2\right)^{3/2}} \tag{11}$$

$$K = \frac{f_p \overline{A^4} + f_p \overline{A^2}\,\tilde{\varphi}^2 + 3\tilde{\varphi}^4}{\left(f_p \overline{A^2} + \tilde{\varphi}^2\right)^2} \tag{12}$$

where we use the short notation $\tilde{\varphi}^2 = \langle(\varphi^w)^2\rangle$ for the variance of the wave part of the field. For $f_p \overline{A^2} > \tilde{\varphi}^2$ the kurtosis is large with $K \simeq 1/f_p$ characteristic of patchy or spatially intermittent turbulence. For $f_p \overline{A^2} \ll \tilde{\varphi}^2$ the kurtosis is $K \simeq 3$ as is required by the expansion in renormalized turbulence theory.

For transport we use computer solutions for the vortex-vortex collisions with various impact parameters b/r_0 while carrying along the passively convected scalar thermodynamic field f in Eq. (4). The results show that the inelastic collisions with $b \simeq r_0$ cross-section $\sigma(b) \simeq b\exp(-b/r_0) \simeq r_0$ give the strongest transport. An example is shown in Fig. 1. The strong transport arises from the mixing of f that occurs during the merging of like regions of vorticity in $b \simeq r_0$ collisions. The mean-free-path between collisions in $\lambda_{\rm mpf} = 1/n_v\sigma$. Assuming the right and left steps have equal probabilities, the vortex diffusion rate is

$$D_v = \nu_v r_0^2 = n_v v_d \sigma r_0^2 = n_v r_0^3 v_d \tag{13}$$

which is quite large for $r_0 > \rho_s$. Only trapped plasma $\pi r_0^2 n_e$ is transported during the collisions, however, so that the net contribution to the plasma diffusion rate is the fraction $\pi r_0^2 n_e N_v/L_x L_y = f_p n_e$. Thus, the vortex-vortex transport plus the wave turbulence transport is given by $D = f_p^2 r_0 v_d + \alpha\overline{\lambda}_x v_d$ where α is the mixing length constant[5] in the saturation of the wave turbulence $e\tilde{\varphi}/T_e = \alpha^{1/2}/k_x r_n$.

Writing the final result in dimensional form we have the anamalous diffusion D given by

$$D = f_p^2 \frac{r_0}{r_n}\frac{cT_e}{eB} + \alpha\frac{\overline{\lambda}_x}{r_n}\frac{cT_e}{eB} \tag{14}$$

where strictly speaking we need $f_p \ll 1$ to justify the ideal gas picture of the vortex-vortex collisions. We suggest, however, that Eq. (14) may apply when $f_p \lesssim 1$ as long as the vortex lifetime is longer than the collision period.

Mode coupling in Eq. (5) leads to the condensation of wave energy into large vortices $r_0 \gg \overline{\lambda}_x$ as shown, for example, in the work of Kono and Miyashita.[6] According to Eq. (14) the vortex-vortex transport dominates the wave transport for

$$f_p > \left(\frac{\overline{\lambda}_x}{r_0}\right)^{1/2} .$$

This condition may be satisfied in the decaying or relaxed states of turbulence where large $r_0 \gg \overline{\lambda}_x$ vortex structures may develop due to coalescence processes.

Certainly many questions remain with this theory of vortex induced transport and its relationship to the conventional wave induced transport. Neutral fluid experiments in rotating water tanks[7,8] suggest that the vortices are a dominant feature of the transport in the Rossby wave-drift wave system.

An interesting new vortex-vortex collision experiment in a non-rotating water tank by Van Heijst and Flor[9] has recently been reported. The experiments show that gravitational stratification of salt water acts to produce 2D flows with dipole vortex structures. The experiments show beautifully the evolution of a 3D jet of fluid into a 2D dipole vortex structure. Head-on collision experiments are reported to produce semi-elastic collisions that closely resemble those given by Makino *et al.*[3] by numerical simulations.

Notwithstanding the difficulty of nonlinear flow dynamics, such experiments and computer simulations suggest that vortices are a natural mechanism for the transport in both fluids and plasma. It is the author's view that they may be the dominant process in numerous, important situations due to the natural coherence and long lifetimes of the vortex structures.

Acknowledgments

The author gratefully acknowledges the work of Lee Leonard and Xiang Su during the course of this investigation.

The work was supported by the U.S. Department of Energy, Contract No. DE-FG05-80ET-53088.

References

1. W. Horton, Phys. Fluids **B1**, 524-537 (1989).

2. J.D. Meiss and W. Horton, Phys. Fluids **26**, 990 (1983).

3. M. Makino, T. Kamimura, and T. Tanuiti, J. Phys. Soc. Japan, Vol. 50, 980 (1981).

4. A. Hasegawa and K. Mima, Phys. Rev. Lett. **39**, 205 (1977) and Phys. Fluids **21**, 87 (1978).

5. W. Horton and R.D. Estes, Nucl. Fusion **19**, 203 (1979).

6. M. Kono and E. Miyashita, Phys. Fluids **31**, 326 (1988).

7. M.V. Nezlin, Sov. Phys. Usp. **29**, 807 (1986). [Usp. Fiz. Nauk **150**, 3 (1986)].

8. H.L Swinney, J. Sommerica and S.D. Meyers, *Nature* 331, 216 (1988).

9. G.J.F. Van Heijst and J.B. Flor, "Laboratory Experiments on Dipole Structures in a Stratified Fluid," preprint University of Utrecht, 1989.

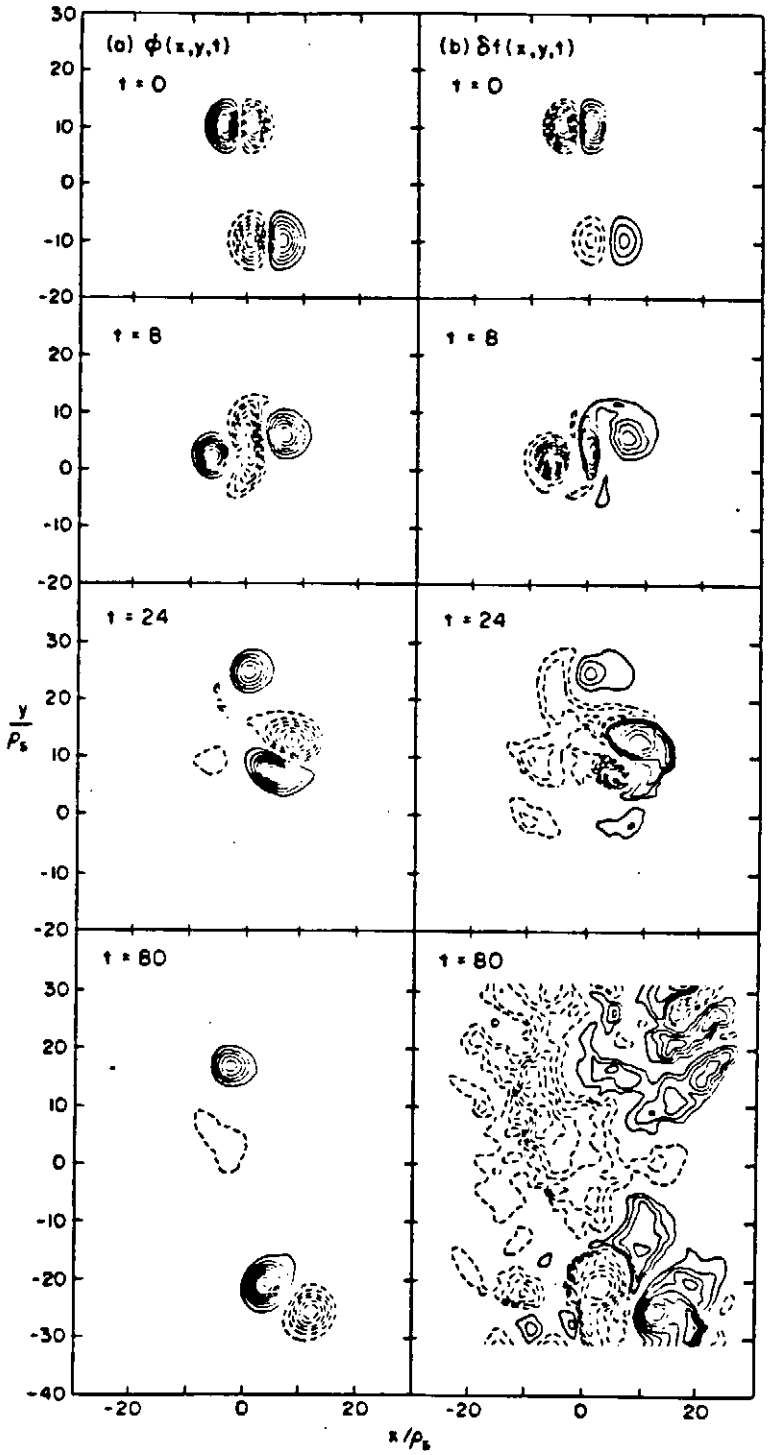

Fig. 1

Fig. 1

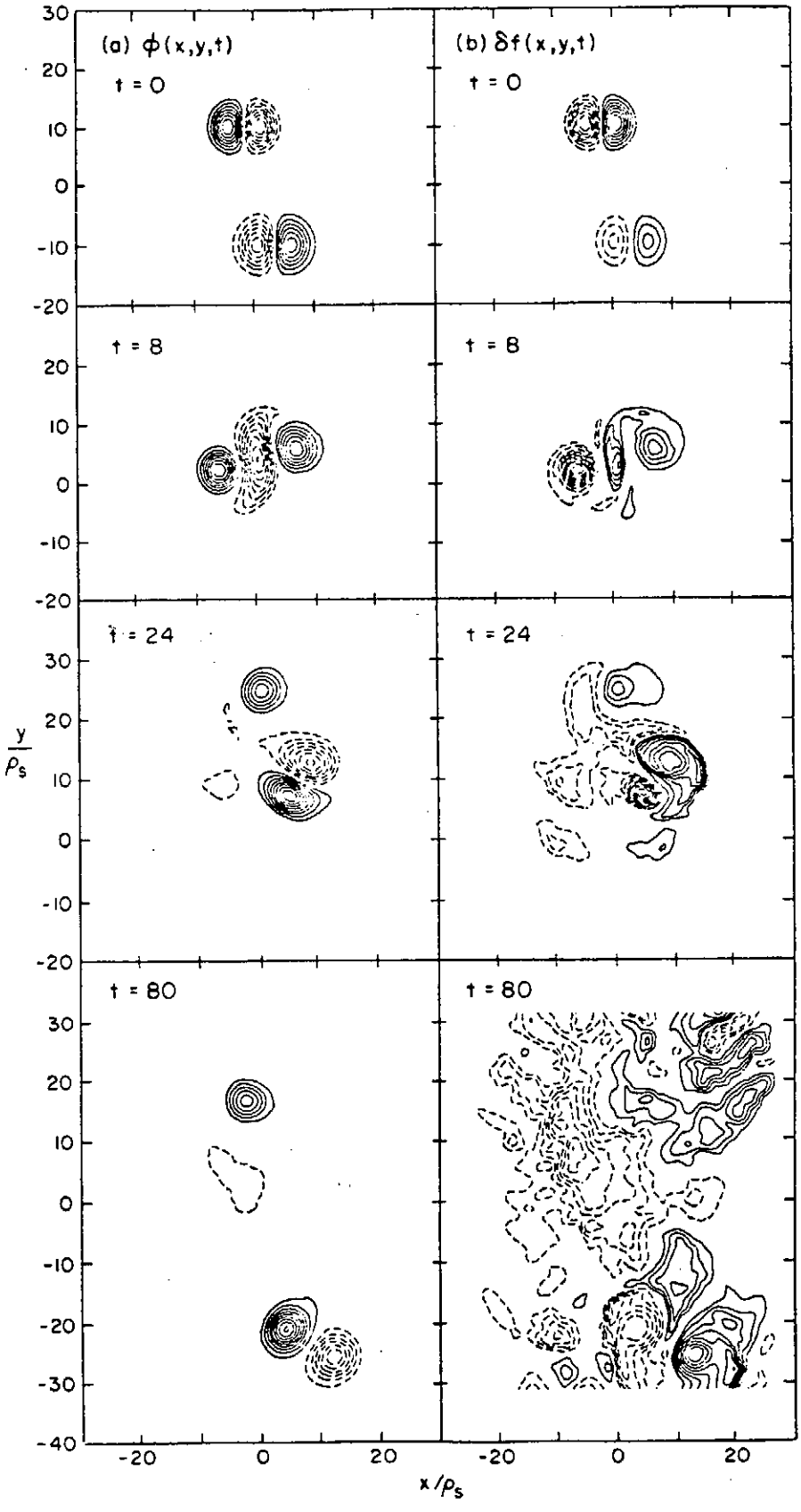
(a) φ(x,y,t)
t = 0
(b) δf(x,y,t)
t = 0
t = 8
t = 8
t = 24
t = 24
t = 80
t = 80
y/ρs
x/ρs
30
20
10
0
-10
-20
-30
-40

A Model for the Effects of Temperature Gradients and Magnetic Shear on the Drift Wave Monopole Solutions

P.J. Morrison, X.N. Su, and W. Horton
Department of Physics and Institute for Fusion Studies
The University of Texas at Austin
Austin, Texas 78712

Abstract

A model that incorporates both the effects of temperature gradients and magnetic shear on the drift wave monopole solutions is analyzed. In the case where the former effect is treated improperly and the latter is neglected, it was shown in Ref. 1 that there exist exact monopole solutions, which can further be shown [Ref. 4] to be equivalent to the existence of a point spectrum for a nonlinear eigenvalue problem. When both the effects are included, this spectrum becomes a banded continuous spectrum. An eigenvalue of this spectrum is associated with a localized vortex structure that undulates in space about a fixed level, eventually matching to a radiative ion acoustic tail. A novel separatrix crossing technique is used to investigate this problem.

In 1977 Petviashvili analyzed[1] nonlinear drift waves with the inclusion of a temperature gradient. He was able to show that the model equation he used admits localized monopole solutions, which come in two types: cyclones with negative vorticity and anticyclones with positive vorticity. Recently, authors[2,3] have come to realize that the model equation used by Petviashili is incomplete; for a consistent ordering an explicit x-dependent term arising from the nonconstancy of the temperature must be included. The inclusion of this term precludes the existence of the exact monopole solutions. If one adds the local effect of magnetic shear, then an additional explicit x-dependence is obtained, and thus further blocking the possibility of exact monopole solutions. The purpose of this paper is to present a technique for analyzing equations that have, in some sense, near monopole solutions.

In a previous work[4] we analyzed Petviashvili's original model, and described the existence of monopole solutions in terms of a nonlinear eigenvalue problem, where the amplitude of the monopole at $r = 0$, r being the cylindrical coordinate, corresponds to the eigenvalue. The spectrum in the case of Petviashvili's model is composed of a single point, assuming $k^2 = 1 - v_d/u$ is fixed. Here u is the monopole speed and v_d is either the drift wave speed or the coriolis parameter β for rotating neutral fluids. In this work, we see that for a model problem the presence of the explicit x-dependence changes the one-point nonlinear eigenvalue spectrum for the monopole into a continuous "banded" spectrum. An element of the banded spectrum corresponds to a localized vortex structure with a nonmonotonic profile. In fact these bands occur upon imposing radiative tail boundary conditions. Qualitatively one can understand the banded spectrum effect as arising from the variation of the Sagdeev potential for a "soliton"; i.e. pure monopole [see Fig. 1(a)], to that of an ion-acoustic wave [see Fig. 1(b)]. This variation arises because of the explicit x-dependence.

The presence of magnetic shear, forces a coupling of the drift wave, where $\omega = k_y v_d/(1 + k^2)$ to ion acoustic waves where $\omega^2 = k_\parallel^2 c_s^2$. This happens because the magnetic field twists

over the scale length L_s. Including both the sheared field and temperature gradient effects, the perpendicular and parallel momentum equations are

$$\left(\frac{1}{\tau(x)} - \nabla^2\right) \frac{\partial \varphi}{\partial t} + v_d \frac{\partial \varphi}{\partial y} + \frac{\tau'(x)}{\tau^2(x)} \varphi \frac{\partial \varphi}{\partial y} - [\varphi, \nabla^2 \varphi] + Sx \frac{\partial v_{\|}^i}{\partial y} = 0 \tag{1}$$

$$\frac{\partial v_{\|}^i}{\partial t} + [\varphi, v_{\|}^i] + Sx \frac{\partial \varphi}{\partial y} = 0 \tag{2}$$

where the normalized electron temperature $\tau(x) \equiv T_e(x)/T_0$, the spatial coordinates are scaled by $\rho_{i0} \equiv (T_0/m_i \omega_{ci}^2)^{1/2}$ with $\omega_{ci} \equiv eB_0/cm_i$, time is scaled by ω_{ci} and as usual φ is made dimensionless by a factor e/T_0. The parallel velocity is scaled by $\rho_{i0}\,\omega_{ci} = c_{s0} = \sqrt{T_0/m_i}$, and the drift velocity is also scaled by c_{s0}. The quantity $S \equiv \rho_{i0}/L_s$ is a measure of the magnetic shear.

For small parallel speed, we take the ion acoustic dynamics as linear. Equation (2) then becomes

$$\frac{\partial v_{\|}^i}{\partial t} = -Sx \frac{\partial \varphi}{\partial y} \,. \tag{3}$$

Combining Eqs. (1) and (3), we get the following model equation:

$$\left(\frac{1}{\tau} - \nabla^2\right) \frac{\partial \varphi}{\partial t} + v_d \frac{\partial \varphi}{\partial y} + \frac{\tau'}{\tau^2} \varphi \frac{\partial \varphi}{\partial y} - [\varphi, \nabla^2 \varphi] - S^2 x^2 \int_0^t \frac{\partial^2 \varphi}{\partial y^2}\, dt = 0 \,. \tag{4}$$

In the limit of $S \to 0$ and in the inconsistent limit $\dfrac{1}{\tau} \to 1$ while $\tau'/\tau^2 \to$ constant we obtain the incomplete Petviashvili model. In this "limit" the monopole solution is obtained upon substituting $\varphi = \varphi_0(r)$ where $r = [x^2 + (y - ut)^2]^{1/2}$ into (4). One obtains the following equation:

$$\frac{1}{r} \frac{d}{dr} \left(r \frac{d\varphi_0}{dr}\right) - 4k^2 \varphi_0 + \frac{\alpha}{2u} \varphi_0^2 = 0 \tag{5}$$

where $k^2 = \dfrac{1}{4}\left(1 - \dfrac{v_d}{u}\right)$ and $\alpha = \tau'/\tau^2$. Note that the presence of shear and temperature gradient removes the radial symmetry of this equation. Assuming $\varphi(x, y - ut)$ Eq. (4) reduces exactly to

$$\nabla^2 \varphi - \frac{1}{\tau(x)} \varphi - \ell n\, n_0(x) + \frac{S^2\, x^3}{3u} = F(\varphi - ux) \tag{6}$$

where, usually $\ell n\, n_0(x) \simeq -v_d\, x$, $v_d = -n_0'/n_0$ is a constant and F is an arbitrary function. Choosing $F = -\frac{v_d}{u}(\varphi - ux) - \frac{S^2}{3u^4}(\varphi - ux)^3$, $\tau(x) = (1-\alpha x)^{-1}$, and defining $X = x + \frac{\alpha u^2}{2S^2}$, Eq. (6) becomes

$$\nabla^2\varphi \;+\; \varphi\left(\frac{v_d}{u} - 1 - \frac{\alpha^2 u^2}{2S^2}\right) + \frac{S^2 X^2}{u^2}\varphi + \frac{\alpha}{2u}\varphi^2$$

$$+ \frac{S^2}{3u^4}\varphi^3 - \frac{S^2}{u^3} X \varphi^2 = 0\ . \tag{7}$$

Equation (7) is a difficult equation to solve, and so for the purposes of this paper we modify it in two ways. For tractibility of mathematics we replace ∇^2 by d^2/dx^2. This semi-tractable simplified mathematical model is of course not rigorously correct; in particular interesting asymmetrical behavior has been eliminated. The model does in some sense capture the behavior in the x-direction and it exhibits the main physical feature of coupling between the integrable solitary wave potential and the ion acoustic wave potential at large x. We thus obtain a one-dimensional nonautonomous problem. Our technique can handle general problems of this kind. For simplicity our second modification is to drop the last two terms of Eq. (7). Elsewhere we will present results including these terms. The qualitative behavior of banded spectra obtained here exists also in the "correct" model.

Taking into account the above assumptions and introducing the new variables $t = \widehat{k}\left(x + \frac{\alpha u^2}{2s^2}\right)$, where $\widehat{k}^2 = \frac{1}{4}\left(1 - \frac{v_d}{u} + \frac{\alpha^2 u^2}{S^2}\right)$, $\varphi = \varphi_m \psi(t)$ and $s = \frac{S}{\widehat{k}u}$, Eq. (7) becomes

$$\frac{d^2\psi}{dt^2} - 4\psi + 6\gamma\psi^2 + s^2 t^2 \psi = 0\ , \tag{8}$$

where we have set

$$\varphi_m = \frac{12\gamma u \widehat{k}^2}{\alpha}$$

and γ is a constant that remains to be determined. The boundary condition $\psi(t \to \infty) \to 0$ and the initial conditions

$$\psi(t=0) = 1 \qquad \text{and} \qquad \frac{d\psi(t=0)}{dt} = 0\ , \tag{9}$$

together with Eq. (8), define a nonlinear eigenvalue problem for γ. In the limit $s \to 0$ the solution of the model Eq. (7) is $\gamma(s=0) \equiv \gamma_0 = 1$ with the homoclinic orbit $\varphi_0 = \mathrm{sech}^2 t$ where v_d, u and α/S are restricted to $\widehat{k}^2 > 0$.

Equation (8) can be written in the form of Hamilton's equation for an effective particle with coordinate $q = \psi$, time t, momentum $p = \dfrac{d\psi}{dt}$ and effective potential $V(\psi, t) = -2\psi^2 + 2\gamma\psi^3 + \dfrac{s^2t^2}{2}\psi^2$. The Hamiltonian is

$$H(\psi, p, t) = \frac{1}{2}p^2 + 2\gamma\psi^3 + 2\psi^2\left(\frac{s^2t^2}{4} - 1\right) , \tag{10}$$

and the dynamical equations are

$$\begin{aligned} \dot{p} &= -\frac{\partial}{\partial\psi}\left(-2\psi^2 + 2\gamma\psi^3 + \frac{s^2t^2}{2}\psi^2\right) = 4\psi - 6\gamma\psi^2 - s^2\,t^2\phi \\ \dot{\psi} &= p\,. \end{aligned} \tag{11}$$

As noted above, the effect of shear is to couple the vortex solution to the ion wave by changing the potential energy $V(\psi, t)$ with time. The critical time for particles passing from the solitary wave potential into ion acoustic wave potential is $t_0 = \dfrac{2}{s}$. At the critical time, the potential can no longer contain trapped particles (see dashed line in Fig. 1(b)). For $t > t_0$ trapped particle orbits exist in the nieghborhood of the origin; i.e. in the ion acoustic potential.

From numerical integration of the model Eqs. (8) and (9), we obtain the spectrum of eigenvalues $\gamma_n(s)$. This is done by choosing a zero momentum initial condition and integrating beyond t_c to determine if there is trapping for all time in the ion acoustic potential. We are interested in the critical value of the amplitude for such trapping. Physically the trapping implies the radiative tailing at large t-values. See. Fig. 2. A detailed study of the numerical spectrum yielded the $\gamma_n(s)$ curve shown in Fig. 3. The curve shows the amplitude at $t = 0\,(\gamma)$ for eigenfunctions $\psi(t)$ that are bounded as $t \to \infty$, versus the shear parameters, s. Observe that the upper and lower boundaries of the "bounded region" oscillate as $s \to 0$

$s \to 0$ (c.f. Fig. 1(b)) with an eventual limit at $\gamma = 2/3$. Each of thse cycles corresponds to a class of eigenfunctions that oscillate a *given* number of times about the minimum of the drift wave part of the potential before becoming trapped in the ion acoustic feature. As one approaches smaller s the effective potential bounces more times before the transition in mode at t_c. Empirically, we have discovered the following relations:

$$\begin{aligned} \gamma_n(s) &= \gamma_{n+1}(s) + \frac{1}{n^2} \quad \text{for even } n \text{ and } \quad \gamma > \frac{2}{3} \\ \gamma_n(s) &= \gamma_{n+1}(s) - \frac{1}{n^2} \quad \text{for odd } n \text{ and } \quad \gamma < \frac{2}{3} \\ \gamma_{n\to\infty} &= \frac{2}{3} \end{aligned} \tag{12}$$

where n is the number of effective particle oscillations that occurs for $0 < t < t_0 = 2/n$. The numerical results show the relation (12) works very well when $n > 4$.

We give a qualitative explanation of Fig. 3 and Eqs. (12) by appealing to the analogy of a dropped ball in the gravitational potential

$$V(\psi, t) = -2\psi^2 + 2\psi^3 + \frac{s^2t^2}{2}\psi^2 \tag{13}$$

as shown in Fig. 1 (setting $\gamma = 1$). From Eq. (13) we find that the depth of the potential at the local minimum is

$$V_m = -\frac{8}{27}\left(1 - \frac{s^2t^2}{4}\right)^3 \qquad \text{at} \qquad \psi_m = \frac{2}{3}\left(1 - \frac{s^2t^2}{4}\right) .$$

We consider the cases without ($s = 0$) and with ($s \neq 0$) shear.

Without shear, the potential depth $V_m = -\frac{8}{27}$, at $\psi_m = \frac{2}{3}$ are constant in time. If we drop the ball within $0 < \psi < 1$ at $t = 0$, it would oscillate around the bottom forever (with $\psi(t = 0) = \frac{2}{3}$, the ball would stay motionless at the bottom); if $\psi(t = 0) = 1$, the ball takes infinite time to get to the $\psi = 0$ point, which is the homoclinic orbit for the solitary wave solution studied in Ref. 1. If $\psi(t = 0) < 0$ or $\psi(t = 0) > 1$, the ball goes over the potential hill at $\psi = 0$ off to negative infinite as $t \to \infty$. Here, the expansion of the

Boltzmann distribution $n_e = N(x)\exp(e\Phi/T_e) = N(1+\varphi)$ used in deriving Eq. (4) breaks down. The potential has depleted the electron density to the unphysical point where n_e becomes negative.

With $s \neq 0$, however, the potential V, depth V_m of the potential well, and position ψ_m of its bottom change with time. The potential well becomes shallower and shallower with increasing t until $V_m = 0$ and $\psi_m = 0$ when $t = t_0(s) = \frac{2}{s}$ as shown by dashed line in Fig. 1(b). When $t > \frac{2}{s}$, the potential well changes its shape into that shown by the solid line in Fig. 1(b). Therefore, the question of whether the ball becomes eventually trapped in the well shown by the solid line in Fig. 1(b), or it goes into the "Hell" as $t \to \infty$, is determined not only by the initial potential energy (the initial position ψ of the ball) but also by the magnitude of s. The shear parameter s serves as an inverse characteristic time for the change of the well. It is also obvious that the number of oscillations that the ball performs around the bottom of the potential well within $t < \frac{2}{s}$ is determined by value $\frac{2}{s}$. The first formula (for $\gamma > \frac{2}{3}$) of Eq. (12) or the upper branch of Fig. 3 corresponds to dropping the ball from the right side of the bottom of the potential well at $t = 0$, while the second one (for $\gamma < \frac{2}{3}$) of Eq. (12), or the lower branch of Fig. 3, from the left side of the bottom.

Although Eqs. (12) have not been proven, we understand that coupling of the waves at large t to the vortex at $t = 0$ results in a spectrum of vortices with an increasing number of oscillations of ψ in the nonlinear trapping region. Thus, the inhomogeneity acts to split up the vortex point spectrum into continuous bands given by $\gamma_n(s)$. The shear inhomogeneity is a defocusing effect.

By introducing the action-angle variables

$$J = \frac{1}{2\pi}\oint p dq = \frac{1}{2\pi}\oint \sqrt{2(H-V)}\, d\varphi$$

and separatrix crossing theory we can relate the action at $t = 0$ for the homoclinic orbit

$$J(t=0,\gamma) = \frac{1}{2\pi}\oint \sqrt{2H(t=0) - 4(\gamma\psi^3 - \psi^2)}\, d\psi \qquad (14)$$

to the orbits for $t = t_c > t_0$

$$J_s(t_c, \gamma) = \frac{1}{2\pi} \oint \sqrt{2H - 4(\gamma\psi^3 - \left(1 - \frac{s^2 t_c^2}{4}\right)\psi^2}\, d\psi \ . \tag{15}$$

The particles will be trapped if their velocities are positive (along positive ψ direction) when

$$J(t = 0, \gamma) = J_s(t_c, \gamma) \ . \tag{16}$$

From Eq. (16), we can find $t_c = t_c(s, \gamma)$. On the other hand we can approximately calculate the period T of oscillation of particles by

$$T(\gamma) = \oint dt = \oint \frac{d\psi}{p} = \oint \frac{d\psi}{[2[H(t=0) - V(t=0)]]^{1/2}} \ . \tag{17}$$

Equation (16) will be true if the particles have completed more than a half cycle. We therefore can write

$$t_c(s, \gamma) \simeq \frac{nT(\gamma)}{2} \tag{18}$$

where $n = 1, 2, 3, \cdots$ is the number of oscillations that the particles makes in the monopole well (Fig. 1) before passing $t = \frac{2}{s}$ into the ion acoustic spectrum. We then can get the critical $\gamma(s)$ from Eq. (18).

In Fig. 4 we compare the analytic and numerical results for $\gamma(s)$. We see from the figure that they agree quantitatively. The agreement is about as good as one would expect, considering the crudeness of the theory. Keeping higher order adiabatic invariants and folding in the result of the phase shift at the crossings would improve the comparison.

The effects of magnetic shear and temperature gradients on a model of the monopole drift wave vortex has been investigated by analytical and numerical methods. The results show that even small shear causes non-perturbative changes from the solitary to the radiative solution, due to the sensitivity of the homoclinic orbit to the defocusing inhomogeneity. The perturbation leads to the banded spectrum $\gamma_n(s)$ with radiative tails coupling to the exterior ion acoustic waves. The numerical results show that the number n of oscillation of φ within

$t < \frac{2}{s}$ satisfies $n = \frac{1}{s}$ and when s is small ($s < .25$), the eigenvalue $\gamma_n(s)$ satisfy the recursion relations of Eq. (12).

Even though the present formulation is an oversimplified model, it exhibits the main physical features of coupling the integrable solitary wave to the ion acoustic wave due to the presence of the magnetic shear. The study of a more comprehensive model which involves the two fields, φ and v_z, will be presented elsewhere.

Acknowledgments

This work was supported by the U.S. Department of Energy contract#DE-FG05-80ET-53088.

References

1. V.I. Petviashvili, Fiz. Plasmy **3**, 270 (1977) [Sov. J. Plasma Phys. **3**, 150 (1977)].

2. Lakhin, V.P., Mikhailovskii, A.B., and Onishchenko, O.G., Phys. Lett. A **119**, 348(1987), and Plasma Physics and Controlled Fusion **30**, 457(1988).

3. Horihata, S. and Sato, M., J. Phys. Soc. Jpn. **56**, 2611(1987).

4. X. Su, W. Horton, P.J. Morrison, and V.P. Pavlenko, "Effect of Scalar Nonlinearity on the Dipole Vortex Solution," Institute for Fusion Studies Report #328, The University of Texas, Austin, Texas (1988).

Figure Captions

1. Effective potential for nonlinear drift waves.

   (a) Behavior of effective potential near the center of the drift wave structure: $t = 0$.

   (b) Behavior of effective potential far from the center of the drift wave structure: $t > 2/s$.

2. (a) Nonlinear eigenfunction for $s = \frac{1}{8}$ showing monopole vortex and wave solutions for $\gamma > \frac{2}{3}$ (upper bound).

   (b) Nonlinear eigenfunction for $s = \frac{1}{7}$ showing monopole vortex and wave solutions for $\gamma < \frac{2}{3}$ (lower bound).

3. Spectrum of critical amplitude γ versus shear s showing vortex branches $\gamma_n(s)$ and nonlinear wave solutions.

4. Comparison of $\gamma(s)$ from separatrix crossing theory with that from numerical integration rsults of Eq. (7). The solid lines represent the analytical results and the dashed lines, numerical results.

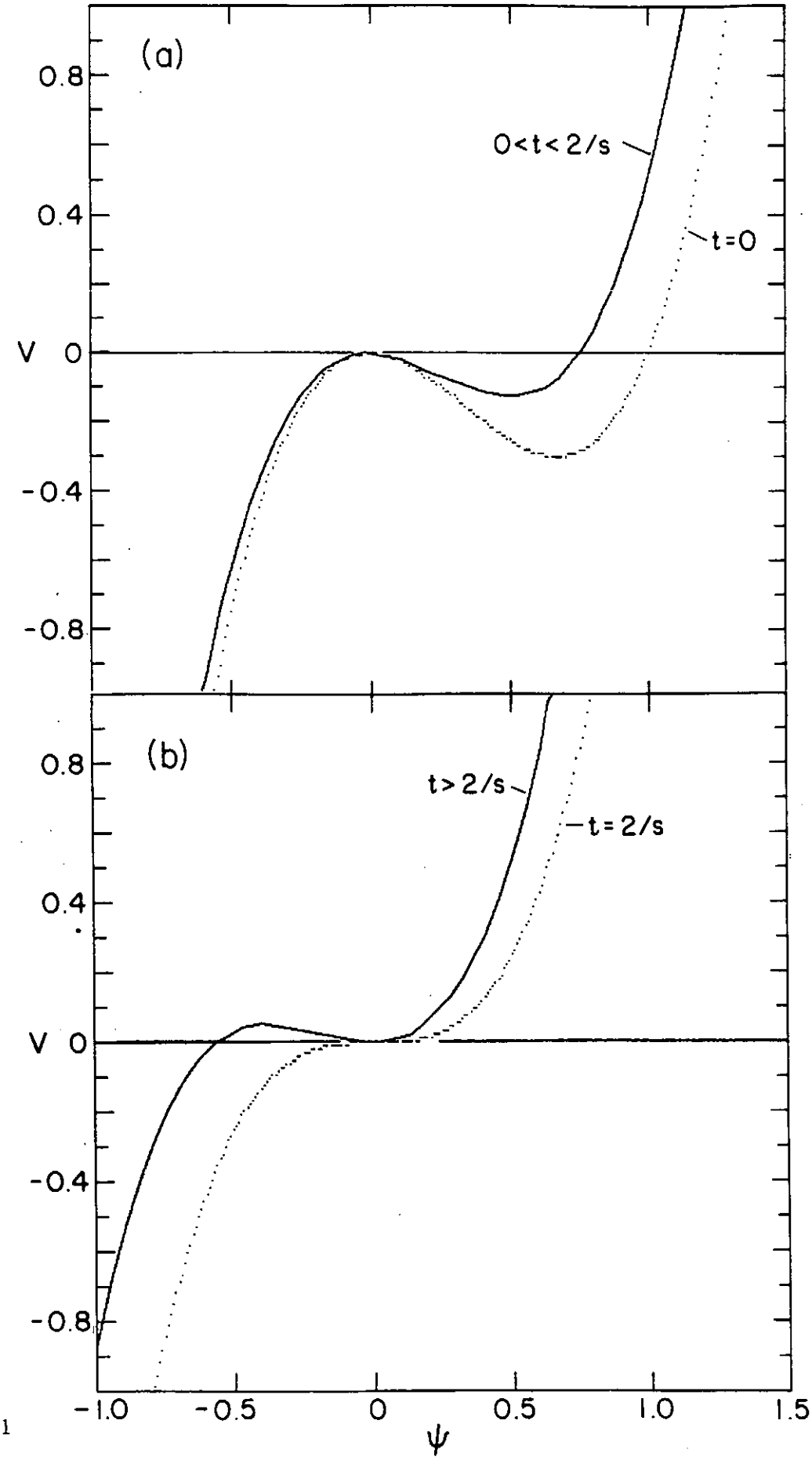

Fig. 1

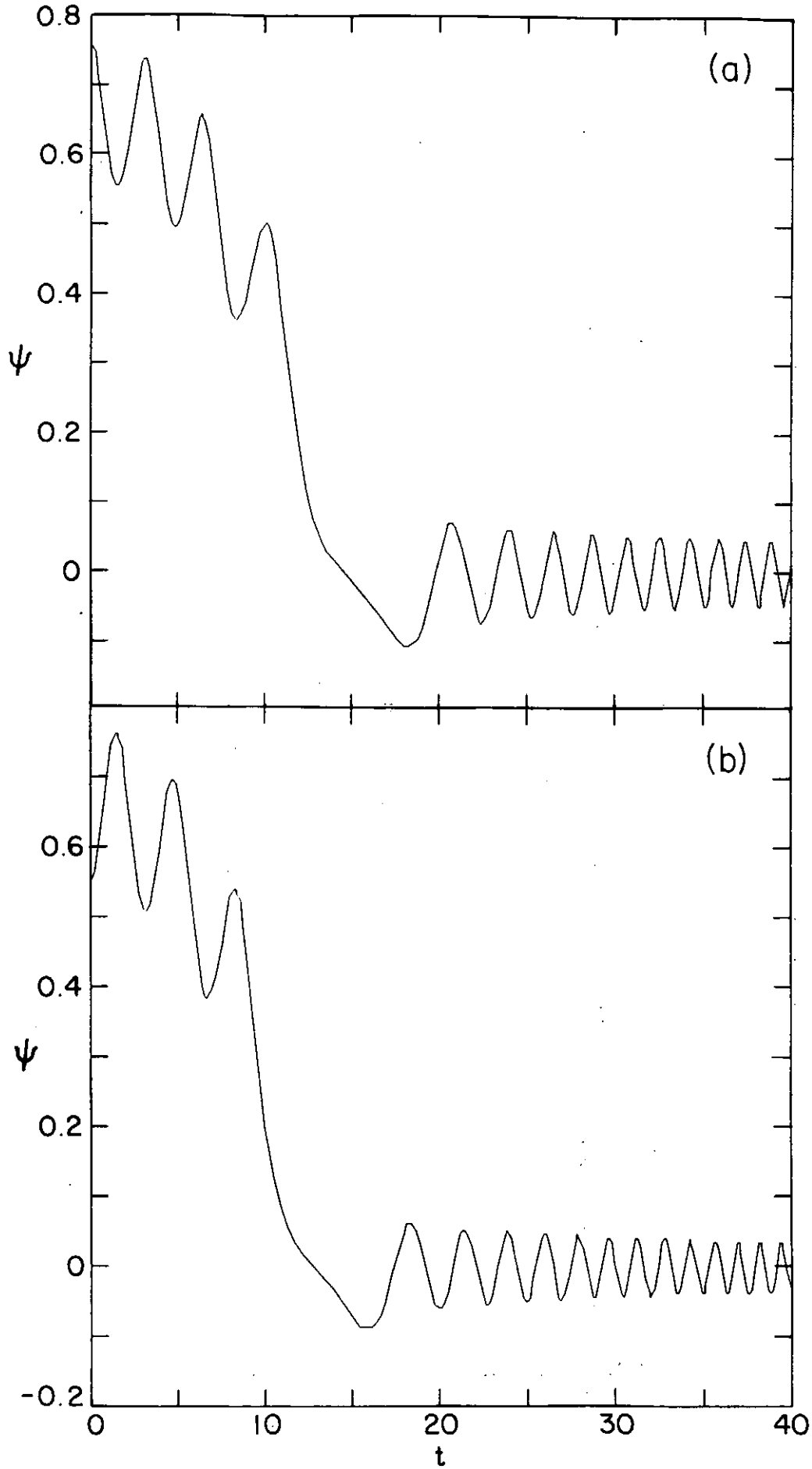

Fig. 2

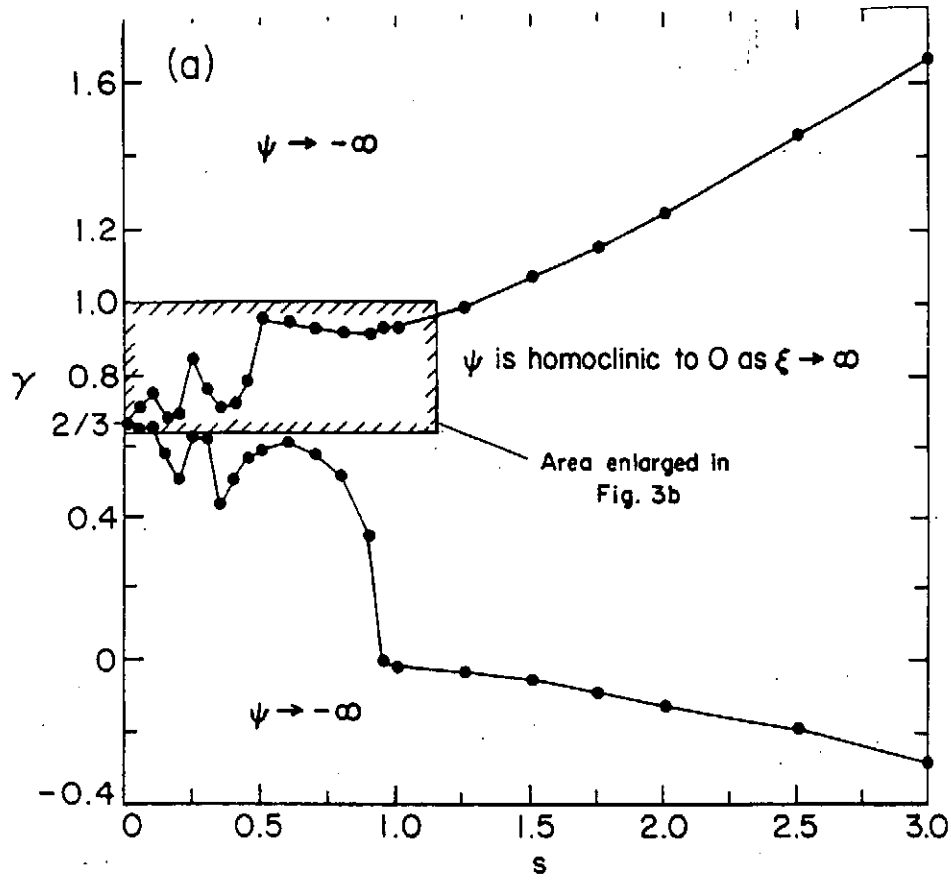
(a)
1.6
1.2
1.0
0.8
2/3
0.4
0
-0.4
γ
ψ → -∞
ψ is homoclinic to O as ξ → ∞
Area enlarged in
Fig. 3b
ψ → -∞
0
0.5
1.0
1.5
2.0
2.5
3.0
s

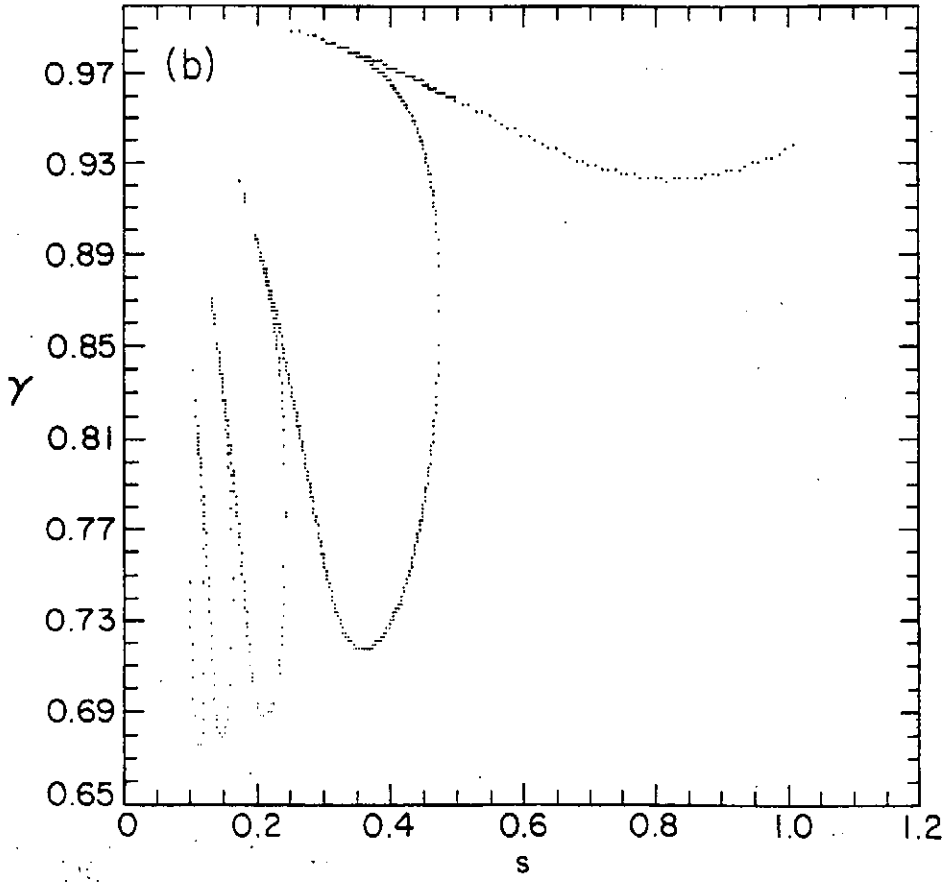
(b)
0.97
0.93
0.89
0.85
0.81
0.77
0.73
0.69
0.65
γ
0
0.2
0.4
0.6
0.8
1.0
1.2
s

Fig. 3

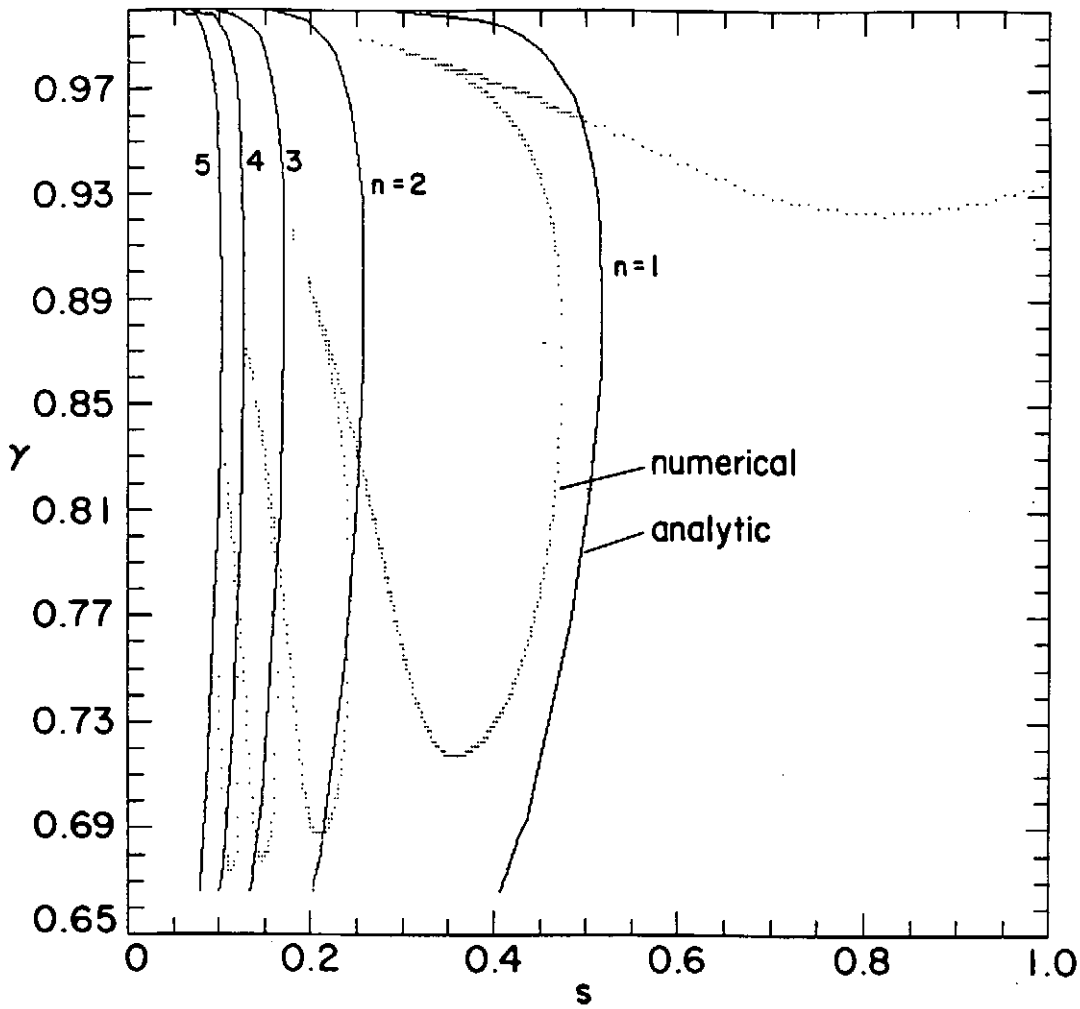
0.97
0.93
0.89
0.85
0.81
0.77
0.73
0.69
0.65
γ
0
0.2
0.4
0.6
0.8
1.0
s
5
4
3
n=2
n=1
numerical
analytic

Fig. 4

Dipolar Vortex Structures in Magnetized Rotating Plasma

Jixing Liu
Institute of Theoretical Physics, Academia Sinica, P.O. Box 2735, Beijing 100080, China

1. Introduction

Since the analogy between nonlinear Rossby wave equation in rotating fluid and the nonlinear drift wave equation in magnetized plasma was recognized [1,2], the dipolar solitary vortex solution first obtained by Larichev and Reznik for nonlinear Rossby wave equation[3] has been widely applied to different modes such as drift wave mode[4,5], flute-exchange mode[6] Alfven mode[7-9] and other modes in magnetized plasma. The main stimulus to this investigation, among other motivations, is the expectation to apply this coherent structure as a candidate constituent of plasma turbulence to understand the anomalous transport phenomena in confined plasma[10].

In this work the main results of our study on solitary vortices in rotating plasma[11-13] are given, which is motivated by seeking understanding of the complicated fluctuation pattern observed at the edge plasma of many confinement devices. Both electrostatic vortices and electromagnetic vortices were obtained according to different physical considerations.

For electrostatic vortices discussed in Sec.3 we present the rotational drift vortices and rotational flute vortices which have the same structures and properties as the Rossby one. The bulk rotation of plasma effects the existence region and the moving speed of the vortices but still keeps the complementary relation between vortices and corresponding wave modes.

For electromagnetic perturbation discussed in Sec.4, two types of vortices could be constructed[12], but the Rossby type vortex shares the same difficulty as its counterparts in nonrotating plasma[13]. To remove this difficulty, new approach is suggested and the intrinsic electromagnetic vortices without discontinuity of perturbed magnetic field $\delta\mathbf{B}$ and parallel current $j_\parallel$ on the border of vortex core is constructed. The existence region of the new type of vortex is found much narrower than the Rossby type one.

In Sec.5 summary and some comments are given.

2. Basic Equation

Suppose a low-β, dense plasma column is immersed in a constant magnetic field $\mathbf{B} = B_0\hat{z}$, the equilibrium density is $n_0(\mathbf{x}) = n_0(r)$, the equilibrium electrostatic potential which drive the plasma into rotation by $\mathbf{E}\times\mathbf{B}$ is $\Phi_0(\mathbf{x}) = \Phi_0(r)$, fictitious gravity $g(r,\theta) = \nabla U(r,\theta)$ is introduced to model the magnetic field line curvature or pondermotive force, by using two-fluid model we can write the nonlinear equations describing the low-frequency perturbation of plasma in the rotating frame as:

$$\frac{m_i c^2}{B^2}\nabla_\perp\cdot\Big(n\frac{\partial}{\partial t}\nabla_\perp\phi + \frac{c}{B_0}n[\phi,\nabla_\perp\phi]\Big) - 2\Omega\frac{m_i c^2}{B_0^2}[n,\phi] - \frac{m_i c}{B_0}[n, U - r^2\Omega^2/2] - \nabla_\parallel J_\parallel = 0\,, \tag{1}$$

$$\frac{\partial\delta n}{\partial t} - \frac{c}{B_0}\frac{dn_0}{dr}\frac{\partial\phi}{r\partial\theta} + \frac{c}{B_0}[\phi,\delta n] - \frac{1}{e}\nabla_\parallel J_\parallel = 0\,, \tag{2}$$

$$m_e n\Big(\frac{\partial}{\partial t} + \frac{c}{B_0}[\phi,\ ]\Big)v_{\parallel e} = -enE_\parallel - T_e\nabla_\parallel j_\parallel = 0\,, \tag{3}$$

where $\nabla_\perp = \partial_r\hat{r} + \frac{1}{r}\partial_\theta\hat{\theta}$, $[f\ ,g\ ] = \frac{1}{r}(\partial_r f\partial_\theta\ g - \partial_\theta f\partial_r g)$, $\Omega = cE_r/rB_0 = \text{const.}$ which implies $\Phi_0(r) = -B_0\Omega r^2/2c$, $n = n_i = n_e = n_0(r) + \delta n(r,\theta,z,t)$, and $E_\parallel, j_\parallel$ are the perturbed parallel electric field and electric current respectively, m_i, m_e is the ion and electron mass, c is the light speed.

Equations (1)-(3) in fact are the quasineutrality condition $\nabla\cdot\mathbf{J} = 0$, electron continuity equation $\partial n_e/\partial t + \nabla\cdot(n_e\mathbf{v}) = 0$ and electron parallel momentum balance equation $m_e n_e dv_{\parallel e}/dt = F_\parallel$, in the following sections different solutions of this set of equations corresponding to various physical problems are discussed.

3. Electrostatic Vortices

When there only low-frequency ($\partial_t \ll \omega_{ci}$) electrostatic perturbation in the inhomogeneous plasma is considered, the magnetic field is not perturbed, depending on different physics we obtained rotational drift vortices and rotational flute vortices which have the same dipolar structure as the Rossby vortices in rotating fluid.

3.1 Rotational Drift Vortices

Neglecting parallel motion of ions, assuming that $T_e \gg T_i$, then in Eqs. 1-3 $\nabla_\parallel j_\parallel = \partial_z j_z$, $E_\parallel = \partial_z \phi$, $\nabla_\parallel n = \partial_z n$. Solve (3) with $\tilde{n} = \delta n/n_0 = e\phi/T_e$ and eliminate j_z by substracting $e \times$ Eq.(1) from Eq.(2), then suppose small scale of the perturbation as $|\nabla\phi/\phi| \ll r_n^{-1} = |(1/n_0)(dn_0/dr)|$, introduce following dimensionless quantities $r \to r/\rho_s$; $t \to \omega_{ci}t$; $\hat{\Omega} = \Omega/\omega_{ci}$; $\hat{g} = g/\rho_s\omega_{ci}^2$; $v_{de} \to v_{de}/v_s$; $\phi \to e\phi/T_e$, $v_s = \sqrt{T_e/m_i}$, $\rho_s = v_s/\omega_{ci}$, $\omega_{ci} = B_0 e/m_i c$, finally we get the equation

$$\partial_t(1-\nabla_\perp^2)\phi + [v_{de} - 2\hat{\Omega}v_{de} - \hat{\Omega}^2 r_0 - \hat{g}(r_0)]\partial_y\phi - [\phi,\ \nabla_\perp^2\phi] = 0 \tag{4}$$

in local Cartesian coordinate frame under transformation $(r - r_0) \to x; r(\theta - \theta_0) \to y; z \to z$. Eq.(4) is modified Charney-Hasegawa-Mima (CHM) equation which has dipolar vortex solution as

$$\phi_{out} = \frac{K_1(kr)}{K_1(ka)} ua\cos\theta \quad (r > a) \quad \phi_{in} = \left[-\frac{k^2}{p^2}\frac{J_1(pr)}{J_1(pa)} + (1+\frac{k^2}{p^2})\frac{r}{a}\right] ua\cos\theta \quad (r < a)\,, \tag{5}$$

where $r = \sqrt{x^2 + (y - \alpha z - ut)^2}$; $\tan\theta = (y - \alpha z - ut)/x$; α, u, a are free parameters to denote the tilting angle of vortex moving plane respect to $\mathbf{B}$, vortex moving speed, and the vortex core size respectively, $J_m(pr)$-mth order Bessel function, $K_m(kr)$-mth order Mcdonald function, k is function of u and other plasma parameters, k and p are related by

$$\frac{1}{ka}\frac{K_2(ka)}{K_1(ka)} + \frac{1}{pa}\frac{J_2(pa)}{J_1(pa)} = 0\,. \tag{6}$$

Remember that as $r \to \infty$, $K_1(kr) \to e^{-kr}/\sqrt{r}$ obviously, solution (5) represents a localized, coherent structure which moves along θ direction with constant speed u. Vortex moving speed is constrained by

$$k^2 = 1 - \left[(1-2\hat{\Omega})v_{de} - \hat{\Omega}^2 r_0 - \hat{g}(r_0)\right]/u > 0\,. \tag{7}$$

Eq.(7) gives the complementary relation between vortex moving speed u and the phase velocity v_{ph} of the linear mode corresponding to Eq.(4). It is very easy to see that the phase velocity of rotational drift wave defined by the linearized version of (4) is inside the region $(0,\ [v_{de}(1-2\hat{\Omega}) - \hat{\Omega}^2 r_0 - \hat{g}(r_0)])$, while Eq.(7) requires $u < 0$, or $u > v_{de}(1-2\hat{\Omega}) - \hat{\Omega}_2 r_0 - \hat{g}(r_0)$, therefore both u and v_{ph} fill the whole velocity space.

3.2 Rotational Flute Vortices

Consider the rotating plasma with only two-dimensional motion, i.e. perturbations ϕ, δn only depend on r, θ, t, $\partial_z = 0$, but including finite Larmor radius (FLR) effect, the basic equations (1)-(3) reduce to

$$\partial_t \delta n + \frac{c}{B}[\delta\phi,\ n] = 0\,, \tag{8}$$

$$\frac{c}{B\omega_{ci}}\nabla\cdot\left(n\partial_t\nabla\delta\phi + \frac{c}{B}n[\delta\phi,\ \nabla\delta\phi] + \frac{cT_i}{Be}[n,\ \delta\phi]\right) - \frac{2\Omega c}{B\omega_{ci}}[n,\ \delta\phi] + \frac{1}{\omega_{ci}}[n,\ U - \frac{r^2\Omega^2}{2}] = 0\,, \tag{9}$$

Take local approximation, i.e. suppose $\left|\frac{d\ln\delta n}{dr}\right|^{-1}, \left|\frac{d\ln\delta\phi}{dr}\right|^{-1} \ll r_n = \left|\frac{d\ln n_0}{dr}\right|^{-1}$, in the local Cartesian coordinate frame Eqs. (8), (9) read as

$$\partial_\tau\tilde{n} + \partial\tilde{\phi} = [\tilde{n},\ \tilde{\phi}]\,, \tag{10}$$

$$\left(\partial_\tau - \frac{T_i}{T_e}\partial_y\right)\nabla^2\tilde{\phi} + v_c\partial_y\tilde{\phi} + v_g\partial_y\tilde{n} = [\nabla^2\tilde{\phi},\ \tilde{\phi} + \frac{T_i}{T_e}\tilde{n}]\,, \tag{11}$$

where $\tilde{n} = \frac{\delta n}{n_0}$; $\tilde{\phi} = \frac{e\delta\phi}{T_e}$; $t\frac{(\rho_s v_s}{r_n^2)} \to \tau; \frac{r}{r_n} \to x; \frac{r\theta}{r_n} \to y$, $v_c = \frac{2\Omega}{\rho_s v_s / r_n^2}$, $v_g = (\frac{r_n}{\rho_s})^2(\frac{\Omega^2 r r_n}{v_s} + \frac{g(r) r_n}{v_s})$;
Following the similar procedure in previous subsection we get

$$\tilde{\phi} = \begin{cases} \left[-\frac{k^2 a}{p^2 r}\frac{J_1(pr)}{J_1(pa)} + \left(1+\frac{k^2}{p^2}\right)\right] ur\cos\theta, & (r<a) \\ \frac{K_1(kr)}{K_1(ka)} ua\cos\theta, & (r>a) \end{cases}, \tag{12}$$

$$\tilde{n} = \begin{cases} \left[\frac{k^2}{p^2}\frac{u(uk^2 - v_c)}{v_g}\left(1 - \frac{J_1(pr)a}{J_1(pa)r}\right) + 1\right] r\cos\theta, & (r<a) \\ \frac{K_1(kr)}{K_1(ka)} a\cos\theta, & (r>a) \end{cases}, \tag{13}$$

where $r = \sqrt{x^2 + (y - u\tau)^2}$, $\tan\theta = (y - u\tau)/x$, vortex core size a and its moving speed u are free parameters, k and p are related with Eq.(6), and the nonlinear dispersion relation which restricts the vortex moving speed u is

$$k^2 = \frac{uv_c + v_g}{u(u + T_i/T_e)} > 0\,. \tag{14}$$

Eq.(14) shows the effects of plasma rotation and FLR on the propagating speed u of vortices as follows

(i). *For inward equilibrium electric field* ($\Omega > 0$) *and bad culvature* ($v_g > 0$)

$$u > 0 \text{ and } -\frac{T_i}{T_e} > u > -\frac{v_g}{v_c} \left(\text{if } \frac{T_i}{T_e} < \frac{v_g}{v_c}\right); \quad -\frac{v_g}{v_c} > u > -\frac{T_i}{T_e} \left(\text{if } \frac{T_i}{T_e} > \frac{v_g}{v_c}\right);$$

(ii). *For outward equilibrium electric field* ($\Omega < 0$) *and bad culvature* ($v_g > 0$)

$$-\frac{v_g}{v_c} > u > 0 \text{ and } u < -\frac{T_i}{T_e}\,.$$

Eq.(14) also gives the complementary relation between u and v_{ph} of the corresponding linear mode, detailed analysis is given in Ref. 11.

4. Electromagnetic Vortices in Rotating Plasma

When the perturbed component of the magnetic field in plasma can not be ignored, a new pertubation function $A_\parallel(r,\theta,z,t)$-the parallel component of vector potential should be introduced into the basic equations. In this case

$$\mathbf{E} = E_0(r)\hat{r} - \nabla\phi - \frac{1}{c}\partial_t A_\parallel \hat{z}; \mathbf{B} = B_0\hat{z} + \nabla\times(A_\parallel\hat{z})\,. \tag{15}$$

The relation between $A_\parallel$ and $j_\parallel$ is given by the Ampere's law

$$\nabla_\perp^2 A_\parallel = \frac{4\pi}{c} j_\parallel\,. \tag{16}$$

Consider the bending of field line, the parallel direction of $\mathbf{B}$ is given by $\hat{b} = \hat{z} + \frac{1}{B_0}\nabla A_\parallel \times \hat{z}$, therefore

$$\nabla_\parallel = \hat{b}\cdot\nabla = \partial_z - \frac{1}{B_0}[A_\parallel, \ ]\,. \tag{17}$$

Substitute Eqs.(15)-(17) into Eqs.(1)-(3) and transform to the local Cartesian coordinate frame, we have

$$\left\{\partial_t + \frac{c}{B_0}[\phi, \ ]\right\}\tilde{n} + \frac{c}{r_n B_0}\partial_y\phi + \frac{c}{4\pi n_0 e}\left\{\partial_t - \frac{1}{B_0}[A_\parallel, \ ]\right\}\nabla_\perp^2 A_\parallel = 0\,, \tag{18}$$

$$m_e\left\{\partial_t + \frac{c}{B}[\phi, \ ]\right\}v_{\parallel e} = \left\{\partial_z - \frac{1}{B_0}[A_\parallel, \ ]\right\}(e\phi - T_e\tilde{n}) + \frac{e}{c}\partial_t A_\parallel + \frac{T_e}{r_n B_0}\partial_y A_\parallel\,, \tag{19}$$

$$\left\{\partial_t + \frac{c}{B_0}[\phi,\ ]\right\}\nabla_\perp^2\phi + \frac{2\Omega}{r_n}\partial_y\phi + \frac{B_0}{c}[\Omega^2 r_0 + g(r_0)]\partial_y\tilde{n} + \frac{c_A^2}{c}\left\{\partial_z - \frac{1}{B_0}[A_\parallel,\ ]\right\}\nabla_\perp^2 A_\parallel = 0\,. \tag{20}$$

Introduce perturbation function ψ such that $\partial_z\psi = \partial_z\phi + (1/c)\partial_t A_\parallel$; $E_z = -\partial_z\psi$ and suppose stational solution form $\phi(x,y,z,t) = \phi(x,\eta)$; $\psi(x,y,z,t) = \psi(x,\eta)$; $\tilde{n}(x,y,z,t) = n(x,\eta)$; $\eta = y+\alpha-ut$, Eq.(19) is solved with

$$\tilde{n} = \frac{e}{T_e}\left\{\frac{v_{de}}{u}\phi + (1 - \frac{v_{de}}{u})\psi\right\}\,. \tag{21}$$

Substituting (21) into (18), (20) yields

$$\hat{\mathcal{L}}_1\left\{\nabla_\perp^2(\phi-\psi) - \beta_1\psi\right\} = 0\,, \tag{22}$$

$$\hat{\mathcal{L}}_2\left\{\nabla_\perp\phi - \beta_2\psi\right\} - \beta_3\partial_\eta\phi - \beta_4\psi = 0\,, \tag{23}$$

where $\hat{\mathcal{L}}_1 = \partial_\eta - \frac{c}{B_0 u}[\phi,\ ]$, $\hat{\mathcal{L}}_2 = \partial_\eta - \frac{c}{B_0 u}[\phi-\psi,\ ]$ are two nonlinear operators, other coefficients are defined as

$$\beta_1 = \frac{\omega_{ci}^2 u(u-v_{de})}{c^2 v_s^2\alpha^2}\,; \qquad \beta_2 = \frac{\omega_{ci}^2 c_A^2}{c^2 v_s^2}(1 - \frac{v_{de}}{u})\,;$$

$$\beta_3 = \frac{2\Omega}{ur_n} + \frac{\omega_{ci}v_{de}}{v_s^2 u^2}[\Omega^2 r_0 + g(r_0)]\,; \qquad \beta_4 = \frac{\omega_{ci}}{v_s^2 u}\left(1 - \frac{v_{de}}{u}\right)[\Omega^2 r_0 + g(r_0)]\,.$$

Two kinds of vortex solution can be constructed for nonlinear equations (22)- (23). Making an ad hoc assumption $\psi = b_1\phi + b_2 x$ like several authors did for nonrotating plasma [7-9], one can find Rossby type vortex solutions for ϕ, ψ, and $\tilde{n}$ of (21)-(23) with the form of (12) and (13), but as pointed out by Ref. 12, these solutions share the same difficulty as their counterparts of nonrotating plasma[7-9]- the discontinuity of the perturbed magnetic field $\delta\mathbf{B}$ and the perturbed parallel current $j_\parallel$ on the border of the vortex core. To remove this discontinuity, Liu and Horton[12,13] suggested to abandon the ad hoc assumption of the relation between ϕ and ψ, retaining the right relation of them as Eqs.(22)-(23) naturally have. This approach leads second kind of vortex solutions of the nonlinear equations (22)-(23) which reads

$$\phi = \begin{cases} \left\{A_1\dfrac{K_1(\lambda_1 r)}{K_1(\lambda_1 a)} + A_2\dfrac{K_1(\lambda_2 r)}{K_1(\lambda_2 a)}\right\}\cos\theta, & (r > a)\,, \\ \left\{A_3\dfrac{J_1(\lambda_3 r)}{J_1(\lambda_3 a)} + A_4\dfrac{I_1(\lambda_4 r)}{I_1(\lambda_4 a)} + \dfrac{\beta_3 + C_2}{C_2}\dfrac{B_0 u}{c}r\right\}\cos\theta, & (r < a)\,, \end{cases} \tag{24}$$

$$\psi = \begin{cases} \dfrac{1}{\beta_2}\left\{(\lambda_1^2 - \beta_3)A_1\dfrac{K_1(\lambda_1 r)}{K_1(\lambda_1 a)} + (\lambda_2^2 - \beta_3)A_2\dfrac{K_1(\lambda_2 r)}{K_1(\lambda_2 a)}\right\}\cos\theta, & (r > a) \\ \dfrac{1}{\beta_2}\left\{-(\lambda_3^2 + C_2 + \beta_3)A_3\dfrac{J_1(\lambda_3 r)}{J_1(\lambda_3 a)} + (\lambda_4^2 - C_2 - \beta_3)A_4\dfrac{I_1(\lambda_4)}{I_1(\lambda_4 a)} + \dfrac{B_0 u}{c}r\right\}\cos\theta, & (r < a) \end{cases} \tag{25}$$

where $\lambda_{1,2,3,4}$ are functions of $\beta_{1,2,3,4}$, $A_{1,2,3,4}$ and C_2 are constants to be determined by the maching conditions of ϕ, ψ and their derivatives.

The differences of this kind of vortex from the Rossby one are that the radial structure of the former is much more complicated and it has two decay scales, i.e $1/\lambda_1$ and $1/lambda_2$, and the existence region of it is much narrower than the latter one due to the following restrictions

$$\beta_2 + \beta_3 - \beta_1 > 0;\ \ (\beta_2 + \beta_3 - \beta_1)^2 > -4\beta_1\beta_3 > 0;\ \text{and}\ \ \beta_1(\beta_3 + C_2) > 0\,, \tag{26}$$

therefore the complementary relation between u and v_{ph} no longer holds. Beside these features the most remarkable property of the new kind of vortices rests on the fact that for them the discontinuity difficulty of $\delta\mathbf{B}$ and $j_\parallel$ no longer exist. Since unlike the other vortices in plasma, the new kind of vortices has no hydrodynamic analogy, we call them intrinsic electromagnetic vortices, the detailed disscusion is given in Refs.12-13.

5. Summary and Conclusion

We systematically presented dipolar solitary vortices of both electrostatic and electromagnetic character in low-β, inhomogeneous rotating plasma confined in a constant external magnetic field. Both

kinds of vortices are well localized and have coherent structure. The nonlinear terms involved have so-called vector or twisted nonlinearity which is represented by $[f, g]$, where f and g are two perturbation functions. The vortex solutions obtained are piecewice continuous special solutions of corresponding nonlinear equations. The electrostatic vortices have similar structure and properties as the Rossby vortices in rotating fluids, the electromagnetic vortices obtained here have no analogy in hydrodynamics and hence are intrinsic to magnetized plasma. It is worthwhile to remark that the intrinsic electromagnetic vortices presented here have no discontinuity of $\delta \mathbf{B}$ and $j_{\parallel}$ which is more natural than those Rossby type electromagnetic vortices constructed by others in different cases.

Here we would like to mention that although for the Rossby vortices in rotating fluid the experiments verified their existence [14,15], numerical simulations on CHM equations revealed their robustness under collision[4,16–18] and analytical investigation shows their linear stability[19,20], up to date no direct observation of dipolar vortices in plasma has been reported yet. Therefore, to set sound ground for applying dipolar vortices as constituents of plasma turbulence to understand the anomalous transport and for other applications extensive experimental and theoretical (both analytical and numerical) studies on the excitation and stability of votices, as well as their robustness under collision (especially for electromagnetic vortices) in magnetized plasma is awaited.

This work is supported by the National Natural Science Foundation of China.

References

1. V.I. Petviashivili, Sov. J. Plasma Phys. **3**, 150 (1977).
2. A. Hasegawa and K. Mima, Phys. Fluids **21**, 87 (1978).
3. V.D. Larichev and G.M. Reznik, Dokl. Acad. Nauk. USSR **231**, 1077 (1976).
4. M. Makino, T.K. Kamimura and T. Tanuiti, J. Phys. Soc. Jpn. **50**, 980 (1981).
5. J.D. Meiss and W. Horton, Phys. Fluids **26**, 990 (1983).
6. V.P. Pavlenko and V.I. Petviashvili, Sov. Plasma Phys. **9**, 603 (1983).
7. A.B. Mikhailovskii, G.D. Aburdzhaniya, O.G. Onishchenko, A.P. Churikov, Phys. Lett. **A 101**, 263 (1984).
8. P.K. Shukla, M.Y. Yu and R.K. Varma, Phys. Fluids **28**, 1719 (1985).
9. P.K. Shukla, M.Y. Yu and R.K. Varma, Phys. Lett.**A 109**, 323 (1985).
10. A.B. Mikhailovskii, V.P. Lakhin, L.A. Mikhailoskaya, and O.G. Onishchenko, Sov. Phys. JETP **59**, 1198 (1985).
11. W. Horton, J. Liu, J.D. Meiss and J. Sedlak, Phys. Fluids **29**, 1004 (1986).
12. J. Liu and W. Horton, Phys. Fluids **29**, 1828 (1986).
13. J. Liu and W. Horton, J. Plasma Phys. **36**, 1 (1986).
14. R.A. Antonova, V.P. Zhvaniya, D.G. Lominadze, D.I. Nanobashivili and V.I. Petviashvili, Sov. Phys. JETP Lett. **37**, 786 (1983).
15. G.R. Flierl, M.E. Stern and J.A. Whitehead, Dyn. Atmos. Oceans **7**, 233 (1983).
16. J.C. McWilliams and N.J. Zabusky, Astrophys. Fluid Dyn. **19**, 207 (1982).
17. N.J. Zabusky and J.C. Mcwilliams, Phys. Fluids **25**, 2175 (1982).
18. T. Tanuiti and A. Hasegawa, Phys. Scripta, **T 2/2**, 529 (1982).
19. E.W. Laedke and K.H. Spatschek, Phys. Fluids **28**, 1008 (1985).
20. E.W. Laedke and K.H. Spatschek, Phys. Fluids **29**, 133 (1986).

Presented at the US-Japan Workshop on Structures in Confined Plasma, March 13–16, 1989. Nagoya University, Nagoya, Japan.

Stationary Drift-Rossby Vortices in Shear Flows

Satoshi HORIHATA, Haruyuki IRIE and Masatomo SATO

Department of Physics, College of Science and Technology,
Nihon University,
Kanda-Surugadai, Chiyoda-ku, Tokyo 101

1. Our study is based on the Hasegawa-Mima equation[1] which describes both electrostatic drift waves in plasmas and Rossby waves in the atmosphere of rotating planets. It is written as follows[2] (in the non-dimensional units),

$$\frac{dq}{dt} = \frac{\partial q}{\partial t} + [\psi, q] = 0, \tag{1}$$

with q, the generalized vorticity, given by

$$q = \nabla^2 \psi - \psi/T(\mathbf{r}) - \ln n_0(\mathbf{r}), \tag{2}$$

where ψ is the stream function which gives the flow velocity by $\mathbf{V} = \hat{z} \times \nabla\psi$. For drift waves, ψ is also the electrostatic potential, $T(\mathbf{r})$ the electron temperature and $n_0(\mathbf{r})$ the equilibrium density, where r denotes two dimensional coordinates.

In equation (1), the Poisson bracket is defined by

$$[A, B] = \hat{z} \cdot (\nabla A \times \nabla B).$$

We have assumed that the ion density obeys the Boltzmann distribution as a result of the quasi-neutrality condition :

$$n_i = n_e = n_0(\mathbf{r}) \exp\{\psi/T(\mathbf{r})\} \tag{3}$$

For Rossby waves, we put $T = 1$; then n_0 is the Coriolis parameter.

Now, we consider stationary solutions of (1) and (2) in the (x, y) plane. First we assume that n_0 depends on x and the electron temperature T_0 is constant ($T = 1$). Since we look for stationary solutions of equation (1) propagating in the y direction with a constant velocity u, we introduce the stream function ϕ in the wave frame ;

$$\phi = \psi(x, y - ut) - ux \tag{4}$$

and transform equation (1) to

$$[\phi, q] = 0, \qquad q = \nabla^2\phi - \phi - (\ln n_0(x) + ux) \tag{5}$$

Equation (5) is integrated once to yield

$$\nabla^2\phi - \phi - (\ln n_0(x) + ux) = F(\phi) \tag{6}$$

where F is an arbitrary function of ϕ. Hereafter, we shall write y instead of y - ut for the sake of simplicity.

The arbitrary function $F(\phi)$ may be taken either linear or nonlinear in ϕ. We first consider the case where F is determined to be linear in ϕ. We will give also a method which determines F as a nonlinear function of ϕ for a given background shear flow. By the later method, we obtain a nonlinear equation which describes isolated vortices in the shear flow.

2. When F is linear, vortex solutions are obtained by dividing the entire plane into internal and external regions by a closed boundary curve. We have a linear equation for ϕ in each region and the internal and external solutions are connected on the boundary. This is the method used by Larichev and Reznik[3] when they obtained dipolar vortex, or the modon solution, in a uniform flow, and we generalize it to the case of shear flows. The conditions at the boundary curve are taken as follows :

(A) The boundary curve itself must be a stream line.

(B) The stream function ϕ and its first derivatives (that is, the velocity components) must be continuous across the boundary.

Now, if we assume that the external flow consists of only the background shear flow with straight stream lines, it is apparent that the stream lines do cross the boundary curve. This is the case of Sagdeev et al[4] who stated that they

obtained a monopolar vortex in a linear shear flow. It is obvious that their solution does not satisfy the exact stationary condition.

In order to satisfy the condition (A), we assume that the external stream function is composed of the background shear flow, $\phi_0(x)$, say, and a part φ which will represent the influence of the internal vortical motion beyond the boundary. Thus we put

$$\phi_{ex} = \phi_0(x) + \varphi \tag{7}$$

and assume, in particular, that the additional flow is vortex-free :

$$\nabla^2 \varphi = 0. \tag{8}$$

Substituting (7) and (8) in (6), we find that $F(\phi)$ must be of the form

$$F(\phi) = -\phi + \Gamma_0 \tag{9}$$

where Γ_0 is a constant. We expand $\ln n_0(x)$ in equation (6) near $x = 0$ and put

$$f(x) = \ln n_0(x) + ux = f_1 x + f_2 x^2 + f_3 x^3 \tag{10}$$

where f_i are constants. Then equation (6) yields an second order differential equation for $\phi_0(x)$, giving

$$\phi_0(x) = a_0 + v_1 x + \frac{1}{2}\Gamma_0 x^2 + \frac{1}{6} f_1 x^3 + \frac{1}{12} f_2 x^4 + \frac{1}{20} f_3 x^5 \tag{11}$$

where a_0 and v_1 are constants.

Using the polar coordinates (r, θ) defined by

$$x = r\cos\theta, \qquad y = r\sin\theta,$$

we take the circle $r = r_0$ as the boundary between the internal and external regions. In the external region, $r > r_0$, the stream function is

$$\phi_{ex} = \phi_0(r,\theta) + \varphi(r, \theta) \tag{12}$$

where $\phi_0(r, \theta)$ is given by putting $x = r\cos\theta$ in (11) and $\varphi(r, \theta)$ by

$$\varphi(r, \theta) = \beta_0 \log\frac{r}{r_0} + \sum_{m=1}^{\infty} \beta_m \frac{\cos m\theta}{r^m} \tag{13}$$

where β_m $(m = 0, 1, 2, \cdots)$ are constants, and we have retained the logarithmic term since the velocity from the term vanishes as $1/r$ at $r \to \infty$.

In the internal region $(r < r_0)$ we choose the function $F(\phi)$ as follows

$$F(\phi) = \lambda^2 C - (1 + \lambda^2)\phi \tag{14}$$

where λ^2 and C are constants. Then, equation (6) becomes

$$\nabla^2\phi + \lambda^2\phi = \lambda^2 C + f(x) \tag{15}$$

where $f(x)$ has been given by equation (10). The solution of (15) can be expressed as follows

$$\phi_{in} = \left(C - \frac{2f_2}{\lambda^4}\right) + \left(\frac{f_1}{\lambda^2} - \frac{6f_3}{\lambda^4}\right)x + \frac{f_2}{\lambda^2}\,x^2 + \frac{f_3}{\lambda^2}\,x^3$$

$$+ \sum_{m=0}^{\infty} G_m J_m(\lambda r) \cos m\theta \qquad (16)$$

where G_m are constants and J_m the Bessel functions.

As we have obtained the solutions in both regions, we can impose the boundary conditions (A) and (B) mentioned above to determine the constants in ϕ_{ex} and ϕ_{in} and the parameter $\xi = \lambda r_0$. We shall show some examples for the case $\ln n_0(x) = -\kappa x$. In this case, $f_1 = (u - \kappa)$, $f_2 = f_3 = 0$,

and the background shear flow is

$$\phi_0(x) = (\text{const}) + v_1 x + \frac{1}{2}\Gamma_0 x^2 + \frac{1}{6}(u - \kappa)x^3 \qquad (17)$$

Taking $\Gamma_0 = 0$ and $u = \kappa$ gives a uniform background flow $v_y^0 = v_1$ (Fig. 1) ; $u = \kappa$ and $\Gamma_0 \neq 0$ gives a background shear flow with a linear velocity profile (a linear shear flow) $v_y^0 = \Gamma_0 x + v_1$ (Fig. 2) ; $u \neq \kappa$ gives a background shear flow with a parabolic velocity profile (a parabolic shear flow) $v_y^0 = \frac{1}{2}(u - \kappa)x^2 + \Gamma_0 x + v_1$ (Figs. 3 and 4).

3. Next, we consider the case where the function F in (6) is nonlinear in the argument.

We start from the Hasegawa-Mima equation

$$\frac{\partial q}{\partial t} + [\psi, q] = 0 \; ; \quad q = \nabla^2 \psi - \ln n(\mathbf{r}, t) \tag{18}$$

where, in the expression for q, we put

$$n(\mathbf{r}, t) = N_0(x) \exp\left(\varphi(\mathbf{r}, t)/T(x)\right). \tag{19}$$

In writing equation (19), we have separated the electrostatic potential $\psi(\mathbf{r}, t)$ as $\psi(\mathbf{r}, t) = \psi_0(x) + \varphi(\mathbf{r}, t)$ and absorbed $\psi_0(x)$ in the definition of equilibrium density $N_0(x)$.

Now we consider stationary solutions of the form $\varphi = \varphi(x, y - ut)$. For φ of this form, equation (18) gives

$$q = F(\psi - ux) = F(\psi_0 - ux + \varphi) \tag{20}$$

where F is an arbitrary function of the argument. We note that q is expressed as

$$q = \nabla^2 \varphi - \frac{1}{T(x)}\varphi + \psi_0''(x) - \ln N_0(x) \tag{21}$$

We consider isolated (localized) vortex, and assume that $\varphi \to 0$ as $|y| \to \infty$. Then equation (20) and (21) give

$$\psi_0''(x) - \ln N_0(x) = F\left(\psi_0(x) - ux\right) \tag{22}$$

and by subtracting (22) from (21), we obtain

$$\nabla^2 \varphi - \frac{1}{T(x)} \varphi = F(\psi_0 - ux + \varphi) - F(\psi_0 - ux) \tag{23}$$

For given functions $\psi_0(x)$ and $N_0(x)$, equation (22) is used to determine the function F. Then equation (23) gives the equation for φ.

Example 1.

A very simple example of determining the function F from (22) is given by putting $\ln N_0(x) = -C$ (constant) and $u = 0$. We assume further

$$v_y^0(x) = \psi_0'(x) = A_0 \tanh(x/L) \tag{24}$$

which represents the shear flow. Then we have

$$\nabla^2\varphi - \frac{1}{T(x)}\varphi = \frac{A_0}{L}\,\mathrm{sech}^2\frac{x}{L}\left(e^{-2\varphi/A_0 L} - 1\right) \tag{25}$$

Expanding for small $\varphi/A_0 L$, we have

$$\nabla^2\varphi = \left(\frac{1}{T(x)} - \frac{2}{L^2}\,\mathrm{sech}^2\frac{x}{L}\right)\varphi. \tag{26}$$

For large $|x|$, the coefficient of φ on the r. h. s. of equation (26) is positive, and the solution is surely localized.

Example 2.

We take

$$\left.\begin{aligned} v_E(x) &= \frac{d\psi_0}{dx} = v_E^0 + v_E' x \\ v_*(x) &= -\frac{d}{dx}\ln N_0(x) = v_*^0 + v_*' x \end{aligned}\right\} \tag{27}$$

for the E × B and diamagnetic drift velocities. After some elementary calculations, we obtain the result

$$\nabla^2\varphi = \left(\frac{1}{T} + \frac{v_*'}{v_E'}\right)\varphi + \frac{v_E' v_*(x) - v_*'\left(v_E(x) - u\right)}{v_E'^{\,2}} \times \left(\mathrm{Root}\left[\left(v_E(x) - u\right)^2 + 2v_E'\varphi\right] - v_E(x) + u\right) \tag{28}$$

where

$$\mathrm{Root}(\epsilon) = \begin{cases} \sqrt{\epsilon} & : \epsilon \leq 0 \\ -\sqrt{|\epsilon|} & : \epsilon < 0 \end{cases} \tag{29}$$

When we can regard φ as small in the root of (28), we will obtain up to the term φ^2 :

$$\nabla^2 \varphi = f(x)\varphi + g(x)\varphi^2 \tag{30}$$

with

$$\begin{cases} f(x) = \dfrac{1}{T(x)} + \dfrac{v_*'(x)}{v_E(x) - u} \\ g(x) = \dfrac{1}{2}\left\{ \dfrac{v_*'}{\left(V_E(x) - u\right)^2} - \dfrac{v_E' v_*(x)}{\left(v_E(x) - u\right)^3} \right\} \end{cases} \tag{31}$$

This is the same result as obtained by Saeki.[5] We must treat the original equation (28) when we consider all the range of x.

References

1) A. Hasegawa and K. Mima : Phys. Fluids 21 (1978) 87.

2) S. Horihata and M. Sato : J. Phys. Soc. Japan 56 (1987) 2611.

3) V.D. Larichev and G.M. Reznik : Dokl. Akad. Nauk. SSSR 231 (1976) 1077.

4) R.Z. Sagdeev, V.D. Shapiro and V.I. Shevchenko : Sov. Astron. Lett. 7 (1981) 279.

5) Private communications with K. Saeki.

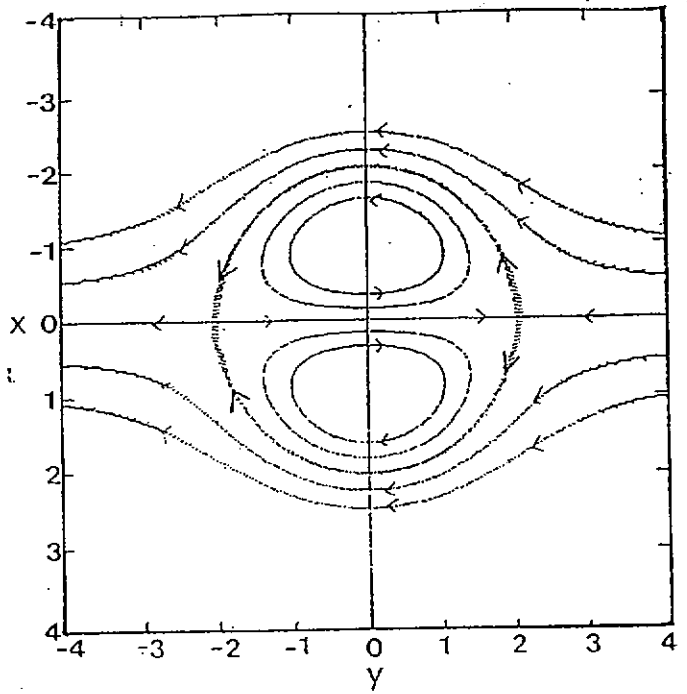

Fig. 1. Dipolar vortex in a uniform background flow (continuous $\nabla^2\phi$ at $r = r_o$).

$$\phi_{ex} = v_1(r - r_o^2/r)\cos\theta$$

$$\phi_{in} = \left[2v_1 r_o/\epsilon J_1(\epsilon)\right] J_1(\lambda r)\cos\theta$$

Condition on $\epsilon = \lambda r_o$: $J_1(\epsilon) = 0$.

Parameters for the above figure : $r_o = 2.0$, $v_1 = -0.5$ and $\epsilon = 3.86$.

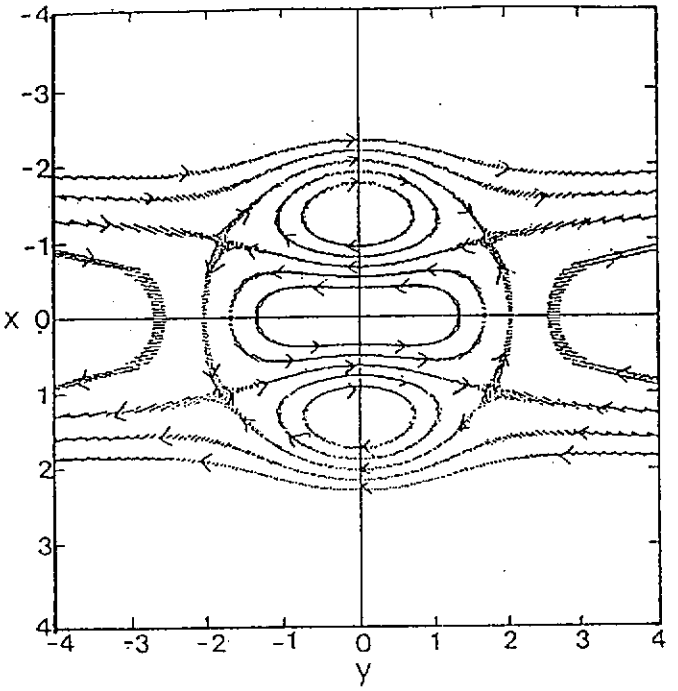

Fig. 2. Tripolar vortex in a linear background shear flow (continuous $\nabla^2\phi$ = at $r = r_o$).

$$\phi_{ex} = \tfrac{1}{4}\Gamma_o\left(r^2 - r_o^2\right) + \beta_o \ln\left(r/r_o\right) + \tfrac{1}{4}\Gamma_o\left[r^2 - \left(r_o^4/r^2\right)\right]\cos 2\theta$$

$$\phi_{in} = -\left(\Gamma_o r_o^2/\epsilon^2\right)\left[J_o(\lambda r)/J_o(\epsilon) - 1\right] + \left[\left(\Gamma_o r_o^2/\epsilon J_1(\epsilon)\right)\right] J_2(\lambda r)\cos 2\theta$$

Condition on $\epsilon = \lambda r_o$: $J_2(\epsilon) = 0$.

Parameters for the above figure : $r_o = 2.0$, $\Gamma_o = -0.25$, $\epsilon = 5.135$ and $\beta_o = -\Gamma_o r_o^2\left[\frac{1}{2} - J_1(\epsilon)/\epsilon J_o(\epsilon)\right] = 0.013$.

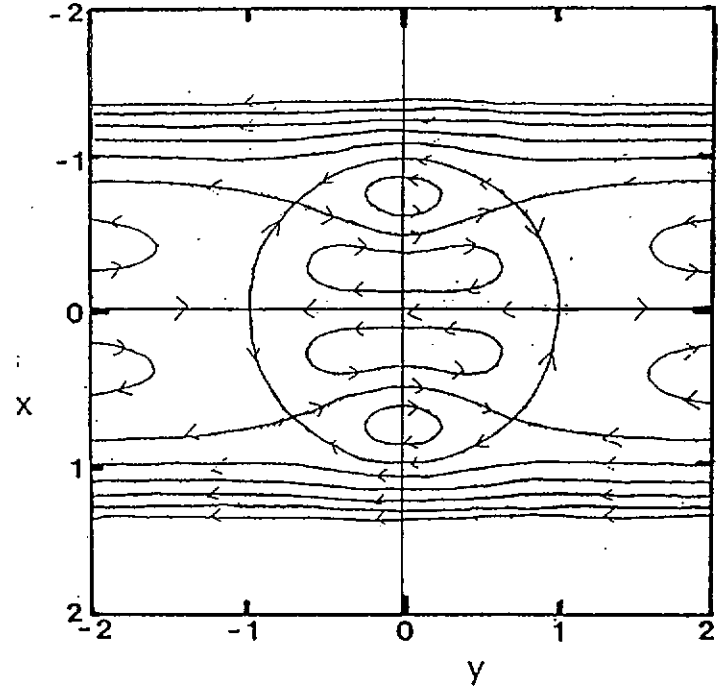

Fig. 3. Quadrupolar vortex in a parabolic background shear flow without log arithmic term (discontinuous $\nabla^2\phi$ at $r = r_o$).

$$\bar{\phi} = \phi/(\kappa - u)r_o^3$$

$$\bar{\phi}_{ex} = -\frac{1}{8}\left[(r/r_o)^3 - (r/r_o)\right]\cos\theta - \frac{1}{24}\left[(r/r_o)^3 - (r_o/r)^3\right]\cos 3\theta$$

$$(\beta_o = 0, \quad v_1 = \tfrac{1}{8}(\kappa - u)r_o^2, \quad \Gamma_o = 0).$$

$$\bar{\phi}_{in} = \frac{1}{\epsilon^2}\left[J_1(\lambda r)/J_1(\epsilon) - (r/r_o)\right]\cos\theta - \frac{1}{4}\left[J_3(\lambda r)/\epsilon J_3'(\epsilon)\right]\cos 3\theta$$

Condition on $\epsilon = \lambda r_o$: $J_3(\epsilon) = 0$.

Parameters for the above figure : $r_o = 1.0$ and $\epsilon = 6.380$.

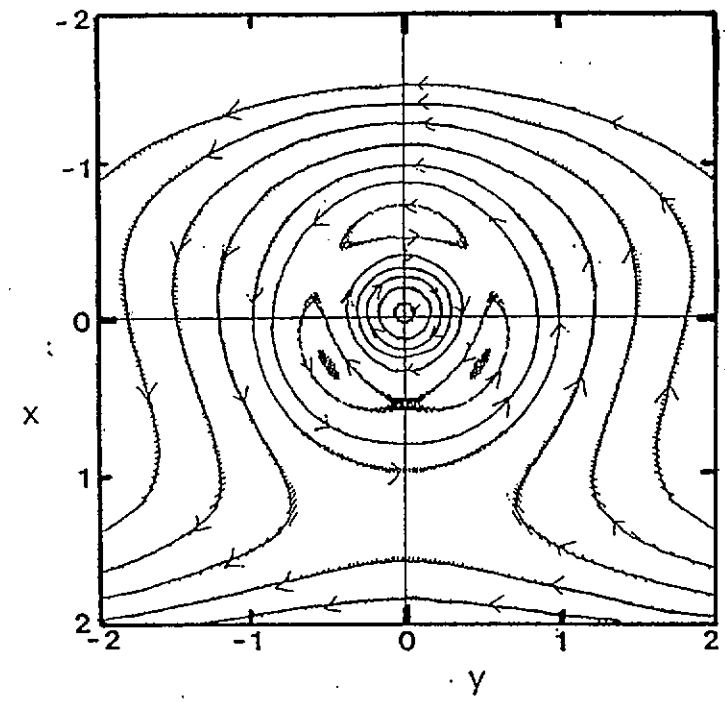

Fig. 4. Quadrupolar vortex in a parabolic background shear flow with log arithmic term (discontinuous $\nabla^2\phi$ at $r = r_o$).

$$\bar{\phi} = \phi/(\kappa - u)r_o^3$$

$$\bar{\phi}_{ex} = C\beta_o \ln(r/r_o) - \frac{1}{8}\left[(r/r_o)^3 - (r/r_o)\right]\cos\theta$$

$$- \frac{1}{24}\left[(r/r_o)^3 - (r_o/r)^3\right]\cos 3\theta$$

$$\bar{\phi}_{in} = C\left[J_o(\lambda r)/J_o(\epsilon) - 1\right] + \frac{1}{\epsilon^2}\left[J_1(\lambda r)/J_1(\epsilon) - (r/r_o)\right]\cos\theta$$

$$- \frac{1}{4}\left[J_3(\lambda r)/\epsilon J_3'(\epsilon)\right]\cos 3\theta$$

Condition on $\epsilon = \lambda r_o$: $J_3(\epsilon) = 0$.

Parameters for the above figure : $r_o = 1.0$, $\epsilon = 6.380$, $C = 0.2$ and $\beta_o = -\epsilon J_1(\epsilon)/J_o(\epsilon) = 4.978$.

Drift Wave Solitons in an Inhomogeneous Magnetized Plasma

Koichi Saeki and Yoshimitsu Amagishi
Faculty of Liberal Arts, Shizuoka University
Ohya, Shizuoka 422, Japan

The shears of electron diamagnetic drift velocity and ExB drift velocity are theoretically verified to give nonlinearities and establish a soliton of drift wave. Experimentally, a drift wave soliton is observed. Both of the propagation velocity of the soliton and the inverse of the soliton width get large with an increase in amplitude

1. Introduction

In this work, the nonlinear behavior of drift wave is investigated theoretically and experimentally. The nonlinearity of drift wave in a nonuniform magnetized plasma permits the formation of solitary waves.[1,2,3] Petviashvili[3] derived a solitary wave solution with the nonlinearity due to electron temperature gradient. The detailed investigation by Horihata-Sato[4] and Lakhin et al.[5] revealed that this nonliearity disappears. In stead of this nonlinearity, they proposed the nonlinearity caused by the nonunifromity of density gradient (the shear of electron diamagnetic drift velocity v_*) for soliton formation, and the latter group tried to explain a saw-shaped wave form observed by Buchel'nikova et al.[6] in a Q-machine as a train of solitons. Here, we study the condition of soliton formation under the existance of the shaers of electron diamagnetic drift velocity v_*

and ExB drift velocty v_E, and show theoretically that the nonlinearities due to the shears of v_* and v_E are cancelled under the normal condition of Q-machine. Experimentally, we observed a drift wave soliton along the shear layer of v_* and v_E in an inhomogeneous magnetized plasma under the condition deviating from the above one.

2. Soliton theory

We start from Hasegawa-Mima equation[7] taking into account of the zeroth order electric field,

$$\left(\frac{\partial}{\partial t} + v_E \frac{\partial}{\partial y} \right)\left(\nabla^2\phi - \phi \right) - \left(v_* + v_E'' \right)\frac{\partial \phi}{\partial y} + \left(- \frac{\partial \phi}{\partial y}\frac{\partial}{\partial x} + \frac{\partial \phi}{\partial x}\frac{\partial}{\partial y} \right)\nabla^2\phi = 0.$$

Here, v_E is steady ExB drift velocity. v_E and v_* are in the direction of y. $v_E'' = d^2v_E/dx^2$. ϕ is the perturbed potential of drift wave. Here, time t, space x and y, velocity v, potential ϕ are normalized by $1/\omega_C$, ρ_S, C_S, T/e, respectively. The dispersion relation is given by

$$\frac{\omega}{k_y} = \frac{v_* + v_E''}{1 + k_x^2 + k_y^2} + v_E \quad .$$

In the case of normal Q-machine condition, The Boltzmann relation $n = n_0 \exp(e\phi/kT)$ is maintained. Thus, $v_E = -v_*$. If $v_E'' \simeq 0$, a linear drift wave propagates in the -y direction.

A stationary solution ϕ propagating with velocity u stisfies the relation expressed by using $\eta = y - ut$ as

$$(u - v_E)\frac{\partial}{\partial \eta} - \left(- \frac{\partial \phi}{\partial \eta}\frac{\partial}{\partial x} + \frac{\partial \phi}{\partial x}\frac{\partial}{\partial \eta} \right)\nabla^2\phi = \left(u - v_E - v_* - v_E'' \right)\frac{\partial \phi}{\partial \eta} \quad .$$

Here, we look for the solution in the form[5]

$$\nabla^2\phi = f(x)\phi + g(x)\phi^2 \quad .$$

Neglecting the term of the order ϕ^3, we obtain the coefficients f, g as

$$f = 1 - \frac{v_* + v_E''}{u - v_E}, \quad g = -\frac{f'}{2(u-v_E)} .$$

For simplicity, we asuume that $v_E'' \simeq 0$ and $\delta u = u - v_E - v_* \ll v_*, u - v_E$. Then,

$$f = \frac{\delta u}{v_*} = a\delta u, \quad g = \frac{v_*' + v_E'}{2\, v_*^2} = -\frac{a}{2A} .$$

Here, $a = 1/v_*$ and $A = -v_*/(v_*' + v_E')$ represent the scale length of density gradient and the scale length of v_* and v_E shear, respectively. In the case of normal Q-machine condition $v_E = -v_*$, the nonlinear coefficient g becomes zero. Thus, the nonlinearity due to the shear of electron diamagnetic drift velocity v_* pointed out by Lakhin et al. is cancelled by the nonlinearity due to the shear of ExB dift velocity v_E under the Q-machine condition. A round soliton solution in the two dimentional space x, η perpendicular to the magnetic field is approximately represented as[3)]

$$\phi(r) = \phi_M \left[\cosh\left(\frac{2}{D} r\right)\right]^{-\frac{4}{3}} .$$

Here, $r^2 = x^2 + \eta^2$. The soliton velocity u and the soliton width D are related to the maximum amplitude ϕ_M as

$$u = v_* + v_E + \frac{v_*\, a}{4.8\, A}\, \phi_M , \qquad D = 5.8 \left(\frac{a}{A}\, \phi_M\right)^{-1/2} .$$

In the above analysis, the wave resonance with ExB plasma flow at the layer x satisfying $u = v_E(x)$ is not taken into account. Thus, this result can be applied in the case that no wave resonance exists or the wave potential at the resonance layer is enough low not to give any crucial effect to the soliton behavior.

3. Experimental setup

A discharge argon plasma is formed in the upper volume of a

cylindrical vacuume chamber, whose axis is aligned along a magnetic field of 1 ~ 2.5 gauss. The experiment is carried out in a plasma diffused from the dicharge plasma into the lower space of the chamber. This diffused plasma is line-tied to a heated oxide cathode at a temperature of 1100 K. Thus, the electron temperature of this plasma is 0.15 eV being close to the cathode temperature.

The diffused plasma has a density gradient whose characteristic length is 3cm. Because of the line-tying effect, the zeroth order density and potential of the plasma follow the Boltzman relation. Thus, this plasma maintains the relation $v_E = -v_*$ as the plasma in a Q-machine, and the wave propagates in the -y direction. In order to excite a drift wave soliton, we set up a grid in front of the cathode to make a deviation from the condition $v_E = -v_*$, and $v_E' = -v_*'$.

4. Experimental results

At first, the dispersion characteristics of linear drift wave is investigated under the condntion that the diffused plasma is line-tied to the cathode as shown in Fig. 1. Waves are excited by applying a pulse voltage to a small target. An excited pulse wave propagates in the direction of -y, and the higher frequency part of the wave propagates faster than the lower one. This is well explained by the dispersion relation under the condition $v_E = -v_*$, which is the same as the normal Q-machine one. In this plasma, drift wave pulses do not change their speed in spite of the increment of the pulse hight.

In order to excite a drift wave soliton, we apply a small dc voltage to the grid and get the situation that $v_E' + v_*' = 0$. Under

this condition, we are able to excite a drift wave soliton as shown in Fig. 2. and a drift wave shock as shown in Fig. 3. Here, v_E is nearly zero. Thus, the wave propagates in the y direction, and A has a positive value. The propagation velocities of the soliton and the shock get fast as the amplitude increases. The width of the soliton becomes narrow with an increase in amplitude. The two dimentional observation reveals that the the soliton is roughly estimated to have a round shape, but its detailed structure behaves in a complicated way.

(References)

1) K. Nozaki et al.: J. Phys. Soc. Japan 46 (1979) 983.

2) M. Makino et al.: J. Phys. Soc. Japan 50 (1981) 954.

3) V. I. Petviashvili: JETP Lett. 32 (1980) 619.

4) S. Horihata and M. Sato: J. Phys. Soc. Japan 56 (1987) 2611.

5) V. P. Lakhin et al.: Phys. Lett. A119 (1987) 348.

6) N. S. Buchel'nikova et al.: Sov. Phys. JETP 25 (1967) 548.

7) A. Hasegawa and K. Mima: Phys. Fluids 21 (1978) 87.

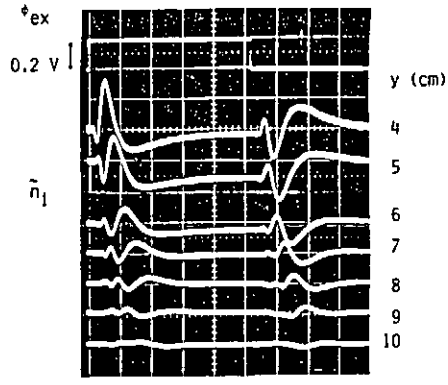

Fig. 1

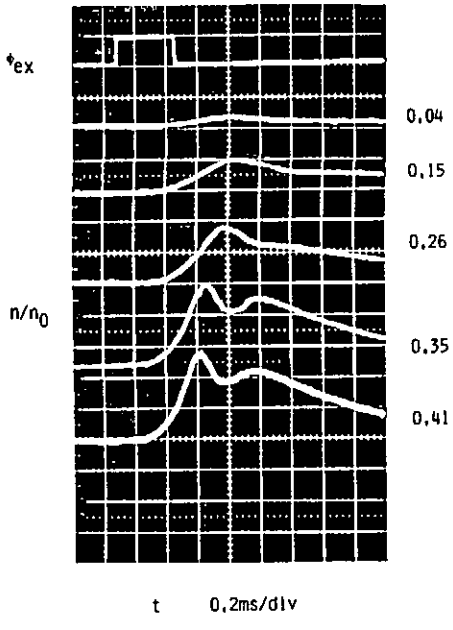

Fig. 2

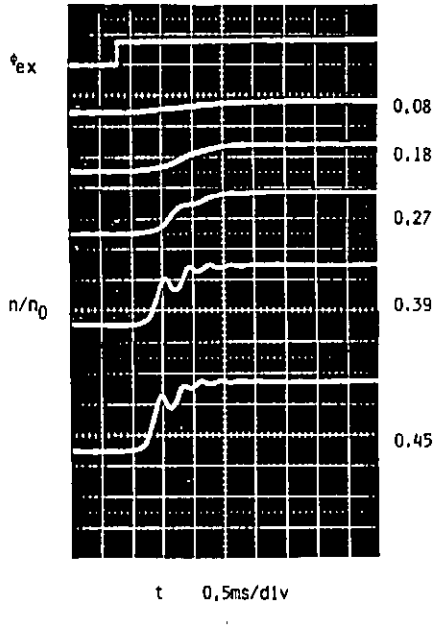

Fig. 3

II. Temperature Gradient Modes

Temperature Gradient Modes, Streamers and Anomalous Transport

A. M. Dimits, J. F. Drake, P. N. Guzdar, and A. B. Hassam
Laboratory for Plasma Research
University of Maryland
College Park, MD 20742-3511

Abstract

The nonlinear evolution of the η_i mode has been studied using a two-dimensional slab fluid model, both without and with shear. For zero shear, the instability evolves to a quasi-one-dimensional state in which streams of plasma flow from cold to hot regions over distances of order the density gradient scale length. The resulting thermal transport is of order the Bohm rate, $\chi_{\rm Bohm} \sim \rho_i v_{ti}$, where v_{ti} and ρ_i are respectively the ion thermal velocity and gyroradius. The one-dimensional fluid nonlinearity is shown to be capable of causing saturation of the instability although the $\vec{E} \times \vec{B}$ nolinearity is likely to be at least as important. In the presence of magnetic shear, the streams become radially localized over a scale length of order $\Delta x \simeq \rho_i L_s/L_t$, where L_s and L_t are respectively the shear and temperature gradient scale lengths, and a transport barrier develops at the rational surface.

1 Introduction

The η_i mode is an instability driven by negative compressibility in the presence of an ion temperature gradient [1]. A renewed interest in the η_i mode has been generated in recent years by experimental evidence for its importance in the observed degradation of energy confinement in tokamak plasmas at high density [2,3,4]. While the linear theory of these modes is fairly well understood, there are still unresolved issues concerning the nonlinear evolution of these modes and the associated transport. Various scaling laws for the thermal diffusivity $\chi_\perp$ have been proposed [5,6,7,8,9,10,11]. Those of references [8,9] are monotonically decreasing with increasing magnetic shear length L_s. This result is implausible in the limit $L_s/L_t \gg 1$ since the η_i mode is very robust in this limit [11,10]. The result of Terry et al. [10] also has a different scaling with respect to L_s than those of references [5,6,7,11]. While some 3-D simulations of the η_i mode have been performed [7,12], the issue remains unresolved.

For $L_s/L_t \gg 1$, the longest wavelength modes are capable of producing the greatest amount of thermal transport, and these modes are unlikely to be strongly affected by FLR effects. To lowest order in ρ_s/L_t, therefore, these modes can be studied using equations valid in the limit of zero gyroradius. Thus we use the following fluid equations for the ion density n, parallel velocity $v_\parallel$, and

*Research supported by the U.S. Department of Energy

temperature T.

$$\frac{dn}{dt} - D_{\|}\nabla_{\|}^2 n + n\nabla_{\|}v_{\|} = 0, \quad (1)$$

$$\frac{dv_{\|}}{dt} - \mu_{\|}\nabla_{\|}^2 v_{\|} + \nabla_{\|}(n + T + \phi) = 0, \quad (2)$$

$$\frac{dT}{dt} - \chi_{\|}\nabla_{\|}^2 T + 2\nabla_{\|}v_{\|} = H, \quad (3)$$

where "$\|$" indicates parallel to the magnetic field direction and $\frac{d}{dt} \doteq \frac{\partial}{\partial t} - \vec{\nabla}_{\perp}\phi \times \hat{z} \cdot \vec{\nabla}_{\perp} + v_{\|}\nabla_{\|}$. Also, ϕ is the potential, quasineutrality is assumed and the electron response is taken to be adiabatic, $n = n_0(x)\exp(\phi/\langle T \rangle)$, where $\langle T \rangle$ is the temperature averaged in the parallel direction. These equations are scaled according to $\frac{n}{n_0(0)} \to n$, $\frac{T}{T_0(0)} \to T$, $\frac{v_{\|}}{v_{ti}} \to v_{\|}$, $\frac{e\phi}{T_0(0)} \to \phi$, $\frac{v_{ti}\rho_i t}{a^2} \to t$, $a\vec{\nabla}_{\perp} \to \vec{\nabla}_{\perp}$, and $\frac{a^2}{\rho_i}\nabla_{\|} \to \nabla_{\|}$, where a is the system size perpendicular to the magnetic field. In these units, D is scaled to the Bohm diffusion rate $\rho_i v_{ti}$.

Equations 1-3 are reduced to 2-D by assuming $\nabla_{\|} = \alpha\frac{\partial}{\partial y}$, where

$$\alpha = \begin{cases} \text{constant} & \text{no shear} \\ \frac{x - x_s}{L_s} & \text{with shear} \end{cases}$$

They were solved numerically with n and T fixed at the boundaries $x = 0$ and 1, and periodicity imposed in the y direction. The line averaged density profile remains unchanged from its initial condition since equation 1 results in no cross-field density transport.

2 Zero-Shear Results

Figure 1 shows the temperature contours at $t = 15.0$ for a run with a 1.5 : 1 central-to-edge density ratio and $H = 1$. Narrow streams of plasma flow all the way from the cold edge to the hot center. While the number of streamers formed initially is dependent on the initial perturbation, the streamers eventually coalesce into one from each boundary. For high heating rate ($H = 2$) and a flat density profile, a "boiling" process takes place in which the streamers repeatedly split into two or more and later coalesce. At low heating rates, given by $H \lesssim \frac{D_{\|}}{L_z^2}$, where L_z is the box size parallel to the magnetic field) the transport is dominated by the lowest mode and can be calculated from quasilinear theory. Also, if the heating rate is lower than the characteristic transport rate above marginal stability then the temperature profile stays close to the marginally stable profile (associated with the particular density profile). In this regime, the energy confinement time $\tau_E \propto H^{-1}$ so that the maximum temperature is very nearly independent of H. This is a quite general statement applicable to any anomalous transport mechanism which has an associated marginally stable profile. For our model, with central to edge density ratios of order unity, the criterion for this is $H \lesssim 1$. Figure 2 shows the variation of confinement time with heating rate for various density profiles. Note that for a flat density profile, the H^{-1} regime occurs at lower heating rates.

3 One-Dimensional Model

Motivated by the quasi-one-dimensional nature of the streamers, a one-dimensional reduction of equations 1-3 was used to study saturation of the η_i instability by the parallel nonlinearity alone.

For $\alpha \doteq \frac{k_\parallel}{k_\perp} \ll \sqrt{\eta_i - 2}$, the $\frac{dn}{dt}$ term can be neglected in equation 1 and linearly, the mode is purely growing. Then the parallel nolinearity becomes comparable to the $\vec{E} \times \vec{B}$ nonlinearity if $\frac{\partial}{\partial x} \leq \frac{1}{L_n}$ for the perturbations. The background density and temperature gradients are fixed with $L_n = a$ and $L_t = a/\eta_i$, the $\vec{E} \times \vec{B}$ nonlinearities are neglected and only the linear part of the adiabatic electron response is kept to obtain the following equations,

$$\frac{\partial v_\parallel}{\partial t} + v_\parallel \nabla_\parallel v_\parallel = \mu_\parallel \nabla_\parallel^2 v_\parallel - \nabla_\parallel T, \tag{4}$$

$$\frac{\partial T}{\partial t} + v_\parallel \nabla_\parallel T = (\eta_i - 2)\nabla_\parallel v_\parallel + \chi_\parallel \nabla_\parallel^2 T + H. \tag{5}$$

T is now the temperature perturbation, H is chosen so that $\frac{d\langle T \rangle}{dt} = 0$, and $\eta_i - 2 \ll 1$ has been assumed. Equations 4 and 5 are easily recognized as sound wave equations with negative compressibility if $\eta_i > 2$. The evolution of this system was followed numerically starting from the linear regime. This evolution has a linear growth phase, a steepening phase and then a phase in which the evolution can be quite chaotic before it reaches a final state. In the case of the boundary conditions $v_\parallel = \nabla_\parallel T = 0$ at the boundaries $z = 0$ and $z = L_z$, velocity and temperature profiles finally reach a steady state such as the one shown in figure 3. These equilibrium profiles can be viewed as consisting of three regions as shown in the figure. In region I, all terms in equations 4 and 5 balance yielding the scaling relations $T \sim \eta_i - 2$, $v_\parallel \sim \sqrt{\eta_i - 2}$, $l \sim \frac{\chi_\parallel}{\sqrt{\eta_i - 2}}$, and $H \sim \frac{(\eta_i - 2)^2}{\chi_\parallel}$, where l is the scale length and $\mu_\parallel \simeq \chi_\parallel$ is assumed. In region II, the dissipation can be neglected, giving $T = C_1 - \frac{1}{2}v_\parallel^2$, and $\frac{1}{3}v_\parallel^3 + (\eta_i - 2)v_\parallel = C_2 - Hz$, where C_1, C_2, and H are determined by connection with region I. Region III is the streamer. Here, $\nabla_\parallel T$ term can be neglected from equation 4. The solution of this equation is then

$$v_\parallel = -\frac{2\mu_\parallel}{l} \tanh \frac{z}{l},$$

where l is determined by connecting to region II. For $\chi_\parallel = \mu_\parallel$, equation 5 can be analytically solved. The size of the temperature drop in region III is found to be $\Delta T = 2(\eta_i - 2)\log 2$, in agreement with the simulation results. Through the density equation, H can be identified with the transport rate. Putting back the normalizations, the above result

$$\chi_{\text{perp}} \sim \frac{L_n^2 v_{ti}^2 (\eta_i - 2)^2}{\chi_\parallel}.$$

For periodic-in-z boundary conditions, the final states also have one streamer per period although they have a nontrivial time dependence. The behavior in this case is qualitatively similar to that of the two-dimensional simulation results.

4 2-D Sheared Slab Results

Some runs with finite magnetic shear have been made. These runs have no heating and the instability is driven by fixing the temperature at different values at the boundaries $x = 0$ and 1. A thermal diffusion term in the x direction is kept to control the heat flux in these runs. Figure 4 shows the flow pattern for a run with the density profile $n(x) = \sqrt{1 + 3x}$, and shear length $L_s = 0.5$. The main observations are as follows. Firstly, the flow streams become localized by the presence of shear

in agreement with the local linear theory. Secondly, a transport barrier is observed at the rational surface where a smooth radial flow would require a large shear in the parallel velocity. This shear is damped by a small perpendicular diffusion of the parallel velocity. Classical or anomalous viscosity can provide this diffusion. FLR effects in the density equation may, however overcome this barrier. Thirdly, if the instablility is localized away from the boundaries, then the temperature profile relaxes to close-to-marginal except at the transport barrier near the rational surface.

References

[1] L. I. Rudakov and R. Z. Sagdeev, Dokl. Akad. Nauk. SSSR **138**, 581 (1961) [Soviet Phys. Doklady **6**, 415, (1961)].

[2] M. Greenwald et al., *10th International Conference on Plasma Physics and Controlled Nuclear Fusion Research,* London (IAEA, Vienna, 1984), Vol. I, p.45.

[3] G. L. Schmidt et al., *12th International Conference on Plasma Physics and Controlled Nuclear Fusion Research,* Nice, France, paper A41 (IAEA, 1988), Vol. I, p.45.

[4] M. Zarnstorff et al., *12th International Conference on Plasma Physics and Controlled Nuclear Fusion Research,* Nice, France, paper A33, (IAEA, 1988).

[5] B. Coppi, M. N. Rosenbluth, and R. Z. Sagdeev, Phys. Fluids **10** 582 (1967).

[6] B. B. Kadomtsev and O. P. Pogutse, in Reviews of Plasma Physics, Vol. 5 (Leontovich, M. A., Ed.), Consultants Bureau, New York, London (1970) 249.

[7] W. Horton, R. Estes, and D. Biskamp, Plasma Phys. 22, 663 (1980).

[8] J. W. Connor, Nucl. Fusion **26** (1986) 193.

[9] G. S. Lee and P. H. Diamond, Phys. Fluids **29**, 3291 (1986).

[10] P. W. Terry et al., Phys. Fluids **31**, 2920 (1988).

[11] T. Antonsen et al., *12th International Conference on Plasma Physics and Controlled Nuclear Fusion Research,* Nice, France paper D47, (IAEA, 1988).

[12] R. D. Sydora et al., UCLA Center for Plasma Phys. and Fusion Eng. Report No. PPG-1185.

Figures

1. (a) Temperature contours for 2-D heated slab at $t = 15.0$ for $H = 1$, center to edge density ratio=1.5. (b) Corresponding flow vectors.
2. Confinement time vs. heating rate for various density profiles.
3. Diagram of steady state temperature and velocity profiles for 1-D model.
4. Velocity vectors for ramped density profile $n(x) = \sqrt{1 + 3x}$ with strong shear $L_s = 0.5$.

Fig. 1a

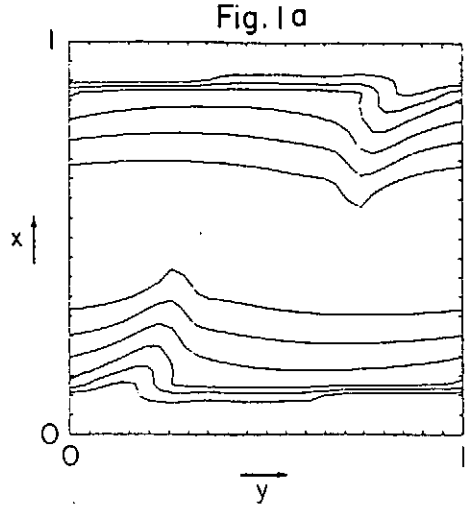

Fig. 1b

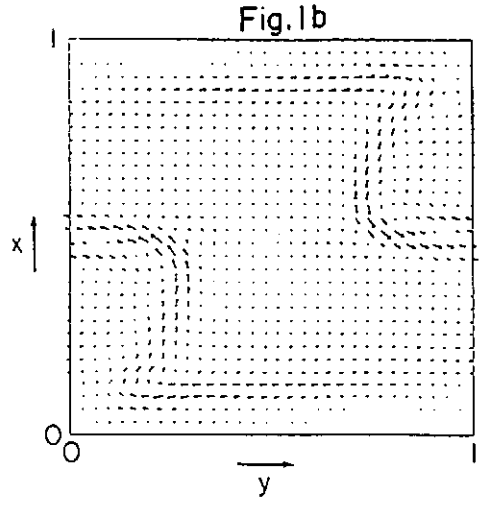

Fig. 2

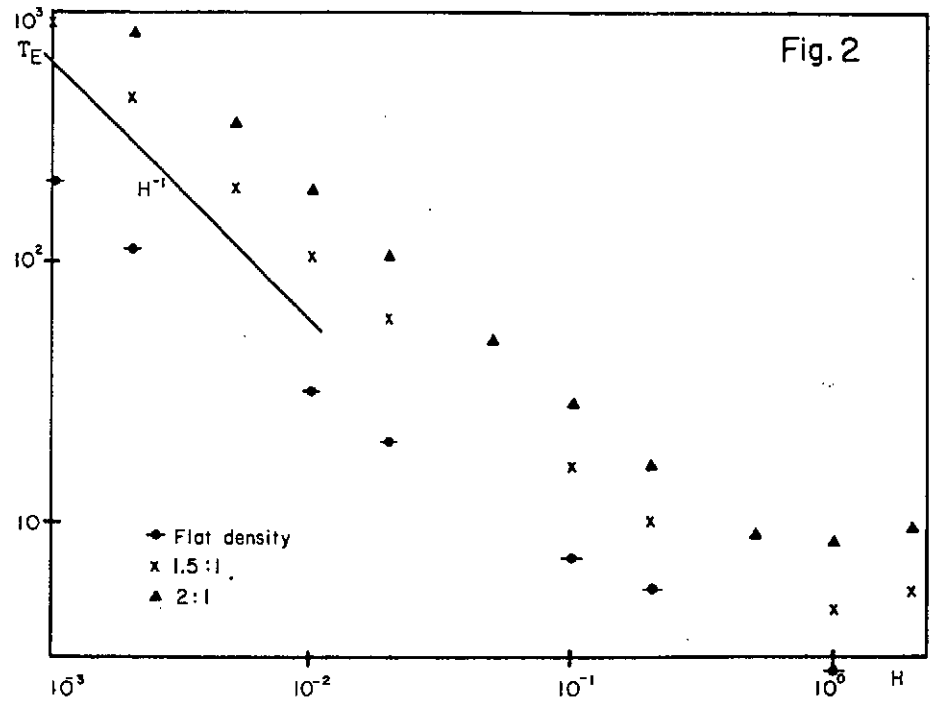

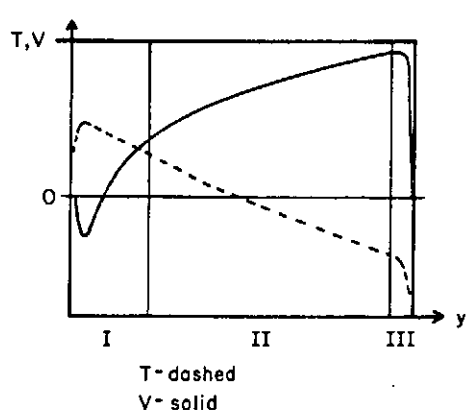

Fig. 3

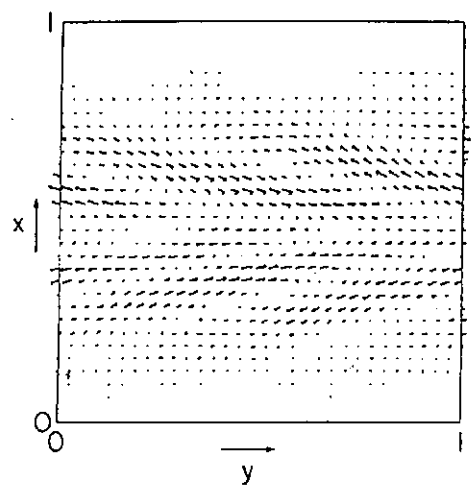

Fig. 4

THEORY OF ION ANOMALOUS TRANSPORT IN IMPROVED CONFINEMENT REGIME

T. S. HAHM and W. M. TANG
Princeton Plasma Physics Laboratory
Princeton, New Jersey 08543

Although the energy confinement time in improved confinement regimes (H-mode and Supershot) is typically longer than L-mode cases, the ion thermal transport nevertheless remains very anomalously large. This work considers: (i) the ion temperature gradient driven turbulence in H-mode plasmas where the density profile is either hollow or flat such that the trapped electron modes are suppressed; and (ii) the collisionless trapped electron modes in supershots were the density profile is peaked enough such that the η_i-modes is relatively feeble. The calculated χ_i from weak turbulence theory of η_i-mode for hollow density profiles increases abruptly from zero near the threshold and remains small into the flat density regime away from the threshold as the density scale length is increased. On the otherhand, the collisionless trapped electron modes for peaked density profiles are shown to be robustly unstable with toroidicity–induced ballooning mode structure and negligible shear-induced damping in the presence of the radial gradients in toroidal plasma rotation and ion temperature. The fluctuations-induced ion thermal diffusivity (χ_i) and ion toroidal momentum diffusivity (χ_ϕ) are roughly the same for this model. The observed improvement in confinement could be due to the fact that there are fewer *resonant* trapped electrons when the density profile is sufficiently peaked.

I. Weak Turbulence Theory of η_i-modes for H-mode Plasmas

Our theoretical model consists of the Boltzmann electron response and collisionless gyrokinetic ion response in a sheared slab geometry. The ion response is simplified by the fluid approximation $\omega \gg k_\parallel v_{ti}$ which has been shown to be good for the inverted density profiles[1] considered here. The quasi-neutrality condition as well as the small gyro-radius expansion for relatively longwavelength modes ($k_\perp^2 \rho_i^2 < 1$) yields the well–known second order differential eigenmode equation (the linear part of Eq. (6)).

The eigenmode equation can easily be solved to yield the following dispersion relation for the lowest harmonic,

$$\Omega\{(1+b_s)\Omega - 1 + b_y(1+\eta_i)\} = i(L_n/L_s)(\{\Omega + (1+\eta_i)/\tau - b_y(\Omega + (1+2\eta_i)/\tau)\}^{1/2}) \{\Omega + (1+\eta_i)/\tau - 3b_y/2(\Omega + (1+2\eta_i)/\tau)\}^{1/2}, \quad (1)$$

where $\Omega = \omega/\omega_{*e}$, $\tau = T_e/T_i$, $b_y = k_y^2\rho_i^2$, and $b_s = \tau b_y$, other notations are standard.

At marginal stability, we have $\Omega_{\rm real} = \{1 - b_y(1+\eta_i)\}/(1+b_s)$, and the threshold;

$$\eta_{c2} = -(1+\tau)(1+\frac{3}{2}b_y), \quad (2)$$

where we have taken a root which gives instability for $|\eta_i|$ above threshold and does not violate the fluid approximation. There exists another root $\eta_{c1} = -(1+\tau)(1+b_y)$ at the same $\Omega_{\rm real}$. However, we obtain

marginally stable (neutral) mode for $|\eta_{c2}| > |\eta_i| > |\eta_{c1}|$. Near marginality, we can obtain the growth rate perturbatively,

$$\mathrm{Im}(\Omega) = (\mathrm{L_n/L_s})[\tau(1+\mathrm{b_s})\{1-\mathrm{b_y}(1+\eta_i)\}]^{-1}(1-\frac{5}{2}\mathrm{b_y})(\eta_i-\eta_{c1})^{1/2}(\eta_i-\eta_{c2})^{1/2}. \quad (3)$$

Therefore we have instability for $|\eta_i| > |\eta_{c2}|$. The $[...]^{-1}$ factor in Eq. (3) shows the trend that $\gamma < |\omega_{\mathrm{real}}|$ is satisfied even away from the marginal stablity for finite b_s. A more stringent condition for the applicability of weak turbulence expansion is $\gamma < |\delta\omega|$, where $\delta\omega = \omega - \omega_{*e}$. From Eqs. (1) and (3) we can easily show that this condition is satisfied for $b_s > |L_n/L_s|$. Thus, we expect the weak turbulence expansion to be valid for a wide range of negative η_i values including the near flat density profile case,$|L_n| \approx L_s$. The radial mode structure is approximately given by $\phi \propto e^{x^2/2\Delta x^2}$, where $\Delta_x \approx |\frac{L_s}{L_n}\Omega|^{1/2}\rho_s$.

We now proceed to study the nonlinear saturation of these fluctuations using the weak turbulence expansion scheme. The dominant nonlinear saturation mechanism is found to be the coherent mode coupling to weakly stable shorter wavelength modes. This is because the ion Compton scattering is negligible for the moderately long ($|L_n/L_s| < b_s \ll 1$) wavelength modes which are most easily excited. The frequency matching condition on the other hand, is approximately satisfied as will be shown later. The electron nonlinearity is assumed to be small. Since the formal expansion scheme is standard, we simply present the final nonlinear eigemode equation which can be obtained from the nonlinear ion gyrokinetic equation,

$$(\partial_t + v_\parallel \hat{b}\times\nabla)g + i[\omega\tau + \omega_{*e}\{1+\frac{\eta_i}{2}(v^2-3)\}]\phi J_0 F_m = \nabla\langle\phi\rangle \mathrm{x}\hat{\mathrm{b}}\cdot\nabla \mathrm{g}, \quad (4)$$

where g is the nonadiabatic part of the perturbed distribution function. By requiring quasineutrality up to third order, we obtain the formal nonlinear eigenmode equation.

$$(1+\frac{T_e}{T_i})\phi_k - \int d^3v J_0^2(-i\hat{L}_k)[\omega\tau + \omega_{*e}\{1+\frac{\eta_i}{2}(v^2-3)\}]F_m\phi_k = \int d^3v J_0 g_k^{(3)}, \quad (5)$$

where $\hat{L}_k = i(\omega - k_\parallel v_\parallel + io)^{-1}$ is the linear test particle propagator, $g^{(3)}$ is the nonlinear correction to the distribution function at k due to the back reaction of the nonlinearly produced modes on the test mode k. Here, the first two terms on L.H.S. are from the adiabatic responses of electrons and ions respectively. The third term is the nonadiabatic linear response, while R.H.S. gives the nonlinear response. After the fluid approximation, Eq. (5) simplifies to

$$[1+\frac{(1+\eta_i)}{\Omega\tau} - \frac{3}{2}b_y\frac{(1+\eta_i)}{\Omega\tau}](\partial_x^2 + Q_L(x))\phi_k = \sum_{k'=k''-k}(\omega\omega'')^{-1}(k\times k'\cdot\hat{b})^2(\frac{\omega_{*e}}{\omega_k} - \frac{\omega'_{*e}}{\omega_{k'}})$$
$$\cdot[\langle J_0^2 J_0'^2\{1+\frac{\eta_i}{2}(v^2-3)\}\rangle - \epsilon^{(1)-1}(\frac{\omega'_{*e}}{\omega_{k'}} - \frac{\omega''_{*e}}{\omega_{k''}})\langle J_0 J_0' J_0''\{1+\frac{\eta_i}{2}(v^2-3)\}\rangle^2$$
$$\langle -J_0 J_0' J_0''\{1+\frac{\eta_i}{2}(v^2-3)\}\rangle^2/\{1-(1-\Gamma_0(b''))(1+\eta_i)\}]|\phi_{k'}^2|\phi_k, \quad (6)$$

where $Q_L(x) = \frac{1}{\Omega} - 1 - b_s\{1+\frac{(1+\eta_i)}{\Omega\tau}\} + \{1+\frac{(1+\eta_i)}{\Omega\tau} - b_y(1+\frac{(1+2\eta_i)}{\Omega\tau})\}\frac{L_n^2x^2}{L_s^2\Omega^2}$, $\langle...\rangle$ is the average over the velocity space. In Eq. (6), the first and second term on R.H.S. correspond to the approximated ion Compton scattering and coherent 3-mode coupling. The last term on R.H.S. is the induced scattering which comes from the low frequency virtual mode contribution to $\epsilon^{(1)}$. We note that for the parameter regime considered, the 3-mode coupling term is dominant due to the following reasons: (1) Although there exists a finite dispersion, this is due to small finite Larmor radius correction ($\approx b_y$). Thus, the frequency mismatch is small such that $\epsilon^{(1)}(\omega'', k'')$ is approximately resonant, and the 3-mode coupling term would be large.

(2) There exists large cancellation between the ion Compton scattering and the induced scattering at the moderately long wavelength regime relevant in this work. The remaining term would be smaller than the 3-mode coupling term by an order b. By keeping only the dominant 3-mode coupling contribution to the nonlinear eigenmode equation, we note that the imaginary part of the nonlinear potential acts effectively as a nonlinear damping on the test mode via energy transfer to shorter wavelength modes. In a sheared slab geometry with multi-rational surfaces, the $Q_{\rm NL}$ can be approximated by $Q_{\rm NL}(0)$, since significant energy transfer to ion can occur through background modes k' at $x = 0$ due to the finiteness of x'. By solving Eq. (6) for Ω treating $\mathrm{ImQ_{NL}}(0)$ as a given quantity, we obtain $\gamma_{NL} = \gamma_L - |\omega_{*e}|\mathrm{ImQ_{NL}}(0)$. This describes a competition between the linear growth and the nonlinear transfer which acts as an effective damping on the test mode. When these two processes balance, we obtain nonlinear saturation.

Finally, we derive the saturation levels of various fluctuation and the turbulent ion thermal diffusivity. By using Eq. (6) for $\mathrm{Im}Q_{NL}(0)$ and the radial mode width Δx for k_r^{-1}, we obtain

$$\frac{\delta T_i}{T_i} \cong (\frac{\gamma}{\delta\omega})^{1/2}\Delta x/L_T = J\rho_i/L_T, \quad \frac{|e|\phi}{T_i} \cong \frac{L_T}{|L_n|}\frac{\delta T_i}{T_i} \tag{7}$$

where

$$J(\eta_i, b_y) = b_y^{-1/2}(1 - \frac{5}{2}b_y)^{1/2}(1 - b_y(1+\eta_i))^{1/2}(|\eta_i| - |\eta_{c2}|)^{1/4}(|\eta_i| - |\eta_{c1}|)^{1/4}(|\eta_i| - 1 - \tau)^{-1/2},$$

and

$$\chi_i = -L_T\mathrm{Im}\Sigma_k(\mathrm{ck}_\theta\phi\delta\mathrm{T_i}/\mathrm{B_0})/\mathrm{T_i} \cong \gamma\omega^{-2}\mathrm{k}_\theta^2|\phi|^2 \cong \mathrm{IcT_i}|\mathrm{e}|^{-1}\mathrm{B_0^{-1}}\rho_\mathrm{i}/\mathrm{L_s}, \tag{8}$$

where

$$I = \pi^{-1}b_y^{-1/2}(1 - \frac{5}{2}b_y)^2(1 + b_s)^{-1}(1 - b_y(1+\eta_i))^{-1}(|\eta_i| - |\eta_{c2}|)(|\eta_i| - |\eta_{c1}|)\{|\eta_i| - (1+\tau)\}^{-1}.$$

It is noteworthy to point out that both saturation levels for fluctuation and thermal diffusivities are considerably smaller than their strong perturbulence counterparts and vanish at the threshold η_{c2}. Near marginality $\chi_i \propto |\eta_{c2} - \eta_i|$, while $\delta T_i/T_i \propto |\eta_{c2} - \eta_i|^{1/4}$. Therefore, the 'turn on' of the ion temperature gradient turbulence is rather sharp near the threshold. On the other hand, away from the threshold.(as $|L_n|$ is increased), the turbulence level and thermal diffusivity remains small. Hence, we should not expect dramatic confinement degradation as the density profile becomes flatter (if threshold has been already exceeded).

II. Collisionless Trapped Electron Mode for Supershots

Previous studies have indicated that collisionless trapped-electron instabilities are likely to be the most prominent type of microinstability active in peaked-density-profile, collisionless plasmas such as TFTR supershots. In the present theoretical analysis, the circulating electrons are assumed to obey the Boltzamnn relation, while the trapped electrons are described by the bounce averaged drift kinetic equation. This is justified by the disparity of frequencies involved ($\omega \ll \omega_{be} < \omega_{te}$). Taking moment, the electron density response can be written formally as $\frac{\delta n_e}{n_0} = (1 - i\delta)\frac{|e|\phi}{T_e}$, where the expression for δ due to resoant contribution from trapped electrons is complicated due to the toroidal coupling and the bounce average.[2] However, it is worthwhile to point out the dependence on the densiy scaling length L_n. Keeping only the resonant part due to the precessional drift resonance, $(\omega - \hat{\omega}_{de})$,

$$\delta \propto \frac{2(2\epsilon)^{1/2}}{\sqrt{\pi}}\mathrm{Im}\int_0^\infty \mathrm{dEE^{1/2}e^{-E}}\frac{\Omega - 1 - \eta_e(\mathrm{E} - 3/2)}{\Omega - \mathrm{C_gE}\epsilon_\mathrm{n}}.$$

$$\simeq (\frac{R}{L_n})^{3/2}(\frac{\Omega}{C_g})^{1/2}\bar{e}^{\frac{\Omega}{C_g}\frac{R}{L_n}}[\eta_e\{\frac{\Omega R}{C_g L_n} - \frac{3}{2}\} + 1 - \Omega], \tag{9}$$

where $\Omega \equiv \omega/\omega_{*e}$, $\epsilon \equiv E/T_e$, $\epsilon = r_o/R$, $\epsilon_n = L_n/R$, $Cg \simeq 1.2$ typically.[3] From Eq. (9), we can see that there are fewer *resonant* trapped electrons when the density profile is sufficiently peaked ($\sim \bar{e}^{\frac{\Omega}{Cg}\frac{R}{L_n}}$). The observed improvement in confinement of TFTR supershot could be due to this effect. For ions, we make the fluid approximation. Following the standard procedure, we obtain the eigenmode equation from the quasi-neutrality condition using ballooning representation θ.

$$[1 - i\delta - \frac{1}{\Omega} + \{b_s + b_y(1+\eta_i)\}(1+\hat{s}^2\theta^2)]\phi + (\eta_s\Omega)^{-2}\{1 + \frac{(1+\eta_i)}{\Omega\tau}\}\partial_\theta^2\phi + iJ(\eta_s\Omega^2)^{-1}\partial_\theta\phi$$
$$+ 2\epsilon_n\Omega^{-1}(\cos\theta + \hat{s}\theta\sin\theta)\{1 + \frac{(1+\eta_i)}{\Omega\tau}\}\phi = 0, \tag{10}$$

where $\eta_s^2 = b_s q^2 R^2 L_n^{-2}$, $J = -(\frac{dV\phi}{dr})\frac{L_n}{C_s}$. It is well known that Eq. (10) in the absence of the radial shear in toroidal plasma rotation v_ϕ (J term)[4] yields the toroidicity induced drift mode for $\epsilon_n \gtrsim 0.1$ typically. Here, we show that this result is not qualitatively affected by the presence of J. By transforming away the third term of Eq. (10) via $\phi = \psi exp[-iJ\eta_s\theta/(1 + \frac{1+\eta_i}{\Omega\tau})]$, we obtain a Schrödinger-like equation for ψ. Following a perturbative analysis described in Ref. 5, it can be shown that the toroidicity induced mode structure is maintained for

$$\epsilon_n > \epsilon_c \cong b_s\hat{s}[1 - b_y(1+\eta_i)(1+\pi^2\hat{s}^2/4) - J^2\{1 + \frac{(1+\eta_i)}{\tau}\}/4]/$$
$$[1 + b_s\{1 + \hat{s}^2(\frac{\pi^2}{4} + \pi(1 + \frac{(1+\eta_i)}{\tau}))\}], \tag{11}$$

This condition is easily satisfied for a typical average value of L_n taken over the plasma profile. Therefore, it is likely that the collisionless trapped electron mode remains robust in the presence of the radial shear in toroidal flow. This is because the mode structure is standing-wave-like along the field line with negligible shear-induced ion Landau damping. This is in contrast to the usual slab-like Pearlstein-Berk mode structure. Finally in our collisionless trapped electron mode model with radial shear in the toroidal rotation, both the ion temperature and toroidal angular momentum are convected randomly by fluctuation-induced E × B plasma motion. Therefore, the diffusivities of those quantities should be approximately the same.

ACKNOWLEDGEMENTS

We are grateful to F.W. Perkins for helpful discussions regarding the role of resonant trapped electrons in plasmas with peaked density regime. This work was supported by the United States Department of Energy Contract No. DE–AC02–76–CHO3073.

References

[1]T.S. Hahm and W.M. Tang, Princeton Plasma Physics Laboratory Report PPPL-2565, 1988 (To appear in Phys. Fluids)

[2]C.Z. Cheng and L. Chen, Nucl. Fusion **21**, 403 (1981).

[3]J.C. Adam, W.M. Tang, and P.H. Rutherford, Phys. Fluids **19**, 561 (1976).

[4]N. Mattor and P.H. Diamond, Phys. Fluids **31**, 1180, (1988).

[5]L. Chen and C.Z. Cheng, Phys. Fluids **23**, 2242 (1980).

The Kolmogorov's spectrum in the η_e-turbulence

N. Bekki,[a] W.Horton, B.G Hong, T.Tajima and H.Moriguchi[b]

Institute for Fusion Studies, The University of Texas at Austin, Austin, Texas 78712, USA

(a) Nihon University, Koriyama, Fukushima 963, JAPAN

(b) Department of Physics, Nagoya University, Nagoya 464, JAPAN

I. Introduction

In order to explain the anomalous transport of electrons in tokamaks, we propose a set of reduced nonlinear equations that describe the coupling of linearly unstable short wavelength (ρ_e) electrostatic fluctuations driven by the electron temperature gradient(η_e) to the longer wavelength (c/ω_{pe}) electromagnetic fluctuations. The instability is the toroidal version of the η_e driven lower hybrid drift mode in the presence of the electron temperature gradient emphasized by Guzdar et al. [1] for a slab. The growth rate is driven by the local bad curvature and the electron temperature gradient.[2] Since the system of the reduced equations is weakly 3D, we may consider the possibility of an inverse cascade in the energy spectrum, as in the 2D Navier-Stokes turbulence. Such an inverse cascade may explain the free energy source of the magnetic fluctuations, which has not been specified previously. For the η_e mode, this inverse cascade, or mode coupling to the larger space scales, drives a coupling to

the magnetic fluctuations at the scale c/ω_{pe} . The nonlinear dynamics of short wavelength drift wave instabilities driven by the electron temperature gradient may reveal the source of the electron collisionless skin depth turbulence. We show numerically that the k-spectrum is peaked in the skin depth wavelength region at the mixing length amplitude. This suggests that the level of magnetic turbulence is sufficient to produce the empirical neo-Alcator type of confinement formula.[3] Spectral structures at the saturation level play an important role in evaluationg the empirical laws. We focus our attention on a spectral structure, indicating the nonlinear interaction between the electrostatic and electromagnetic vortices at the saturation level, in the η_e-turbulence.

II. Nonlinear Model Equations

The equations describing the toroidal η_e used here are based on the hydrodynamic electron equations assuming an adiabatic ion density response, quasineutrality, and the conservatin of particles, parallel electron momentum and electron thermal energy in the region on the outside of the torus. The dominant nonlinearities consist of the $\mathbf{E}\times\mathbf{B}$ convective derivative and the $\mathbf{B}\cdot\nabla$ gradient due to the perturbation in th magnetic field lines. In writing these nonlinearities we use the Poisson bracket operator defined by $[\ f,g\ ]=\hat{\mathbf{z}}\cdot\nabla f\times\nabla g$. The derivation of the nonlinear equations and comparison of the linear hydrodynamic models with linear Vlasov theory, and the normalizations are given in Horton et al.[2] For the perturbed electrostatic potential ϕ , the parallel vector potential A, and the perturbed

electron pressure $\tilde{p}$, we have nonlinear model equations as follows :

$$\left(1-\nabla_\perp^2\right)\frac{\partial\phi}{\partial t} = \left(1-2\epsilon_n+\tau(1+\eta_e)\nabla_\perp^2\right)\frac{\partial\phi}{\partial y}+2\epsilon_n\frac{\partial\tilde{p}}{\partial y}+\tau[\phi,\nabla_\perp^2\phi] + \frac{1}{\tau}\left(\frac{\partial}{\partial z}\nabla_\perp^2 A-\frac{\beta_i}{2}[A,\nabla_\perp^2 A]\right)+d_c\nabla_\perp^2\phi \quad (1)$$

$$\left(\nabla_\perp^2-\frac{\beta_i}{2}\right)\frac{\partial A}{\partial t} = \tau\frac{\partial\phi}{\partial z}-\tau\frac{\beta_i}{2}[A,\phi]-\tau\frac{\partial\tilde{p}}{\partial z}+\tau\frac{\beta_i}{2}[A,\tilde{p}] + \tau\frac{(1+\eta_e)}{2}\beta_i\frac{\partial A}{\partial y}-\tau[\phi,\nabla_\perp^2 A]-\eta\nabla_\perp^2 A \quad (2)$$

$$\frac{\partial\tilde{p}}{\partial t} = -[\tau(1+\eta_e)-2\tau\Gamma\epsilon_n]\frac{\partial\phi}{\partial y}-2\tau\Gamma\epsilon_n\frac{\partial\tilde{p}}{\partial y}-\tau[\phi,\tilde{p}] - 2\tau\Gamma\epsilon_n\frac{\partial}{\partial y}(\tilde{p}+\tau\phi)-\Gamma\left(\frac{\partial\nabla_\perp^2 A}{\partial z}-\frac{\beta_i}{2}[A,\nabla_\perp^2 A]\right)+\chi_\perp\nabla_\perp^2\tilde{p} \quad (3)$$

where $\Gamma = 5/3$ in the fluid theory, ϵ_n=Ln/R, η_e=Ln/LT, τ=Te/Ti, $\beta_i = 8\pi n\mathrm{Ti}/B_0^2$, the classical diffusion coeficients are (d_c , η , $\chi_\perp$) to absorb energy transformed to $|k|\to\infty$ which is outside the range of the fluid equations. We define the volume average by $\langle F\rangle = V^{-1}\int d^3x\, F(x,y,z,t) = L_x^{-1}\int dx\,\bar{F}(x,t)$ with the property $\overline{[f,g]}_{y,z} = -\partial_x\overline{\left(\frac{\partial f}{\partial y}g\right)} = \partial_x\overline{\left(f\frac{\partial g}{\partial y}\right)}$ where the bar denotes the y,z average. The crossfield correlation function, giving the $\mathbf{E}\times\mathbf{B}$ transport of thermal energy,

$$Q_{es}(x) = \overline{v_x\tilde{p}_e}\ , \quad (4)$$

determines the input from the gradient to the total fluctuation energy. The three fields energy components are

$$E_\phi = \frac{1}{2}\left\langle\phi^2+(\nabla\phi)^2\right\rangle\ ,\ E_A = \frac{1}{2}\left\langle(\nabla^2 A)^2+\frac{\beta_i}{2\tau}(\nabla A)^2\right\rangle\ ,\ E_p = \frac{1}{2}\left\langle(\tilde{p})^2\right\rangle\ . \quad (5)$$

The total energy $E_T = E_\phi + E_A/\tau^2 + E_p/\tau\Gamma$ grows and decays according to

$$\frac{dE_T}{dt} = \left(\frac{1+\eta_e}{\Gamma}+2\tau\epsilon_n\right)\langle Q_{es}\rangle - d_c\left\langle(\nabla_\perp\phi)^2\right\rangle-\frac{\eta}{\tau^2}\left\langle(\nabla_\perp^2 A)^2\right\rangle-\frac{\chi_\perp}{\tau\Gamma}\left\langle(\nabla_\perp p)^2\right\rangle\ . \quad (6)$$

III. Numerical Simulation

Equations (1)-(3) are solved numerically as an initial-value problem with periodic boundary conditions. In order to avoid aliasing errors, we use the efficient truncation scheme[4] with respect to the x-y plane and the finite-difference scheme with respect to the z direction in a cubical box (Lx, Ly, Lz) with periodic boundary conditions. The time marching is accomplished by use of the Runge-Kutta scheme. We choose the parameters that the system is unstable linearly ; $\eta_e > 1$, $\varepsilon_n < 0.4$, $\beta_i = 0.01$, Te=Ti, $d_c = 0.1$, $\eta = 0.05$, $\chi_\perp = 0.1$. Then the maximum growth rate is approximately $0.2 \sim 0.4$ at the short wavelength regions.[2] The number of grid points is 64*64*8 ; $Lx = Ly = 10\pi$ scaled by ρ_e, $Lz = 20\pi$ scaled by Ln. The magnetic shear is neglected in our simulation.

The saturation levels are independet of the initial phase conditions and amplitudes since our system grows with linear instability. Our simulations show that the nonlinear mode-coupling terminates the exponential growth phase of linear instability and excites the convective-cells (kz=0 modes). We observe a transfer of energy along the spectrum to longer wavelength of order c/ω_{pe} . The spectral features are established by the long wavelength components produced after the break of the exponential linear growth phase. The magnetic fluctuations saturate into large scale magnetic votex structures (See Figure) formed in the steady state. The total energy approximately equals to the pressure energy since $E_p > E_\phi > E_A$.

IV. Concluding Remarks

In Fig.1 the x-y contour plots of $\phi(x,t)$, $A(x,t)$ and $\tilde{p}(x,t)$ at the fixed z and t=50 (the steady turbulent state) are shown. The contours of potential fluctuation, which are the streamline of $E \times B$ drift motion, show that the $E \times B$ flows are turbulent. The characteristic scale is approximately the long wavelength collisionless skin depth, which leads to the Ohkawa type scaling formula.[5] The final levels of the steady state are weakly enhanced over the mixing length level with the appropriate dissipations used here to stop the slow built-up of high k-modes, but the saturation level, which is characterized by the break of the exponential growth, is determined by the dissipationless mixing length formulas.[2] Figure 2 shows that the evaluation of the local heat flux by the mixing length formula is valid for $3 \gtrsim \eta_e \approx 1$, other parameters are fixed. The mixing length formula overestimates the heat flux for $\eta_e \gtrsim 3$. Figure 3 is the wave-number spectrum of the pressure energy ; $E_p(k_y) = \sum_{k_x} E_p(k)$ and $E_p(k_x) = \sum_{k_y} E_p(k)$. This spectrum is corresponding to the contour plot of the pressure fluctuation in Fig.1. Figure 3 shows that the pressure energy spectrum, approximately equals to the total energy spectrum, is almost isotropic and proportional to k^{-m} with $1.5 < m < 1.7$ in the appropriate wavenumber range (we may call an inertial-range), which is a Kolmogorov type spectrum[6] based on an assumption that the action of energy-range excitation on inertial-range excitation is asymptotically a distortion-free convection. A phenomenology was first proposed by Kraichnan for uncorrelated MHD.[6] Grappin

et al.[7] found that the energy has a -3/2 power-law index as in the Kraichnan theory.[6] A power-low exponent in the η_e-turbulence shows m=1.5 ~ 1.7 after averaging over z. It is clear that the η_e-turbulence is different from the electrostatic drift wave turbulence scaled by ρ_s.[8] It should be noted that the energy spectrum of η_e-turbulence is proportional to k^{-m} with 1.5< m < 1.7, instead of m=3.

References

[1]. P.N.Gudzar, C.S.Liu, J.Q.Dong and Y.C.Lee, Phys. Rev.Lett. 57, 2818(1986).

[2]. W.Horton, B.G.Hong and W.M.Tang, Phys. Fluids 31, 2971 (1988).

[3]. R.R.Parker, M.Greenwald, S.C.Luckhardt, E.S.Marmar, M. Porkolab and S.M.Wolfe, Nucl.Fusion 25, 1127(1985).

[4]. G.S.Patterson and S.A.Orszag, Phys. Fluids 14, 2538(1971).

[5]. T.Ohkawa, Phys. Lett. 67A, 35(1978).

[6]. R.H. Kraichnan, Phys. Fluids 7,1385(1965).

[7]. R.Grappin, U.Frisch, J.Leorat and A. Pouquet, Astron. Astrophys. 105, 6-14(1982).

[8]. D. Fyfe and D. Montgomery, Phys. Fluids 22, 246(1979).

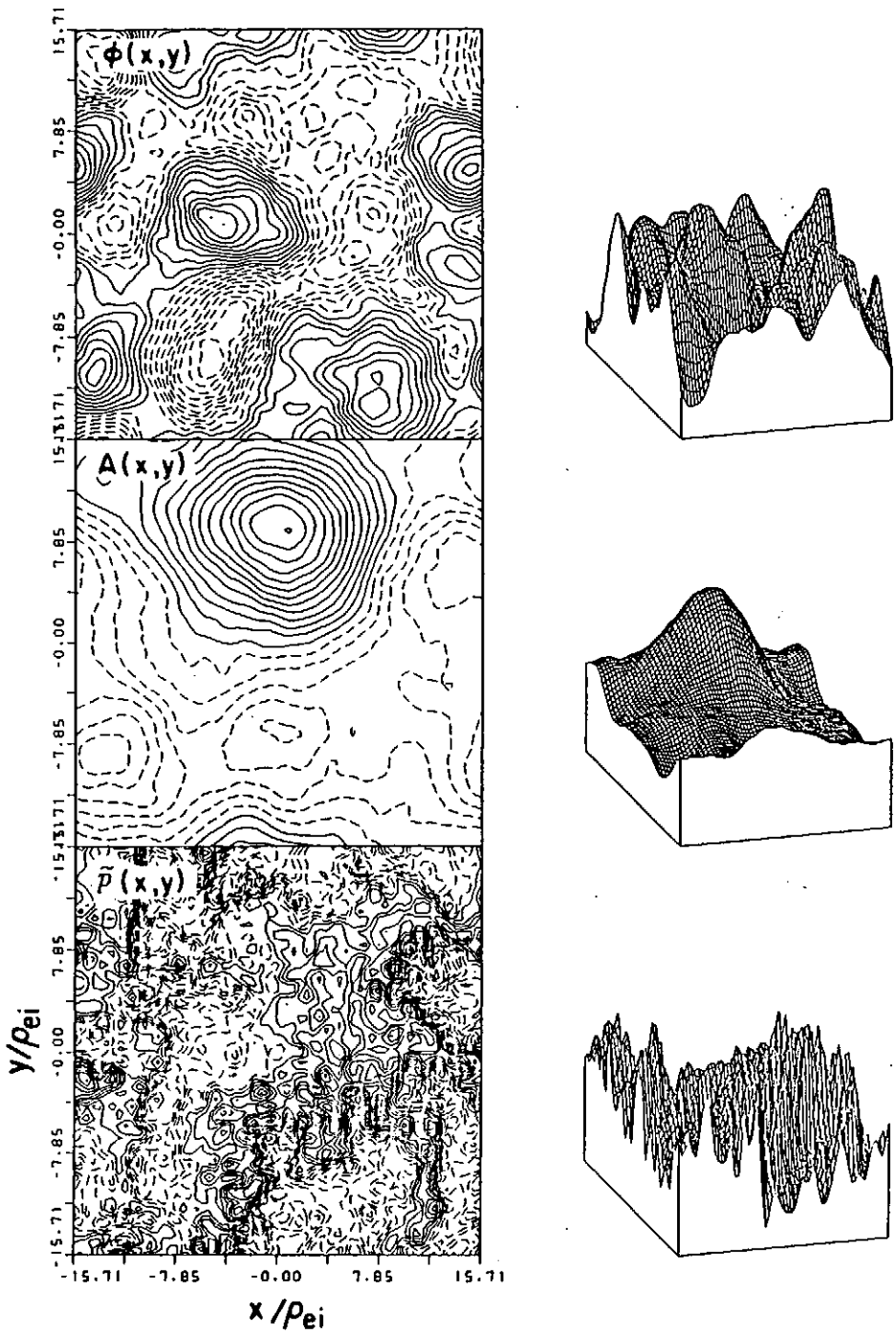

Fig. 1 Contours of electrostatic potential $\phi(\mathrm{x},t)$, magnetic flux function $A(\mathrm{x},t)$ and pressure fluctuation $\tilde{p}(\mathrm{x},t)$ in the strongly turbulent state.

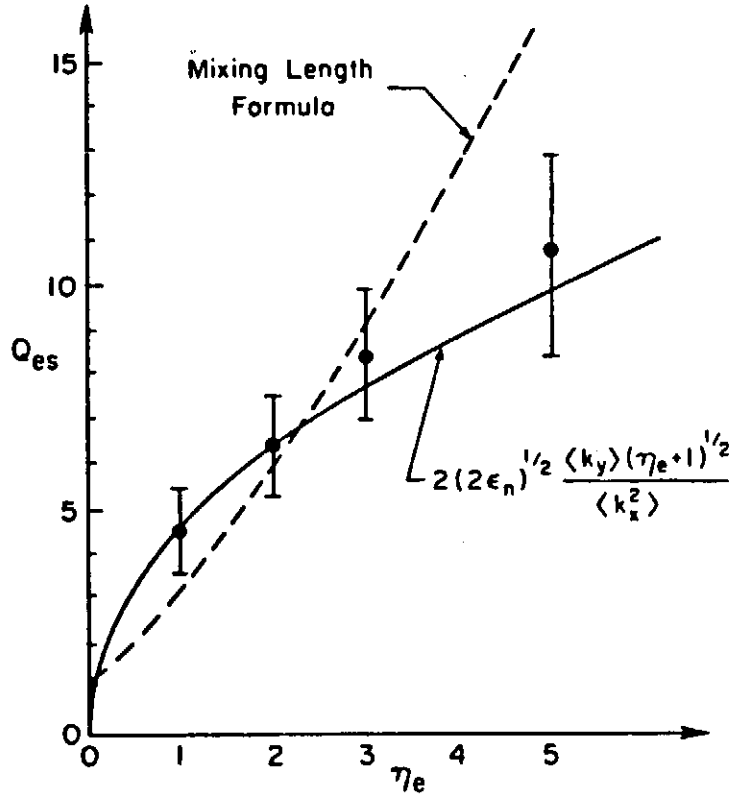

Fig. 2 The steady-state $\mathbf{E} \times \mathbf{B}$ heat flux component versus the temperature gradient parameter η_e.

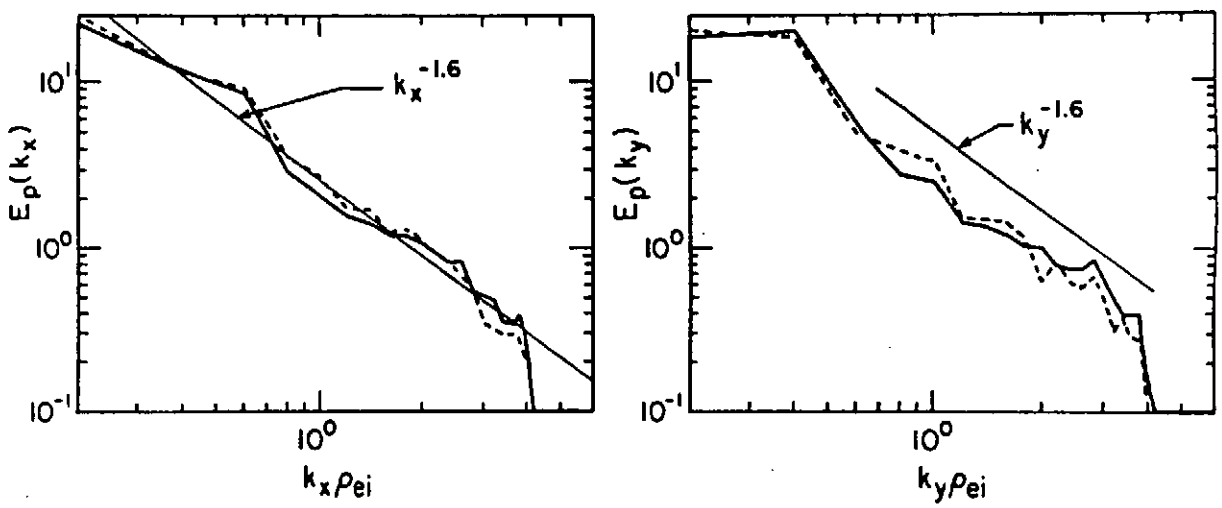

Fig. 3 Steady state wavenumber spectrum. (a) The k_x spectrum and (b) the k_y spectrum.

III. Structures in One-Fluid Plasmas

Submitted to Proceedings of U.S.-Japan Workshop on Structures in Confined Plasmas, Nagoya, Japan (March 1989)

GROWTH AND DECAY OF VORTEX STRUCTURES IN PURE ELECTRON PLASMAS

C.F. Driscoll, R.A. Smith, X.-P. Huang and J.H. Malmberg

Abstract

Magnetized hollow electron columns exhibit linear instabilies which evolve to a state of saturated non-linear vortex structures. These vortices then cause rapid cross-field particle transport giving a noisy, non-hollow state. In the linear regime, we observe both unstable and stable $k_z \approx 0$ diocotron modes; these have been studied for azimuthal mode numbers $l = 1$ and 2. For $l = 2$, measured frequencies and exponential growth rates are in factor-of-two agreement with predictions of 2-D theory. For $l = 1$, exponential instability is also observed, in contradiction to 2-D fluid theory. In the non-linear regime, experiments show two vortices merging into a single vortex in the center, with the formation of small scale structures; this merger is in general agreement with numerical calculations. At late times, the measured density fluctuations typically decay exponentially to the level of a few percent.

Introduction

Pure electron plasmas are excellent model systems for precision studies of plasma waves and transport. The electron column is contained radially by a uniform magnetic field, B_z, and contained axially by voltages applied to end sections of the cylindrical wall. These plasmas are very longlived and quiescent, with shot-to-shot variations at the 0.1% level [1]. The plasma columns have an $\mathbf{E}\times\mathbf{B}$ rotation $\omega_E(r)$ due to the unneutralized space charge potential. There is generally substantial shear in this rotational flow, but the flow can be shown to be stable as long as the plasma density is monotonically decreasing [2,3]. In the absence of shear-instability or externally-induced losses, the plasma evolves so as to remove the shear on a "viscous" transport time scale of 10 seconds.

By contrast, when we create hollow density profiles, we observe one or more unstable diocotron modes; that is, shear-driven instabilities appear when $n(r)$ is non-monotonic [4]. For our profiles, an $l = 2$, $k_z \approx 0$ diocotron mode is the most unstable. For plasmas or beams with a thin shell structure, high l modes can be the most unstable [3,5]. In our system, the unstable mode evolves to non-linear vortices which cause transport to a stable, monotonically decreasing radial density profile, on a time scale of 10^{-4} seconds.

Vortex Evolution

Our experiments measure the z-averaged dynamics of the plasma in both the linear and non-linear regimes. We begin with a hollow radial profile, with a single intentionally applied azimuthal asymmetry as the initial condition. We allow the plasma to evolve for a time t, then dump the plasma axially and collect the charges which pass through a moveable 3mm collimator hole. We obtain the z–integrated plasma density $n(r,\theta,t)$ by taking many shots, varying the radial position of the collimator hole, the phase of the seed wave, and the evolution time. We note that this measurement does not detect perturbations with $k_z \neq 0$. Our plasmas typically have length to radius ratios of approximately 20.

Figure 1 displays $n(r,\theta)$ at 4 evolution times for an initially hollow plasma with a small initial asymmetry varying as $e^{i2\theta}$. The initial $l=2$ asymmetry is barely noticeable at $t=0$ (Fig. 1a). However, the $l=2$ perturbation grows exponentially with an e–folding time of 17 μs. At $t=110$ μs, the mode is fully saturated, and would best be described as two isolated vortex structures with density plateaus about 50% above the density minima (Fig. 1b). For 2-D $\mathbf{E}\times\mathbf{B}$ flow, the vorticity is proportional to the density. The two vortices rotate around their own centers and around each other with both periods ~ 10 μs.

The two vortices persist for many rotations, then begin to merge by moving towards the center at $t=160$ μs (Fig. 1c). Presumably, the two-vortex state is unstable, and the merger is the result of a vortex instability [6]. There may be extended filamentary structures arising during the vortex formation and disintegration, as suggested in (b), giving rise to density fluctuations on smaller spatial scales. The dynamics of the large vortices seems to be in general agreement with recent numerical calculations [7]. Finally, by 1000 μs the density is monotonically decreasing and therefore stable, and only small fluctuations are observed (Fig. 1d).

When the initially applied asymmetry is $l=1$, we observe a qualitatively different evolution which leads to a similar monotonically decreasing profile. In this case, the low density region moves off center, and the high density ridge collapses azimuthally to a single vortex which then moves in to the center. Again, there can be small-scale filamentary structures associated with this process.

Linear Modes

From our data, we are able to characterize the linear modes rather completely. For any given l, two similar but distinct classes of diocotron mode propagate on the hollow plasma column: One is unstable, similar to that first observed in the filamentation of hollow beams [8]; while the other is stable, and is similar to the stable (or damped) modes observed on monotonic density profiles [9]. These two modes have distinct frequencies and distinct radial eigenfunctions. Here, we use the terms "mode" and "eigenfunction" in reference to the data even though there is some question as to whether the $l=1$ instability is strictly speaking an eigenmode of the system.

For any given l, we obtain the mode frequencies, f_{lq}, growth rates γ_{lq}, and eigenfunctions, $\delta n_{lq}(r)$, by fitting the $e^{il\theta}$ component of the experimental data, as

$$\delta n_l(r,t) = \sum_{q=s,u} \delta n_{lq}(r)\, e^{i2\pi f_{lq} t + \gamma_{lq} t} \quad .$$

Here $q = s,u$ indexes the stable and unstable modes. The data is well fit by two modes, with residuals typically below 10%. This process readily detects the oscillations at each f_{lq}, and gives accurate growth rates so long as the modes are linear. To verify the exponential growth and to obtain the mode amplitudes in the non-linear regime, we use a second fit. Given the eigenfunctions from the first fit (normalized to a maximum of 1), we obtain the mode amplitudes $A_{lq}(t)$ directly from the data, as $\delta n_l(r,t) = n_{\max} \sum_{q=s,u} \delta n_{lq}(r) A_{lq}(t)$.

The left side of Fig. 2 shows the amplitudes of the unstable and stable $l = 2$ modes $|A_{2u}|$ and $|A_{2s}|$ for the evolution of Fig. 1. The unstable mode is observed to grow exponentially from an initial level of 0.3% to a saturation level of 20%, while the stable mode varies only slightly until the non-linear regime.

We have measured $l = 2$ frequencies and growth rates for hollowed plasmas with ratios of central density to peak density ranging from 95% down to 40%. The frequency of the unstable mode is essentially twice the rotation frequency at the radius of the peak density. We measure γ_{2u}/f_{2u} in the range 0.1 to 0.3; that is, the perturbation e–folding time ranges from 5 to 1½ full rotation times. These measured growth rates are generally 20-100% greater than predicted by 2-D guiding center theory, whereas the frequencies agree well with theory [4,7,10]. For the plasma of Figs. 1 and 2, theory predicts $\tau_e \approx 30$ μs, versus the measured 17 μs. As yet, we do not know the source of this discrepancy.

For $l = 1$, the linear regime looks very similar experimentally. An unstable $l = 1$ mode is observed to grow exponentially over two decades in amplitude, while the stable $l = 1$ mode remains constant. The frequency f_{1u} is equal to the rotation frequency at the radius of peak density to within the 10% accuracy of our present determination of $\omega_E(r)$. The unstable mode is observed to e–fold in 5 to 7 rotation periods; that is, $0.14 < \gamma_{1u}/f_{1u} < 0.2$ for a wide range of initial density profiles. This exponential signature is not an artifact of the eigenfunction fitting procedure described above, since the same growth is observed in the oscillatory signal at a particular point, i.e. $\delta n(r_0,\theta_0,t)$.

As yet, there is no satisfactory theoretical explanation for the observed exponential growth of the $l = 1$ mode. One can show with linear 2-D fluid theory that there can be no exponentially growing $l = 1$ modes. However, recent theory work [10] has found an *algebraically* growing instability (which is *not* rigorously an eigenmode).

Long-time Noise Measurements

The phase-locked measurements of $n(r,\theta,t)$ can follow the dynamical evolution only until the initial shot-to-shot noise grows to be as large as the structures of interest. This begins to occur at (c) in Fig. 1, where shot-to-shot noise can be seen as a deviation from the nominal 180° symmetry of the picture. We have made long-term noise and correlation measurements for evolutions similar to that of Fig. 1 [11]. Here,

the measurements are not synchronous with the internal waves.

The righthand side of Fig. 2 gives the RMS variations in the measured density versus time at a radius near the initial density peak. Here, since we are measuring the density asynchronous with any internal processes, density variations in θ appear as shot-to-shot density variations, or "noise". This noise grows exponentially before 100 μs (not shown), due to the unstable $l=2$ mode. When we measure the density at several angles θ on the same shot, however, we see positive spatial correlations between collectors separated by 180°, corroborating the $l=2$ nature of the disturbance. The peak in the noise occurs when the two vortices are fully formed and are merging towards the center. After 250 μs, the noise asymptotes to 1.6%, where it remains for hundreds of milliseconds.

By subtracting off the asymptotic value of 1.6% noise, we obtain an accurately exponential decay of one "type" of noise over a range of 2 decades. The data to date suggest that the θ-asymmetries are decaying away, and that the long term noise represents shot-to-shot differences in the resulting radial profile. That is, we see positive correlations on collectors separated by 90° and by 180°, but negative correlations between collectors at the same angle but different radius. The 1.6% noise persists until "collisional" radial transport occurs, typically on the time-scale of seconds.

Conclusions

The progression from linear shear-driven instability to vortex formation to vortex-driven transport to long-term noise fluctuations has been observed experimentally. When unstable modes are present and vortices are formed, the cross-field particle transport rate is about 10^5 times greater than the rate from viscous transport alone. Some, but not all, of the instability and nonlinear dynamics properties of the drifting plasma column are explained by 2-D fluid theory. The experiments are highly controllable and repeatable, and should provide continuing tests of nonlinear transport and turbulence theories.

Acknowledgments

The authors would like to acknowledge stimulating discussions with K. S. Fine, R. W. Gould, T. B. Mitchell, T. M. O'Neil, and M. N. Rosenbluth. This work was supported by ONR Contract N00014-82-K-0621 and DOE Grant DE-FG03-85ER53199.

References

[1] Driscoll, C.F., Malmberg, J.H., Fine, K.S., Phys. Rev. Lett. **60** (1988) 1290.

[2] Briggs, R.J., Daugherty, J.D., Levy, R.H., Phys. Fluids **13** (1970) 421.

[3] Davidson, R.C., Theory of Nonneutral Plasmas, W. A. Benjamin, Reading (1974).

[4] Driscoll, C.F., Malmberg, J.H., Fine, K.S., Smith, R.A., Huang, X.-P., Gould, R.W. in *Plasma Physics and Controlled Nuclear Fusion Research* (IAEA, Vienna, 1988).

[5] Levy, R.H., Phys. Fluids **8** (1965) 1288.

[6] Pierrehumbert, R.T., Windall, S.E., J. Fluid Mech. **114** (1982) 59.

[7] Gould, R.W. Bull. APS **33**, 1898 (1988).

[8] Kyle, R. L., Webster, H.F., IRE Trans. Elect. Dev. **3** (1956) 172.

[9] DeGrassie, J.S., Malmberg, J.H., Phys. Rev. Lett. **39** (1977) 1333.

[10] Smith, R.A., Rosenbluth, M.N., Driscoll, C.F., O'Neil, T.M., Bull. APS **33**, 1898 (1988).

[11] Huang, X-P., Driscoll, C.F., Malmberg, J.H., Bull. APS **33**, 1898 (1988).

Figure Captions

Fig. 1 Measured z-averaged density $n(r,\theta)$ at four times, as the initially hollow profile becomes monotonic.

Fig. 2 Mode amplitudes $|A_{2s}|$ (open circles) and $|A_{2u}|$ (solid diamonds) for the stable and unstable modes; RMS density fluctuations (plusses), with the 1.6% asymptote subtracted (crosses).

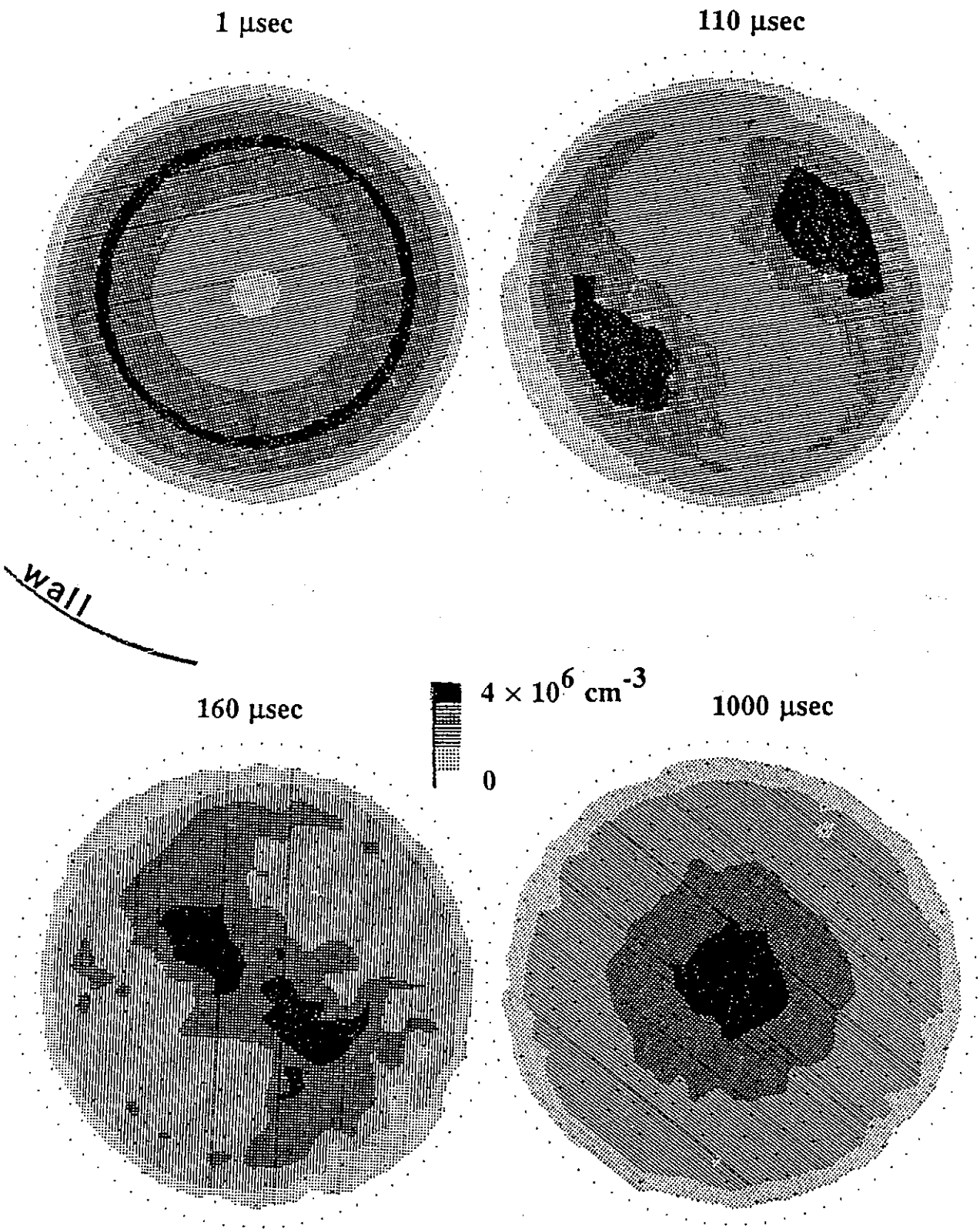

Fig. 1 Measured z-averaged density $n(r,\theta)$ at four times, as the initially hollow profile becomes monotonic.

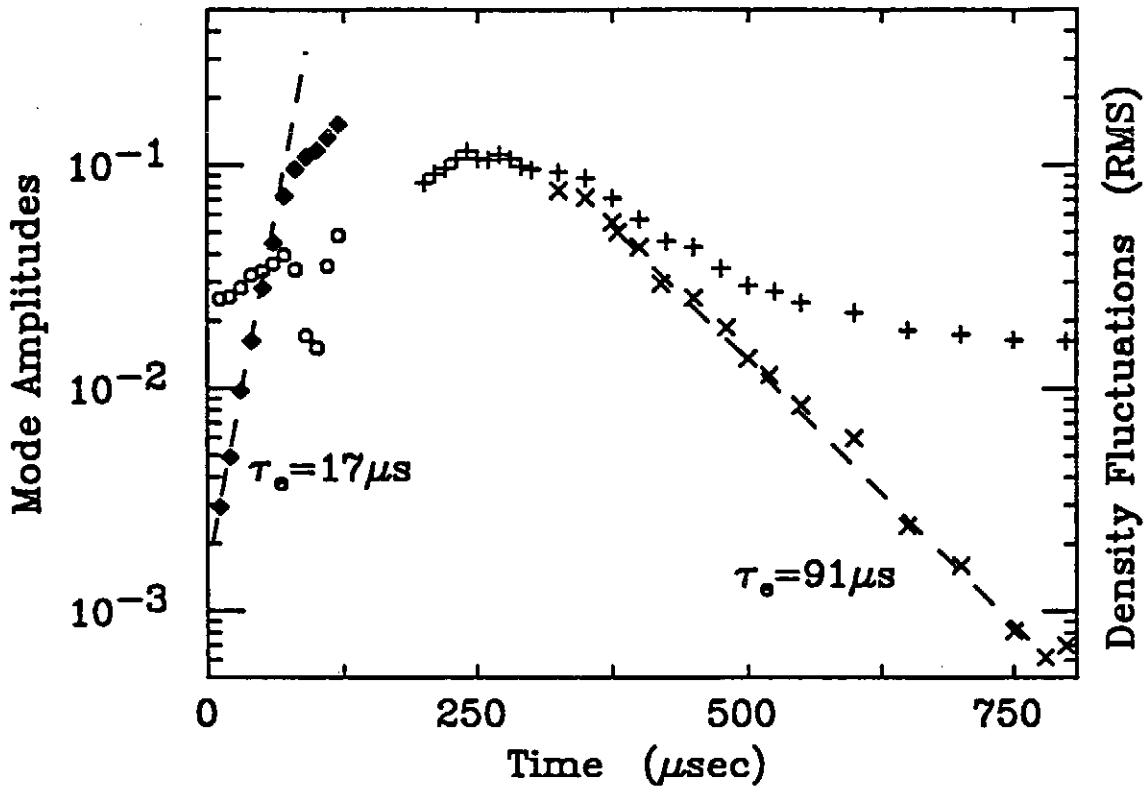

Fig. 2 Mode amplitudes $|A_{2s}|$ (open circles) and $|A_{2u}|$ (solid diamonds) for the stable and unstable modes; RMS density fluctuations (plusses), with the 1.6% asymptote subtracted (crosses).

PRESSURE-DRIVEN INTERNATIONAL DISRUPTIONS IN HELIOTRON E

M. WAKATANI

Plasma Physics Laboratory

Kyoto University, Gokasho, Uji, Japan

ABSTRACT

In the high beta experiments of Heliotron E the internal disruptions similar to those in tokamaks were observed. For a highly peaked pressure profile of $\beta(0)/\bar{\beta} > 3 \sim 4$ and $\beta(0) > (2 \sim 3)\%$, the internal disruption occurs and the pressure profile becomes suddenly flat in the central region, where $\beta(0)$ denotes a central value and $\bar{\beta}$ an averaged value. It is caused by the non-linear evolution of g mode with $m = 3/n = 2$, where m and n are poloidal and toroidal mode number, respectively. For a moderately peaked pressure profile of $\beta(0)/\bar{\beta} \simeq 2 \sim 3$ and $\beta(0) > (2 \sim 3)\%$, a relaxation oscillation ended with the internal disruption explained by the g mode with $m = 1/n = 1$ was observed. For a flat pressure profile of $\beta(0)/\bar{\beta} < 1.5 - 2$, the highest average beta value was obtained; however, at $\bar{\beta} \sim 2\%$ an edge localized relaxation was observed recently. When the pressure gradient is steep in the edge region, the expected dangerous instability is g mode with $m = 2/n = 3$. Recently it is found that the internal disruptions appeared at the lower beta value than that in the above case, when the magnetic axis is shifted inside by the vertical magnetic field.

1. REDUCED MHD EQUATIONS FOR STELLARATOR/HELIOTRON

The non-linear reduced MHD equations for stellarator/heliotron were derived by the averaging the field period of the stellarator field based on the stellarator expansion[1,2]. Without the averaging the following reduced MHD equations are given by using the similar procedures to those for high beta tokamaks[3],

$$(1)\frac{\partial A}{\partial t} + E_{||} = B \cdot \nabla u$$

$$(2) - \frac{\rho}{B_0}\frac{d}{dt}\nabla_\perp^2 u = B \cdot \nabla \sigma + \frac{\nabla B^2 \times \nabla p \cdot B}{B^4}$$

$$(3)\frac{\partial p}{\partial t} + (\nabla u \times \hat{z}) \cdot \nabla p = 0$$

$$(4)p + B_0^2 \frac{I_1}{I_0} = const.,$$

where A is a parallel component of vector potential, u is a stream function related to the perpendicular velocity, $\vec{v} = \vec{\nabla} u \times \hat{z}, \sigma = -\nabla_\perp^2 A/B_0$. The poloidal current in the coil producing toroidal field is given by I through the relation $B_z = I/R$. I_0 and I_1 are the zeroth order and the first order current expanded with respect to the inverse aspect ratio $\varepsilon = r/R << 1$. Equation (1) is obtained from Ohm's law along the magnetic field line, and eq. (2) is equivalent to $\vec{\nabla} \cdot \vec{J} = 0$. It is called vorticity equation. Equation (3) describes convective motion of pressure, and eq. (4) shows a pressure balance in the lowest order, which means that plasmas are confined by the toroidal magnetic field dominantly in the stellarator/heliotron.

In the stellarator expansion a small parameter related to the magnitude of stellarator field is employed and it has an ordering of $\delta^2 \sim \varepsilon$. The magnetic field is described by

$$(5) B = B_0\hat{z} + \delta\nabla\Phi + \delta^2\nabla Ax\hat{z} + \delta^2 B_0(\frac{I_1}{I_0} - \frac{x}{R_0})\hat{z},$$

where $x = R - R_0$ and R_0 is a major radius of torus. It is noted that there are some non-uniformity with respect to the ordering parameter δ in eqs. (1) and (2) because of the stellarator field, $\vec{B} = \vec{\nabla}\Phi$. Here the magnetic potential is assumed by

$$(6) \Phi = 2\Phi_\iota I_\iota(hr)\sin(\iota\theta + hz),$$

where I_ℓ is a modified Bessel function, ℓ is a pole number and $h = \ell N/R_0$. N is called a pitch number and $N >> 1$. The magnetic potential (6) describes only dominant component produced by helical coils with a winding law determined by ℓ and N. By applying the averaging over the one pitch length defined by

$$(7) \bar{f}(r,\theta,\bar{z}) = \frac{N}{2\pi R_0}\int_0^{\frac{2\pi R_0}{N}} f(r,\theta,z,\bar{z})dz$$

to eqs. (1) and (2), the non-uniformity of the ordering can be removed. Here z shows the rapid variation of the stellarator field, while $\bar{z}$ is related to a slowly vary part. By using the averaging (7),

$$(8) \bar{B}\cdot\nabla = B_0\frac{\partial}{\partial\bar{z}} + \nabla\Psi\times\hat{z}\cdot\nabla$$

$$(9) \Psi = A - \frac{1}{2B_0}\overline{\nabla < \Phi > \times\nabla\Phi}\cdot\hat{z}$$

is obtained, where the bracket is defined by

$$(10) < f > (r,\theta,z,\bar{z}) = \int_0^z f(r,\theta,z,\bar{z})dz + C(r,\theta,\bar{z}).$$

Here $C(r,\theta,\bar{z})$ is given by the condition of $< \bar{f} >= 0$. It is noted that $\vec{\mathbf{B}}$ has ordering of δ^2. By using (7), (8), (9) for eqs. (1) and (2),

$$(11)\rho\frac{d}{dt}\nabla_\perp^2 u = \bar{B}\cdot\nabla\nabla_\perp^2 A + \nabla[\frac{2x}{R_0} + \frac{\overline{(\nabla\Phi)^2}}{B_0^2}]\times\nabla p\cdot\hat{z},$$

$$(12)\frac{\partial A}{\partial t} = \bar{B}\cdot\nabla u - \eta J_z$$

are obtained, where $J_z = -\nabla_\perp^2 A$ and η is resistivity. Here the pressure equation is written by

$$(13)\frac{\partial p}{\partial t} + (\nabla u\times\hat{z})\cdot\nabla p = \nabla_{||}\cdot(k_{||}\nabla_{||}p) + \nabla_\perp\cdot(k_\perp\nabla_\perp p),$$

where $k_\perp$ and $k_{||}$ are perpendicular and parallel thermal conductivity, respectively.

By using the expression (6), the second term of (9) is written by

$$(14)\Psi_h = -\frac{1}{2B_0}\overline{\nabla < \Phi > \times\nabla\Phi}\cdot\hat{z} = \frac{2\Phi_\iota^2}{rB_0}I_\iota(hr)I_\iota'(hr),$$

By noting that the rotational transform is given by

$$(15)\iota = \frac{R_0}{rB_0}(-\frac{d\Psi h}{dr}),$$

a different expression for Ψ_h is found as

$$(16)\Psi_h = -\frac{B_0}{R_0}\int r\iota(r)dr.$$

The curvature term is eq. (11) is written by using the modified Bessel function as

$$(17)\Omega = \frac{2\pi}{R_0} + \frac{2\Phi_t^2 h^2}{B_0^2} G(hr)$$

where

$$(18)G(hr) = [I_\iota'(hr)]^2 + \frac{\iota^2 + h^2 r^2}{h^2 r^2} I_\iota^2(hr).$$

Here the prime means derivative with respect to hr. A different expression of the curvature is given by

$$(19)\Omega = \frac{2\pi}{R_0} + \frac{h}{\iota R_0}\{r^2 \iota(r) - 2\int_0^r r\iota(r)dr\}.$$

2. LINEAR AND NON-LINEAR ANALYSES OF RESISTIVE INTERCHANGE MODES (OR G MODES)

In order to investigate the internal disruption, we solve the reduced MHD equations (11), (12) and (13) as an initial and boundary value problem in a cylindrical coordinates (r, θ, z). It is considered that the toroidal effect on the non-linear evolution of g mode is weak in the Helioton E because of the large aspect ratio of about ten. The numerical procedures are similar to those shown in ref.[4] for low-beta current carrying plasmas. We use Fourier expansions for θ and z directions and finite difference approximation for r direction.

The rotational transform profile is chosen as $\iota(r) = 0.51 + 1.69(r/a)^{2.5}$, which approximates ι of Heliotron E as obtained by the line-tracing method. The pressure profile is chosen as $P = P_0(1-(r/a)^i)^j$, where the central pressure P_0 is determined by the central beta value $\beta(0)$. For a highly peaked profile, $i = 2$ and $j = 4$, for a moderately peaked profile, $i = 2$ and $j = 2$, and for a almost flat profile, $i = 6$ and $j = 1$ are given to simulate

experimental pressure profiles.

MHD equilibrium is given by neglecting resistivity and time derivatives in eqs. (11), (12), (13) and assuming $u = 0$. Thus the equilibrium equation is that the right hand side of eq. (11) is equal zero. A cylindrical configuration with $P(r)$ and $J_z = 0$ satisfies this equation. This state corresponds to MHD equilibrium in the lowest order of the stellarator expansion[2].

First we will explain linear mode structure of g mode with $m = 1/n = 1$ and $S = 10^5$. Figure 1 shows the radial mode structures of the magnetic potential A and the stream function in the linearly growing phase for the pressure profile with $i = j = 2$. It is noted that the most unstable g mode has the mixed parity in the cylindrical geometry, which means $A(r_s) \neq 0$. Usually in the slab model, g mode with odd parity of A or $A(r_s) = 0$ case is the most unstable. This make a significant difference in the nonlinear regime, since $A(r_s) \neq 0$ case produces a magnetic island easily.

In the non-linear calculation with $S = 10^4, i = j = 2, \beta(0) = 3.54\%, k_\perp = 10^{-4}$ and $k_{||} = 2$ the time evolution of kinetic energy is shown in Fig.2. Figure 3 shows contours of flux surfaces. At $T = 90$ small-magnetic island appears and at $T = 105$ two reconnection points exist. This means that $m = 2$ type magnetic island is seen for the g mode of $m = 1$. This behaviors are consistent with the high β experiment in H-E[5]. Figure 4 shows contours of pressure. In this particular result, we included parallel thermal conductivity. This works to make the pressure constant on the flux surface. By comparing Fig.3 and Fig.4 we can see such a tendency. After the saturation the pressure profile becomes very flat in the region inside the $\iota = 1$ surface. This result corresponds to the flat density profile after the internal disruption and is consistent with the experimental data[6].

Recently in Heliotron E experiments the magnetic axis position is controlled by the additional vertical magnetic field. When the magnetic axis position changed, we observed different characteristics of the internal disruption. Figure 5 shows the phase inversion radius versus the magnetic axis positions at $\beta = 0$. This figure shows that the internal

disruption occurs at $q = 1$(or $\iota = 1$), $q = 1.5$(or $\iota = 2/3$) and $q = 2$(or $\iota = 0.5$). These inversion radii depend on the pressure profile. For peaked pressure profile $q = 2$ or $q = 1.5$ becomes the inversion radius and the resistive interchange instability triggering the internal disruption is $m = 2/n = 1$ or $m = 3/n = 2$, respectively. When the magnetic axis is shifted inward or $\Delta < 0$, usually the internal disruption appears at the lower beta value than the case of $\Delta = 0$ or $\Delta > 0$. For $\Delta > 0$ case, the internal disruption is usually triggered at $\iota = 1$ surface by the $m = 1/n = 1$ mode.

This kind of the internal disruption is also seen in the Heliotron-DR, which has the $\ell = 2$ and 15 pitches helical winding. The major radius is 90 cm and the minor radius is 7 cm, characteristics of the vacuum magnetic field is similar to the Heliotron E. We developed a numerical code called RESORM to study effects of the toroidal geometry and the shift of the magnetic axis on the linear stability of g mode[7]. We are planning to extend the RESORM code to the non-linear evolution of the g mode in the toroidal geometry.

REFERENCES

[1] WAKATANI, M., in Proc. Int. Conf. on Plasma Physics (Nagoya, 1980) vol. 1, p. 82.

[2] STRAUSS, H. R., Plasma Phys. 22 (1980) 733.

[3] STRAUSS, H. R., Phys. Fluids 19 (1976) 134.

[4] WAKATANI, M., Nucl. Fusion 18 (1978) 1499.

[5] HARRIS, J. H., et al., Phys. Rev. Lett. 53 (1984) 1359.

[6] ZUSHI, H., et al., Nucl. Fusion 27 (1987) 835.

[7] ICHIGUCHI, K., et al., submitted in NUCLEAR FUSION.

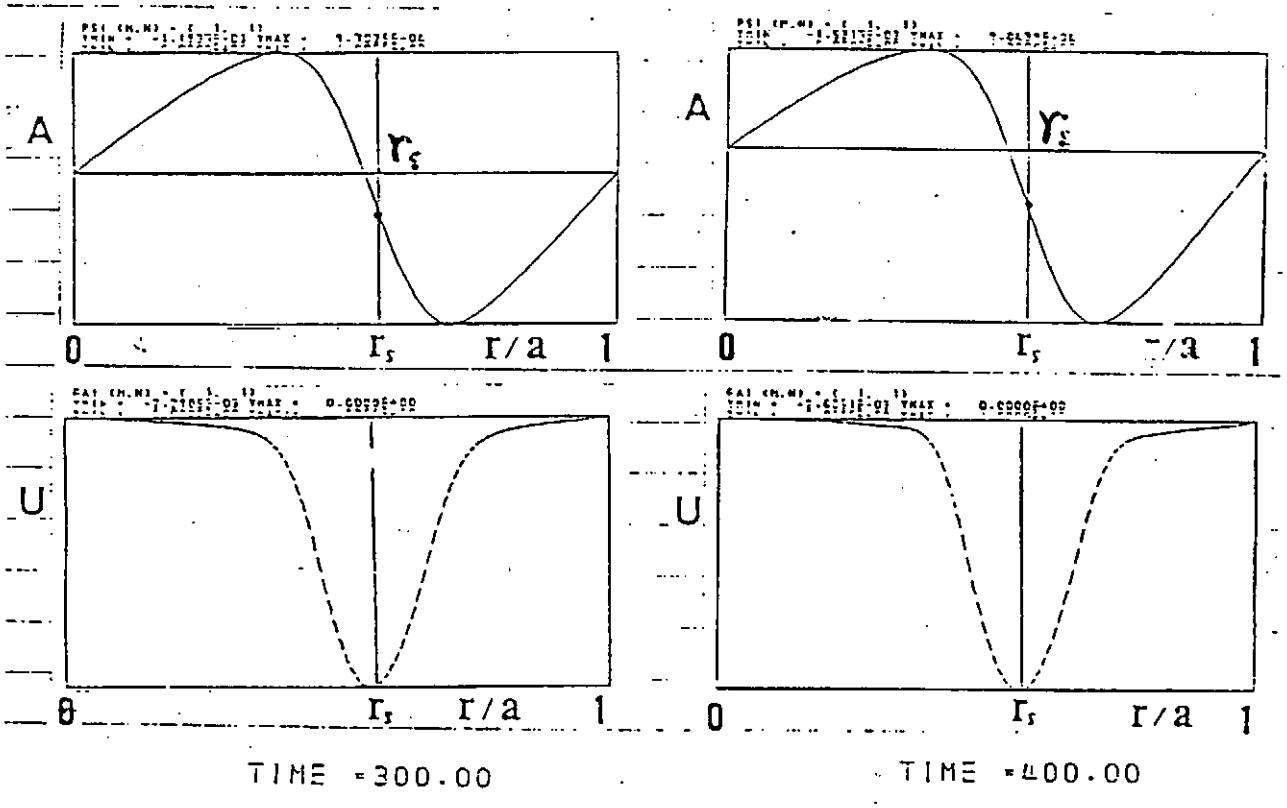

Fig. 1

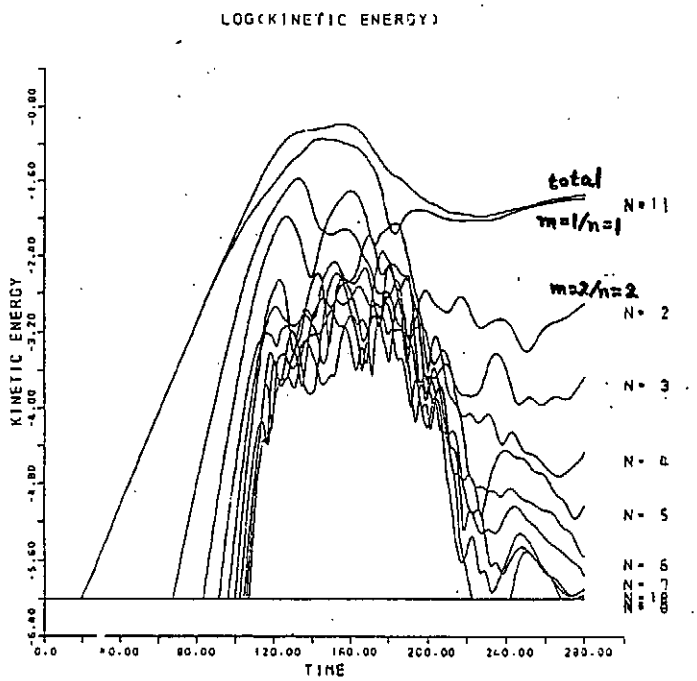

$\kappa_{\parallel} = 2.0$
$\kappa_{\perp} = 10^{-4}$
$S = 10^4$
$\beta(0) = 3.5\%$
$P = P_0(1-r^2)^2$

Fig. 2

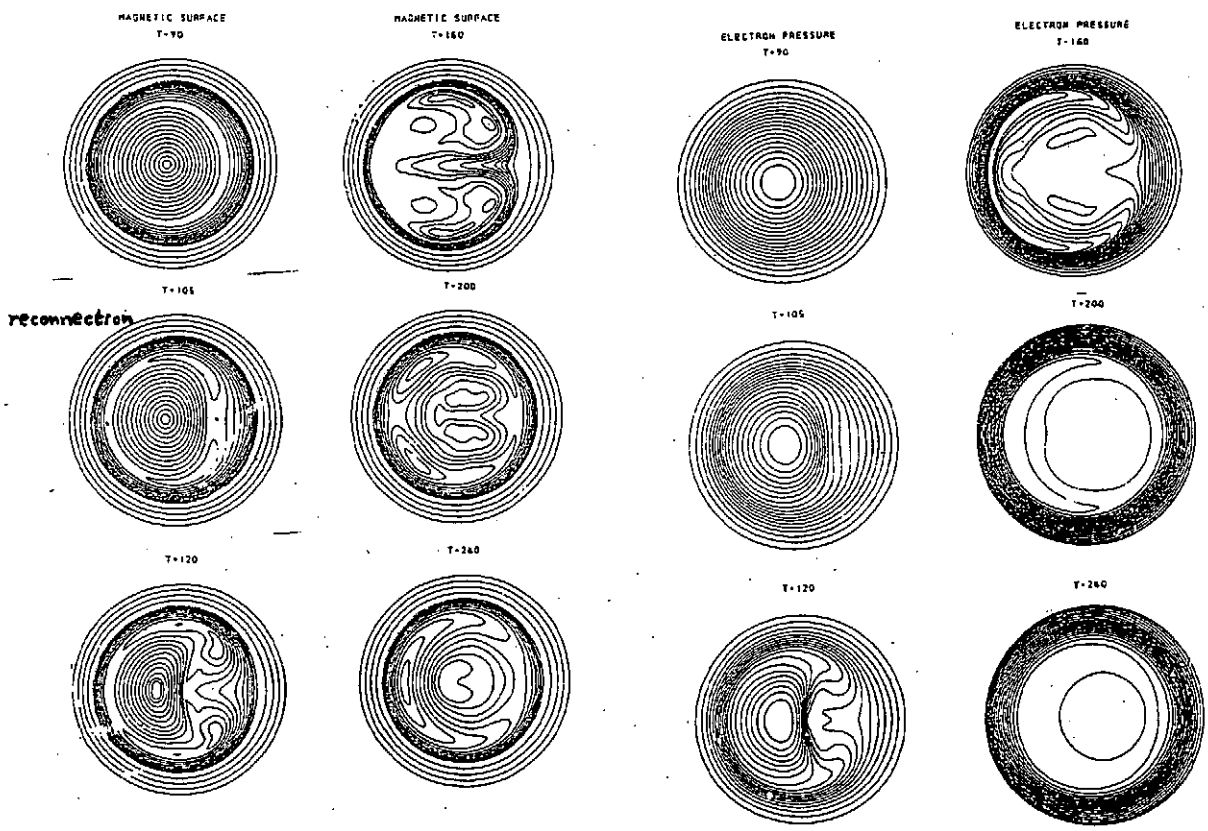

Fig. 3

Fig. 4

Phase Inversion Radius and Rotational Transform

▲: Pellet fueled (high β)

●: gas fueled (low β)

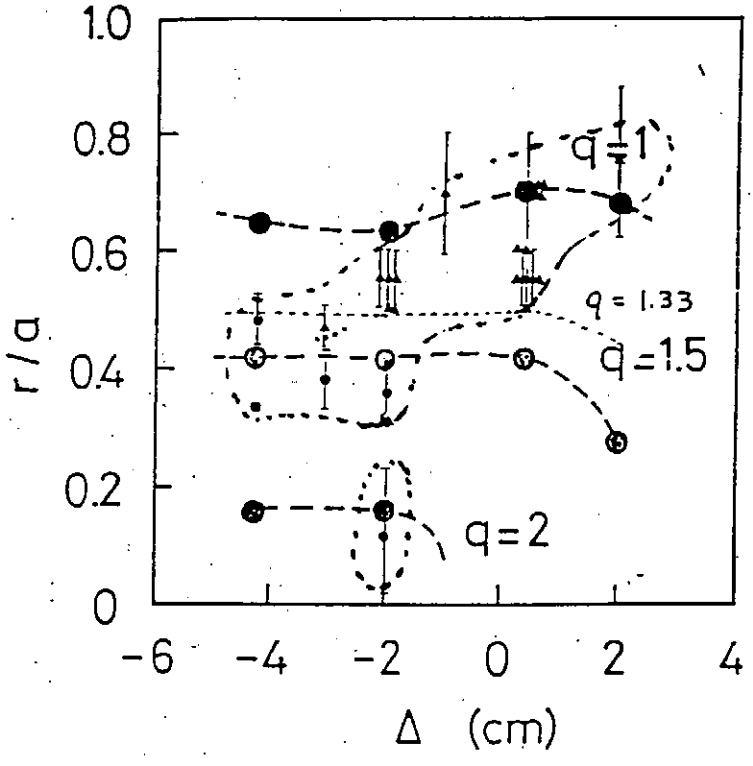

Fig. 5

Anomalous Transport in Resistive Interchange Turbulence

Hideo Sugama and Masahiro Wakatani

Plasma Physics Laboratory, Kyoto University
Gokasho, Uji 611

Abstract

Resistive interchange mode driven turbulence in a magnetically confined plasma is studied by using renormalization technique for a reduced fluid model. It is related to the anomalous transport in tokamaks and stellarator/heliotron.

§1. Introduction

In experiments of magnetically confined plasmas, particle and energy transports usually exceed estimations based on Coulomb collisions or the neoclassical transport theory. This anomalous transport is supposed to be explained based on the turbulence originated from plasma instabilities since the observed fluctuations show the strong turbulence character e.g. broad spectra of wavenumbers and frequencies [1]. Here we consider the resistive interchange mode, which is driven by the magnetic curvature and the pressure gradient in the resistive plasma, as a cause of the turbulence and the resultant anomalous transport in tokamaks and stellarator/heliotron.

In Sec.2, the model equations are given and the results of a linear theory and a dimensional analysis are shown. In Sec.3, we find the nonlinear analysis of the model equation using the two-point renormalization technique. A summary is given in Sec.4. We also comment on the effect of the radial electric field on the turbulence in Appendix.

§2. Model Equations

The electrostatic resistive interchange turbulence is described by the resistive RMHD equations [2], which consists of the pressure convection equation:

$$\left(\frac{\partial}{\partial t} + \boldsymbol{v}\cdot\nabla\right) p = -\kappa\frac{\partial\phi}{\partial y} \tag{1}$$

and the vorticity equation:

$$\left(\frac{\partial}{\partial t} + \boldsymbol{v}\cdot\nabla\right) \nabla_\perp^2\phi = -\frac{1}{\eta}\nabla_\parallel^2\phi - g\frac{\partial p}{\partial y}. \tag{2}$$

Here $\boldsymbol{v} = \hat{z}\times\nabla\phi$ is the $\boldsymbol{E}\times\boldsymbol{B}$ drift velocity, ϕ the electrostatic potential, p the pressure fluctuation, η the resistivity, $\kappa = -dp_0/dx$ the pressure gradient and g the effective gravity in the x-direction due to the magnetic curvature. These quantities are written in the normalized form. The derivative along the magnetic field line is represented by $\nabla_\parallel = \hat{b}\cdot\nabla$, where we assume the sheared magnetic field $\hat{b} = \hat{z} + sx\hat{y}$. s denotes the shear strength. The viscosity and pressure diffusion terms due to the Coulomb collision are not included in

Eqs.(1) and (2). Such dissipation terms are needed as the energy sink at high wavenumbers in the stationary turbulence state, but they are neglected here for simplicity by assuming that the magnitudes of turbulent diffusion and fluctuations do not depend on their values.

If we assume the perturbation of the form $\phi_k(x)\exp(ik_y y + ik_z z)$, linearization of Eqs.(1) and (2) gives the following growth rate

$$\gamma_k = \eta^{1/3}(g\kappa)^{2/3}s^{-2/3}k_y^{2/3} \tag{3}$$

and the eigenfunction

$$\phi_k(x) = \exp\left[-\frac{1}{\Delta_k^2}\left(x + \frac{k_z}{sk_y}\right)^2\right] \tag{4}$$

where the mode width Δ_k is given by

$$\Delta_k = \eta^{1/3}(g\kappa)^{1/6}s^{-2/3}k_y^{-1/3}. \tag{5}$$

Before proceeding into the complex nonlinear analysis, simple dimensional analysis [3] is helpful especially for our model equations (1) and (2). We can easily derive the following result: If the potential and pressure fluctuation amplitudes and turbulent diffusivity are dependent only on the four local parameters η, g, κ and s, then their expressions are given by

$$\langle\phi^2\rangle^{1/2} = \text{const}\cdot\eta s^{-2}g\kappa \tag{6}$$

$$\langle p^2\rangle^{1/2} = \text{const}\cdot\eta^{1/2}s^{-1}g^{1/4}\kappa^{5/4} \tag{7}$$

$$D = \text{const}\cdot\eta s^{-2}g\kappa. \tag{8}$$

Here the potential fluctuation amplitude $\langle\phi^2\rangle^{1/2}$ and the turbulent diffusivity D obey the same scaling law, which can be also written as $\gamma_k\Delta_k^2$.

Here we assume dependence on other parameters such as the system sizes, the viscosity and pressure diffusivity due to the Coulomb collision to be weak for the strong turbulence in the sheared magnetic field since the fluctuations may be localized around the mode resonant surface as expected from Eq.(4) and the turbulent diffusivity are much larger than the collisional one.

When we rewrite Eq.(8) in terms of physical parameters in the stellarator/heliotron plasma, we have

$$D = \text{const}\cdot D_{cl}\frac{q^2}{\epsilon^2}\left(\frac{r}{q}\frac{dq}{dr}\right)^{-2}\left(\frac{-r}{p_0}\frac{dp_0}{dr}\right)\left(r\frac{d\Omega}{dr}\right) \tag{9}$$

where D_{cl} is a classical diffusion coefficient, $\epsilon = r/R$ an inverse aspect ratio, q a safety factor and $d\Omega/dr$ an averaged magnetic curvature.

§3. Nonlinear analysis

Here we apply the renormalization technique [4–10] to the pressure convection equation (1). It is assumed that the electrostatic potential has no mean value.

$$\langle \phi \rangle = 0. \tag{10}$$

The pressure equation is formally solved for p,

$$p(t) = \int_{-\infty}^{t} d\tau U(t,\tau) \left(-\kappa \frac{\partial \phi(\tau)}{\partial y} \right) \tag{11}$$

where U is the propagator defined by

$$\left(\frac{\partial}{\partial t} + \boldsymbol{v}(t) \cdot \nabla \right) U(t,t_0) = \delta(t-t_0). \tag{12}$$

U is expanded in terms of $\boldsymbol{v}$ and the averaged propagator $\langle U \rangle$ as follows [4,8,9]

$$\begin{aligned} U(t,t_0) &= \langle U(t-t_0) \rangle - \int_{t_0}^{t} d\tau \langle U(t-\tau) \rangle \boldsymbol{v}(\tau) \cdot \nabla \langle U(\tau - t_0) \rangle + O(v^2) \\ &= \langle U(t-t_0) \rangle - \left[\int_0^{\infty} d\tau \langle U(\tau) \rangle \boldsymbol{v}(t-\tau) \right] \cdot \nabla \langle U(t-t_0) \rangle. \end{aligned} \tag{13}$$

Here, $O(v^2)$ terms are neglected and Markovian approximation is employed. Substituting this into Eq.(12) and averaging give

$$\left(\frac{\partial}{\partial t} - \nabla \cdot \mathsf{D} \cdot \nabla \right) \langle U(t-t_0) \rangle = \delta(t-t_0). \tag{14}$$

The turbulent diffusion tensor D is given by

$$\mathsf{D} \equiv \int_0^{\infty} d\tau \underline{\langle U(\tau) \rangle} \langle \boldsymbol{v}(t) \underline{\boldsymbol{v}(t-\tau)} \rangle. \tag{15}$$

Here an arrow shows the operand of the averaged propagator $\langle U \rangle$. If we replace U with $\langle U \rangle$ in Eq.(11), we have

$$p^c(t) = \int_{-\infty}^{t} d\tau \langle U(t-\tau) \rangle \left(-\kappa \frac{\partial \phi(\tau)}{\partial y} \right) \tag{16}$$

which is the solution of the one-point renormalized equation,

$$\left(\frac{\partial}{\partial t} + \nabla \cdot \mathsf{D} \cdot \nabla\right) p^c = -\kappa \frac{\partial \phi}{\partial y}. \tag{17}$$

Next, we consider the two-point propagator $U(1)U(2)$ $(1 = \boldsymbol{x}_1, 2 = \boldsymbol{x}_2)$

$$\left(\frac{\partial}{\partial t} + \boldsymbol{v}(1) \cdot \nabla_1 + \boldsymbol{v}(2) \cdot \nabla_2\right) U(1,t,t_0)U(2,t,t_0) = \delta(t - t_0). \tag{18}$$

We can derive the equation of the averaged two-point propagator $\langle UU \rangle$ by the same procedure as applied to $\langle U \rangle$. The result is

$$\left(\frac{\partial}{\partial t} - \sum_{i,j=1,2} \nabla_i \cdot \mathsf{D}(i,j) \cdot \nabla_j\right) \langle UU \rangle (1,2,t-t_0) = \delta(t - t_0) \tag{19}$$

where the two-point turbulent diffusion tensor $\mathsf{D}(i,j)$ is written as

$$\mathsf{D}(i,j) \equiv \int_0^\infty d\tau \langle U(j,\tau) \rangle \langle \boldsymbol{v}(i,t) \boldsymbol{v}(j,t-\tau) \rangle. \tag{20}$$

Introducing the centric and relative coordinates $(\boldsymbol{x}_+, \boldsymbol{x}_-)$ defined by

$$\boldsymbol{x}_+ = \frac{1}{2}(\boldsymbol{x}_1 + \boldsymbol{x}_2), \qquad \boldsymbol{x}_- = \boldsymbol{x}_1 - \boldsymbol{x}_2. \tag{21}$$

We can approximate $\langle UU \rangle$ by the product of the centric and relative propagators in the small relative distance,

$$\langle U(1)U(2) \rangle \simeq \langle U_+ \rangle \langle U_- \rangle. \tag{22}$$

The centric and relative propagators are given by

$$\left(\frac{\partial}{\partial t} - \frac{\partial}{\partial \boldsymbol{x}_+} \cdot \mathsf{D}_+ \cdot \frac{\partial}{\partial \boldsymbol{x}_+}\right) \langle U_+(t) \rangle = \delta(t) \tag{23}$$

$$\left(\frac{\partial}{\partial t} - \frac{\partial}{\partial \boldsymbol{x}_-} \cdot \mathsf{D}_- \cdot \frac{\partial}{\partial \boldsymbol{x}_-}\right) \langle U_-(t) \rangle = \delta(t). \tag{24}$$

Here the centric and relative diffusion tensors are

$$\mathsf{D}_+ \equiv \frac{1}{4}[\mathsf{D}(1,1) + \mathsf{D}(1,2) + \mathsf{D}(2,1) + \mathsf{D}(2,2)] \simeq \mathsf{D}(\boldsymbol{x}_+) \tag{25}$$

$$\mathsf{D}_- \equiv \mathsf{D}(1,1) + \mathsf{D}(2,2) - \mathsf{D}(1,2) - \mathsf{D}(2,1). \tag{26}$$

Now let us consider the two-point pressure correlation $\langle p(1)p(2) \rangle$, the single-time evolution of which is described by the two-point renormalized equation

$$\left(\frac{\partial}{\partial t} - \frac{\partial}{\partial x_-} D_- \frac{\partial}{\partial x_-}\right) \langle p(1)p(2) \rangle (\boldsymbol{x}_-)$$

$$= \left\langle -\kappa \frac{\partial \phi(1)}{\partial y} p(2) \right\rangle + (1 \leftrightarrow 2) \equiv S(\boldsymbol{x}_-) \tag{27}$$

where we put $\nabla_- \cdot \mathrm{D}_- \cdot \nabla_- \simeq (\partial/\partial x_-) D_- (\partial/\partial x_-)$ assuming $\partial/\partial x_- \gg \partial/\partial y_-$. The relative diffusivity D_- is approximated by

$$\begin{aligned} D_- &\simeq 2\int_0^\infty d\tau \int \frac{d^3k}{(2\pi)^3} g(\boldsymbol{k},\tau)\langle v_x v_y\rangle(\boldsymbol{k},\tau)[1-\cos(\boldsymbol{k}\cdot\boldsymbol{x}_-)] \\ &\simeq D(k_{0x}^2 x_-^2 + k_{0y}^2 y_-^2 + k_{0z}^2 z_-^2). \end{aligned} \tag{28}$$

where D is the one-point diffusivity and (k_{0x}, k_{0y}, k_{0z}) are the representative or characteristic wavenumbers of the turbulence. The solution of the two-point equation is given by

$$\begin{aligned} \langle p(1)p(2)\rangle(\boldsymbol{x}_-) &= \int_{-\infty}^t d\tau \langle U_-(t-\tau)\rangle S(\boldsymbol{x}_-,\tau) \\ &\simeq \tau_{cl} S(\boldsymbol{x}_-) \\ &\simeq \tau_{cl} S^0 \end{aligned} \tag{29}$$

where $S^0 = S(\boldsymbol{x}_- = 0)$. Here the clump lifetime $\tau_{cl}(\boldsymbol{x}_-)$ is defined as the time for two points initially separated by $\boldsymbol{x}_-$ to diverge such that $\langle R_-^2(t)\rangle \equiv k_{0x}^2\langle x_-^2\rangle + k_{0y}^2\langle y_-^2\rangle + k_{0z}^2\langle z_-^2\rangle = 1$. Taking the second moment of the relative propagator equation, we have

$$\frac{\partial}{\partial t}\langle R_-^2(t)\rangle = 2k_{0x}^2 D\langle R_-^2(t)\rangle. \tag{30}$$

From the solution of this, we obtain the clump lifetime,

$$\tau_{cl}(\boldsymbol{x}_-) = \begin{cases} \dfrac{1}{2k_{0x}^2 D} \ln\left(\dfrac{1}{k_{0x}^2 x_-^2 + k_{0y}^2 y_-^2 + k_{0z}^2 z_-^2}\right) & (k_{0x}^2 x_-^2 + k_{0y}^2 y_-^2 + k_{0z}^2 z_-^2 < 1) \\ 0 & (k_{0x}^2 x_-^2 + k_{0y}^2 y_-^2 + k_{0z}^2 z_-^2 > 1). \end{cases} \tag{31}$$

Fourier transform of the two-point pressure correlation $\langle pp\rangle = \tau_{cl} S^0$ gives the wavenumber spectrum [5,7,8]

$$\langle \tilde{p}\tilde{p}\rangle_{k_y} \equiv \int \frac{dk_z}{2\pi}\langle \tilde{p}\tilde{p}\rangle_{k_y,k_z} = \frac{2\pi S^0}{k_{0x}^2 D k_{0y}} \left(\frac{k_y}{k_{0y}}\right)^{-2} \left[1 - J_0\left(\frac{k_y}{k_{0y}}\right)\right]. \tag{32}$$

This wavenumber spectrum has been compared with the result of numerical simulation by Lee and Carreras [10]. In the above analysis, the characteristic wavenumbers k_{0x}, k_{0y} and k_{0z} are undetermined and adjustable parameters.

Now we pay attention to the source term S^0, which is approximated by

$$\begin{aligned} S^0 &= 2\kappa \int \frac{dk_y}{2\pi} k_y \mathrm{Im}\langle \phi p \rangle_{k_y} \\ &\simeq 2\eta s^{-2} g\kappa k_{0x}^2 \int \frac{dk_y}{2\pi} \langle pp \rangle_{k_y}. \end{aligned} \tag{33}$$

Here we put $igk_y p_k \simeq (s^2 k_y^2/\eta k_{0x}^2)\phi_k$ which is derived by equating the gravity term to the parallel diffusion term in the vorticity equation.

Substituting Eq.(33) into Eq.(32) and integrating with respect to k_y give the (one-point) turbulent diffusivity

$$D = C \cdot \eta s^{-2} g\kappa \tag{34}$$

where the dimensionless constant factor C is calculated as

$$C = 2 \int \frac{dk_y}{k_{0y}} \left(\frac{k_y}{k_{0y}} \right)^{-2} \left[1 - J_0 \left(\frac{k_y}{k_{0y}} \right) \right] = 4. \tag{35}$$

The expression of D, of course, agrees with the result of dimension analysis, but here the constant factor is determined by using the clump lifetime approximation to the two-point pressure correlation and assuming the ad hoc relation between pressure and potential fluctuations.

§4. Summary

We have studied the resistive interchange mode turbulence in the sheared magnetic field based on the electrostatic resistive MHD equations. Assuming that turbulent fluctuations and diffusivity depend mainly on four local parameters η, g, κ and s, the dimensional analysis uniquely determines the parameter dependence of the fluctuation amplitudes and the turbulent diffusivity in this model.

Applying the renormalization technique to the pressure equation gives the shape of the wavenumber spectrum (which is in agreement with the results of numerical simulation) and determines the turbulent diffusivity of pressure fluctuations including a constant factor, four.

In this nonlinear analysis, undetermined parameters such as a characteristic wavenumber k_0 still remain.

Acknowledgements

We acknowledge support from the Grant-in-Aid program from the Ministry of Education, Science and Culture.

Appendix: Comments on the Effects of the Radial Electric Field

Up to this point, we assumed there is no background electric field (or potential), $\langle\phi\rangle = 0$. Recently it is pointed out that the radial electric field $E_x = -d\langle\phi\rangle/dx$ plays a role on the plasma confinement. E_x produces $\boldsymbol{E} \times \boldsymbol{B}$ mean flow in the y-direction, which is possible to change the properties of instabilities and turbulence.

Recently, Shaing et al. reported that the saturation amplitudes in the resistivity-gradient-driven turbulence are lower for $E_x < 0$ than for $E_x > 0$ based on the MHD model [11]. However, their model equations as well as ours are invariant with the following transformation [8]

$$\begin{aligned}
\phi(x,y,z) &\rightarrow -\phi(x,-y,-z) \\
\langle\phi\rangle(x) &\rightarrow -\langle\phi\rangle(x) \\
E_x(x) &\rightarrow -E_x(x) \\
p(x,y,z) &\rightarrow p(x,-y,-z) \\
\eta(x,y,z) &\rightarrow \eta(x,-y,-z).
\end{aligned}$$

Therefore if we have a turbulent solution, in which $E_x < 0$, then the transformation gives the corresponding solution, in which $E_x > 0$. This means that the saturation amplitudes do not depend on the sign of E_x. But in other models such as FLR-MHD equations [12], the difference between positive E_x and negative E_x would appear.

References

[1] P. C. Liewer, Nucl. Fusion **25**, 543 (1985).

[2] H. R. Strauss, Plasma Phys. **22**, 733 (1980).

[3] J. W. Connor, Plasma Phys. Contr. Fusion **30**, 619 (1988).

[4] T. H. Dupree, Phys. Fluids **9**, 1773 (1966).

[5] T. H. Dupree, Phys. Fluids **15**, 334 (1972).

[6] P. W. Terry, P. H. Diamond, K. C. Shaing, L. Garcia, and B. A. Carreras, Phys. Fluids **29**, 2501 (1986).

[7] R. D. Sydora, J. N. Leboeuf, Z. G. An, P. H. Diamond, G. S. Lee, and T. S. Hahm, Phys. Fluids **29**, 2871 (1986).

[8] H. Sugama and M. Wakatani, J. Phys. Soc. Jpn. **57**, 2010 (1988).

[9] H. Sugama, *Study of Interchange Instabilities and Anomalous Transport Based on Reduced Two-Fluid Model*, Doctoral Thesis for Electrical Engineering, Kyoto University, 1988.

[10] G. S. Lee and B. A. Carreras, Phys. Fluids B **1**, 119 (1989).

[11] K. C. Shaing, G. S. Lee, B. A. Carreras, W. A. Houlberg, and E. C. Crume, Jr., 12th Int. Conf. on Plasma Physics and Controlled Nucl. Fusion Res. (Nice, 1988) IAEA–CN–50/D–V–2.

[12] A. Hasegawa and M. Wakatani, Phys. Fluids **26**, 2770 (1983).

Formation of a Current Bubble in a Coupling Process of Resistive Tearing Modes

Kazuhiro Urata* and Tadatsugu Hatori*
Institute of Plasma physics
Nagoya University
Nagoya 464-01, Japan

Abstract

The current bubble means a helical duct with low current density invading the inner high current region of current carrying toroidal plasmas. The numerical simulations show that it appears right after the absorbtion of a small magnetic island into the chaotic layer along the separatrix of large magnetic island.

*Present address : National Institute for Fusion Science,
Nagoya 464-01, Japan

We study numerically the mode-coupling process of resistive tearing modes with different helicities based on a reduced set of magnetohydrodynamics (MHD) in the tokamak ordering. Dominant two tearing modes are $m = 2/n = 1$ (2/1 in shorthand notaion) and 3/2. Here m and n represent the poloidal and the toroidal mode numbers, respectively. B.V.Waddell et al.[1] and B.Carreras et al.[2] studied the nonlinear destabilization of the 3/2 mode and the nonlinear coupling of the 3/2 mode and the 2/1 mode resulting in the chaotic magnetic field.

We find out an unexpected new phenomenon, the formation of a current bubble, which occurs right after the disappearance of the 3/2 magnetic islands. The current bubble is a duct with nearly zero toroidal current density J_z , which invades the central region of high J_z around the magnetic axis in the poloidal cross-section. It deforms into an erregular pattern after a finite time and is at last followed by a turbulent state.

Figure 1 shows a time evolution of confours of the equal toroidal current density J_z (upper) and their horizontal profiles (lower) at different times t = 0, 2.5×10^{-3} and 3.0×10^{-3} , where the time is scaled by the resistive time τ_r. Starting from an initially unstable state, the dominant 2/1 structure grows at time t = 2.5×10^{-3} then at t = 3.0×10^{-3} a current bubble forms on the right region. It is to be noted that the bubble structure appears well inside the chaotic magnetic region as shown in Fig.2. In this run, the value of S (= resistive time τ_r / Alfven time τ_A) is chosen to be 1.3×10^5, the radial mesh is a/200 where a is the radius of the plasma, and the time mesh is variable ranging from $0.66 \sim 2 \times 10^{-7}$.

The current bubble is created by a pair of votices which are originally formed in the chaotic magnetic layer at the reparatrix of 2/1-island and are suddenly enhanced right after the merging of the 3/2-island into the chaotic layer. The chaos induces the vorticity in the chaotic layer through the vorticity equation,

$$\frac{d}{dt}\omega = S^2 \nabla_{11} J_z . \qquad (1)$$

Here ω is vorticity defined by the stream function ϕ as $\omega = -\Delta_\perp \phi$, ∇_{11} means the parallel gradient along be magnetic field.

In the presence of 3/2-island $\nabla_{11} J_z \simeq 0$, but in the chaotic region $\nabla_{11} J_z$ takes a finite value, resulting in a large value of the right-hand ride of eq.(1). Figure 3 illustrates the contour of the equal stream function ϕ (upper), and the direction and the magnitude of the flow velocity (lower) at time $t = 3.0 \times 10^{-3}$. From Fig.3, we can easily imagine a strong inflow toword the center on the right region, which is responsible to the current bubble formation.

Formation of a current bubble means the local interchange of the high and low current density regions, therefore it gives one of the mechanisms for the rapid radial transport of the toroidal current density. It is well known that the force-free equilibrium states are frequently realized in the laboratory and astrophysical plasmas through the rapid magnetic relaxation process. The associated violent transport of the current density is explicable by the current bubble.

In conclusion, the current bubble formation in the coupling process of resistive tearing modes is found by numerical simulations based on the reduced set of MHD equations. It is formed right after the disappearance of 3/2 island. This indicates that it is a sturcture induced by the magnetic chaos. It persists wighin a time interval of the order of $10\tau_A$. It is to be noted there exists a spatial structure which we call the current bubble even in the chaotic magnetic field. Current bubbles are formed anywhere O-points of different modes face each other.

References

[1] B.V.Waddell, B.Carreras, H.R.Hicks, and J.A.Holmes, Phys.Fluids 22, 896 (1979)

[2] B.Carreras, H.R.Hicks, J.A.Holmes, and B.V.Waddell, Phys.Fluids 23, 1811 (1980)

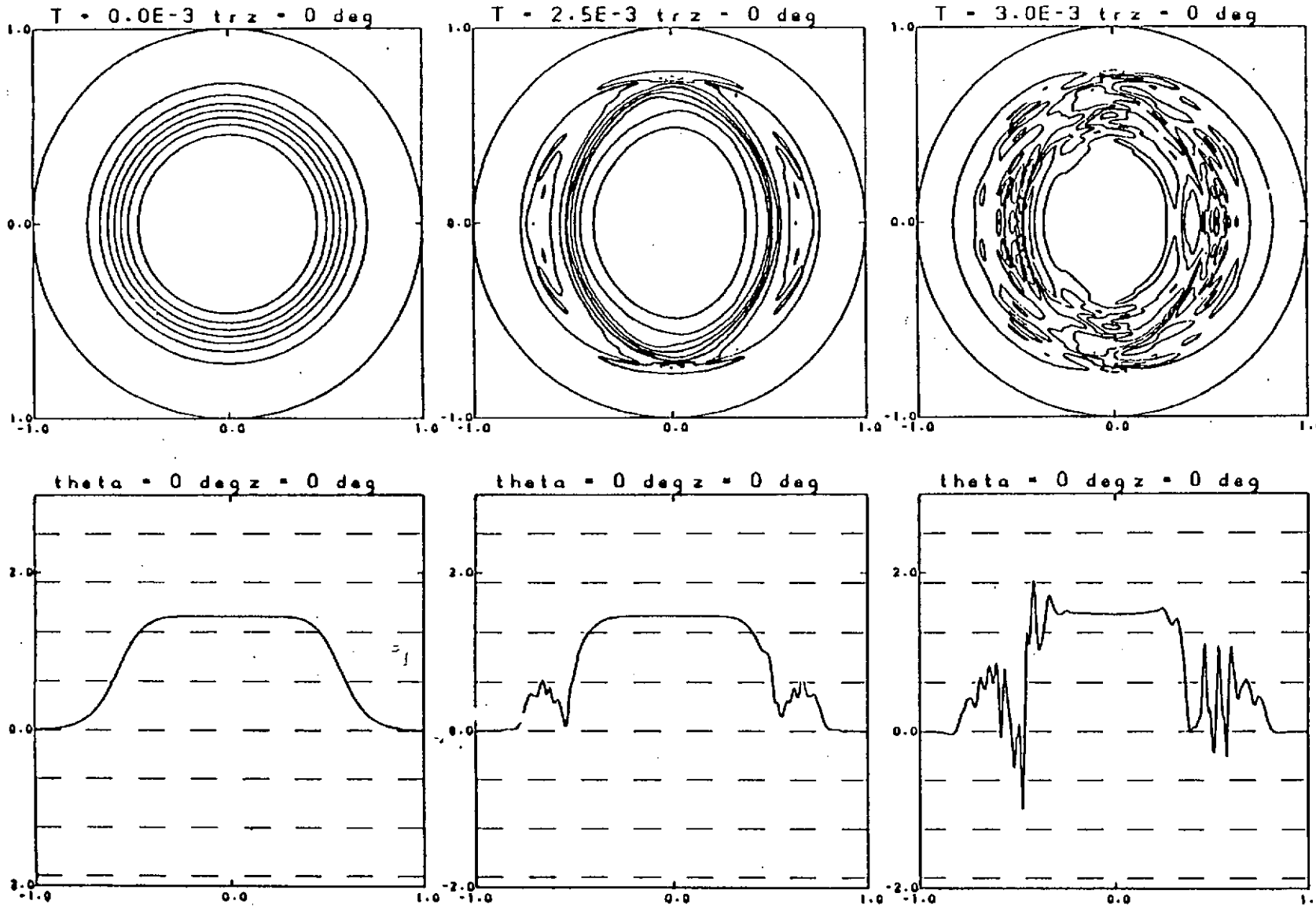
T = 0.0E-3 trz = 0 deg
T = 2.5E-3 trz = 0 deg
T = 3.0E-3 trz = 0 deg
theta = 0 degz = 0 deg
theta = 0 degz = 0 deg
theta = 0 degz = 0 deg

Fig. 1.

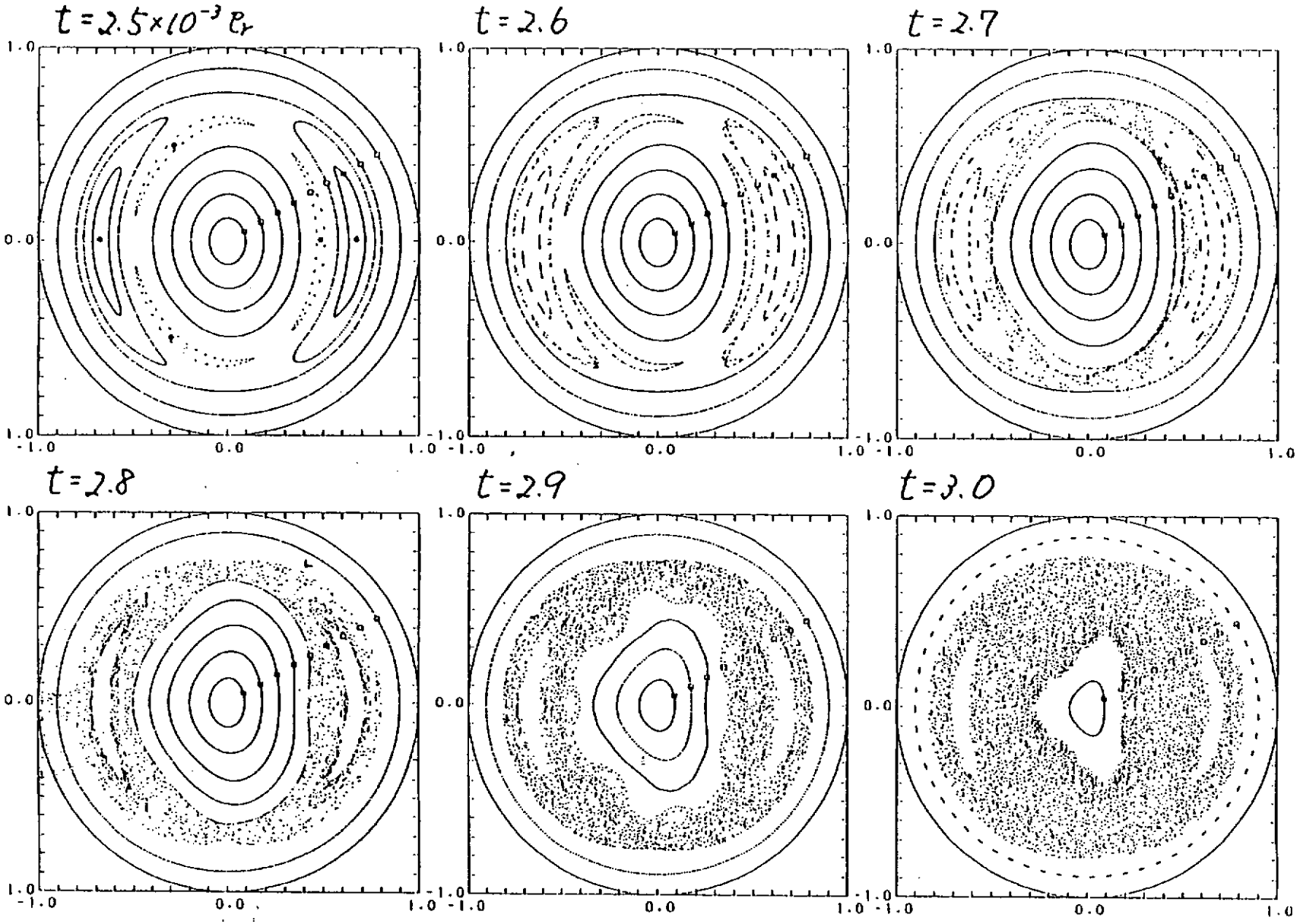

Fig. 2.

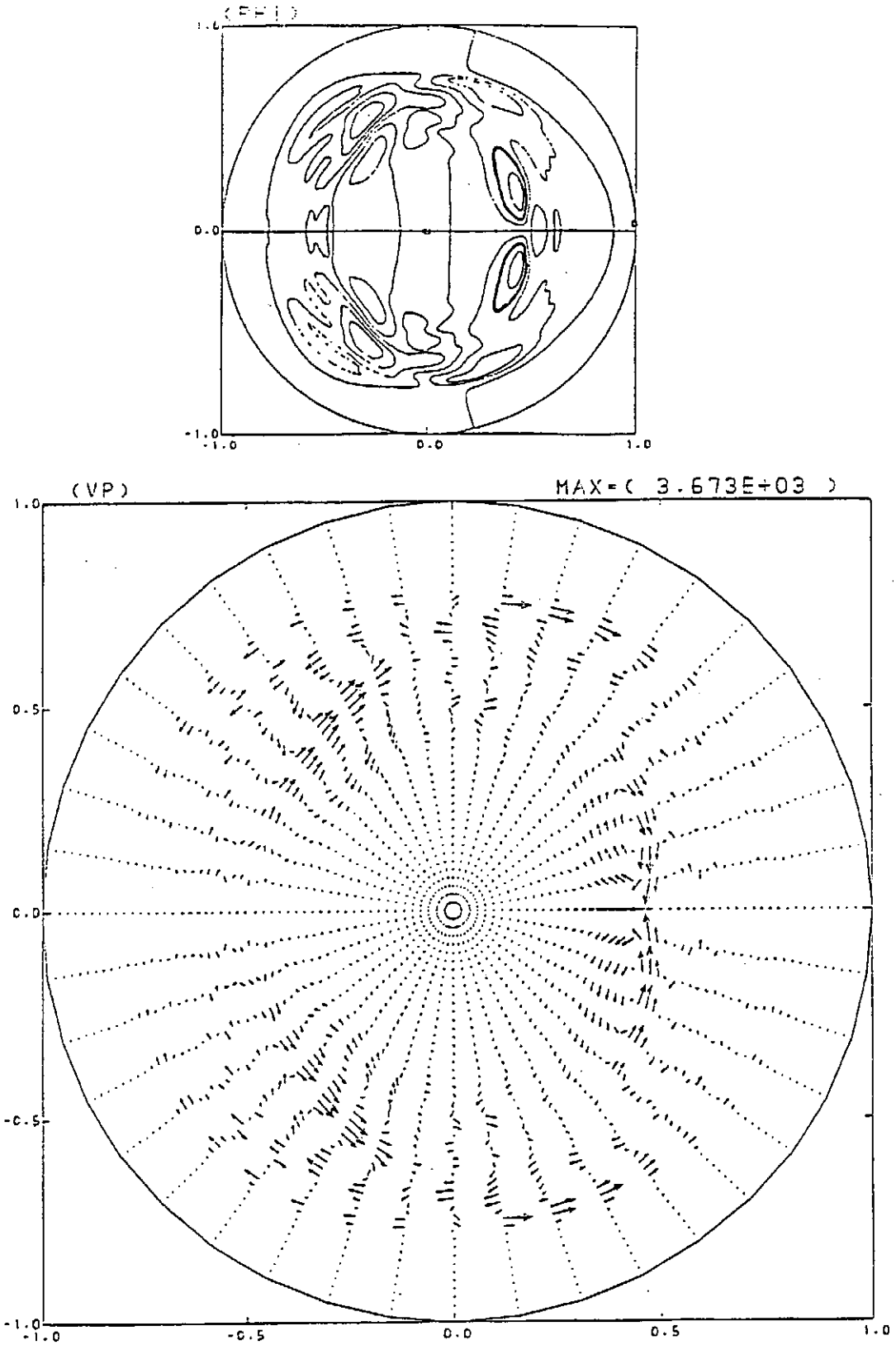
T = (3.000E-03)
(PHI)
1.0
0.0
-1.0
-1.0
0.0
1.0
(VP)
MAX=(3.673E+03)
1.0
0.5
0.0
-0.5
-1.0
-1.0
-0.5
0.0
0.5
1.0

Fig. 3.

IV. Structures in Vlasov Plasmas

Nonlinear Wave Coupling and Clumps in Drift Wave Turbulence Theory

R.R. DOMINGUEZ

General Atomics
San Diego, California, U.S.A.

Abstract

Anomalous transport mediated by drift wave turbulence has been studied by many authors using weak and renormalized turbulence theory. Additional nonlinear effects coming from three-wave coupling have been studied in simple models by Waltz [1] and for drift waves by Waltz and Dominguez [2]. At the same time, the "clump" theory of Dupree has been extended and applied to drift wave turbulence [3,4]. In the present work, we discuss how the discreteness effects associated with clumps may be combined with the nonlinear wave coupling formalism [2]. It is shown that both the nonlinear wave coupling and clump correlation act as sources for the spectral density in $\underline{k}$, and ω, with a comparison between the two effects being presented.

Drift wave turbulence theory has come to be divided into two subcategories, weak turbulence and strong turbulence. The former includes quasi-linear theory and three wave coupling (mode-coupling) while the latter is generally synonymous with clump theory (renormalized two point theory) originated by Dupree in the study of turbulence in homogeneous plasmas. The renormalized one point theory associated with effects such as Compton scattering seems to be viewed as an intermediate step between the weak and strong turbulence limits. Here we wish to point out that this convenient decomposition of turbulence theory can be ambiguous. Further, we attempt to estimate (at least qualitatively) the relative importance of the "weak" turbulence mode coupling process versus the "strong" turbulence clump decorrelation process.

Elements of non-linear theory:

1. Quasi-linear theory, three-wave interaction, 1 point renormalization (weak turbulence).

2. Two point renormalization ("clumps"), Dupree 1972, 1978; Hirschman and Diamond 1979; Terry and Diamond 1983 (strong turbulence).

Non-linear gyro-kinetic equation (at guiding center position)

$$(\omega - k_{\|} v_{\|})\, \delta \hat{H}_{\underline{k},\omega} = \hat{L}_{\underline{k}\,\omega}\, \mathrm{F}_{os} - i\, \frac{c}{\mathrm{B}_o} \sum_{\underline{k}',\omega'} \hat{\underline{b}} \cdot (\underline{k} \times \underline{k}') \times \widehat{\langle \delta \mathrm{L} \rangle}_{\underline{k}',\omega'}\, \delta \hat{H}_{\underline{k}-\underline{k}',\omega-\omega'} \quad , \quad (1)$$

$$\delta \hat{\mathrm{F}}_{\underline{k}\,\omega} = q_s\, \frac{\partial \mathrm{F}_{os}}{\partial \epsilon}\, \delta \Phi_{\underline{k}\,\omega} + \delta \hat{H}_{\underline{k},\omega} \quad ,$$

$$\hat{L}_{\underline{k},\omega}\, \mathrm{F}_{os} = -q_s \left(\omega\, \frac{\partial}{\partial \epsilon} + \frac{k_\theta}{M_s \Omega_s}\, \frac{\partial}{\partial r} \right) \mathrm{F}_{os}\, \widehat{\langle \delta \mathrm{L} \rangle}_{\underline{k},\omega} \quad ,$$

$$\widehat{\langle \delta \mathrm{L} \rangle}_{\underline{k},\omega} = \delta \hat{\Phi}_{\underline{k},\omega}\, J_o\, (k_\perp v_\perp / \Omega_s) \quad .$$

Frieman and Chen extract from Eq. (1)

1. Renormalized piece
2. Three-wave piece
3. "Clump" piece

We decompose the potential fluctuations as

$$\delta\Phi_{\underline{k},\omega} = \underset{\text{(undriven)}}{\delta\Phi^{(c)}_{\underline{k},\omega}} + \underset{\text{(3-wave driven)}}{\delta\Phi^{(3)}_{\underline{k},\omega}} + \underset{\text{(clump driven)}}{\delta\tilde{\Phi}_{\underline{k},\omega}} \quad , \tag{2}$$

("^" is dropped).

1. Renormalized Piece:

$$C_{\underline{k},\omega}\,\delta H^{(c)}_{\underline{k},\omega} = d_{\underline{k},\omega}\,\delta H^{(c)}_{\underline{k},\omega} - b_{\underline{k},\omega}\langle\delta \mathrm{L}\rangle^{(c)}_{\underline{k},\omega} \quad , \tag{3}$$

$$d_{\underline{k},\omega} = i\sum_{\underline{k}',\omega'}\left|\frac{c}{\mathrm{B_o}}\,\hat{\underline{b}}\cdot(\underline{k}\times\underline{b}')\right|^2\left|\langle\delta \mathrm{L}\rangle^{(c)}_{\underline{k}',\omega'}\right|^2 G_{\underline{k}-\underline{k}',\omega-\omega'}$$

$$b_{\underline{k},\omega} = i\sum_{\underline{k}',\omega'}\left|\frac{c}{\mathrm{B_o}}\,\hat{\underline{b}}\cdot(\underline{k}\times\underline{k}')\right|^2\langle\delta \mathrm{L}\rangle^{(c)}_{\underline{k}',\omega'}\,\delta H^{(c)*}_{\underline{k}',\omega'}\;G_{\underline{k}-\underline{k}',\omega-\omega'} \tag{4}$$

and $G_{\underline{k},\omega} = (\omega - k_\parallel v_\parallel + i\,d_{\underline{k},\omega})^{-1}$.

2. Three Wave Piece:

$$\left(\omega - k_\parallel v_\parallel + i\,C_{\underline{k},\omega}\right)\delta H^{(3)}_{\underline{k},\omega} = L^{(3)}_{\underline{k},\omega}\,\mathrm{F}_{os}$$
$$- \frac{i\,c}{\mathrm{B_o}}\sum_{\underline{k}',\omega'}\hat{\underline{b}}\cdot\left(\underline{k}\times\underline{k}'\right)\langle\delta \mathrm{L}\rangle^{(c)}_{\underline{k}',\omega'}\,\delta H^{(c)}_{\underline{k}-\underline{k}',\omega-\omega'} \tag{5}$$

Adding the renormalization and three wave results:

$$(\omega - k_\parallel v_\parallel + i\,C_{\underline{k},\omega})\left(\delta H^{(c)}_{\underline{k},\omega} + \delta H^{(3)}_{\underline{k},\omega}\right) = \left(L^{(c)}_{\underline{k},\omega} + L^{(3)}_{\underline{k},\omega}\right) \mathrm{F}_{os}$$
$$- i\,\frac{c}{\mathrm{B_o}} \sum_{\underline{k}',\omega'} \hat{\underline{b}} \cdot (\underline{k} \times \underline{k}')\langle \delta \mathrm{L}\rangle^{(c)}_{\underline{k}',\omega'}\, \delta H^{(c)}_{\underline{k}-\underline{k}'\,\omega-\omega'} \quad .$$

Inverting this expression and adding the clump piece, the non-adiabatic perturbed distribution becomes

$$\delta H_{\underline{k},\omega} = e^{i\mathrm{L}\underline{k}}\, G_{\underline{k},\omega}\left[\left(\mathrm{L}^{(c)}_{\underline{k},\omega} + \mathrm{L}^{(3)}_{\underline{k},\omega}\right)\mathrm{F}_{os} + i\,b_{\underline{k},\omega}\left(\langle\delta\mathrm{L}\rangle^{(c)}_{\underline{k},\omega} + \langle\delta\mathrm{L}\rangle^{(3)}_{\underline{k},\omega}\right)\right]$$
$$- \frac{i\,c}{\mathrm{B_o}} \sum_{\underline{k}',\omega'} \hat{\underline{b}} \cdot (\underline{k} \times \underline{k}')\langle\delta\mathrm{L}\rangle^{(c)}_{\underline{k}',\omega'}\, G_{\underline{k},\omega}\, G_{\underline{k}-\underline{k}',\omega-\omega'}$$
$$\times \left(L^{(c)}_{\underline{k}-\underline{k}',\omega-\omega'}\,\mathrm{F}_{os} + i\,b_{\underline{k}-\underline{k}',\omega-\omega'}\,\langle\delta\mathrm{L}\rangle^{(c)}_{\underline{k}'-\underline{k}',\omega-\omega'}\right)$$
$$\times e^{i\mathrm{L}\underline{k}} + \delta\tilde{H}_{\underline{k},\omega}\,(\text{clump piece}) \qquad (6)$$

the factors $\exp i\,\mathrm{L}\underline{k}$;$\mathrm{L}_{\underline{k}} = \underline{k}\cdot(\underline{v}\times\hat{\underline{b}})/\Omega_s$, convert from guiding center to particle position. The object is to use Eq. (6) to obtain mode coupling spectral equations and estimate relative importance of clumps.

Assume $\delta\Phi^{(c)}_{\underline{k},\omega}$, $\delta\Phi^{(3)}_{\underline{k},\omega}$, $\delta\tilde{\Phi}_{\underline{k},\omega}$ are uncorrelated. Following standard techniques — [R.E. Waltz and R.R. Dominguez, Phys. Fluids **26**, 3338 (1982)] we obtain mode coupling equations for $I_{\underline{k},\omega} = \langle|\frac{e\,\delta\Phi}{\mathrm{T_e}}\underline{k},\,\omega|^2\rangle$

$$\left[-i\,(\omega - \hat{\omega}\underline{k}) + \hat{\eta}_{\underline{k},\omega}\right] I_{\underline{k},\omega} = \sum_{\underline{k}',\omega'} \frac{\hat{V}_{\underline{k}\,\omega;\,\underline{k}',\omega'}}{\left[-i\,(\omega - \hat{\omega}_{\underline{k}}) + \hat{\eta}_{\underline{k},\omega}\right]^*}$$
$$\times \left(\hat{V}_{\underline{k},\omega;\,\underline{k}',\omega'} + \hat{V}_{\underline{k},\omega;\,\underline{k}'',\,\omega''}\right)^* I_{\underline{k}',\omega'}\, I_{\underline{k}'',\omega''}$$
$$- i\,\tau\,\frac{\omega}{\omega^*_e}\,\widehat{\omega_{\underline{k}}}\left\langle\left|\frac{e\widetilde{\delta\Phi}}{\mathrm{T_e}}\underline{k},\,\omega\right|^2\right\rangle \quad , \qquad (7a)$$

$$-\hat{\eta}_{\underline{k},\omega} = \sum_{\underline{k}',\omega'} \hat{V}_{\underline{k},\omega;\underline{k}',\omega'} \left[\frac{\hat{V}_{\underline{k}',\omega';\underline{k},\omega} + \hat{V}_{\underline{k}',\omega';-\underline{k}'',-\omega''}}{-i\left(\omega' - \hat{\omega}_{\underline{k}'}\right) + \hat{\eta}_{\underline{k}',\omega'}} I_{\underline{k}'',\omega''} \right.$$

$$\left. + \frac{\hat{V}_{\underline{k}'',\omega'';\underline{k},\omega} + \hat{V}_{\underline{k}'',\omega'';-\underline{k}',-\omega'}}{-i\left(\omega'' - \hat{\omega}_{\underline{k}''}\right) + \hat{\eta}_{\underline{k}'',\omega''}} I_{\underline{k}',\omega'} \right] \quad , \tag{7b}$$

where the last term in Eq. (7a) is the clump contribution.

Definitions:

- $\hat{\omega}_{\underline{k}} = \omega_e^* / \chi_{\underline{k},\omega}$,
- $\chi_{\underline{k},\omega} = \left(\frac{\omega_e^*}{\omega} - 1\right) + i\,\delta_{\underline{k},\omega} - \tau \left\{ 1 - \int d\underline{v} \left[g_{\max}\left(\omega - \omega_i^*\right) + i\, b_{\underline{k},\omega} \frac{T_i}{n_o e} \right] \right.$
  $\left. \times\, G_{\underline{k},\omega}\, J_{oi}^2 \left(k_\perp v_\perp / \Omega_i\right) \right\}$,
- $\hat{V}_{\underline{k},\omega;\underline{k}',\omega'} = V_{\underline{k},\omega;\underline{k}'\omega'} / \chi_{\underline{k},\omega}$,
- $V_{\underline{k},\omega;\underline{k}',\omega'} = \tau\,\omega\,\frac{c}{B_o}\,\hat{\underline{b}} \cdot \left(\underline{k} \times \underline{k}'\right) \int d\underline{v}\, G_{\underline{k},\omega}\, G_{\underline{k}-\underline{k}',\omega-\omega'} \left\{ g_{\max}\left[\left(\omega - \omega'\right)\right.\right.$
  $\left.\left. - \left(\omega_i^* - \omega_i^{*\prime}\right)\right] + i\, b_{\underline{k}-\underline{k}',\omega-\omega'} \frac{T_i}{n_o e} \right\} J_{oi}\left(\frac{k_\perp v_\perp}{\Omega_i}\right) J_{oi}\left(\frac{k'_\perp v_\perp}{\Omega_i}\right) J_{oi}\left(\left|\underline{k}_\perp - \underline{k}_i\right| \frac{v_\perp}{\Omega_i}\right)$

Also, electrons are linear $\delta n_{\underline{k},\omega}^{(e)} = \frac{n_o e}{T_e}\left(1 - i\,\delta_{\underline{k},\omega}\right) \delta\Phi_{\underline{k},\omega}^{(c)}$.

3. Clump Contribution to Mode-Coupling:

The clump contribution is obtained from

$$\left\langle \widetilde{\delta\Phi}_{\underline{k},\omega}^* \left(\delta\tilde{n}_{\underline{k},\omega}^{ion} + \frac{n_o e}{T_i} \delta\tilde{\Phi}_{\underline{k},\omega} \right) \right\rangle \equiv \left\langle \delta\tilde{\Phi}_{\underline{k},\omega}^* \delta\tilde{n}_{\underline{k},\omega}^{ion} + \frac{n_o e}{T_i} \left|\delta\tilde{\Phi}_{\underline{k},\omega}\right|^2 \right\rangle$$

Ion clumps generate $\delta\tilde{\Phi}$:

$$k^2 \delta\tilde{\Phi}_{\underline{k},\omega} = 4\pi e\, \delta\tilde{n}_{\underline{k},\omega}^{ion}$$

Hence

$$\left\langle \delta\tilde{\Phi}^{*}_{\underline{k},\omega}\,\delta\tilde{n}^{\rm ion}_{\underline{k},\omega} + \frac{n_o\,e}{T_i}\left|\delta\tilde{\Phi}_{\underline{k},\omega}\right|^2 \right\rangle \approx \frac{n_o\,e}{T_i}\left\langle \left|\delta\tilde{\Phi}_{\underline{k},\omega}\right|^2 \right\rangle$$

waves provide screening so use shielded clump potential $\delta\tilde{\Phi} \rightarrow \delta\tilde{\Phi}/\epsilon_{\underline{k},\omega}$.

To calculate clump potential, first need quick review:

Two Point Correlation Function

$$\left(\frac{\partial}{\partial t} + \underline{v}^{(-)}_{\parallel}\cdot\frac{\partial}{\partial \underline{z}^{-}} - \frac{\partial}{\partial \underline{r}^{-}}\cdot\underline{\underline{D}}^{-}\cdot\frac{\partial}{\partial \underline{r}^{-}}\right)\langle \delta f(1)\,\delta f(2)\rangle = D_{\perp}\left(\frac{\partial\langle f\rangle}{\partial r}\right)^2 \quad .$$

$$\underline{\underline{D}}^{-} = \underline{\underline{D}}(0) - \underline{\underline{D}}(\underline{r}^{-}) \quad .$$

Coherent Response

$$\left(\frac{\partial}{\partial t} + v^{(-)}_{\parallel}\cdot\frac{\partial}{\partial \underline{z}^{-}} - \frac{\partial}{\partial \underline{r}^{-}}\cdot\underline{\underline{D}}(0)\cdot\frac{\partial}{\partial \underline{r}^{-}}\right)\langle \delta f^{(c)}\,\delta f^{(c)}\rangle = D_{\perp}\left(\frac{\partial\langle f\rangle}{\partial r}\right)^2 \quad ,$$

$$\frac{b}{d} \sim 0\left(\frac{\omega}{k_z\,v\,T}\right) \quad , \qquad \omega \ll k_z\,v_T \quad .$$

From this one can calculate the clump correlation $\langle \tilde{\delta f}\,\tilde{\delta f}\rangle$. Approximate calculation by Dupree 1978 for ion clumps:

$$\langle \tilde{\delta f}\,\tilde{\delta f}\rangle = \delta(\tilde{v_{\parallel}})\frac{D_{\perp}\,f^2_{\rm max}\,(v_{\parallel})}{L^2_n\,k_{oz}}\,A(\underline{W}) \quad , \tag{8}$$

$L_n^{-1} = |\partial \ell n\, n/\partial r|$, $f_{\rm max}$ = Maxwellian, $\underline{W} = (k_{ox},\, x^{-},\, k_{oy}\,y,\, k_{oz}\,z^{-})$, $\tilde{v_{\parallel}} = v_{\parallel 1} - v_{\parallel 2}$. Further

$$\langle |\tilde{\delta f}_{\underline{k},\omega}|^2\rangle = 2\,\pi\,\delta\,(\omega - k_z\,v_{\parallel 1}) \times \langle |\tilde{\delta f}_{\underline{k}}|^2\rangle \quad , \tag{9}$$

where

$$\langle|\tilde{\delta f}_{\underline{k}}|^2\rangle = \frac{\delta(v_{\|}^{-})\, D_{\perp}\, f_{\max}^2\,(v_{\|\,2})}{\mathrm{L}_{\mathrm{n}}^2\, k_{oz}^2\, k_{ox} k_{oy}} \times A(\underset{\sim}{K}) \quad , \tag{10}$$

and

$$A(\underset{\sim}{K}) = \int d\underset{\sim}{W}\, A(\underset{\sim}{W})\, e^{-i\underset{\sim}{K}\cdot\underset{\sim}{W}}$$

$$\underset{\sim}{K} = \left(\frac{k_x}{k_{x_o}}, \frac{k_y}{k_{y_o}}, \frac{k_z}{k_{z_o}}\right)$$

From Eqs. (9) and (10), the clump potential contribution to spectral density equation can be obtained. Clump source, including shielding

$$\left\langle \left| \frac{e\,\widetilde{\delta\Phi}_{\underline{k},\omega}}{\mathrm{T_e}} \right|^2 \right\rangle = \frac{1}{|\epsilon_{\underline{k},\omega}|^2}\, \frac{2\pi}{k_z}\, (k\lambda_{\mathrm{de}})^{-4}\, \frac{D_{\perp}\, f_{\max}^2\left(\frac{\omega}{kz}\right)}{\mathrm{L}_{\mathrm{n}}^2\, k_{oz}^2\, k_{ox}\, k_{oy}}\, A(\underset{\sim}{K}) \quad , \tag{11}$$

where λ_{de} = Debye length, $\epsilon_{\underline{k},\omega}$ = dielectric function

$$\epsilon_{\underline{k},\omega} = 1 + (k\lambda_{de})^{-2} \left(1 - \frac{\omega_e^*}{\omega} - i\delta_{\underline{k},\omega} + \tau\left\{1 - \int d\underset{\sim}{v}\left[g_{\max}\,(\omega - \omega_i^*)\right.\right.\right.$$

$$\left.\left.\left. + ib_{\underline{k},\omega}\frac{\mathrm{T_i}}{\mathrm{n_o} e}\right] G_{\underline{k},\omega} J_{oi}^2 \left(\frac{k_{\perp}\, v_{\perp}}{\Omega_i}\right)\right\}\right) \quad . \tag{12}$$

Also, $\epsilon_{\underline{k},\omega} = 1 - \chi_{\underline{k},\omega}/k^2\lambda_{de}^2$.

Use Eq. (11) to estimate magnitude of clump contribution in spectral equation

$$\tau\,\frac{\omega}{\omega_e^*}\,\hat{\omega}_{\underline{k}} \left\langle \left| \frac{e\,\bar{\delta\Phi}_{\underline{k},\omega}}{\mathrm{T_e}} \right|^2 \right\rangle = \frac{2\tau}{k_z}\, \frac{\omega}{(k_z v_{\mathrm{T_i}})^2} \times \frac{1}{\chi_{\underline{k},\omega}|\chi_{\underline{k},\omega}|^2}\, \frac{D_{\perp}}{(k_z \mathrm{L_n})^2}$$

$$\times \left(\frac{k_x}{k_{ox}}\right)^2 \left(\frac{k_z}{k_{oz}}\right)^2 A(\underset{\sim}{K}) \times \exp - 2\left(\frac{\omega}{k_z v_{\mathrm{T_i}}}\right)^2 \quad , \tag{13}$$

where $k_{ox} = k_{oy}$ is assumed.

$$A(\underset{\sim}{K}) \sim \exp -(\underset{\sim}{K} \cdot \underset{\sim}{W}_o)^2 \sim \exp -(\underset{\sim}{k} \cdot \underset{\sim}{x}_o^-)^2$$

only contribution from $\underset{\sim}{k} \cdot \underset{\sim}{x}_o^- \lesssim 1$, $\omega/k_z v_{T_i} \lesssim 1$. Taking $|A(\underset{\sim}{k})| \sim 1$, $\omega/k_z v_{T_i} < 1$, k_x/k_{oz} and $k_z/k_{oz} \sim 1$, $|\chi_{\underset{\sim}{k},\omega}| \sim 1$ (significant mode-coupling frequency shift) the relative magnitude of the spectral intensity to the clump term in Eq. (7a) becomes

$$\underset{\text{(density amplitude)}}{\left\langle \left| \frac{\delta n}{n} \right|^2 \right\rangle} \quad : \quad \underset{\text{(clump amplitude)}}{\left(\frac{\omega}{k_z v_{T_i}} \right)^2 (\omega \tau_c)^{-1} \frac{1}{(k_x L_n)^2}} \quad .$$

Evidently, the clump amplitude is smaller by $0\left[\left(\frac{\omega}{k_z v_{T_i}}\right)^2\right]$, or more.

If mode-coupling is weak, then $\chi_{\underset{\sim}{k},\omega} \to 0$ determines modes and there is a much stronger clump effect. If mode-coupling is very strong, can't separate wave-wave nonlinearity from clumps, but perturbative treatment is not possible.

To summarize the conclusions:

1. Clumps can generate finite line width spectra.
2. Moderately strong non-linear wave-wave interactions can dominate the clump mechanism; clump contribution $\propto |\chi_{\underset{\sim}{k},\omega}|^{-3}$, three-wave contribution $\propto |\chi_{\underset{\sim}{k},\omega}|^{-2}$.
3. Very strong turbulence has no natural wave-wave/clump decomposition.

References

[1] R.E. Waltz, Phys. Fluids **26**, 169 (1983).

[2] R.E. Waltz and R.R. Dominguez, Phys. Fluids **26**, 3338 (1983).

[3] P.W. Terry and P.H. Diamond, University of Texas IFS Report #91 (1983).

[4] G.S. Lee and P.H. Diamond, Phys. Fluids **29**, 3291 (1986).

A Computationally Exact Method of Dawson's Model for Hole Dynamics of One-Dimensional Plasma

Kazuo KITAHARA
Department of Applied Physics,
Tokyo Institute of Technology,
Meguro-ku, Tokyo 152
and
Institute of Molecular Science,
Myodaiji, Okazaki 444

Kohki TANNO and Toshio TAKADA
Department of Applied Physics,
Tokyo Institute of technology,
Meguro-ku, Tokyo 152

Tadatsugu HATORI and Kazuhiro URATA
Institute of Plasma Physics,
Nagoya University,
Chikusa-ku, Nagoya 464

Haruyuki IRIE
Department of Physics,
College of Science and Technology,
Nihon University,
Chiyoda-ku, Tokyo 103

Mitsuhiro NAMBU
Department of Liberal Arts
Kyushu University
Higashi-ku, Fukuoka 812

Kohichi SAEKI
Department of Liberal Arts,
shizuoka University,
Ohya, Shizuoka 422

ABSTRACT

We show a simple but computationally exact solution of the one-dimensional plasma model, so-called "Dawson's model". Using this solution, we can describe the evolution of the plasma and find the relative stabilization of a big hole after the instability of two streams.

1. Introduction

The evolution of a collisionless plasma is a highly non-linear and with strong correlation between particles and waves. Although the Vlasov equation for a one-dimensional collisionless plasma is the simplest model, only the steady state solution is known as BGK solution.[1] The stability of BGK solutions has been studied: For example, the stability of vortex structures in phase space was discussed by Schamel.[2] The stability of a two-stream plasma was numerically studied and it was found that a number of holes which appear will coalesce into a big hole.[3]

In this respect, it is also interesting to perform particle-simulation in order to see the dynamics of holes in phase space. A clear exposition of a one-dimensional particle model was shown by Dawson[4,5] a long time ago. This model is a mechanical model of interacting electron sheets with positive ion background. Here we propose an efficient computational method, for this model. We transform the equations of motion of sheets into a finite-time mapping in the phase space, which can be analyzed exactly by numerical computation. Thus, whatever errors may enter, they are just due to the limitation of the computer precision.

In Sec.2, we show our formulation. In Sec.3, we give some results concerning the two-stream instability, especially we show that a big hole persists for a long time at the late stage of evolution.

Sec.4 is devoted to conclusions.

2. Exact Solution of Dawson's Model and the Method of Computation

Dawson's model consists of N negatively-charged sheets and uniform positive background of ions in a box of length L. We number the sheets from the left boundary. Thus if we denote the position of the i-th sheet by x_i, then we have $x_1<x_2<\ldots<x_N$ by the definition. The equation of motion for the i-th sheet is

$$\frac{d^2x_i}{dt^2} = -\omega_p^2 \left[x_i-(i-\tfrac{1}{2})\delta \right] \tag{1}$$

where ω_p is the plasma frequency and $\delta\equiv L/N$. The solution of Eq.(1) is written as

$$x_i(t)=F_i(t;x_i^0,v_i^0) \tag{2}$$

where x_i^0 and v_i^0 are the initial position and initial velocity of the i-th sheet and the function $F_i(t;x,v)$ is defined by

$$F_i(t;x,v)\equiv(i-\tfrac{1}{2})\delta + \left[x -(i-\tfrac{1}{2})\delta \right]\cos(\omega_p t)+ \frac{v}{\omega_p}\sin(\omega_p t) \tag{3}$$

The velocity at time t is given by

$$v_i(t)=\dot{x}_i(t)=G_i(t;x_i^0,v_i^0) \tag{4}$$

where

$$G(t;x,v)\equiv v\cos(\omega_p t)-\omega_p\left[x-(i-\tfrac{1}{2})\delta\right]\sin(\omega_p t) \tag{5}$$

It is possible that a pair of neighboring sheets may crossing each other. Suppose at time $t_c(i)$ the i-th sheet and the (i+1)-th sheet cross each other for the first time from a given initial conditon. Then $t_c(i)$ is given as the solution of the following equation for t,

$$F_i(t;x_i^0,v_i^0)=F_{i+1}(t;x_{i+1}^0,v_{i+1}^0) \tag{6}$$

which can be explicitly solved. Namely, $t_c(i)$ is expressed as a function of the initial positions, x_i^0, x_{i+1}^0 and the initial

velocities, v_i^0, v_{i+1}^0 [see details in Appendix]. After the crossing, the sheet, which was the i-th from the left boundary before the crossing, becomes the (i+1)-th sheet and vice versa for the (i+1)-th sheet.

Suppose we start from an initial condition of the entire system, $x^0 \equiv (x_1^0, x_2^0, \ldots, x_N^0)$, $v^0 \equiv (v_1^0, v_2^0, \ldots, v_N^0)$. Then we can evaluate $t_c(i)$ for each neighboring pairs of sheets. We then find the minimum of these crossing times,

$$\tau_c^{(0)} = \min_i t_c(i), \tag{7}$$

and define i^* as the number i which gives the minimum. Thus, i^* stands for the pair of sheets, which cross each other for the first time among all sheets from a given initial condition, (x^0, v^0). $\tau_c^{(0)}$ is also determined completely by the initial configuration, (x^0, v^0). After the first crossing at $\tau_c^{(0)}$, the electric fields on the i^*-th and the (i^*+1)-th sheets are exchanged. But if we exchange names of these sheets, the equations of motion remain unchanged. Thus we define new initial conditions

$$x_i^{(1)} \equiv F_i(\tau_c^{(0)}, x_i^0, v_i^0), \quad v_i^{(1)} \equiv G_i(\tau_c^{(0)}, x_i^0, v_i^0) \tag{8}$$

for $i \neq i^*, i^*+1$ and

$$x_{i^*}^{(1)} \equiv F_{i^*}(\tau_c^{(0)}; x_{i^*}^0, v_{i^*}^0), \quad v_{i^*}^{(1)} \equiv G_{i^*+1}(\tau_c^{(0)}; x_{i^*+1}^0, v_{i^*+1}^0) \tag{9}$$

$$x_{i^*+1}^{(1)} \equiv F_{i^*}(\tau_c^{(0)}; x_{i^*+1}^0, v_{i^*+1}^0), \quad v_{i^*+1}^{(1)} \equiv G_{i^*}(\tau_c^{(0)}; x_{i^*}^0, v_{i^*}^0) \tag{10}$$

and restart the equations of motion (1). Then the evolution of the sheets after the crossing is described by

$$x_i(t+\tau_c^{(0)}) = F_i(t; x_i^{(1)}, v_i^{(1)}), \quad v_i(t+\tau_c^{(0)}) = G_i(t; x_i^{(1)}, v_i^{(1)}) \tag{11}$$

We can again determine the next crossing time $t_c^{(1)}(i)$ for each pair of sheets by solving $F_i(t; x_i^{(1)}, v_i^{(1)}) = F_{i+1}(t; x_{i+1}^{(1)}, v_{i+1}^{(1)})$ for t. Then

by the same procedure as before, we determine the crossing time for the whole system, $\tau_c^{(1)}=\min_i t_c^{(1)}(i)$ and the positions and velocities of the particles, $x^{(2)}\equiv(x_1^{(2)},\ldots,x_N^{(2)})$, $v^{(2)}\equiv(v_1^{(2)},\ldots,v_N^{(2)})$, at time $\tau_c^{(0)}+\tau_c^{(1)}$.

. Thus the time interval $\tau_c^{(k)}$ between the k-th and the (k+1)-th crossing and the configuration of the entire system at the (k+1)-th crossing, $x^{(k+1)}$, $v^{(k+1)}$ are explicitly given as functions of the configuration, $x^{(k)}$, $v^{(k)}$ at the k-th crossing,

$$\tau_c^{(k)}= T(x^{(k)},v^{(k)}),\quad x^{(k+1)}=X(x^{(k)},x^{(k)}),\quad x^{(k+1)}=V(x^{(k)},v^{(k)}). \tag{12}$$

Thus these are the mappings for discrete steps. This procedure has advantage compared to the mumerical calculation of the equation of motion (1) itself. Indeed, in performing the mappings (12) by a computer, there is no error such as caused by finite time steps which appear in the usual Runge-Kutta method. T, X, V are now explicit functions of x and v. So if errors may enter, they are due to the precision limit of the computer.

We take a periodic boundary condition for the crossing of the first sheet and the N-th sheet. Namely, If we have $x_N(t)-x_1(t)=L$, we assume that the two sheets cross each other. Under this assumption, the total energy of the system is conserved.

3. Results

We studied the two-stream instability.[3] The system consists of 1000 sheets, of which 500 have the same positive velocity and 500 have negative velocity of the same magnitude initially. Sheets of velocities of opposite signs are located in the alternating order initially but the spatial intervals between neighboring sheets are chosen by random numbers. In Figs.1, we show here a typical development of instability and the formation of holes and the coalescence of holes into a relatively stable hole together with the evoluition of the electric potential.

In order to see disorder in the plasma, we evaluate the relative diffusion defined by

$$D_o(t) \equiv \frac{1}{N-1} \sum_{i=1}^{N-1} [x_i(t)-x_{i+1}(t)]^2 \qquad (13)$$

$$D_e(t) \equiv \frac{1}{N-2} \sum_{i=1}^{N-2} [x_i(t)-x_{i+2}(t)]^2 \qquad (14)$$

Since nearest neighbor sheets have initial velocities of opposite directions and next nearest sheets have the same initial velocity, $D_o(t)$ and $D_e(t)$ may behave differently. Indeed, initially $D_o(t)$ increases faster than $D_e(t)$. After the instabilities are amplified, they behave in a similar manner. This implies that a large scale motion becomes more dominant at the late stage.

Fig.3 shows typical trajectories of sheets in the phase space. and the potential profile at the late stage. Trajectories (a), (b) and (c) represent an untrapped particle, a bounced particle, and a trapped particle, respectively.

Figs.4 show the separation of trajectories in the phase space starting from slightly different initial conditions. One trajectory $x_a(t)$ starts from the initial condition of Fig.1(a) and the other $x_b(t)$ starts from the initial condition in which one sheet in the middle is slightly deviated, as shown Fig.4(a). The separation is defined by

$$L(t)\equiv\sqrt{|x_a(t)-x_b(t)|^2+|v_a(t)-v_b(t)|^2} \tag{15}$$

where

$$v_a(t)\equiv \frac{d}{dt}\, x_a(t), \quad v_b(t)\equiv \frac{d}{dt}\, x_b(t) \tag{16}$$

Initially L(t) grows exponentially and later linearly in time. The initial exponential growth is due to the two-stream instability and the linear growth at the late stage is probably due to the large scale motion of the hole. It would be interesting to evaluate the Liapunov exponents at the late stage where the pattern in the phase space looks stationary.

4. Conclusions

In this paper, we present an exact and efficient method of computation of Dawson's sheet model and show the evolution of two streams in the phase space into a one-hole state corresponding to a BGK solution of the Vlasov equation. The relative stability of the one-hole state was pointed out by Ghizzo et al.[3] from their computer simulation of the Vlasov equation. This is in agreement with our result of exact dynamics.

Our method of mapping can be applied to a one-dimensional gravitational system of sheets.[6]

Acknowledgements

This research is supported by the Cooperative Research Program of Institute of Plasma Physics, Nagoya University and the computation is performed on VP200, IPP, Nagoya University.

Appendix: Explicit form of $\tau_c(i)$

Eq.(6) can be written explicitly as

$$\delta+(x^0_{i+1}-x^0_i-\delta)\cos(\omega_p t)+\frac{1}{\omega_p}(v^0_{i+1}-v^0_i)\sin(\omega_p t)=0 \qquad (A.1)$$

Hence we have

$$R\sin(\omega_p t+\theta)=-\delta \qquad (A.2)$$

where

$$x^0_{i+1}-x^0_i-\delta\equiv R\sin\theta \quad \text{and} \quad v^0_{i+1}-v^0_i\equiv\omega_p R\cos\theta \quad [R\geq 0]. \qquad (A.3)$$

There are several cases as follows. We put $\Delta\equiv\arccos(\delta/R)$.

(1) $R<\delta$: There is no solution of Eq.(A.2). Namely, sheets, i+1 and i, do not cross.

(2) $R\geq\delta$, $-\frac{\pi}{2}-\Delta\leq\theta\leq-\frac{\pi}{2}+\Delta$: Then, we have $\omega_p\tau_c=-\frac{\pi}{2}+\Delta-\theta$.

(3) $R\geq\delta$, $-\frac{\pi}{2}+\Delta\leq\theta\leq\frac{3\pi}{2}-\Delta$: Then, we have $\omega_p\tau_c=\frac{3\pi}{2}-\Delta-\theta$.

References

(1)I.B.Bernstein, J.M.Greene and M.D.Kruskal, Phys.Rev.108(1957)546.

(2)H.Schamel, Phys.Rev.Lett.48(1982)481.

(3)A.Ghizzo, B.Izrar, P.Bertrand, E.Fijakow, M.R.Feix and M.Shoucri, Phys.Fluids 31(1988)72.

(4)J.Dawson, Phys. Fluids 5(1962)445.

(5)J.M.Dawson, Methods in Computational Physics vol.9(Ed. B.Alder et al., Academic Press, New York, 1970)1.

(6)Froeschle andJ.-P.Scheidecker, Phys.Rev.A12(1975)2137.

Figure Captions

Figs.1. Evolution of two-stream instability in the phase space and corresponding electric potential in the x-space: (a) initial condition; (b) at time $t=24.0/\omega_p$; (c) at time $t=28.8/\omega_p$; (d) at time $t=38.4/\omega_p$; (e) at time $t=55.2/\omega_p$; (f) at time $t=76.8\omega_p$.

Fig.2. Evolution of relative diffusion: D_o corresponds to the separation of neighboring sheets and D_e to the separation of next neighboring sheets.

Fig.3. Typical trajectories of sheets in the phase space at a late stage($t=76.8/\omega_p$): (a)an untrapped particle; (b) a bounced particle; (c) a trapped particle.

Fig.4. Separation of trajectories in the phase space starting from slightly different initial conditions. One initial condition is the one given in Fig.1(a). The other is chosen so that one middle sheet has a slightly larger initial velocity.

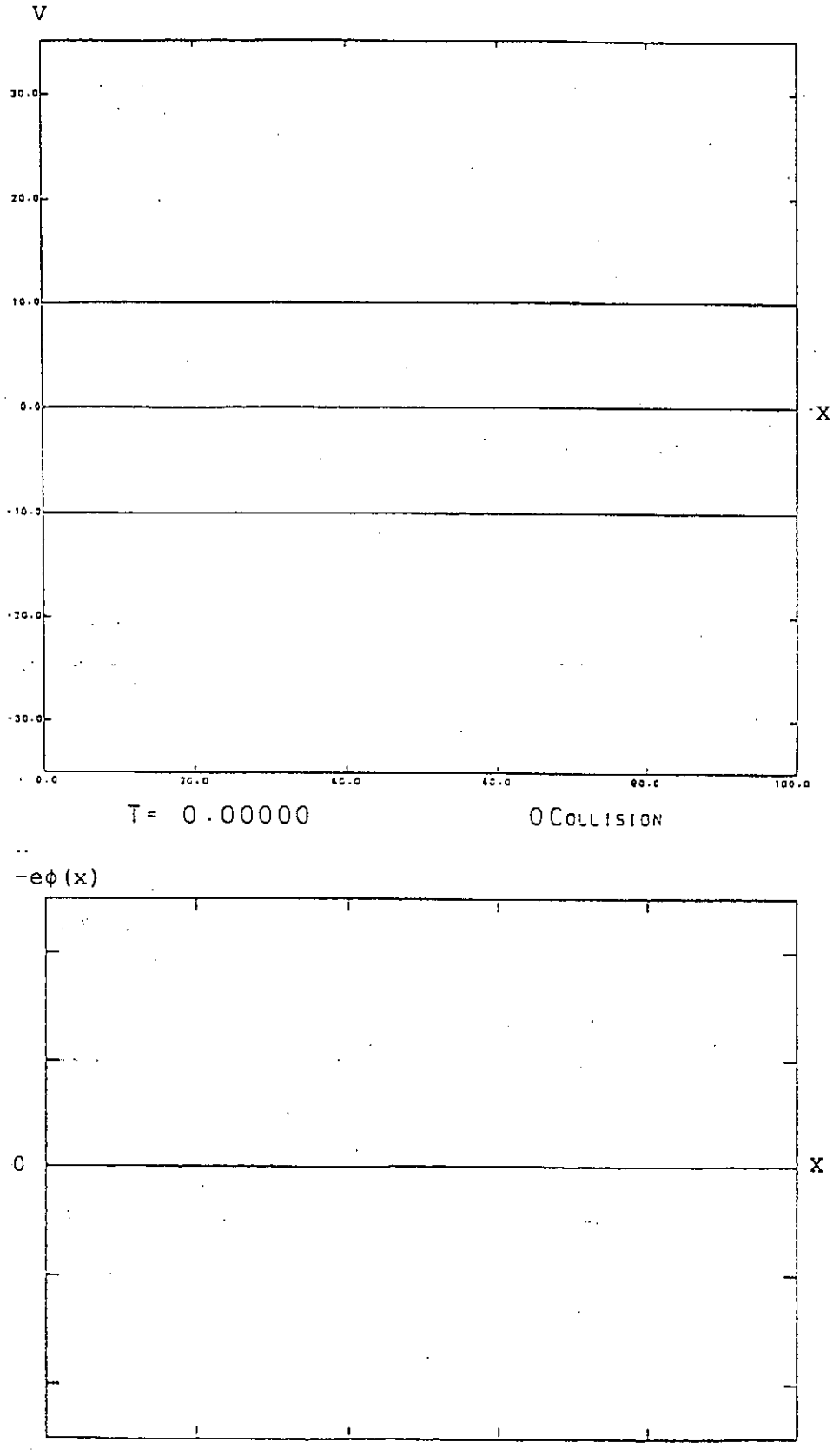
V
30.0
20.0
10.0
0.0
-10.0
-20.0
-30.0
0.0
20.0
40.0
60.0
80.0
100.0
X
T= 0.00000
0 COLLISION
-eφ(x)
0
X

Fig.1(a)

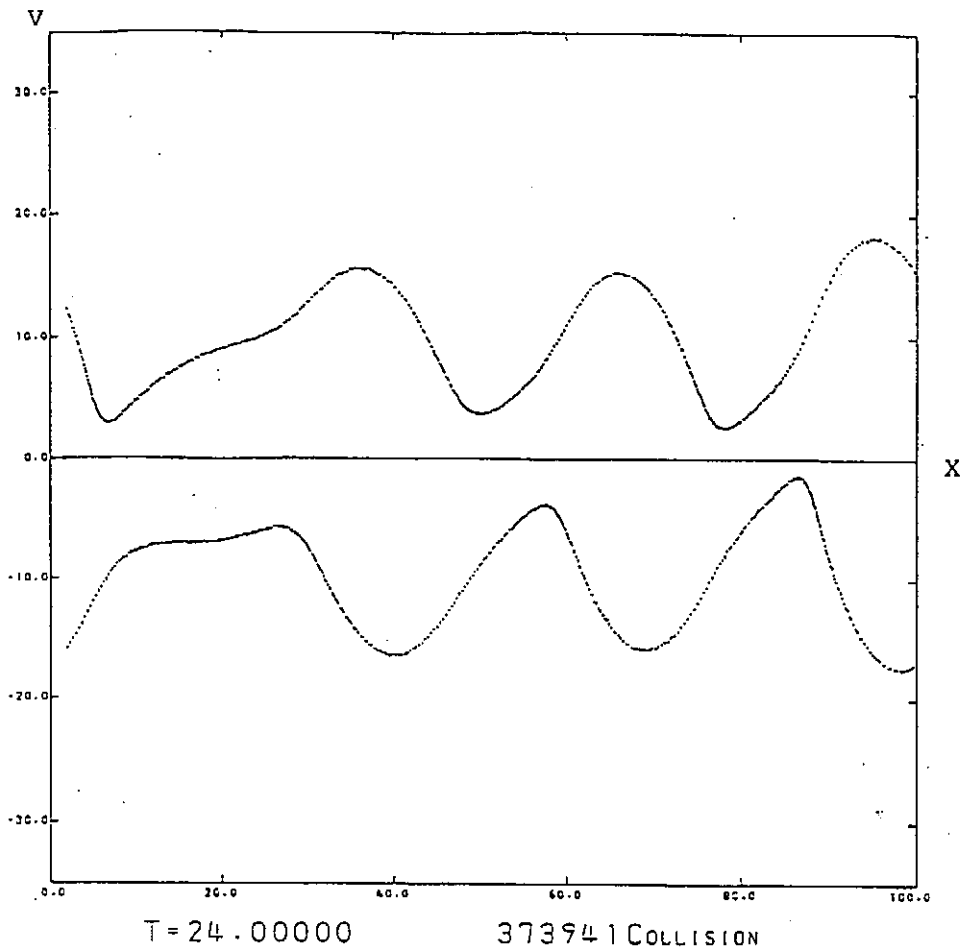
V
30.0
20.0
10.0
0.0
-10.0
-20.0
-30.0
0.0
20.0
40.0
60.0
80.0
100.0
X
T=24.00000
373941 COLLISION

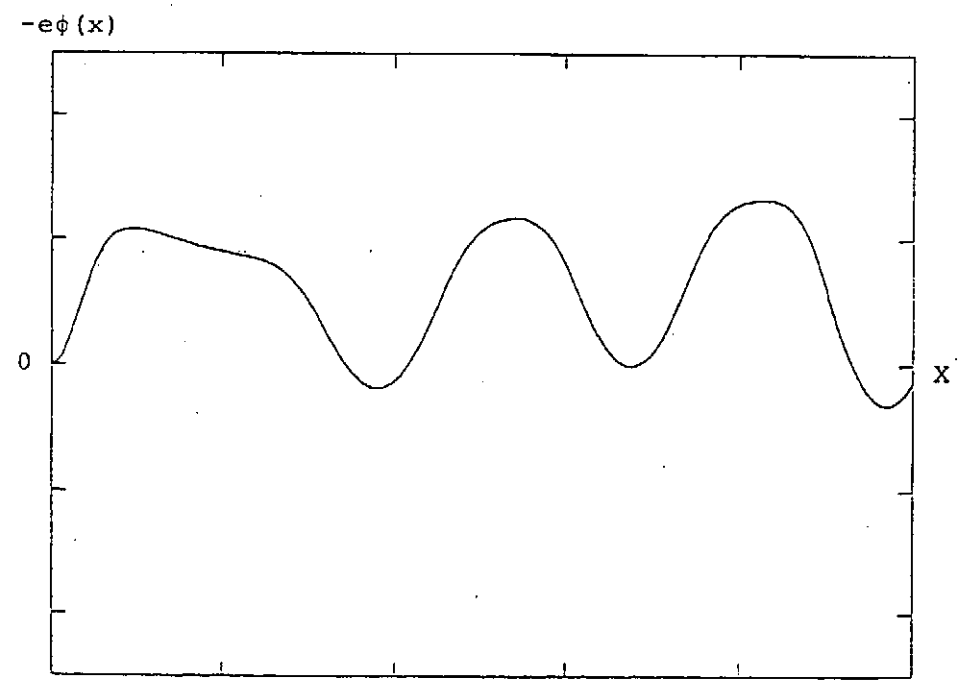
-eφ(x)
0
X

Fig. 1 (b)

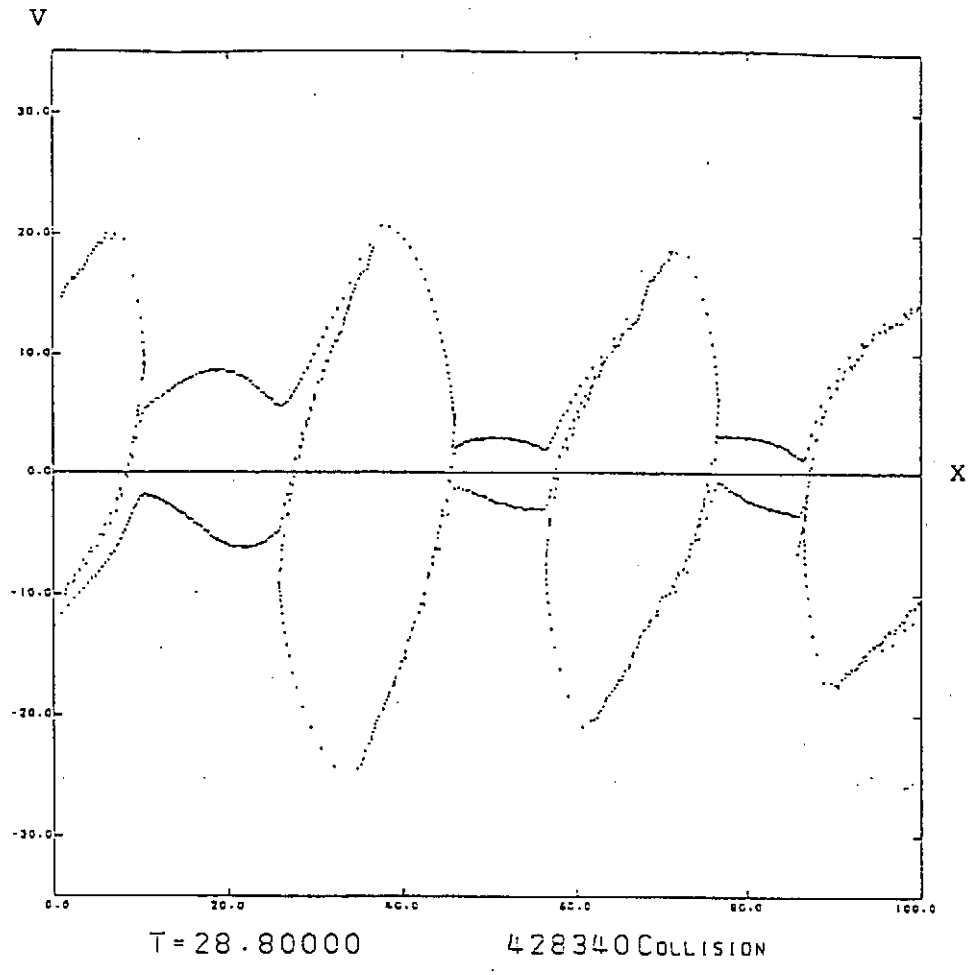
V
30.0
20.0
10.0
0.0
-10.0
-20.0
-30.0
0.0
20.0
40.0
60.0
80.0
100.0
X
T=28.80000
428340 COLLISION

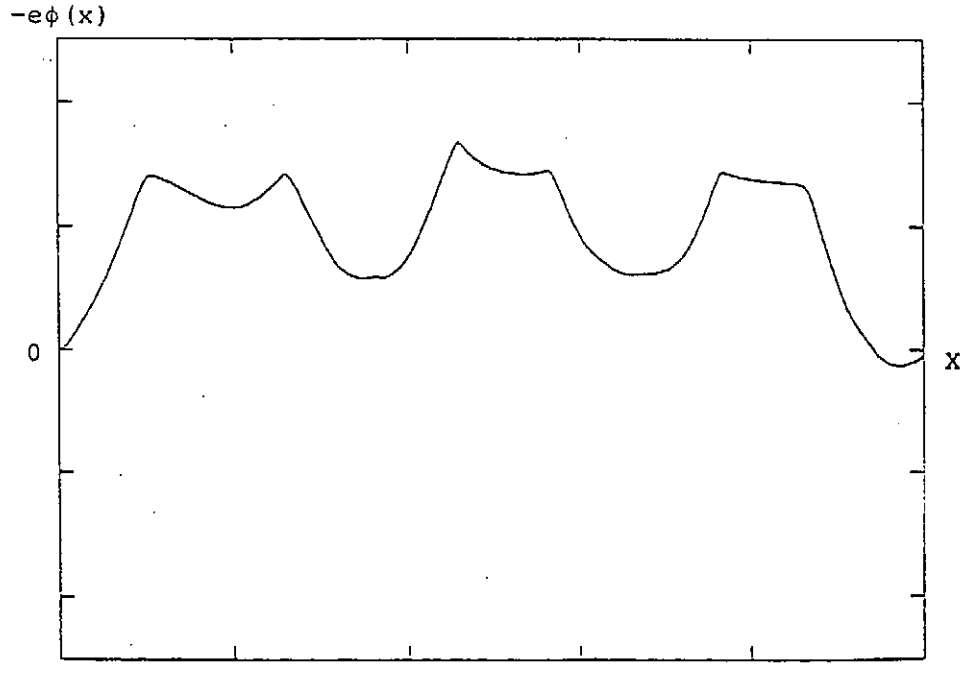
-eφ(x)
0
X

Fig.1(c)

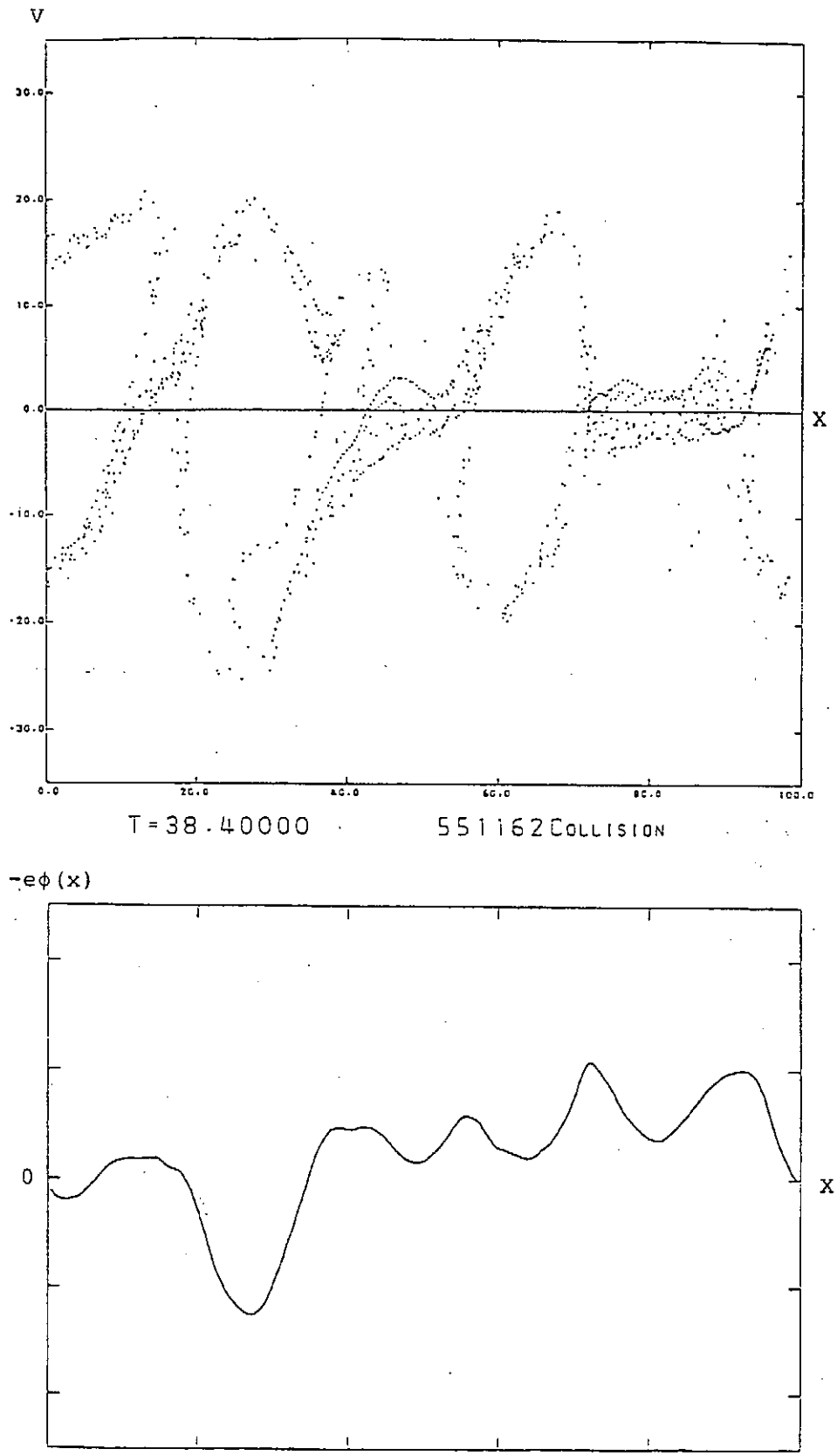
V
30.0
20.0
10.0
0.0
-10.0
-20.0
-30.0
0.0
20.0
40.0
60.0
80.0
100.0
X
T=38.40000
551162 COLLISION
-eφ(x)
0
X

Fig.1(d)

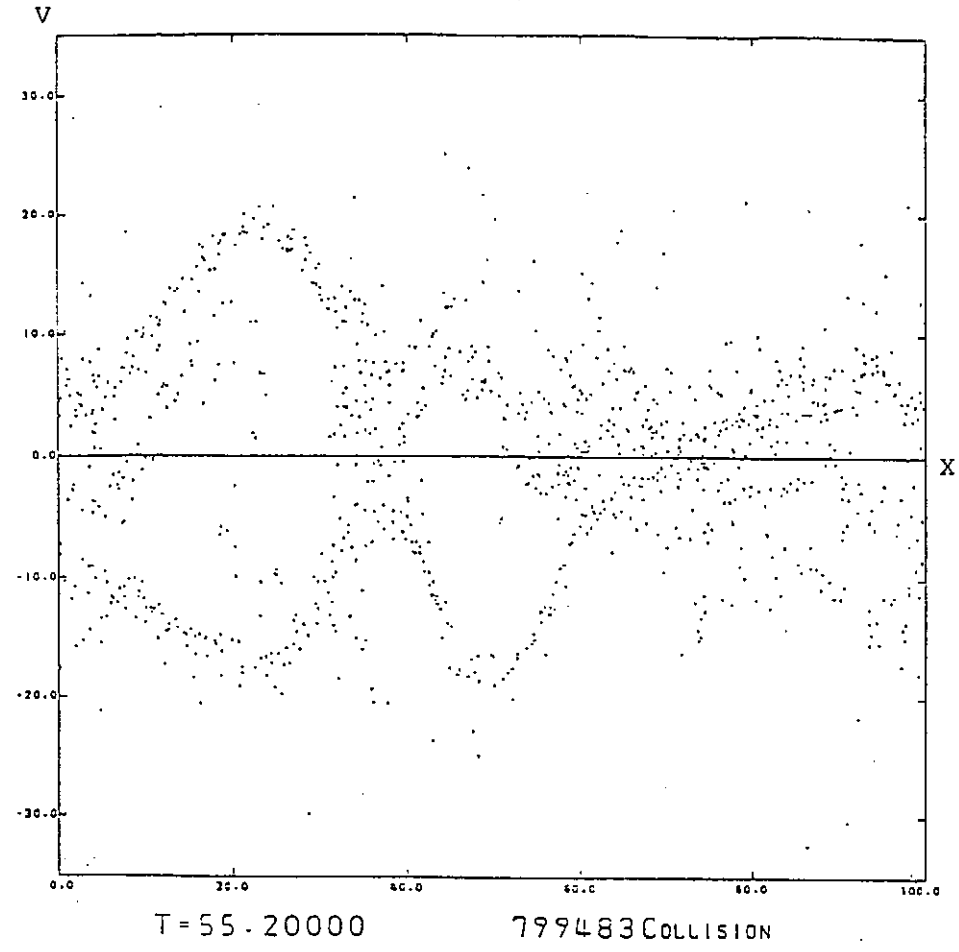
V
30.0
20.0
10.0
0.0
-10.0
-20.0
-30.0
X
0.0
100.0
T=55.20000
799483 COLLISION

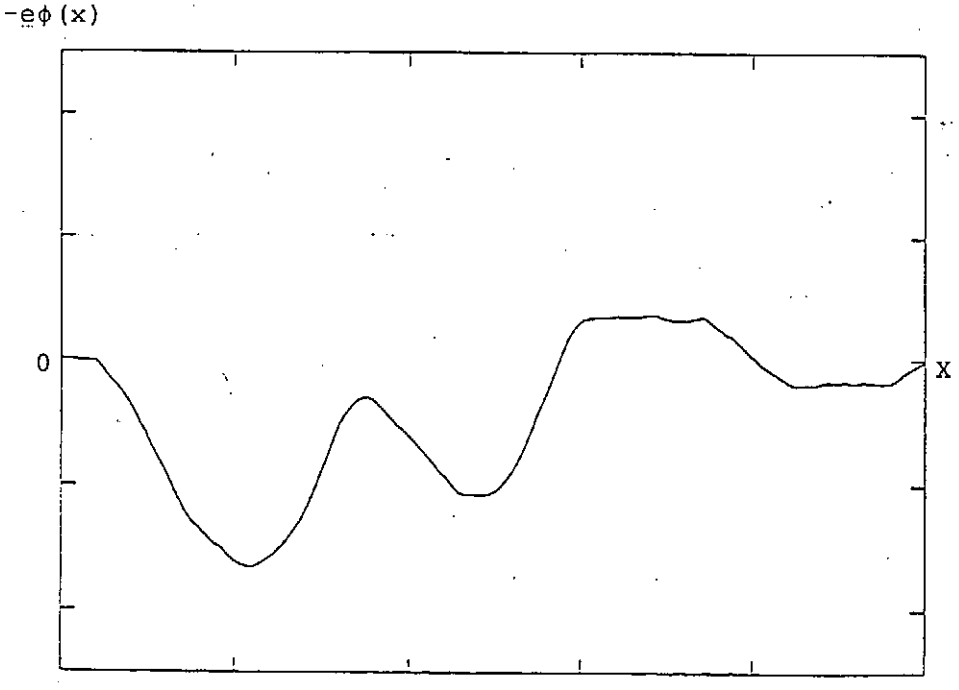
-eφ(x)
0
X

Fig.1(e)

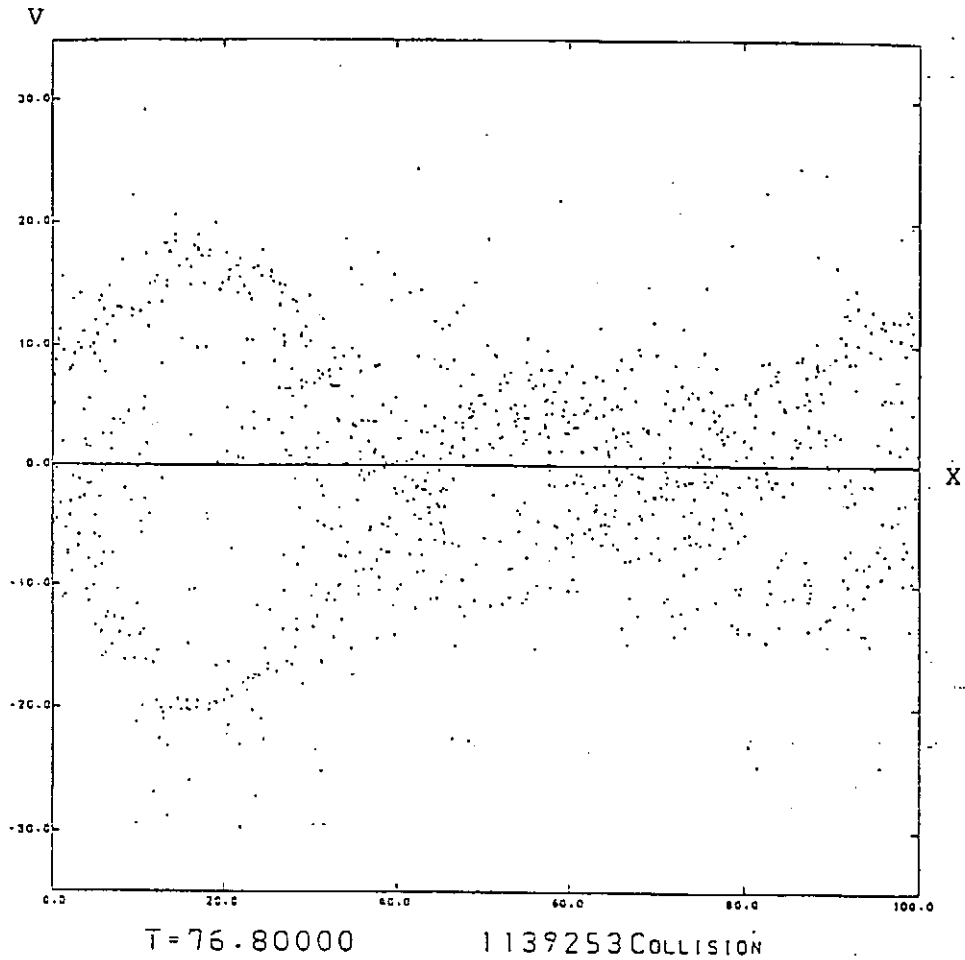

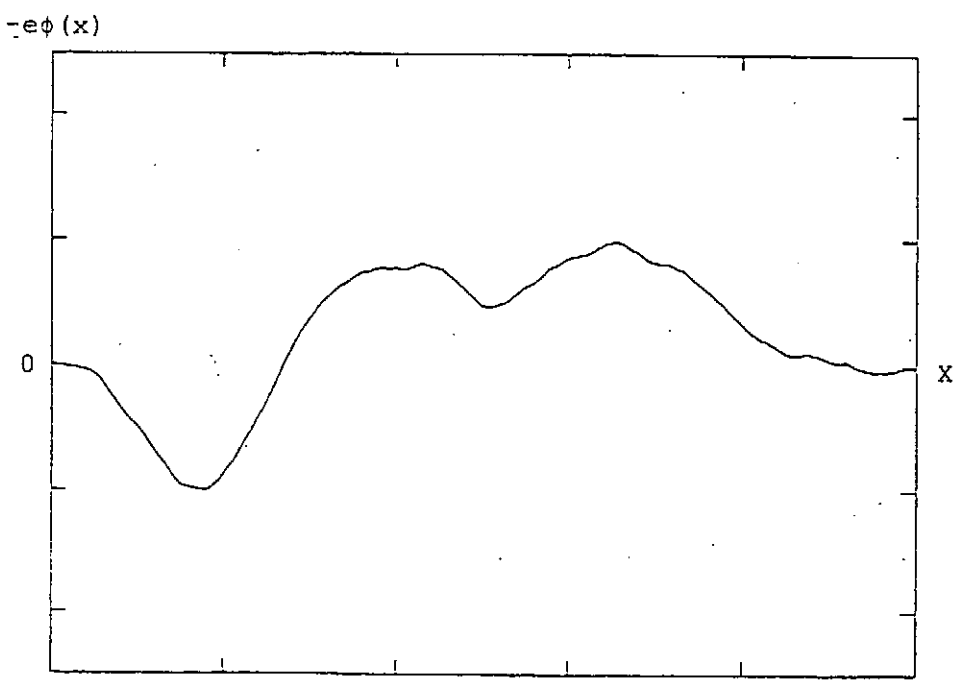

Fig.1(f)

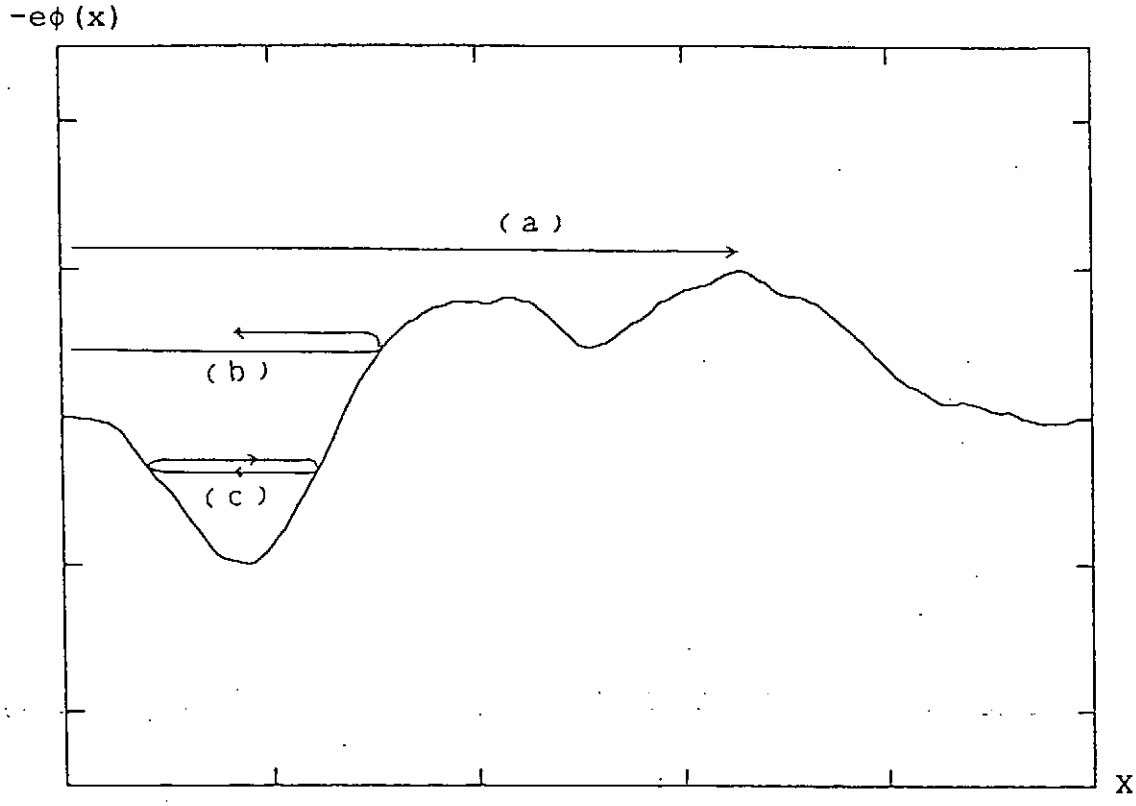

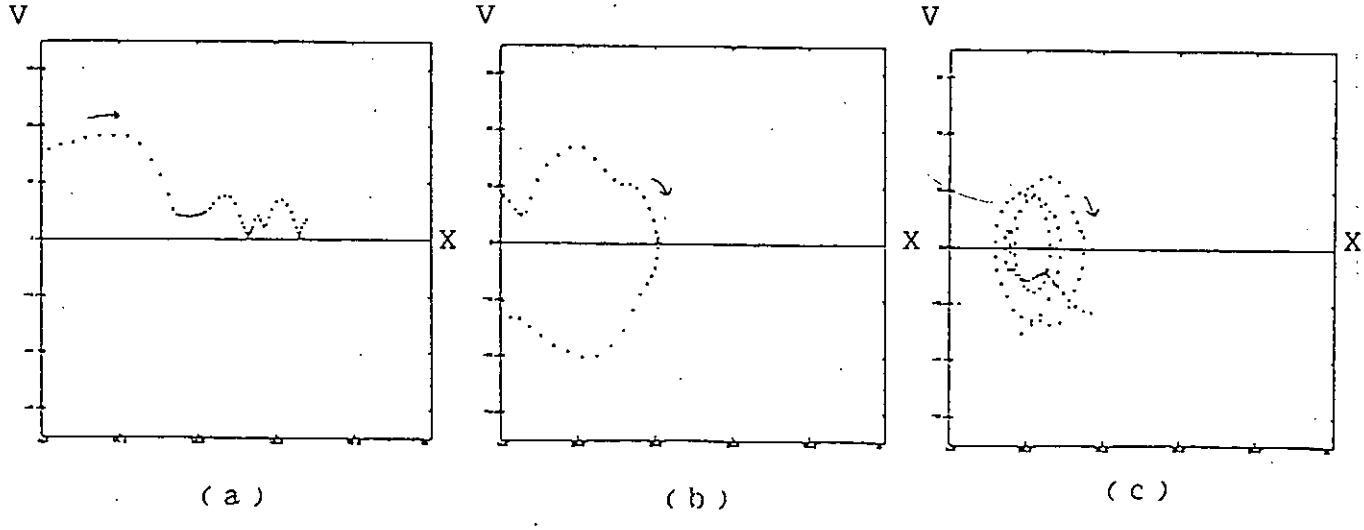

Fig.3

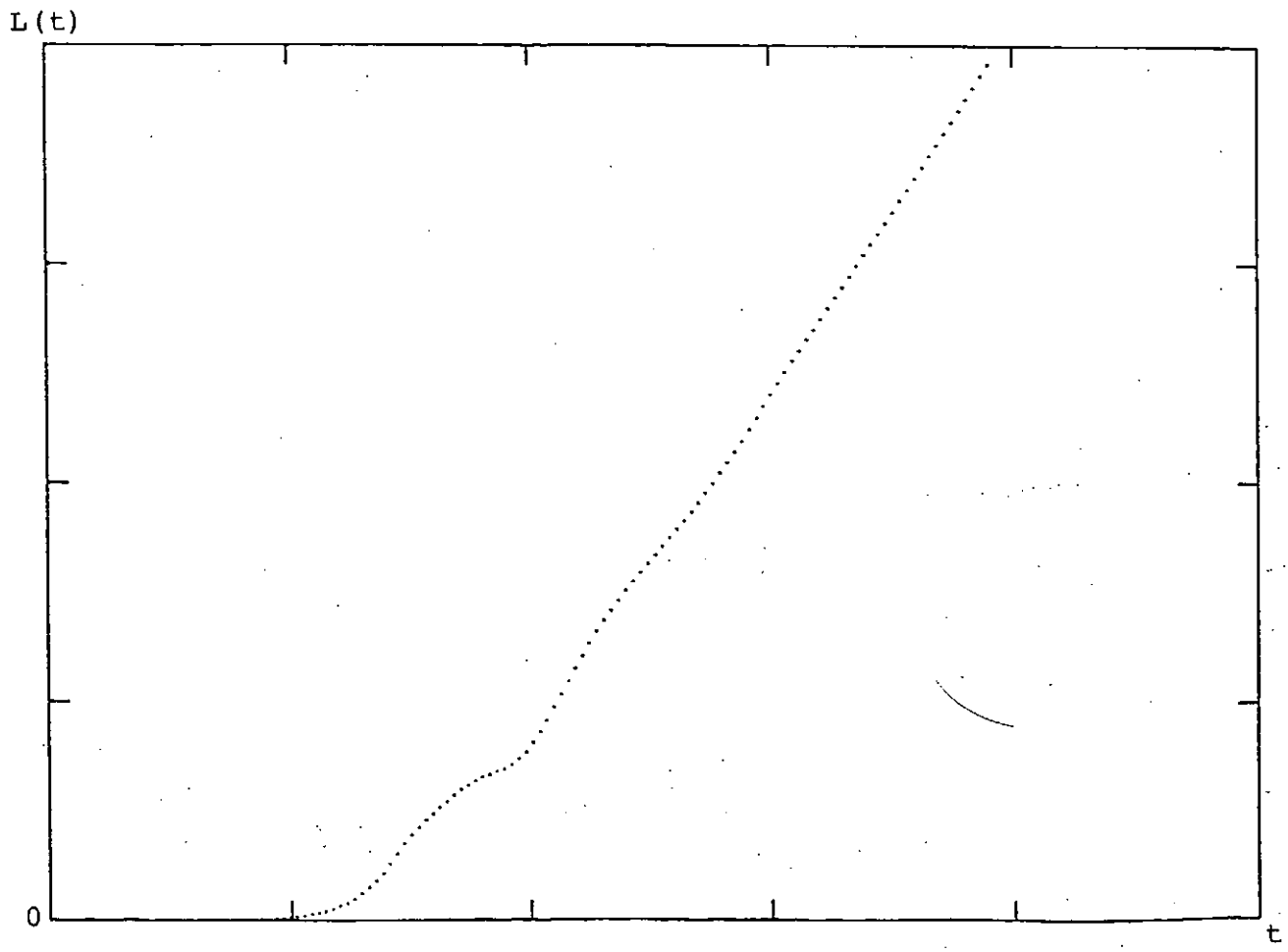

Fig.4

V. Vortex Structures in Fluids

Multifractal Distribution in Turbulence

Tohru Nakano

Department of Physics, Chuo University,

Kasuga 1-13-27, Bunkyo-ku, Tokyo 112

abstract

A multifractal analysis is applied to turbulence in two and three dimensions. The generalized dimensions and $f(\alpha)$–α curve are calculated for two-dimensional turbulence simulated on 512^2 mesh points. As far as three dimensional turbulence is concerned, we compute the generalized dimensions and $f(\alpha)$–α curve from a model previously proposed by Nelkin and the present author and compare them in a satisfactory way with the data by Meneveau and Sreenivasan.

§1. Introduction

It has been quite argued that fully-developed turbulence has an intermittent small-scale structure, which is characterized by its fractal nature.[1] Since Landau indicated that the energy dissipation rate would not be uniform in space, the spatial distribution of the dissipation rate has been taken into account in the prediction of the velocity correlation functions. The most famous attempts in that direction are the log-normal[2] and β-model.[3]

The β-model is based on the assumption on the fractal distribution in turbulence. When an eddy cascades into half-size eddies, a number of active daughter eddies is 2^D instead of 2^d, where d and D are geometrical and fractal dimension, respectively. Here D was supposed to be not larger than d. Although the idea behind the β-model is simple and clear, it does not fit experiment well.[4,5,6] Namely, a single parameter D is

not enough to describe a fractal nature of turbulence. Frisch and Parisi[4] introduced a multifractal idea to interpret the discrepancy betweeen the predicted values of the β-model and the observational result by Anselmet *et al.*[7]

Let us consider why the multifractal analysis is necessary. The spatial distribution of the energy dissipation rate introduces a fractal dimension. However, the squared value of the rate may define another fractal dimension, although both dimensions happen to coincide. Different fractal dimensions must be introduced, depending on how the dissipation rate is processed. The same situation is encountered in phenomena of chaos, where Hentschel and Procaccia[8] defined the generalized dimensions D_q for the qth order moments of the distribution measure. Then D_0 is just the fractal dimension of the measure itself and the same as in the β-model.

In the present paper we consider two-dimensional as well as three-dimensional turbulence from a multifractal point of view. (1) In two dimensions the Navier-Stokes equations are simulated and the data are processed following a multifractal analysis. The generalized dimensions and $f(\alpha)$–α curve are derived. (2) In three dimensions we calculate the generalized dimensions from an intermittent-turbulence theory previously proposed by Nelkin and the present author[5] and compare them with the ones observed by Meneveau and Sreenivasan.[9,10]

§2. Generalized Dimensions of Two-Dimensional Turbulence

We calculated the generalized dimensions for the simulated two-dimensional turbulence by following the recipe by Halsey *et al.*[11]. The Navier-Stokes equation is simulated on 512^2 mesh points with various initial velocity fields of a Gaussian ensemble, viscosities being 0.01, 0.002 and 0.001 corresponding to Reynolds numbers ranging from 50 to 850. The initial vorticity contour is rather round. As a time elapses, the vorticity contour gets elongated as shown in Fig.1 and the distribution looks intermittent in

space. Of interest is the quantitative evaluation of the pattern from a multifractal point of view. In the following we summarize the results. See the details in Ref.12.

Figure 2 is the D_q vs q curve of the enstrophy dissipation rate for five runs with $\nu = 0.002$, in which the inertial region with the spectrum k^{-4} is reached. D_q are slightly scattered depending on the runs, but within the standard deviation. As q goes to infinity, the D_q is $1.2 \sim 1.3$(estimated at $q = 40$). The simulated flows with $\nu = 0.01$ and 0.001 yield the same value for D_q. The corresponding $f(\alpha)$–α curve is depicted in Fig.3, from which we read that α tends to 1.2 and $f(\alpha) = 0 \sim 0.5$ as q goes to infinity. This implies that the intense enstrophy dissipation, whose distribution is characterized by large q, occurs in localized regions with dimension 1.2, and on the other hand, the global distribution of the intense regions has dimension less than 0.5.

We took the same procedure for the energy dissipation rate. The estimated D_q for positive q is almost 2.0 for any run in contrast to the enstrophy dissipation rate. The results obtained in the analysis implies that the enstrophy dissipation occurs intermittently at small-scale in space, while the energy dissipation does rather uniformly in space. This is completely consistent with the well-known picture of two dimensional turbulence, in which enstrophy cascades toward high wave numbers and energy does in the opposite way.[13]

§3. Generalized Dimensions of Three-Dimensional Turbulence

The generalized dimensions D_q in three dimensional turbulence are related to the intermittency exponents associated with the energy dissipation rate. The log-normal and β-model for intermittent turbulence predict D_q as

$$D_q = \begin{cases} d - \mu q/2 & \text{for the log-normal model} \\ d - \mu & \text{for the } \beta\text{-model,} \end{cases} \tag{1}$$

where μ is a single parameter adjusted to experiment and $\mu = 0.2$ is usually chosen.

Recently Meneveau and Sreenivasan[9,10] observed the multifractal spectrum of the dissipation field in various turbulent flows and determined D_q up to $q = 20$, the D_q–q curve being depicted in Fig.4. The observed values of D_q are far from the corresponding ones calculated by the β-model. The log-normal model is reasonable for small q, but desperate for large q. The dashed and dot-dashed line stand for the log-normal and β-model. Note that the two-scale Cantor set model with equal scales but unequal weights ($p_1 = 0.7$, $p_2 = 0.3$) can interpret the observed data quite well.[10]

Years ago Nelkin and the present author[5] proposed a new model for intermittent turbulence, which shows a crossover from the Kolmogorov scaling at lower order structure functions to the intermittent one at the higher order functions. The resultant generalized dimensions are in the infinite Reynolds number limit

$$D_q = \begin{cases} d & \text{for } 0 \le q \le q_c \equiv z/(3z-2) \\ d - [(3z-2)q - z]/(q-1) & \text{for } q > q_c, \end{cases} \tag{2}$$

(see the details in Ref.14) where z is a parameter to be consulted with experiment. We have shown[6] that $z = 0.84$ gives a best fit to the exponents associated with the longitudinal structure functions observed by Anselmet *et al.*[7] and the other intermittency exponents. The solid line in Fig.4 is the curve of D_q vs q by our model. The agreement with the experimental data is remarkable. Our model has a crossover at $q = q_c = 1.62$, which cannot be seen in Meneveau and Sreenivasan. Hence D_q must be determined for various (non-integer as well as integer) values of small q. In particular, D_1 is very interesting: $d - \mu/2$ for the log-normal model, $d - \mu$ for the β-model, and d for our model. The three kinds of values are considerably different from each other.

Finally turn to the $f(\alpha)$–α curve. In Fig.5 the squares with error bars are the data by Meneveau and Sreenivasan.[9,10] Our model predicts a pair of points: $(\alpha = f(\alpha) = d)$ and $(\alpha = d+2-3z = 2.48, f(\alpha) = d-z = 2.16)$, which are marked by the solid circles in Fig.5. The prediction by our model falls on the experimental curve. As q goes to infinity, the most intense region contributes to D_q. There $\alpha = 0.48$ and $f(\alpha)$=2.16 in

our model, which are close to $\alpha = 0.51$ and $f(\alpha) = 2.0$ in the observation. This implies that the most intense regions are globally distributed nearly in two-dimensional space.

Let us cosider why our model produces a pair of points in contrast to the continuous experimental curve. As discussed in Ref.14, the prediction (2) is correct only in the infinite Reynolds number limit. In real flows with finite Reynolds number the crossover in (2) occurs smoothly as q varies. As far as the $f(\alpha) - \alpha$ curve is concerned, point $1(\alpha = f(\alpha) = 0)$ and point $2(\alpha = 2.48, f(\alpha) = 2.16)$ are accumulation points for infinite Reynolds number; the former corresponds to D_q for $0 \leq q < q_c$, while the latter does to D_q for $q > q_c$. As the Reynolds number decreases, both accumulation points are dissolved into separate points between the point 1 and 2. How those points are distributed between the point 1 and 2 with varying q depends, therefore, on a value of Reynolds number. It will be an interesting problem to know the density of points on the line of $f(\alpha)$–α curve with respect to q. The determination of the curve $f(\alpha)$–α is a delicate task since the curve is sensitive to the differentiability of $(q-1)D_q$. On the other hand, the curve of D_q vs q is obtained directly from experiment, so that it is the most important object to make comparison with experiment. In this context our model is in a good position in interpreting experiment.

In the present paper we have shown the usefullness of a multifractal analysis. The ordinary method of analysis employed in a study of turbulence is mainly (1) to calculate the low order moments such as the energy spectrum and the energy transfer rate, and (2) to present diagrams such as the flow and dissipation rate contour. The multifractal analysis helps understand the contour diagrams quantitatively. The generalized dimensions are equivalent to the exponents associated with all order of the moments of the turbulence variables such as the energy and enstrophy dissipation rate. In this connection the multifractal analysis is strongly recommended in a study of fully-developed turbulence.

References

[1] B. Mandelbrot, in *Statistical Models and Turbulence*, ed. M. Rosenblatt and C. Van Atta, p.333, (Springer, New York), 1972.

[2] A.N. Kolmogorov, J. Fluid Mech. **13** (1962), 82.

[3] U. Frisch, P.L. Sulem and M. Nelkin, J. Fluid Mech. **50** (1978), 719.

[4] U. Frisch and G. Parisi, in *Turbulence and Predictability in Geophysical Fluid Dynamics and Climate Dynamics, Proceedings of the International School of Physics, Enrico Fermi, Course LXXXVIII*, ed. M. Ghil, R. Benzi and G. Parisi (North Holland, Amsterdam, 1985), p. 84.

[5] T. Nakano and M. Nelkin, Phys. Rev. **A31** (1985), 1980.

[6] T. Nakano, Prog. Theor. Phys. **75** (1986), 1295.

[7] F. Anselmet, Y. Gagne, E.J. Hopfinger and R.A. Antonia, J. Fluid Mech. 88 (1984), 63.

[8] H.G.E. Hentschel and I. Procaccia, Physica 8D (1983), 435.

[9] C. Meneveau and K.R. Sreenivasan, Nucl. Phys. B (Proc. Suppl.) **2** (1987), 49.

[10] C. Meneveau and K.R. Sreenivasan, Phys. Rev. Lett. **59** (1987), 1424.

[11] T.C. Halsey, M.H. Jensen, L.P. Kadanoff, I. Procaccia and B.I. Shraiman, Phys. Rev. **A33** (1986), 1141.

[12] H. Mizutani and T. Nakano, to be published in J. Phys. Soc. Japan 58 (May, 1989).

[13] R.H. Kraichnan, Phys. Fluids **10** (1967), 1417.

[14] T. Nakano, submitted to Phys. Lett. A (1988).

Figure Captions

Figure 1: The vorticity contours for a run with $\nu = 0.002$ at $t = 1.0$. The thick solid lines represent the positive value contour and the thin ones, the negetive value contour. The boundaries are marked by the broken lines.

Figure 2: The D_q vs q curves for the enstrophy dissipation rate in the five runs with $\nu = 0.002$ at $t = 1.0$. The initial velocity fields are different in those five runs. The symbols $\bigcirc$, $\triangle$, $+$, $\times$, and $\diamond$ correspond to the runs.

Figure 3: The $f(\alpha)$ vs α curves corresponding to Fig.2. The symbols have the same legend in Fig.2.

Figure 4: Generalized dimensions for three-dimensional turbulence. The squares with error bars are the data observed in fully developed turbulence (grid turbulence, wake of a circular cylinder, laboratory boundary layer and atmospheric boundary layer) by Meneveau and Sreenivasan.[9,10] The dashed line corresponds to the log-normal model, and the dot-dashed line to the β-model, both for $\mu = 0.2$. The solid line stands for our model with $q \geq 0$ in the infinite Reynolds number limit.

Figure 5: The curve of f vs α correspoding to the curve of D_q vs q in Fig.4. The squares are the data by Meneveau and Sreenivasan[9,10]. The solid circles are given by our model in the infinite Reynolds number limit. The model cannot produce a right half of the curve corresponding to $q < 0$.

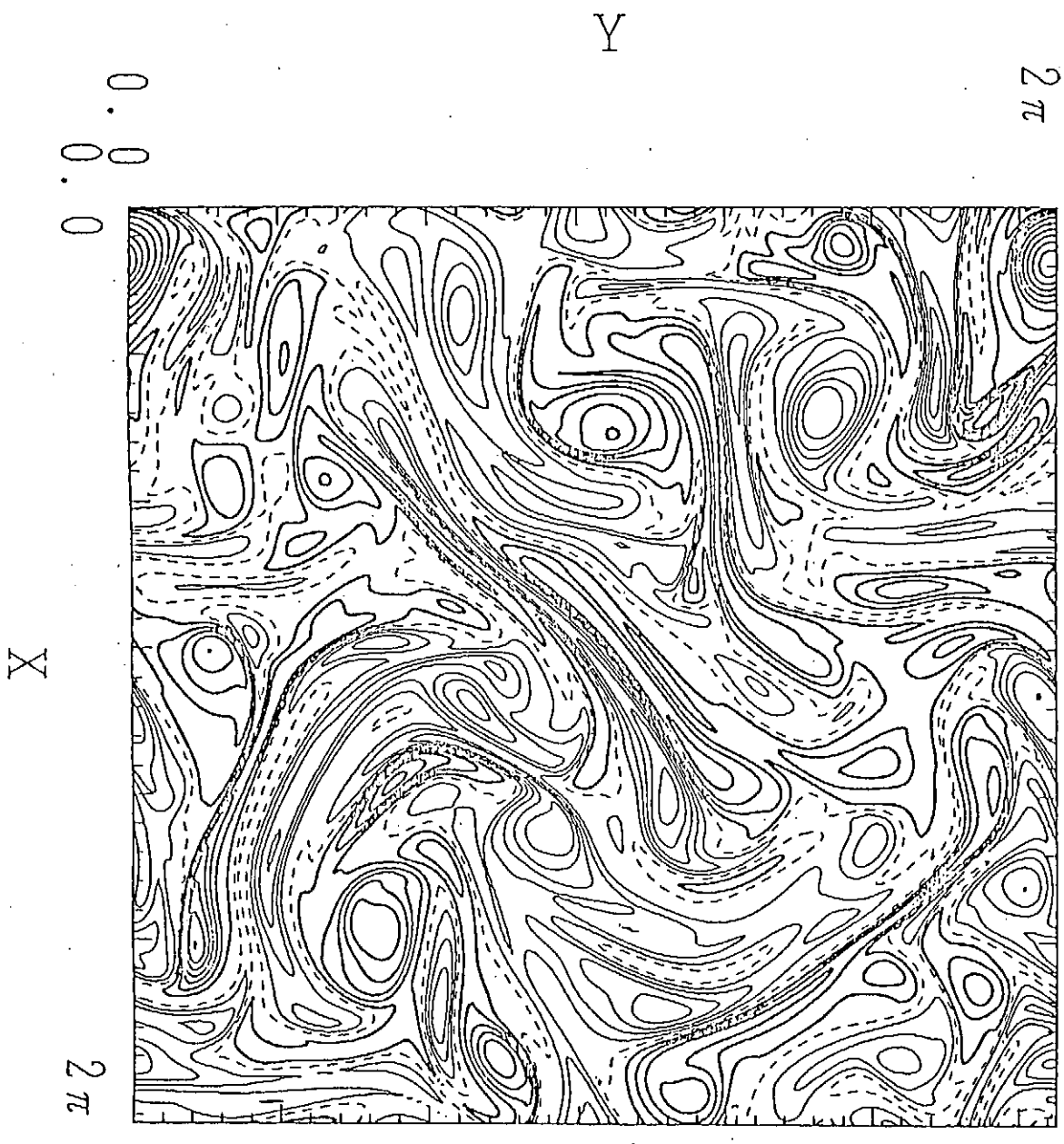

Figure 1

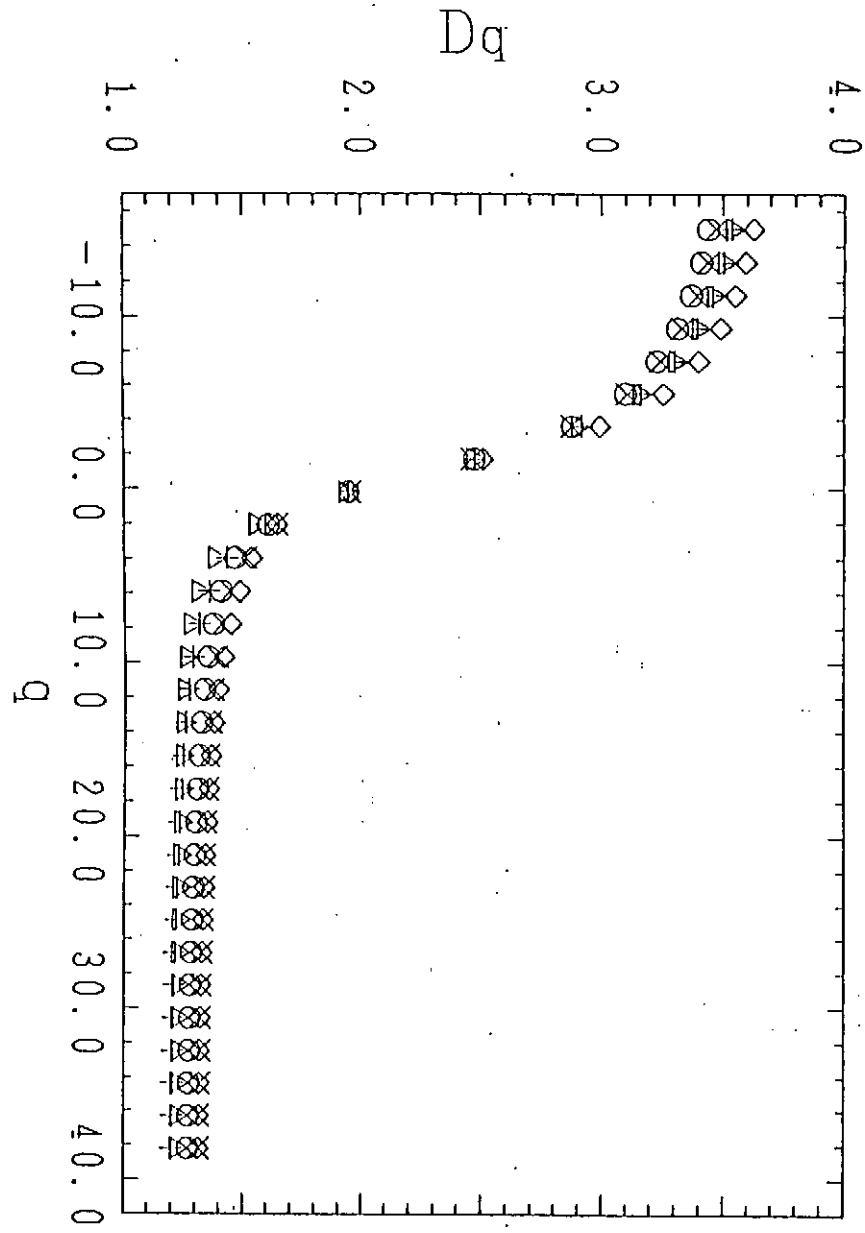

Figure 2

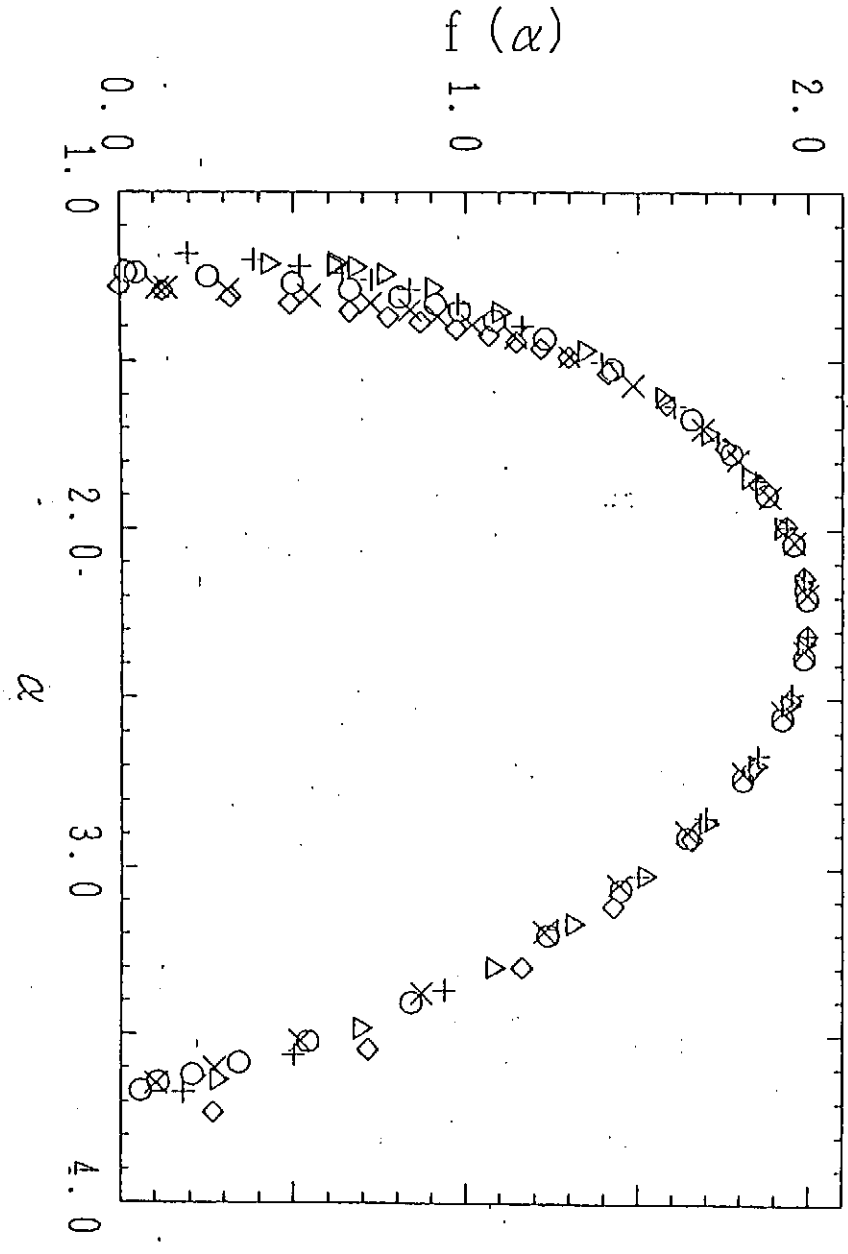

Figure 3

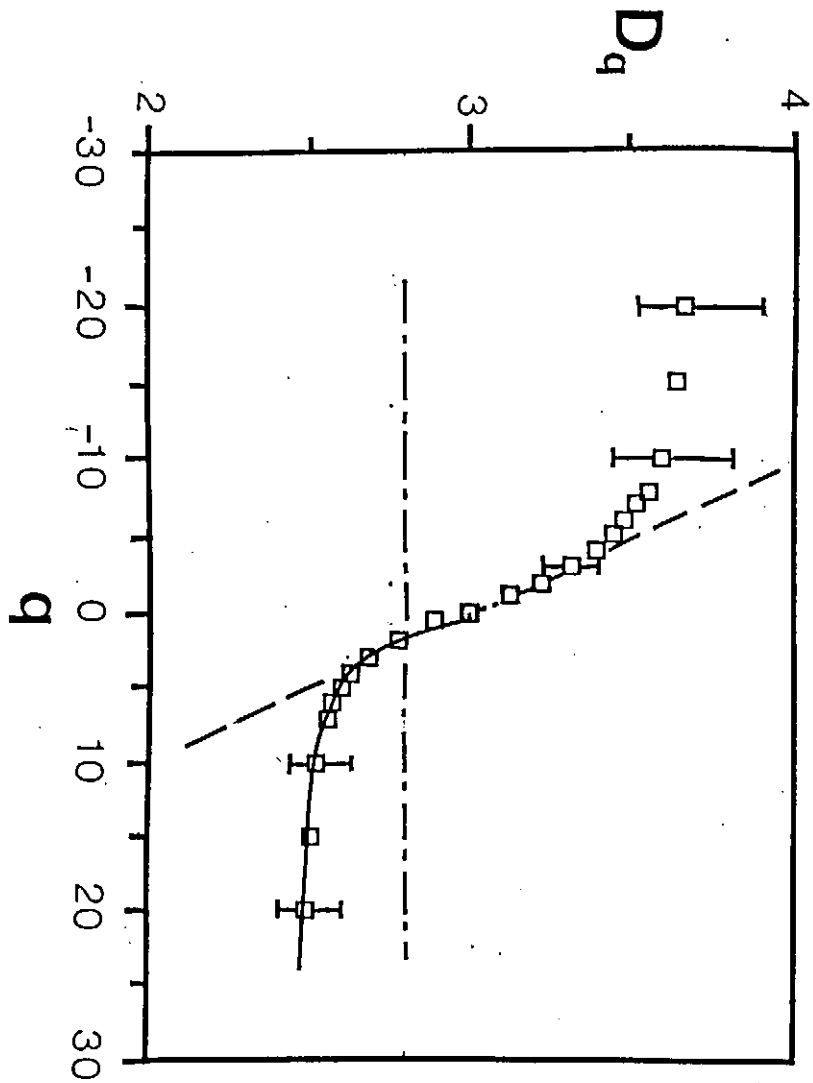

Figure 4

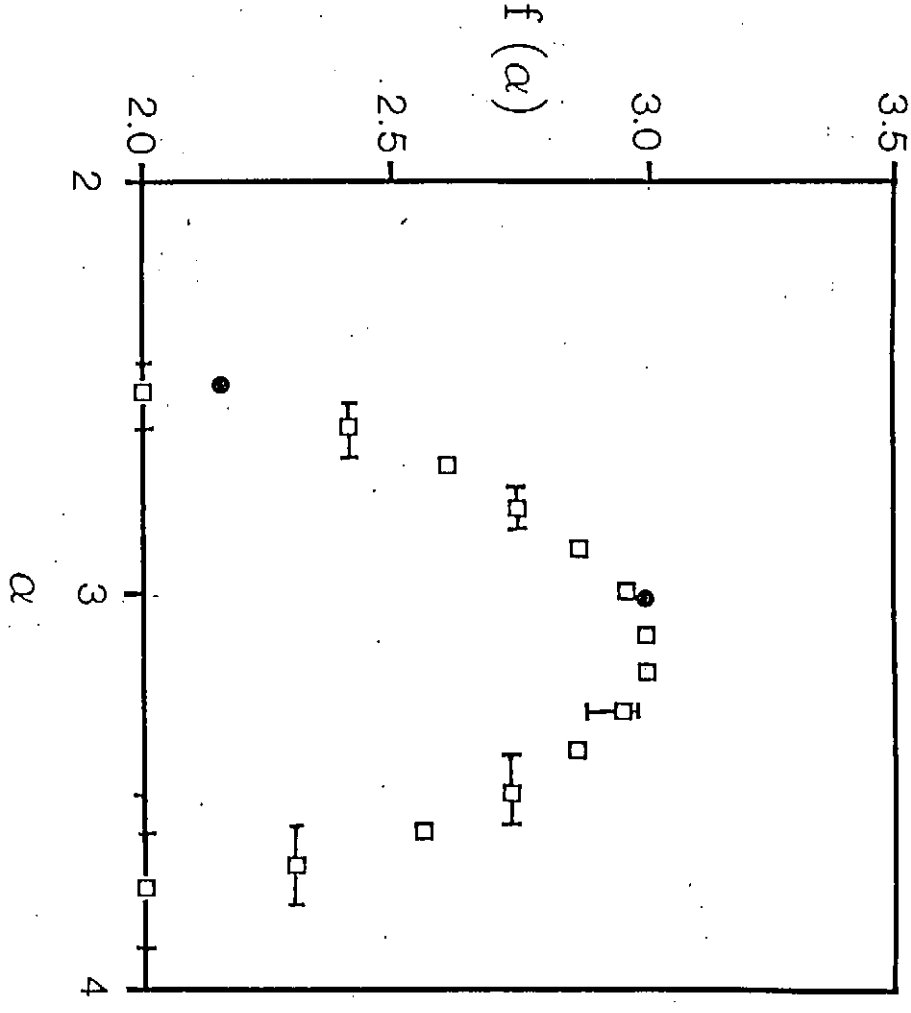

Figure 5

Vortex Associated with Rayleigh-Taylor Instability in Cylindrically Stagnating Targets

H.Sakagami
Institute for Supercomputing Research, Recruit Co. Ltd

K.Nishihara
Institute of Laser Engineering, Osaka University

Rayleigh-Taylor instability can occur whenever a dense fluid is accelerated by a less dense fluid. Small perturbation of the interface between the two fluids will grow in time and eventually form the nonlinear bubble-spike structure, which can lead to a Kelvin-Helmholts like instability.

In inertial confinement fusion with ablatively accelerated targets, Rayleigh-Taylor instability can be induced both in the acceleration phase and in the deceleration phase and can destroy the spherical symmetry of the imploding target.

In the acceleration phase, the cold, dense pusher is imploded by the ablation of hot, low density plasma and Rayleigh-Taylor instability occurs at the ablation front. Many authors have investigated the growth rate and have found stabilization mechanisms that are expected to reduce the instability growth rate to a value below the classically predicted value.[1-5]

On the other hand, the perturbation at the pusher-fuel contact surface is unstable to Rayleigh-Taylor instability during the deceleration of the contact surface after the reflected shock collides and is re-reflected by the surface to the center of target. Fig. 1 shows a schematic Radius-Time diagram near the final compression, $t = t_M$. The deceleration phase starts at $t = t_S$ and we call the $t_S < t < t_M$ phase the stagnation phase. In the stagnation phase, the fuel is compressed almost adiabatically and the temperature of fuel becomes too high to construct the shock front clearly. From one dimensional simulations, nuclear reaction takes place predominantly near the maximum compression and neutron yield increases by more than two orders of magnitude in the stagnation phase. Thus the fuel-pusher mixing, which is associated with the Rayleigh-Taylor instability of the contact surface, will reduce the final compression to that below the density required for fusion (1000 times solid density) and the total nuclear reaction yield to significantly lower than the value predicted by one dimensional simulations.

We investigated the linear and nonlinear features of the Rayleigh-Taylor instability in cylindrically stagnating targets through numerical simulations of

our two dimensional Eulerian fluid code (IMPACT2D) and the self-similar analysis which includes the cylindrical stagnation dynamics.

IMPACT2D (IMPlosion Analysis Code with TVD scheme) is fully Eulerian which is necessitated by the requirement to accurately model rotational flows. The Rayleigh-Taylor instability leads to form nonlinear bubble-spike structure, which generates vorticities in the unstable regions of the flow and distorts the contact surface boundaries tremendously. Therefore, the flows induced by the Rayleigh-Taylor instability are typically rotational and Lagrangian algorithms cannot model such flows accurately without rezoning (reconstruction of the mesh) which introduces an unacceptable amount of numerical diffusion.

Cartesian coordinate system is employed in IMPACT2D to accurately model convergent asymmetric flows. Other coordinate systems contain singularity at the origin and would cause unaccuracies.

The basic conservation equations for mass, momentum, and total energy are solved numerically with an explicit Total Variation Diminishing (TVD) scheme.[6]

The TVD scheme can capture discontinuities such as shock wave fronts and contact surfaces within a few meshes even after many time steps, and it has a second order accuracy both spatially and temporally without introducing non-physical oscillations at the discontinuity.

At the start of each simulations, small ($\delta r/r_0 < 0.001$) sinusoidal single mode perturbations in the density profile are impressed on the contact surface and we investigate the linear growth rate as a function of mode number.

Simulations are performed in the cylindrical system where the acceleration and the wavelength vary in time and space.

The linear growth rates are shown as a function of mode number in Fig. 2, where the solid circles represent the simulation results.

As for the theoretical analysis of the linear aspect, we assume that the fluids are subject to an adiabatic motion and introduce self-similar motion to describe the stagnation dynamics, which includes the effects of cylindrical geometry, acceleration and wavelength varying in space and time. The Rayleigh-Taylor instability is investigated by using the linearized equation for perturbations from the self-similar solution. The linearized equation is separated into the spatial and temporal equations, and the spatial equation is reduced to a second order differential eigenvalue equations. The eigenvalue is uniquely determined for the given initial conditions and mode number.[7-9]

The initial conditions are evaluated by simulation results and the eigenvalue equations are numerically calculated.

The growth rates at maximum compression, which is associated with the eigenvalue, are shown in Fig. 2 as the dash line.

For a given eigenvalue, the temporal evolution of the perturbation is numerically solved. The effective growth rate which includes the effect of the acceleration and the wavelength varying in time and space is evaluated by time averaging.

The calculated results are also shown in Fig. 2 as the solid line.

There are remarkable agreement between the effective growth rate and the simulated results.

To investigate the nonlinear features of the Rayleigh-Taylor instability, we introduce a single mode perturbations on the contact surface, which are large enough to saturate during the stagnation phase.

Fig. 3 shows the logarithm and square root of the perturbation mode amplitude as a function of time. The exponential growth saturates around t = 0.4 nsec and the perturbation goes into the free-falling phase, where the time evolution of the amplitude is described by $\delta = \eta\, g\, t^2$.

The time evolution of vorticity mode amplitude is shown in Fig. 4. The vorticity mode amplitude drastically increases around t = 0.4 nsec, when the free-falling phase begins.

According to many parameter runs of simulations, the saturation levels of the exponential growth are shown as a function of mode numbers in Fig. 5. The exponential growth is found to saturate around $\delta \sim 0.35\lambda$ for large mode numbers, but the saturation levels are reduced if mode numbers are small. The free-falling coefficient η is almost a constant value ~ 0.2 regardless of mode number.

The fluid equations which are solved in IMPACT2D have no characteristic scale length and the wavelength is the only scale length. Thus, the saturation levels normalized by the wavelength should not be depend on mode numbers and no reduction is expected for small mode numbers. Therefore, the reduction of the saturation levels in small mode numbers is caused by the effects of the cylindrical geometry.

The contour plots of the density and the vorticity, where the initial perturbation of mode 5 is introduced, are shown in Fig. 6.

After the saturation of the exponential growth, the instability shifts from the exponential linear growth phase to the free-falling phase and forms the nonlinear bubble (less dense fluid, fuel) - spike (dense fluid, pusher) structures[10-12].

Around $\delta \sim \lambda$, the dense spikes penetrate into the fuel and the strong shear flows are developed to increase vorticity especially in the spike tips and eventually leads to the roll-up of the spike tips as the Kelvin-Helmholts like instability.

One spike generates a pair of vorticities at the right and left side of the tip, which have the opposite direction. Namely, the right side vorticity has the clockwise direction and the left has counter clockwise.

The pseudo particle trajectory and the contour plot of vorticity in the final stage are shown in Fig. 7.

As the pusher spikes penetrate to the center of the target, the amplitude of vorticities increases and the distance between vorticities of next spike tips decreases. Finally, two vorticities, which are generated by the next spike tips and have opposite direction, collide and burst to the outer side. The fuel is also accelerated and blown off to outside by such a dipole structure of vorticities, and the fuel jet inflates the bubbles.

We have investigated, through a series of simulations with our two dimensional fluid code IMPACT2D, the linear and nonlinear features of the Rayleigh-Taylor instability of the pusher-fuel contact surface of cylindrically stagnating targets.

First of all, the linear growth rates are shown as a function of mode numbers.

The linear stability of the stagnation dynamics was investigated, assuming the cylindrical symmetric dynamics to be in self-similar motion, where the acceleration and the wavelength vary both in time and space. The linearized equation to space component was numerically solved as an eigenvalue problem. For a given eigenvalue, the temporal evolution of the perturbation was also numerically solved and we found that the effective growth rate was in good agreement with simulation results.

As nonlinear feature, the saturation amplitude of the exponential growth was evaluated by simulations and the free-falling phase was characterized with the vorticity induced by the Kelvin-Helmholts like instability. It was found that the vorticities accompanying with the spike tips collide each other near the center of target and form the inner fluid jet to the outer side.

We would like to thank Dr.H.Takabe and K.M.Lue for useful discussions and Dr.R.H.Mendez for his interest and encouragement.

REFERENCES

[1]H. Takabe, L. Montierth, and R. L. Morse, Phys. Fluids **26**, 2299(1983)

[2]H. Takabe, K. Mima, L. Montierth, and R. L. Morse, Phys. Fluid **28**, 3676(1985)

[3]M. H. Emery, J. H. Gardner, and J. P. Boris, Appl. Phys. Lett. **41**, 808(1982)

[4]W. M. Manheimer and D. G. Colombant, Phys. Fluids **27**, 983(1982)

[5]M. J. de C. Henshaw, G. J. Pert, and D. L. Youngs, Plasma Phys. Controlled Fusion **29**, 405(1987)

[6]A. Harten, J. Comput. Phys. **49**, 357(1983)

[7]R. E. Kidder, Nucl. Fusion **16**, 3(1976)

[8]D. L. Book and I. B. Bernstein, J. Plasma Phys. **23**, 521(1980)

[9]F. Hattori, H. Takabe, and K. Mima, Phys. Fluid **29**., 1719(1986)

[10]D.L.Youngs, Physica **12D**, 32(1984)

[11]K.I.Read, Physica **12D**, 45(1984)

[12]M.H.Emery, J.P.Dahlburg, and J.H.Gardner, NRL Memorandum Report 6061(1987)

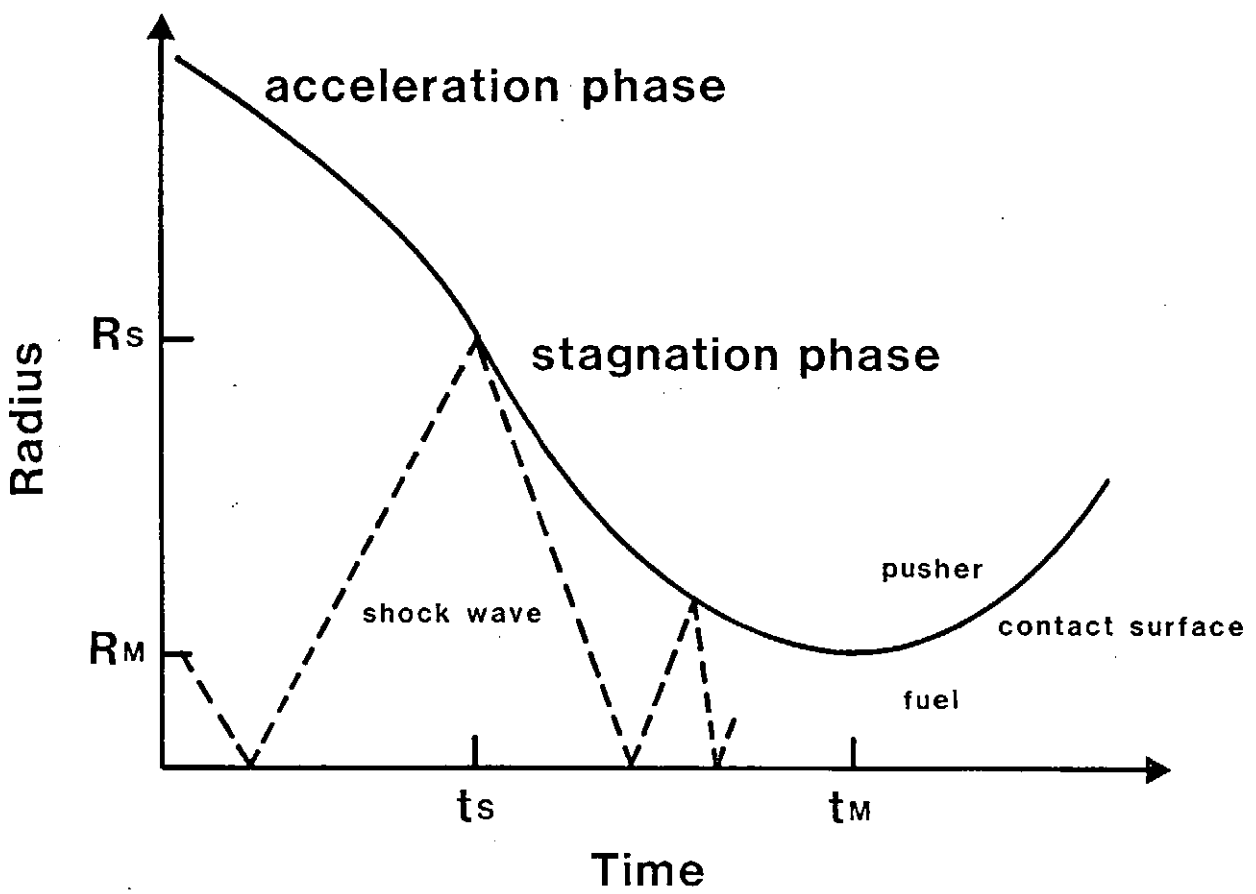

FIGURE 1. schematic R-T diagram of an imploding target

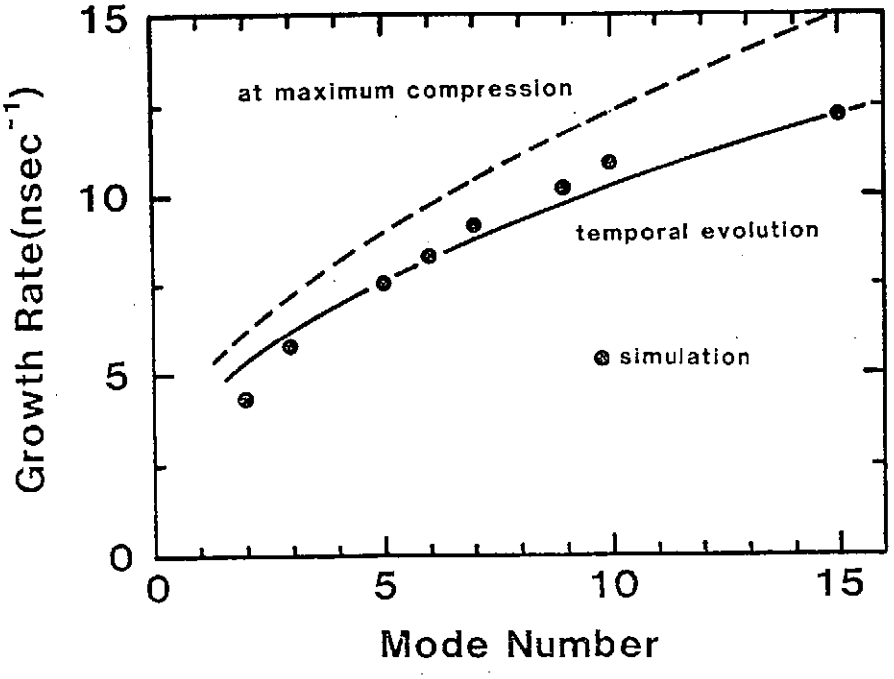

FIGURE 2. growth rate of simulation results and theoretical results

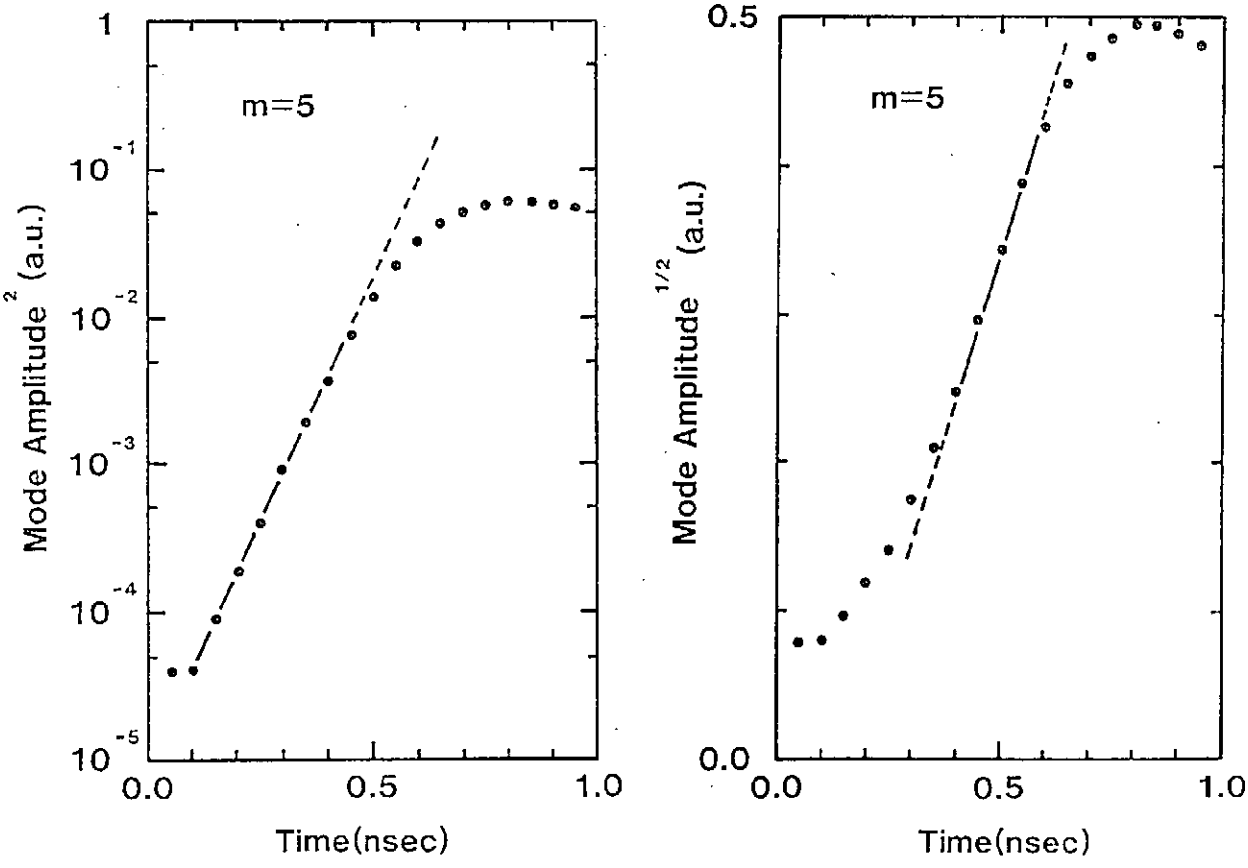

(a) logarithm

(b) square root

FIGURE 3. time evolution of the perturbation mode amplitude

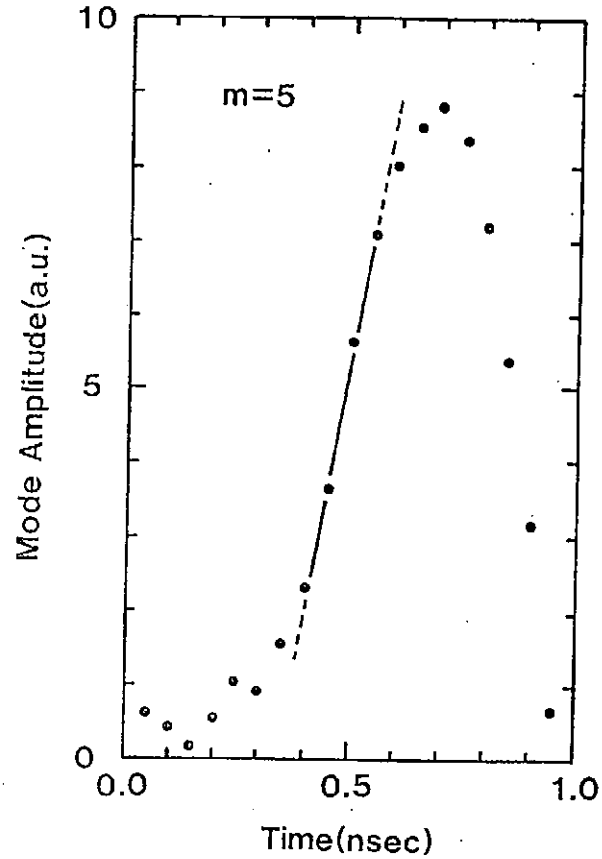

FIGURE 4. time evolution of the vorticity mode amplitude

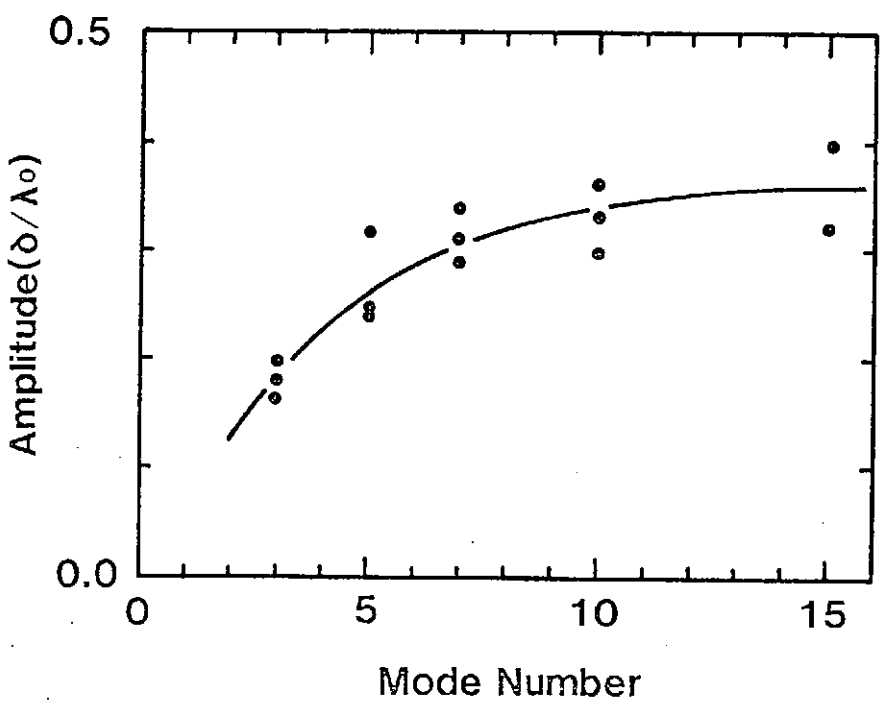

FIGURE 5. saturation amplitude of the exponential growth

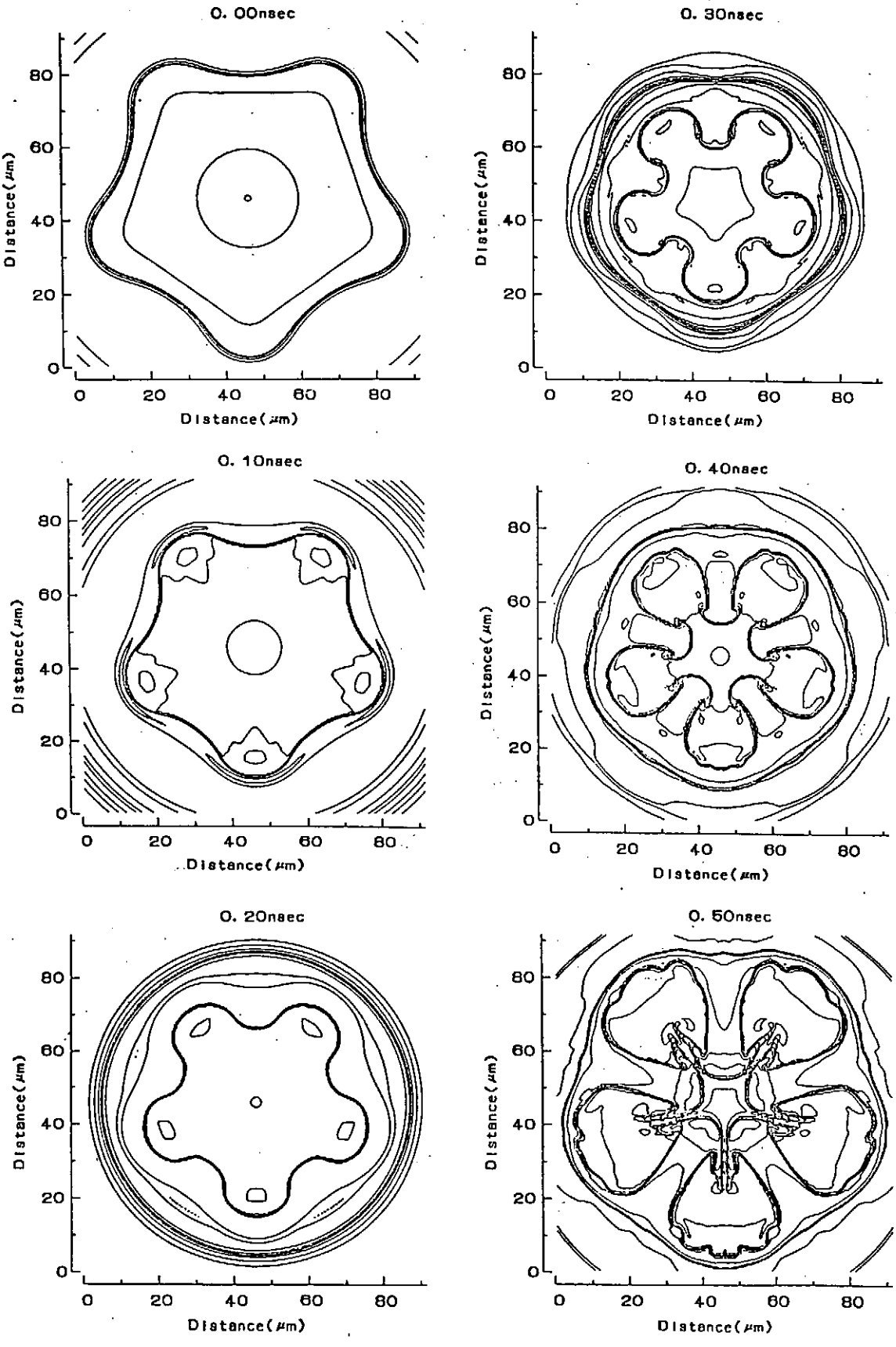

(a) density

FIGURE 6. contour plots of the density and vorticity for mode 5

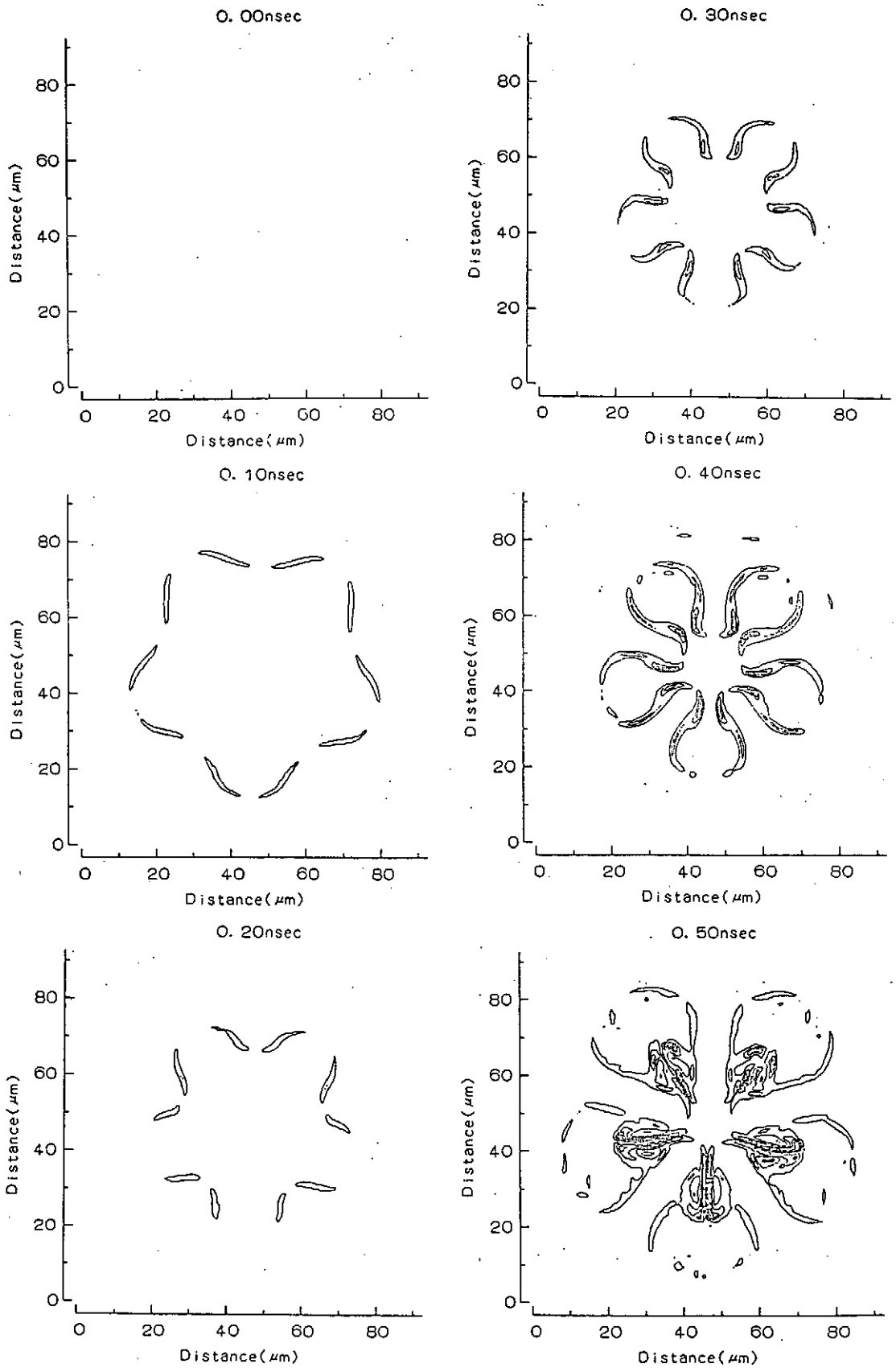
0. 00nsec
0. 30nsec
0. 10nsec
0. 40nsec
0. 20nsec
0. 50nsec
Distance(μm)
0
20
40
60
80

(b) vorticity

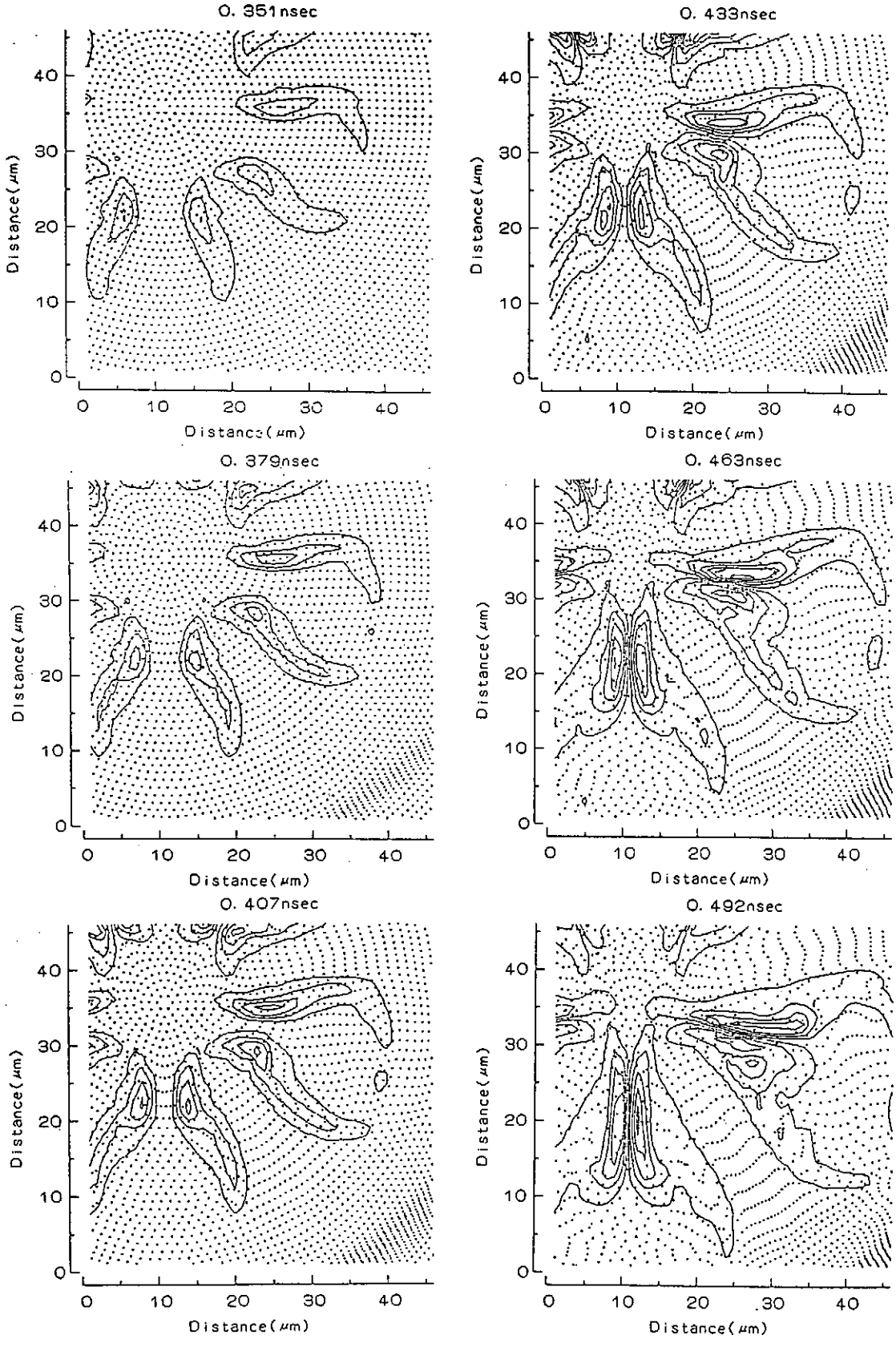

FIGURE 7. particle trajectory and contour plot of vorticity

VI. Hybrid Code —— Particle Electron and Fluid Ion

Two-Dimensional k-space Structure of Shearless Drift Waves, Hybrid Code Simulations

P.M. Lyster and J-N. Leboeuf*
Institute for Fusion Studies
The University of Texas at Austin
Austin, Texas 78712

In this work we have studied simple electrostatic drift-wave models in shearless slab geometry using a new hybrid, particle electron and fluid ion, technique.[1] The two types of drift waves are the density-gradient-driven (or Universal) mode, and the ion temperature gradient driven (or ETA-I) mode. These problems, as shown schematically in Fig. 1, are considered to be basic since they are the simplest cases of inhomogeneous collisionless plasmas in magnetic fields.

Kinetic or wave-particle interactions may be important in these modes, hence the need for particle simulations. This creates a difficulty since the time and space scales of drift waves can be long compared with particle times and spatial scales. A typical frequency for the Universal mode is $\omega_{*e} = k_\perp \rho_s (\rho_s/L_n)\Omega_i$, where $k_\perp$ is the wave number perpendicular to the ambient magnetic field B_0, $\rho_s = c_s/\Omega_i$, $c_s = \sqrt{T_e/m_i}$, $\Omega_i = eB_0/m_c$, and L_n is the density scale length. Usually $k_\perp \rho_s \lesssim 1$, but $\rho_s/L_n \ll 1$, so ω_{*e} is smaller than the ion cyclotron frequency Ω_i.

The simplest electrostatic simulation solves the field equation $\nabla^2\varphi = -4\pi e(n_i - n_e)$, where φ is the electrostatic field and n_i and n_e are the plasma ion and electron densities,

*ORNL, Oak Ridge, TN 37831

respectively. An accurate solution of this will involve small spatial scales of the Debye length. We can remove this by using ion and electron continuity equations, as well as the expression for the ion polarization drift $\mathbf{v}_p = (c/\Omega_i\, B_0)\partial_t\, \mathbf{E}_\perp$. We take the partial time derivative of the field equation, and the right-hand side of this can be rewritten $-(c/v_A)^2\partial_t\, \nabla_\perp^2\varphi + 4\pi\, \nabla_{||}\, J_{||}$, where $v_A = B_0/\sqrt{4\pi n_0\, m_i}$ and $J_{||} = e(n_i\, v_{||i} - n_e\, v_{||e})$. Since $(c/v_A)^2 \gg 1$ the left-hand side of the field equation may be neglected. This assumption of quasineutrality is the basis of the vorticity ($\nabla_\perp^2\varphi$) equation that is used in this hybrid model, and is central to the Hasegawa-Mima equation,[2] reduced MHD,[3] as well as gyrokinetic models.[4] The heuristic description is: in the perpendicular direction the electrons and ions do $\mathbf{E}\times\mathbf{B}$ drifts and their net current cancels. Therefore, only the perpendicular ion polarization drift causes a charge separation, and this is balanced by net parallel current flow. The hybrid model was first proposed by Okuda.[5] The ions are described by the vorticity Eq. (1), along with the parallel velocity ($v_{||i}$) and the temperature (T_i) equations.

$$\rho_s^2(\partial_t + v_{Di}\cdot\nabla)\nabla_\perp^2\left(\frac{e\varphi}{T_e}\right) = \nabla_{||}(v_{||i} - v_{||e}) \tag{1}$$

$$m_i\, n_i\left(\partial_t + (\mathbf{v}_E + \mathbf{v}_{||i})\cdot\nabla\right) v_{||i} = -en_i\, \nabla_{||}\varphi - \nabla_{||}\, P_i \tag{2}$$

$$\frac{3}{2}\left(\partial_t + (\mathbf{v}_E + \mathbf{v}_{||i})\cdot\nabla\right) T_i + T_i\, \nabla_{||}\, v_{||i} = 0 \tag{3}$$

where $\mathbf{v}_{Di} = \mathbf{v}_E + \mathbf{v}_M$, $\mathbf{v}_E = c\mathbf{E}\times\mathbf{B}_0/B_0^2$, and $\mathbf{v}_M = -c\nabla\, P_i \times B_0/eB_0^2$, $P_i = n_i\, T_i$. The electrons are guiding center particles; they do $\mathbf{E}\times\mathbf{B}$ drifts perpendicular to the ambient magnetic field, but are modeled kinetically in the parallel direction.

$$\begin{aligned} &\mathbf{v}_{\perp j} = c\mathbf{E}\times\mathbf{B}_0/B_0^2\,, \qquad j = 1,\ldots,NP \\ &m_e\, \tfrac{d}{dt}\, v_{||j} = e\nabla_{||}\varphi\,. \end{aligned} \tag{4}$$

The density is collected using a particle-mesh weighting scheme, $n_e(\mathbf{x}_k) = n_i(\mathbf{x}k) = \sum_j\, S(\mathbf{x}_k - \mathbf{x}_j)$, where NP is the number of simulation particles, and $\mathbf{x}_k$ is the grid point position. We note that the usual hybrid technique models the electrons as a fluid and the ions as particles.[6]

This removes the faster electron times as a determinant of code accuracy or stability. Paradoxically we use the opposite scheme, and its rationalization lies in the above development of the vorticity equation.

Consider now the Universal mode. In shearless slab geometry, where a collisionless plasma has a density scale length L_n, this mode is unstable with real frequency of order ω_{*e}, and growth rate $\omega_{*e}^2\, k_\perp^2\, \rho_s^2/k_\parallel\, v_{the}$. We should note that in sheared slab geometry this mode is stable,[7] although the issue becomes more complicated in toroidal geometry.[8] Note that a kinetic electron model is necessary because this mode is driven unstable by wave-particle resonances. The simple case was used by the present authors to check the hybrid algorithm. There, the unstable mode saturated by quasilinear saturation, that is, the perturbed density $n^{(1)}$ caused a flattening of the ambient density gradient. The field amplitude was given approximately by the mixing length estimate $n^{(1)}/n_0 \sim 1/k_\perp\, L_n$. We are presently interested in the roles played by nonlinearities in the saturation mechanism. The ion continuity equation $\partial_t\, n_i = -\boldsymbol{\nabla}\cdot(n_i\, \mathbf{v}_i)$ can be rewritten

$$\partial_t(\tilde{n} - \nabla_\perp^2\tilde{\varphi}) + i\omega_{*e}\tilde{\varphi} - \nabla_\perp\cdot(\hat{b}\times\nabla\tilde{\varphi}\cdot\nabla)\nabla_\perp\tilde{\varphi} + \nabla\cdot(\hat{b}\times\nabla\tilde{\varphi}\,\tilde{n}_{NA}) = -\nabla_\parallel\, v_{\parallel i} \qquad (5)$$

where we have substituted $\mathbf{v}_{\perp i} = \mathbf{v}_E + \mathbf{v}_m + \mathbf{v}_p$, and $\tilde{n} = n^{(1)}/n_0$, $\tilde{\varphi} = e\varphi^{(1)}/T_e$, $\hat{b} = \mathbf{B}_0/B_0$, the frequencies are normalized to Ω_i, and spatial scales to ρ_s. The principal nonlinearities are retained on the left-hand side. The first we denote the polarization nonlinearity was considered by Hasegawa-Mima,[2] note that it is present in most studies involving the vorticity equation. The second, denoted the non-adiabatic nonlinearity because it is only present when there is a finite deviation from electron adiabaticity, that is, $\tilde{n}_e = \tilde{\varphi} + \tilde{n}_{NA}$. The adiabatic electron assumption ($\tilde{n}_{NA} = 0$) was made in the Hasegawa-Mima formulation. The non-adiabatic nonlinearity was considered by Horton.[9] So, an important comparison is the ratio of the non-adiabatic nonlinearity to the ion polarization nonlinearity, which is approximately $\tilde{n}/k_\perp^2\tilde{\varphi}$. We are also interested in the $k_\perp$-spectrum of the field φ. The term in

Eq. (5) proportional to ω_{*e} is responsible for the linear drive of the mode. The resulting $\varphi_{\mathbf{k}}$ spectrum has components primarily in the k_y-direction. Either of the nonlinearities may alter this structure. Hasegawa[10] *et al.* considered the ion polarization nonlinearity; comparing this term to the linear drive it is easy to see that the spectrum may be modified for the range of $k_\perp > k_{c1} = (\tilde{\varphi}\, L_n)^{-1/3}$, in normalized units. In particular, the spectrum tends to "rotate" into the k_x-direction. They predicted that there would be a condensation of the energy spectrum toward finite $k_x \to k_{c1}$ and $k_y \to 0$. Simulations of spectral behavior were done by Fyfe and Montgomery.[11] Presumably, the non-adiabatic nonlinearity may have a similar effect for $k_\perp > k_{c2} = (\tilde{n}_{NA}\, L_n)^{-1}$.

The basic simulation parameters are: $\rho_s/L_n = 0.063$, $k_\parallel/k_\perp = 0.00262$, $\rho_s/\Delta x = 2.5$, $\Omega_e/\omega_{pe} = 10$, $m_e/m_i = 1/100$ and $T_e/T_i = 1$, where Δx is the grid spacing. Also $\Omega_i\, \Delta t = 0.4$, where Δt is the timestep. We used a $64(x)$ by $32(y)$ grid. With these parameters, we have $\omega_{*e}/k_\parallel\, v_{the} \sim 1$, which is the condition for electron wave particle effects to be important. Figure 2 shows plots of the electrostatic energy against time for: (a) both nonlinearities present, (b) the ion polarization nonlinearity removed (c) the non-adiabatic nonlinearity removed, and (d) no nonlinearities present. In the first case the mode shows the initial linear growth phase followed by saturation due to profile flattening. In the following two cases the saturation level has increased, however it is not clear which nonlinearity is most significant. Finally, with no nonlinearities in the vorticity equation the mode fails to saturate in a physically consistent way. We observed that the whole electron Maxwellian distribution is accelerated, and a non-physical parallel current is generated as $\int d\mathbf{x}\, E^2/8\pi \sim \int d\mathbf{x}\, nT_e$. Figure 3(a)–(d) shows the respective plots of field amplitude $|\varphi_k|$ in $\mathbf{k}$-space, after saturation has occurred. The linear spectrum is seen in (d) where the mode number $\ell_y = 1$ dominates. The plots (a)–(d) show how the effect of the ion polarization nonlinearities is to rotate the spectrum to $\ell_x = 1$. A check of the field amplitude shows that $k_{c1} = 0.8$, corresponding to $\ell_x = 8$. Clearly case (c) shows the spectrum to be altered for mode numbers less than

this value. The estimate k_{c1} is approximate, also as the saturation occurs the effective density scale length L_n becomes longer and k_c goes down. Figure 4 shows contour plots of $\varphi(x,y)$ for the full nonlinear case (a), and the linear case (b). In the former case the mode $(\ell_x, \ell_y) = (1,0)$ dominates, while in the latter there is a preponderance of the $(0,1)$ mode.

We finish with a brief summary of the ion-temperature gradient driven mode. This is also called the ETA-I mode, where $\eta_i = L_n/L_T$. Once again this was discussed in Ref. 1. This mode may be studied with purely fluid equations. In fact, apart from the kinetic hybrid model we have used a fluid ion (including the vorticity equation) — Boltzmann electron model. The mode is accessed through the negative compressibility term $(-\frac{2}{3}\nabla_{\|} v_{\|i})$ in the ion temperature equation. In slab model there are two possible roots[11] corresponding to growth rates $\gamma = \left((\eta_i - \frac{2}{3})k_{\|}^2 v_{thi}^2\right)^{1/2}$ for $\omega_r \ll \eta_i \omega_{*i}, \omega_{*e}$; and $\gamma = (k_{\|}^2 c_s^2 \eta_i \omega_{*i})^{1/3}$ for $\omega_r \sim \gamma \ll \eta_i \omega_{*i}$, and $\gg \omega_{*e}$ where $\omega_{*i} = -(T_i/T_e)\omega_{*e}$. We have considered the case where $\eta_i = 16$, $k_{\|}/k_{\perp} = 0.1$, $\omega_{*e}/k_{\|} v_{the} = 0.06$, that is, wave particle resonances are not important. The behavior in k-space is summarized in Fig. 5. On the left column is the field amplitude for the hybrid model; on the top for $(k_x, k_y) = (0.0, 0.37)$ and at the bottom for $(k_x, k_y) = (0.12, 0.0)$. Both modes grow to finite amplitude indicating that some spectrum rotation is occurring from the linear drive at $(0, 0.37)$. The Boltzmann case is shown in the right column, where the mode $(0.0, 0.37)$ displays the same behavior as for the hybrid model. However, the finite k_x component, $(0.12, 0.0)$, does not grow to the same amplitude. Clearly the non-adiabatic nonlinearity is the dominant one here in determining the spectrum rotation.

We have considered aspects of nonlinear saturation as well as the structure of the field amplitude in $\mathbf{k}_{\perp}$ space. At present, some qualitative observations have been made about the effects of the ion-polarization and the non-adiabatic nonlinearities. A more detailed study would involve similar runs over a wider range of physical parameters and with a greater

resolution of the k-space spectrum, that is, a larger number of grid points.

Acknowledgments

We would like to acknowledge the help of G.S. Lee and Ben Carreras at Oak Ridge National Laboratory, P. Terry at University of Wisconsin, and P.H. Diamond at University of California, San Diego. Also, one of us (PML) would like to thank R. Dory and workers at ORNL for their help during my stay there.

1. P.M. Lyster and J-N.Leboeuf, "A Fluid-Ion and Particle-Electron Simulation Model for Plasma Microinstabilities" submitted to *Journal of Computational Physics*, March 1989.

2. A. Hasegawa and K. Mima, *Phys. Rev. Lett.* **39**, 205 (1979).

3. see for example L. Garcia, H.R. Hicks, B.A. Carreras, L.A. Charlton, J.A. Holmes, *J. Comput. Phys.* **65**, 253 (1986); and R.D. Hazeltine, M. Kotschenreuther, and P.J. Morrison, *Phys. Fluids* **28**, 2466 (1985).

4. W.W. Lee, *J. Comput. Phys.* **72**, 243 (1987).

5. H. Okuda, *Space Sci. Rev.* **47**, 41 (1985).

6. see for example J.A. Byers, B.I. Cohen, W.C. Condit, and J.D. Hanson, *J. Comput. Phys.* **27**, 363 (1978).

7. D.W. Ross and S.W. Mahajan, *Phys. Rev. Lett.* **40**, 324 (1978).

8. see for example R.J. Hastie, K.W. Hesketh, and J.B. Taylor, *Nucl. Fusion* **19**, 1223 (1979).

9. W. Horton, *Phys. Rev. Lett.* **37**, 1269 (1976).

10. A. Hasegawa, C. Maclennan, and Y. Kodama, *Phys. Fluids* **22**, 2122 (1979).

11. D. Fyfe and D. Montgomery, *Phys. Fluids* **22**, 246 (1979).

12. B. Kadomtsev and O.P. Pogutse, in **Reviews of Plasma Physics**, Vol. V, p. 249, (Consultants Bureau, NY, 1970).

Figure Captions

Fig. 1. Schematic drawing of the slab geometry used for the hybrid model.

Fig. 2. Plots of electrostatic energy normalized to the total electron particle energy against time for: (a) both nonlinearities in the vorticity equation present, (b)the ion polarization nonlinearity removed, (c) the non-adiabatic nonlinearity removed, and (d) both nonlinearities removed.

Fig. 3. The field amplitude $|\varphi_{\mathbf{k}}|$ for the respective cases considered in Fig. 2.

Fig. 4. Contour plots of $\varphi(x,y)$ for (a) both nonlinearities retained in the vorticity equation, and (b) both nonlinearities removed.

Fig. 5. Plots of the electrostatic energy, normalized to the total electron particle energy, for the ETA-I mode.

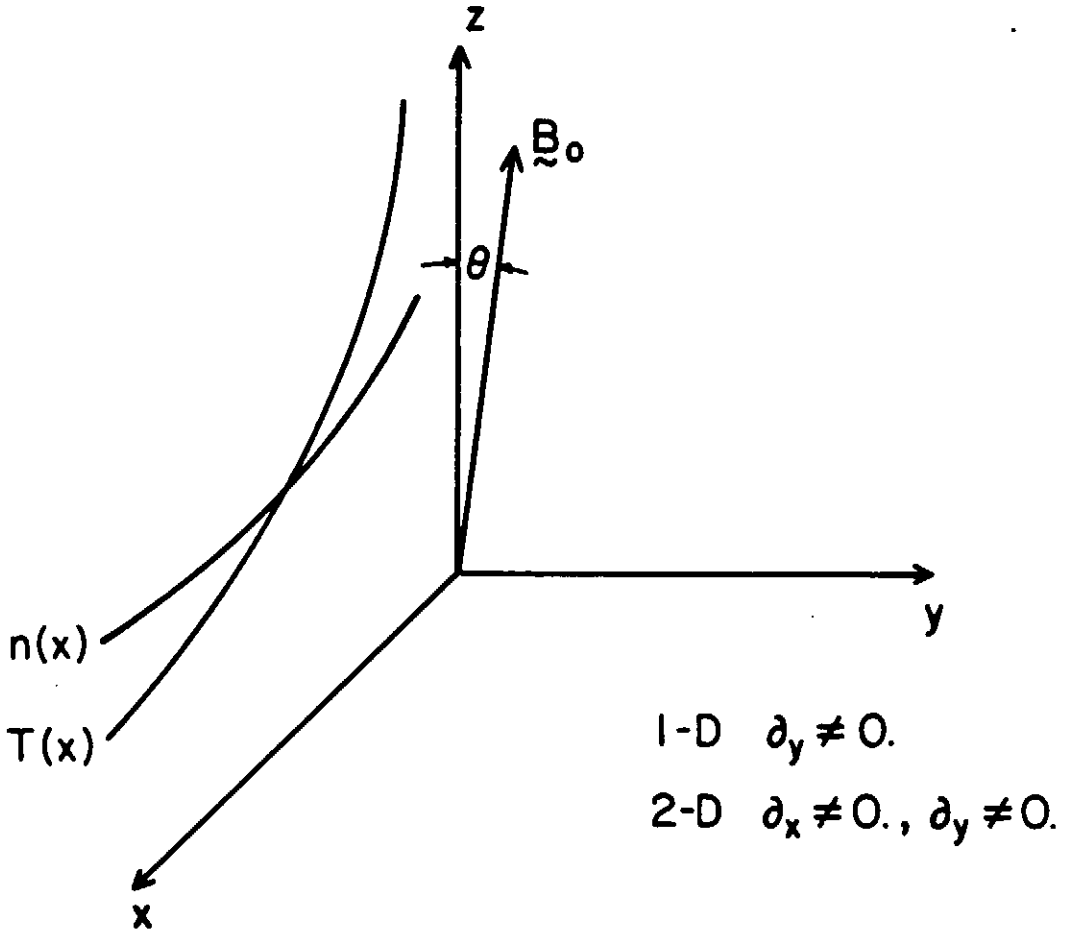

Fig. 1

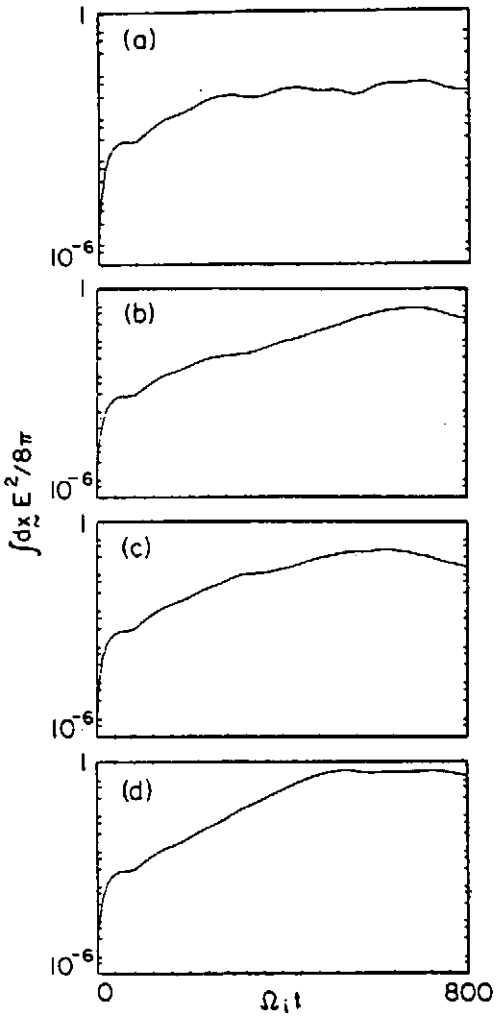
(a)
(b)
(c)
(d)
1
10^{-6}
$\int d\underset{\sim}{x}\, E^2/8\pi$
0
$\Omega_i t$
800

Fig. 2

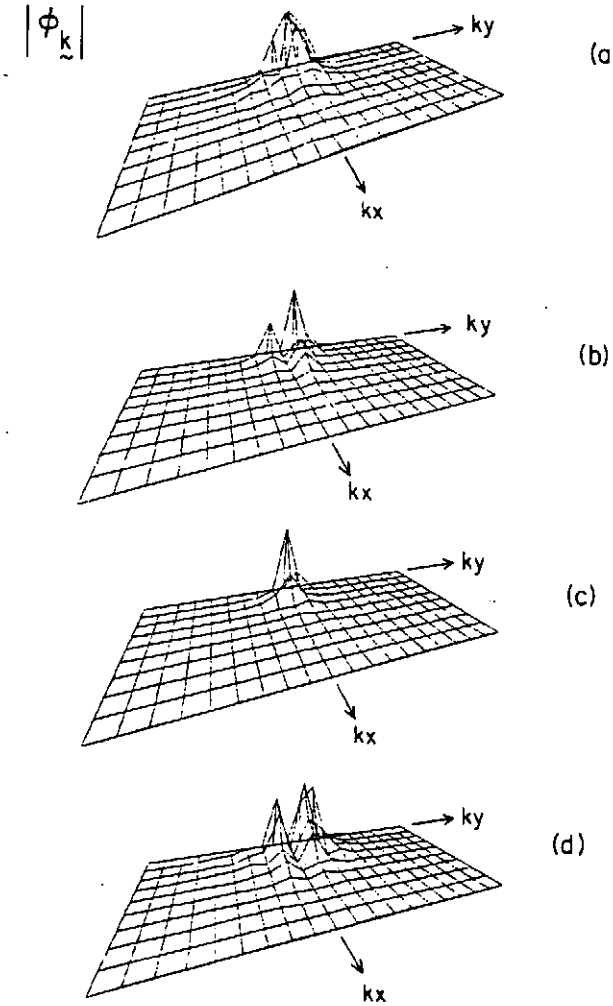
$|\Phi_{\underset{\sim}{k}}|$
ky
kx
(a)
(b)
(c)
(d)

Fig. 3

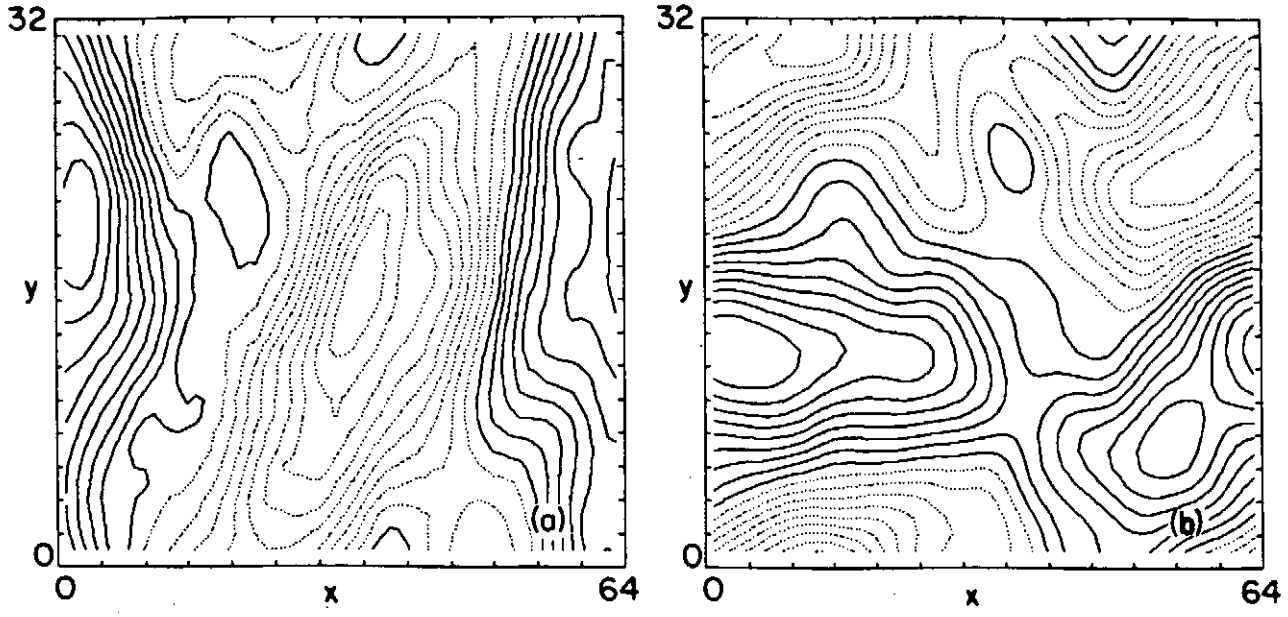
32
y
0
0
x
64
(a)
32
y
0
0
x
64
(b)

Fig. 4

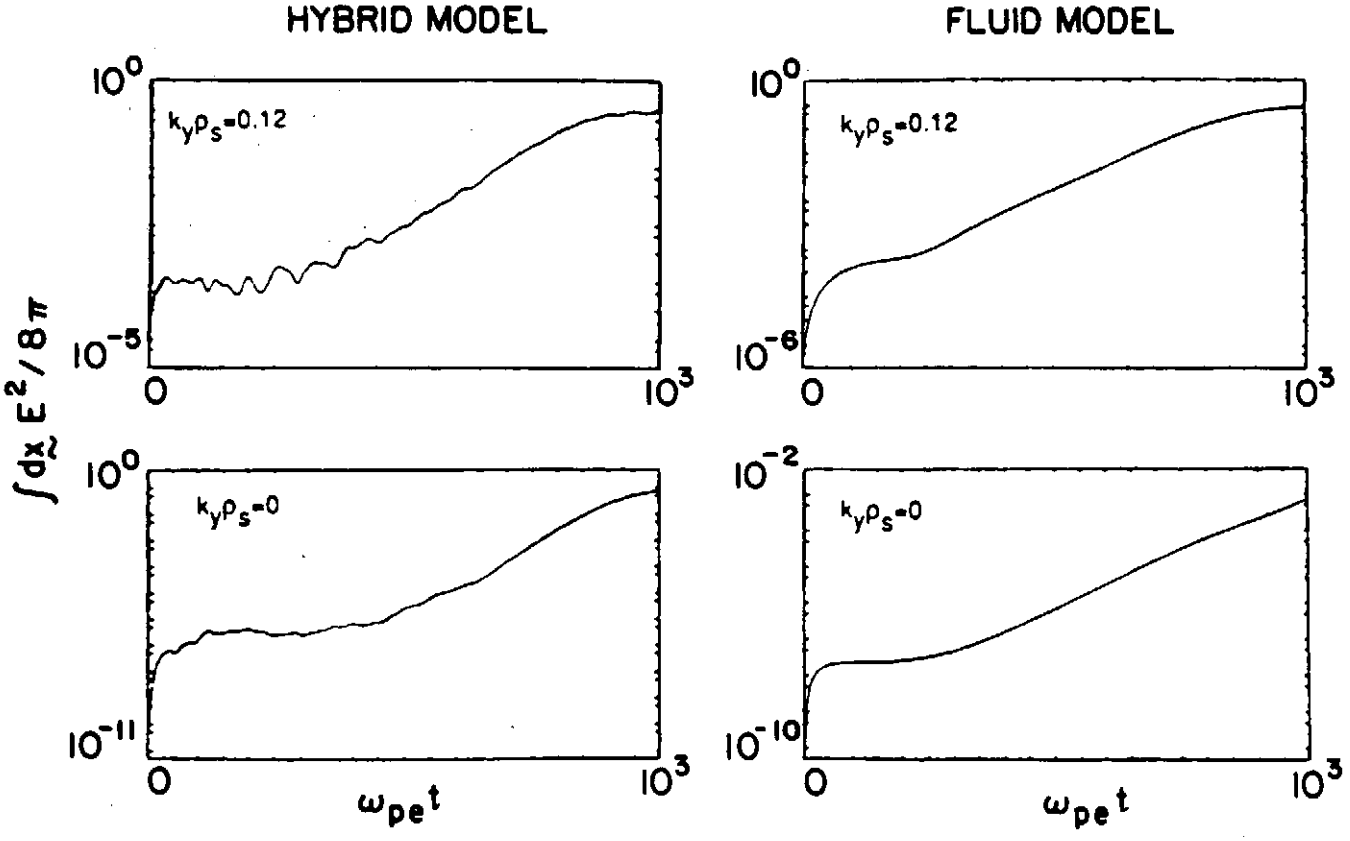
HYBRID MODEL
FLUID MODEL
$\int dx\, E^2/8\pi$
10^0
$k_y\rho_s$=0.12
10^{-5}
10^{-6}
0
10^3
10^0
$k_y\rho_s$=0
10^{-11}
10^{-2}
10^{-10}
$\omega_{pe}t$

Fig. 5

Magnetohydrodynamic Transport Code (MHDT-Code)

Masatoshi Yagi and Masahiro Wakatani[†] *Akira Hasegawa*[‡]

Nuclear Engineering Department, Faculty of Engineering,
Kyoto University,
Sakyo-ku, Kyoto

[†]*Plasma Physics Laboratory, Kyoto University,*
Gokasho Uji

[‡]*AT&T Bell Laboratories,*
Murrary Hill,
New Jersey U.S.A.

Abstract

We have been developed a hybrid computer code for the study of electron transport in micro-MHD turbulence. Ions are treated in fluid approximation and electrons are treated as particles with guiding center approximation. The parpendicular and parallel grid sizes are determined by c/ω_{pe} and Alfven wave length respectively, while the integration time step by ω_{ci}^{-1}, hence the code is suitable to study microscopic MHD phenomena with arbitarary electron and ion mass ratio. Initial results are discussed.

§1. Model equations

Fluid equation for ions can be derived from the charge neutrality condition.

$$\nabla \cdot \boldsymbol{J} = 0 \tag{1}$$

where $\boldsymbol{J} = \boldsymbol{J}^{(i)} + \boldsymbol{J}^{(e)}$ and

$$\boldsymbol{J}^{(i)} = \boldsymbol{J}_P + \boldsymbol{J}_\perp^{(i)} + \boldsymbol{J}_\parallel^{(i)} \tag{2}$$

$$\boldsymbol{J}^{(e)} = \boldsymbol{J}_\perp^{(e)} + \boldsymbol{J}_\parallel^{(e)}. \tag{3}$$

Here $\boldsymbol{J}_P$ denotes a polarization current. Electric field $\boldsymbol{E}$ and magnetic field $\boldsymbol{B}$ are described by using potential φ and $A_\parallel$

$$\boldsymbol{E} = -\nabla\varphi - \frac{\partial A_\parallel}{\partial t}\boldsymbol{b} \tag{4}$$

$$\boldsymbol{B} = \nabla \times A_\parallel \boldsymbol{b}\,. \tag{5}$$

where $A_\parallel$ is related to $J_\parallel$,

$$J_\parallel^{(i)} + J_\parallel^{(e)} = -\frac{1}{\mu_0}\nabla_\perp^2 A_\parallel \tag{6}$$

For the ion, we use $\boldsymbol{V}_{\perp i} = \boldsymbol{V}_{Di} + \boldsymbol{V}_P$, where $\boldsymbol{V}_{Di} = \frac{1}{B}\boldsymbol{b} \times \nabla\varphi + \frac{1}{\omega_{ci} m_i n_i}\boldsymbol{b} \times \nabla p_i$ and $\boldsymbol{V}_P = -\frac{1}{B\omega_{ci}}(\partial_t + \boldsymbol{V}_{Di}\cdot\nabla)\nabla_\perp\varphi$. From eq.(1), we obtain

$$\frac{1}{B_0^2}(n_i m_i \frac{d}{dt}\nabla_\perp^2\varphi + \frac{1}{\omega_{ci}}\nabla_\perp \cdot \boldsymbol{z} \times \nabla p_i \cdot \nabla\nabla_\perp\varphi)) = \nabla_\parallel(J_\parallel^{(i)} + J_\parallel^{(e)}) + \frac{2}{B}\boldsymbol{z} \times \boldsymbol{\kappa} \cdot \nabla(p_i + p_e) \tag{7}$$

where $\frac{d}{dt} = \frac{\partial}{\partial t} + \frac{1}{B}[\varphi,\ ]$, $\boldsymbol{\kappa} = (\boldsymbol{b}\cdot\nabla)\boldsymbol{b} \sim \frac{\nabla_\perp B}{B_0}$, $\nabla_\parallel = \frac{\partial}{\partial z} - \frac{1}{B_0}[A_\parallel,\ ]$. We assume that ion parallel velocity eq. is simply given by using $\nabla\cdot\boldsymbol{v}_e = 0$,

$$n_i m_i \frac{d}{dt} V_{\parallel i} = -\nabla_\parallel(p_i + p_e) + \frac{m_e}{e}\frac{dJ_\parallel^{(e)}}{dt} \tag{8}$$

and ion pressure eq. is written as

$$\frac{d}{dt}p_i = 0. \tag{9}$$

Using eq.(9) we rewrite eq.(7) as

$$\frac{1}{B_0}(n_i m_i \frac{d}{dt}\nabla_\perp^2 F - \frac{1}{\omega_{ci}}\nabla_\perp \cdot \boldsymbol{z} \times \nabla p_i \cdot \nabla\nabla_\perp F)) = \nabla_\parallel (J_\parallel^{(i)} + J_\parallel^{(e)}) + \frac{2}{B}\boldsymbol{z} \times \boldsymbol{\kappa} \cdot \nabla(p_i + p_e) \quad (10)$$

where $F = \frac{1}{B_0}(\varphi + \frac{P_i}{en_0})$. Under the assumption of $n_i = n_e$, we need electron current $\boldsymbol{J}_\parallel^{(e)}$ and P_e to close our model equations. In the hybrid model electron currents are estimated from guiding center motions.The guiding center current and parallel current are given by

$$\boldsymbol{J}_{\perp D}^{(e)} = -\sum_j e\, \dot{\boldsymbol{X}}_\perp^j(t)\delta(\boldsymbol{X} - \boldsymbol{X}^j(t)) \quad (11)$$

$$\boldsymbol{J}_\parallel^{(e)} = -\sum_j e\, \boldsymbol{V}_\parallel^j(t)\delta(\boldsymbol{X} - \boldsymbol{X}^j(t)) \quad (12)$$

The guiding center trajectory is obtained from the guiding center Lagrangean[1),2)]

,

$$\frac{d}{dt}(\frac{\partial L_G}{\partial \dot{X}_j}) - \frac{\partial L_G}{\partial X_j} = 0, j = x, y, z \quad (13)$$

with $L_G = (m_e\dot{X}_3 - eA_i)\cdot\dot{X}_i - < H >$, $< H >= \frac{m_e}{2}\dot{X}_3\frac{B^2}{B_0^2} + m_e\mu B - e\varphi$ The vector potential is described by $A = B_0 x\, \boldsymbol{y} + (A - \frac{B_0}{2L_s}x^2)\, \boldsymbol{z}$. By using these relations eq.(13) gives

$$\boldsymbol{v}_{\perp e} = \frac{1}{B_0}\boldsymbol{z} \times \nabla\varphi - \frac{v_{\parallel e}}{B_0}\boldsymbol{z} \times \nabla A + [\frac{1}{\omega_{ce}}(\frac{v_{\perp e}^2}{2} + v_{\parallel e}^2)]\, \boldsymbol{\kappa} \times \boldsymbol{z} \quad (14)$$

$$m_e\frac{dv_{\parallel e}}{dt} = e(\frac{\partial A}{\partial t} + \nabla_\parallel\varphi) + \frac{e}{\omega_{ce}}(\frac{v_{\perp e}^2}{2} + v_{\parallel e}^2)\nabla(A - \frac{B_0}{2L_s}x^2) \times \boldsymbol{\kappa} \cdot \boldsymbol{z} . \quad (15)$$

Here we assume the term proportional to $\boldsymbol{\kappa}$ in eq.(15) is of higher order and negligible . In this case electron parallel motion equation becomes

$$m_e\frac{dv_{\parallel e}}{dt} = e(\frac{\partial A}{\partial t} + \nabla_\parallel\varphi) \quad (16)$$

Instead of $v_\parallel$, we use canonical momentum, $P_e = m_e v_{\parallel e} - eA$, in eq.(16),

$$\frac{dP_e}{dt} = e(\frac{\partial\varphi}{\partial z} - \frac{\partial A}{\partial z}v_{\parallel e}) \quad (17)$$

The electron pressure is defines as

$$p_e = \int d^3v \frac{m_e}{2}[\frac{v_\perp^2}{2} + v_{\|e}^2]f_e = \frac{p_{\perp e} + p_{\|e}}{2}. \tag{18}$$

Instead of the guiding center equations (14), (15), or (17), we can write equivalent fluid type equations for electrons . For simplicity, we neglect curvature terms in eqs.(14) and (15). By using $\nabla \cdot \boldsymbol{J}_e$, the electron continuity eq. is given by

$$\frac{d}{dt}\frac{n_e}{n_0} = \frac{1}{en_0}\nabla_\| J_{\|e}. \tag{19}$$

And Ohm's law is written as

$$\frac{\partial A}{\partial t} = -\nabla\varphi + \frac{1}{en_0}\nabla_\| p_{\|e} - \frac{m_e}{e^2 n_0}\frac{dJ_{\|e}}{dt} \tag{20}$$

Further we assume $T_e = const.$ and $p_{\perp e} = p_{\|e} = T_e n_e$. Then from eqs. (8),(9),(10),(11),(19),and (20), a total energy conservation becomes

$$\frac{d}{dt}\int d^3r(\frac{|\nabla_\perp A|^2}{2\mu} + \frac{n_0 m_i V_{\|i}^2}{2} + n_0 m_i \frac{|\nabla_\perp F|^2}{2} + p_i\frac{n_e}{n_0} + \frac{T_e}{n_0}\frac{n_e^2}{2} + \frac{m_e}{e^2 n_0}\frac{J_{\|e}^2}{2}) = 0. \tag{21}$$

The hybrid model is composed of fluid ion eqs. (8), (9), and (10) and guiding center electron eqs. (14), (15). In this case we can treat resonant wave particle interaction due to electrons in the fluid type turbulence.

§2. Application of MHDT model

In order to test our hybrid model we firstly study high frequency electromagnetic mode due to electrons and kinetic Alfven waves(KAW) in a homogeneous magnetized plasma[3),4)] . We normalize the equations using ω_{ci} for time and $c/\omega_{ci}$for length . Here ω_{ce}, and ω_{pe} are the electron cyclotron and the plasma frequencies, respectively. For electrons, by neglecting the curvature term, the guiding center equations become

$$v_{xe} = \frac{m_e}{m_i}[-\frac{\partial\varphi}{\partial y} + \frac{\partial A}{\partial y}v_{\|e}] \tag{22}$$

$$v_{ye} = \frac{m_e}{m_i}[\frac{\partial\varphi}{\partial x} - \frac{\partial A}{\partial x}v_{\|e}] \tag{23}$$

$$\frac{dP_e}{dt} = \frac{\partial \varphi}{\partial z} - \frac{\partial A}{\partial z} v_{\|e} \tag{24}$$

By integrating eq.(24) over all particles in one cell and using eq.(6), we obtain

$$\nabla_\perp^2 A - \frac{1}{nprcll} \sum_{j \in g} A(r_j) = \frac{1}{nprcll} \sum_{j \in g} P_{je} S(r - r_j) \tag{25}$$

where the parallel ion current is neglected. Here we normalize A , φ and P_e with $\frac{m_e B_0 c}{m_i \omega_{pe}}$, $\frac{m_e B_0 \omega_{ci} c^2}{m_i \omega_{pe}^2}$ and $\frac{m_e \omega_{ci} c}{\omega_{pe}}$. Also $P_e = v_{\|} - A$ and $\nabla = \frac{\partial}{\partial z} - [A, \ ]$, and nprcll is an averaged particle number per cell. In R.H.S. of eq.(25) $S(r - r_j)$ denotes the shaping factor of finite size particle[5),6)]. Equation (7) is simply written as

$$\frac{d}{dt} \nabla_\perp^2 \varphi = \frac{m_i}{m_e} \nabla_{\|} J_{\|e} \tag{26}$$

by neglecting the curvature term and parallel ion current term. Here electron parallel current is given by $J_{\|e} = -\nabla_\perp^2 A$.

The use of the canonical momentum P_e in the equation of electron motion allows us to avoid the use of the predictor corrector and to save computation time[7)] . The electron equation of motion is explicitly integrated in time by using the Leap frog scheme. The vector potential A is obtained from eq.(25) . For the mederate range of β_e , $\frac{m_e}{m_i} \leq \beta_e \leq \sqrt{\frac{m_e}{m_i}}$, the relation of $\frac{c}{\omega_{pe}} \leq \rho_s$ and $\omega_{ci} \ll \omega_{pe}$ is always satisfied. In our normalization the normalized thermal velocity determines β_e.

We show two preliminary results. To check of the particle pushing in the hybrid code, we have studied high frequency electromagnetic waves due to electron motions and assumed $\varphi = 0$. The dispersion relation for a homogeneous magnetized plasma is described by $\omega = v_{th} k_z / \sqrt{1 + 1/k_\perp^2}$ which is compared with the numerical result. Figure 1 shows the total energy evolution. The total energy, $E = 1/2 \sum_I \sum_{j \in I} v_{zj}^2 + nprcll \sum_I |\nabla_\perp A|^2/2$ is conserved with the accuracy of less than 1 % . Figure 2 shows the evolution of the canonical momentum . And Figure 3 shows the dispersion relation by the code. The agreement between the numerically obtained results and the analitic dispersion relation is resonable .

The KAW can be studied by the hybrid code. Before appling it we solved the FLR-MHD model composed of eqs.(19), (20), (26), $J_{\|e} = -\nabla_\perp^2 A$ and $T_e = const.$ Initially a potential perturbation is given and time evolution density perturbation is shown in Figure 4. It propergates according to the dispersion relation $\omega = k_z v_A(1 + k_\perp^2 \rho_s^2)$. Since the conducting walls are placed at x = 0 and x = 1 , k_x is determined from the dispersion relation. For the y and z directions , period boundary conditions are assumed .

§3. Summary

We discussed a new hybrid computer code for the study of electron transport in micro-MHD turbulence and some preliminary results. For the next step, we apply it to KAW instead of FLR-MHD model using the generalized Ohm's law.

Acknowlegement

One of the authers, M.Yagi , thanks Dr. Naito in Yamaguchi University for his kind advise about the particle pushing scheme and Dr.Nakamura in Plasma Phiscis Laboratory , Kyoto University for his support of the code development. We acknowledge Dr.Lyster in IFS for the comparision with his hybrid code. This work was supported by a Grant-in-Aid for Special Project Research on Energy (Nuclear Fusion) of the Ministry of Education , Science and Culture. The travel expense of Hasegawa's visit to kyoto was partially supported by US-DOE.

References

1) W. W. Lee: J. of Comp. Phys. **72** (1987) 243.

2) T. S. Hahm: Phys. Fluids **31** (1988) 2760.

3) A. Hasegawa, L. Chen: Phys. Fluids **19** (1976) 1924.

4) M. Tanaka: J. of Comp. Phys. **79** (1988) 209.

5) C. K. Birdsall, A. B. Langdon: *PLASMA PHYSICS VIA COMPUTER SIMULATION* (McGraw-Hill Book Co. Singapore, 1985)

6) T. Tajima: *COMPUTATIONAL PLASMA PHYSICS WITH APPLICATIONS TO FUSION AND ASTROPHYSICS* (Addison-Wesley Publishing Co.,Inc. Tokyo 1989)

7) A. T. Lin: Phys. Fluids **21** (1978) 1026.

Figure Captions

Fig.1 Time evolution of total energy :$E = 1/2 \sum_I \sum_{j \in I} v_{zj}^2 + nprcll \sum_I |\nabla_\perp A|^2/2$ Here system size is given by $L_x = L_y = 1c/\omega_{pe}$, $L_z = 200c/\omega_{pe}$, the cell number, $N_x \times N_y \times N_z = 16 * 16 * 32$,thermal velocity, $v_{the}/c = 4.42 \times 10^{-2}$, mass retio $m_e/m_i = 1/1836$, $\beta_e = 3.6 \times \frac{m_e}{m_i}$, time step $\Delta t = 10/\omega_{pe} = 5.44 \times 10^{-3}/\omega_{ci}$.

Fig.2 Time evolution of canonical momentum :$P_e = v_\parallel - A$

Fig.3 Dispersion relation corresponding to electron wave:$\omega = v_{th} k_z / \sqrt{1 + 1/k_\perp^2}$

Fig.4 Time evolution of density fluctuation corresponding to KAW obtained from FLR-MHD model.

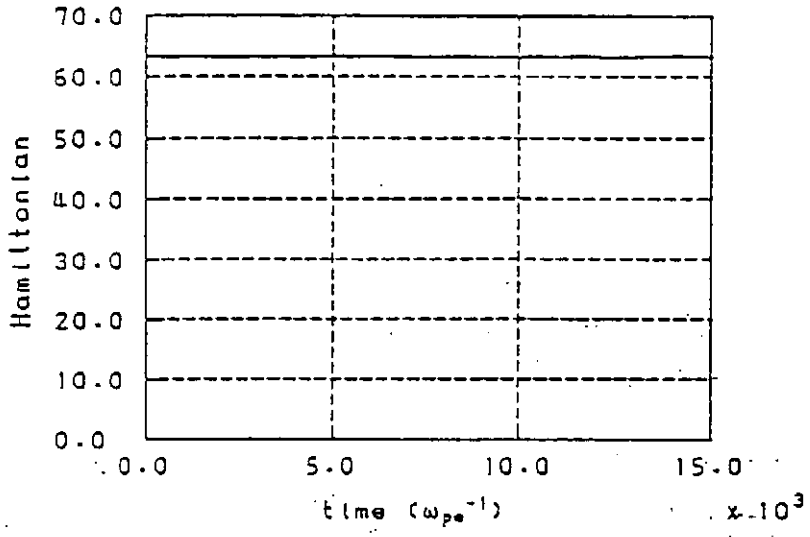
70.0
60.0
50.0
40.0
30.0
20.0
10.0
0.0
Hamiltonian
0.0
5.0
10.0
15.0
time (ωpe⁻¹)
x 10³

Fig. 1

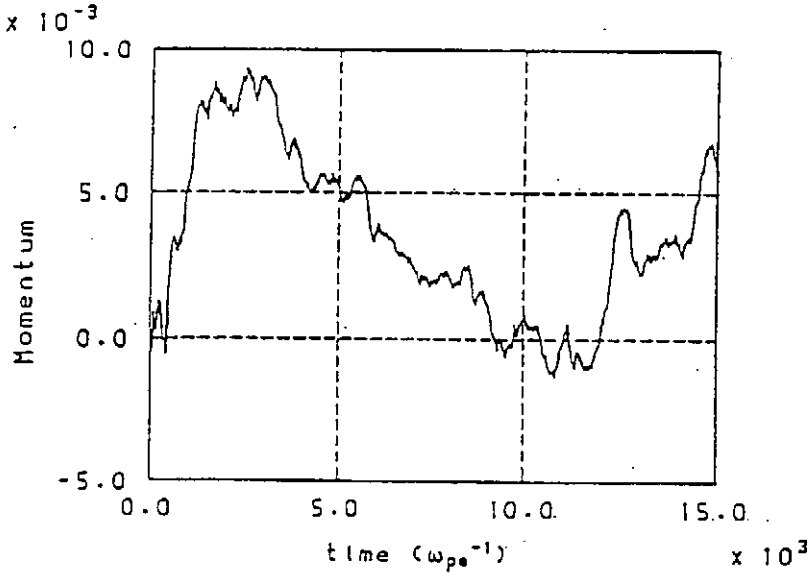
x 10⁻³
10.0
5.0
0.0
-5.0
Momentum
0.0
5.0
10.0
15.0
time (ωpe⁻¹)
x 10³

Fig. 2

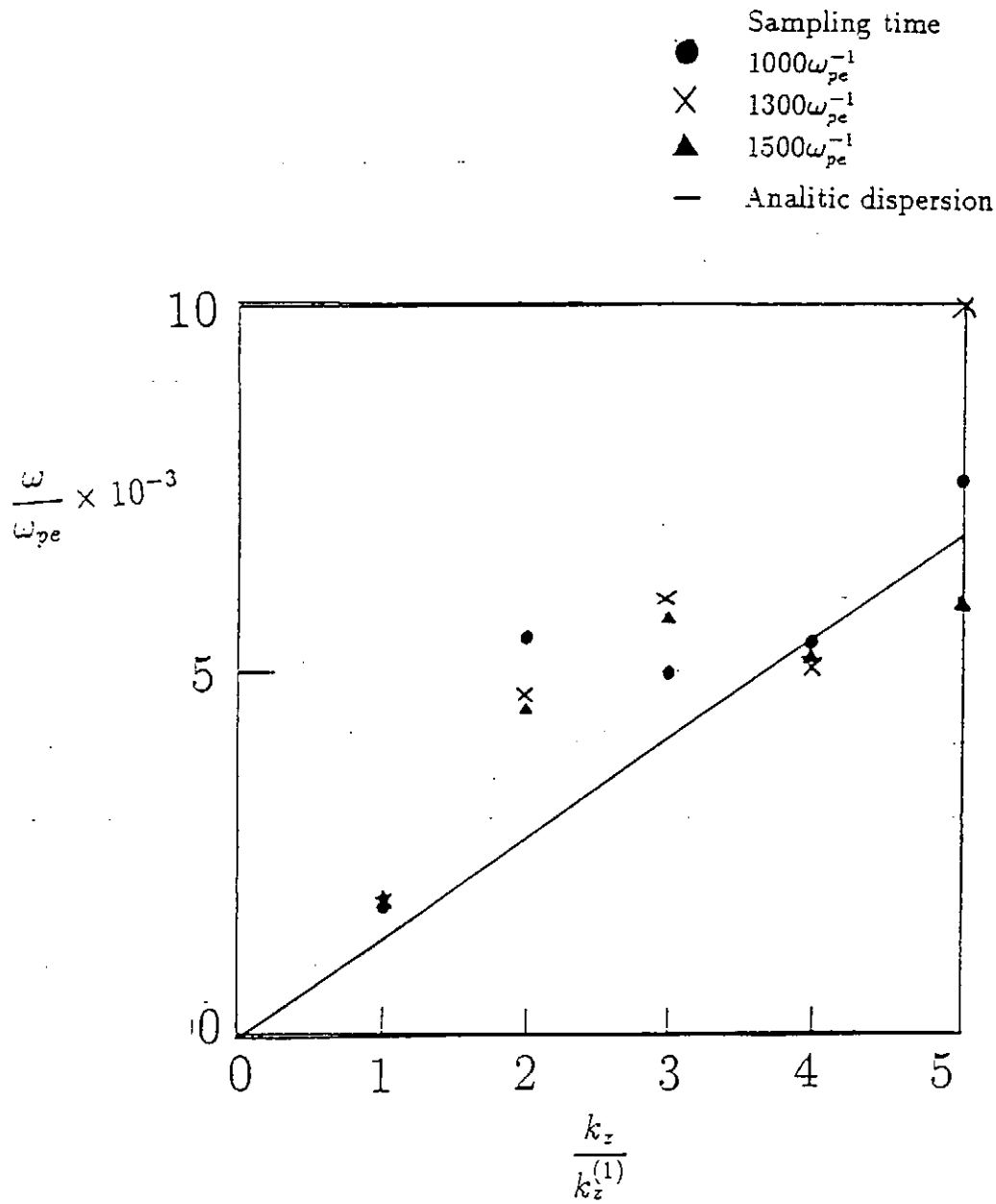
Sampling time
$1000\omega_{pe}^{-1}$
$1300\omega_{pe}^{-1}$
$1500\omega_{pe}^{-1}$
Analitic dispersion
10
5
0
$\frac{\omega}{\omega_{pe}} \times 10^{-3}$
0
1
2
3
4
5
$\frac{k_z}{k_z^{(1)}}$

Fig. 3

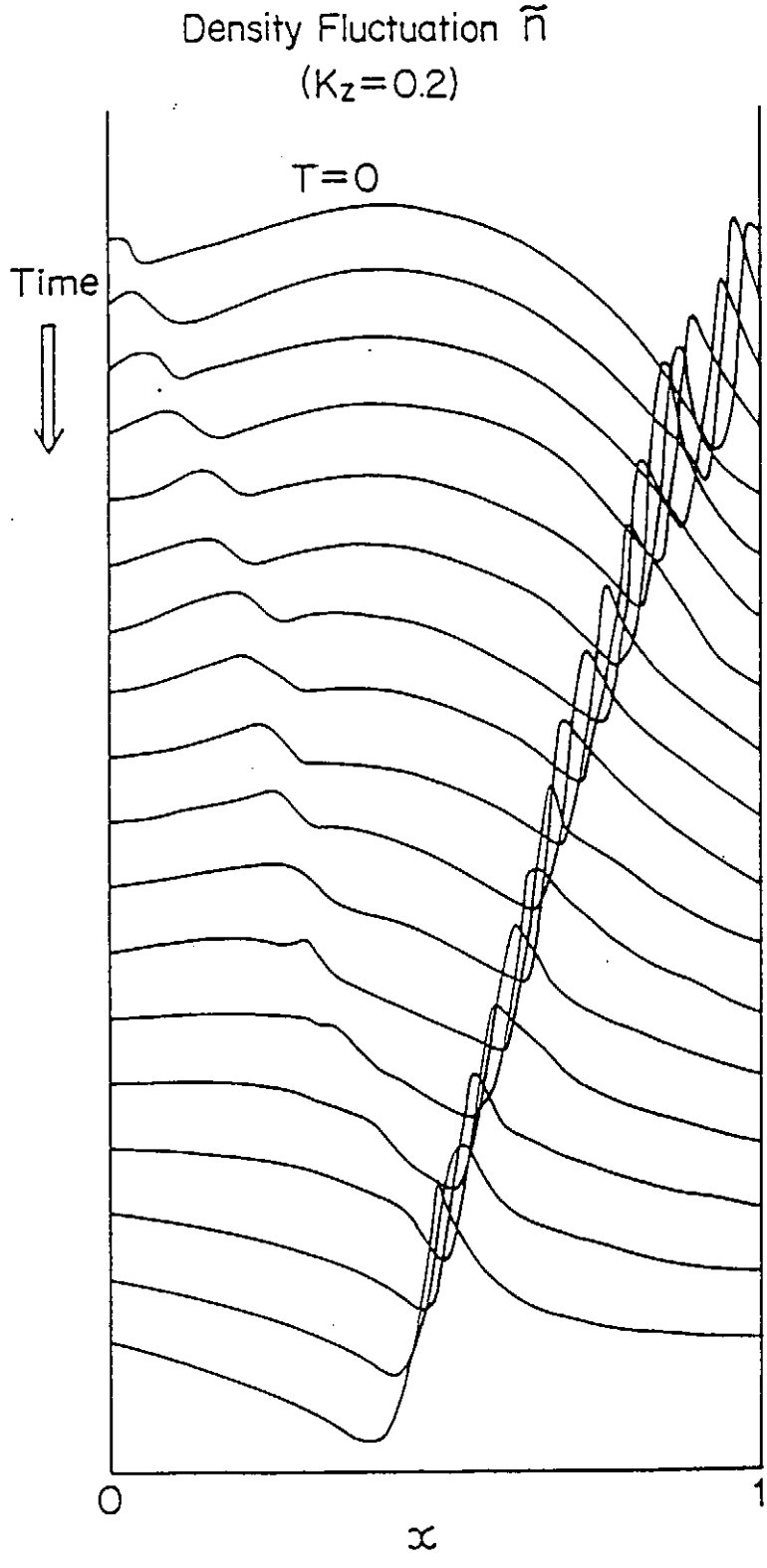

Fig. 4

VII. Basic Theories

A D-He^3 Fusion Reactor Based on Dipole Magnetic Field

Akira Hasegawa

AT & T Bell Laboratories
Murray Hill, New Jersey 07974

ABSTRACT

An innovative fusion reactor suitable for D-He^3 fuel is proposed based on a dipole magnetic field produced by a simple one turn coil with $\lesssim$ 16T near field intensity. The equilibrium plasma whose phase space density satisfies $\partial f_0(\mu, J, \psi)/\partial\psi = 0$, where ψ is the flux function, has a steep enough pressue profile for an efficient fusion reaction yet is stable for low frequency instabilities to local beta exceeding unity. The semi-open field configuration is particularly suitable for D-He^3 reactions.

A magnetic confinement scheme for D-He^3 requires a configuration which can provide a stable plasma confinement for beta (ratio of plasma to magnetic field energy density) near unity with no or little anomalous transport loss. It is further desirable to have an open configuration such that charged particles of the fusion product can be readily extracted for an efficient energy conversion.

The dipole magnetic field configuration proposed here suffices these requirements[1]. Figure 1 shows a schematic diagram of such a reactor. The magnetic field is produced by a properly shielded one turn super-conducting coil which is magnetically floated or mechanically supported in such a way that the confinement field lines do not cross the support. The plasma is produced primarily from the source at the wall by radially inward diffusion induced by RF fields with frequencies tuned at azimuthal drift frequencies, $\bar{\omega}_d$ (μ, ε, ψ) ($\simeq$ 1kHz) of the plasma which breaks the third adiabatic invariant ψ, where μ is the magnetic moment and ε is the particle energy.

Let us first discuss the plama physics issue. The plasma produced here has an intrinsic phase space density satisfying $\partial \hat{f}_0 (\mu, J, \psi) / \partial \psi = 0$ where $J(= \oint v_\parallel d\ell)$ is the second adiabatic invariant. The corresponding equilibrium density, n(r) perpendicular and parallel pressures $P_\perp(r)$ and $P_\parallel(r)$ are given respectively by

$$n = \int \hat{f}_0(\mu, J) \frac{B}{v_\parallel \oint \frac{d\ell}{v_\parallel}} d\mu dJ \propto \frac{B}{\ell} \tag{1}$$

$$P_\perp = \int \mu B \hat{f}_0(\mu, J) \frac{B}{v_\parallel \oint \frac{d\ell}{v_\parallel}} d\mu dJ \propto \frac{B^2}{\ell} \tag{2}$$

$$P_{\parallel} = \int m v_{\parallel}^2 \hat{f}_0(\mu, J) \frac{B}{v_{\parallel} \oint \frac{d\ell}{v_{\parallel}}} d\mu dJ \propto \frac{B}{\ell^3} \tag{3}$$

where ℓ (B, ψ) is the lengths of the field line, $v_{\parallel}$ is the parallel component of the particle velocity and the J conservation is assumed. For a low β plasma, B is approximately given by the vacuum dipole field,

$$\mathbf{B} = \nabla\psi \times \nabla\phi ; \ \psi = \frac{M\sin^2\theta}{r} \tag{4}$$

thus for a low β plasma, $n \sim r^{-4}$, $P_{\perp} \sim r^{-7}$ and $P_{\parallel} \sim r^{-6}$.

Collisions would isotropize the pressure. If the inward diffusion is made adiabatically, the plasma pressure would vary, $P \sim V^{-\gamma}$, where γ (= 5/3) is the adiabatic constant and V (= $\int d\ell/B$) is the flux tube volume with a constant total flux, then $P \sim r^{-4\gamma} \sim r^{-20/3}$. Since the fusion reaction rate is proportional to p^2, the reaction occurs only near the core region even if the plasma is extended to a large radius. We note that the centrally peaked density and pressure profiles even for $\partial \hat{f}_0/\partial\psi = 0$ are a unique consequence of the dipole field, i.e., in a toroidal field $\partial \hat{f}_0/\partial\psi = 0$ gives a practically flat distribution (no confinement).

The equilibrium isotropic pressure distribution is given by $p(\psi)$ while $\psi \simeq M\sin^2\theta/r$. Thus if $P \sim r^{-20/3} \sim \psi^{20/3}$, the equilibrium plasma pressure is concentrated near the equatorial plane,

$$P(\theta) \sim \sin^{40/3}\theta \tag{5}$$

Instabilities at $\omega \sim \omega_d$ can be studied by means of the phase space distribution function $\hat{f}(\mu, J, \psi, \phi)$ which satisfies [2],

$$\frac{\partial \hat{f}}{\partial t} + \dot{\phi} \frac{\partial \hat{f}}{\partial \phi} + \dot{\psi} \frac{\partial \hat{f}}{\partial \psi} = 0 , \tag{6}$$

where

$$\dot{\phi} = \left. \frac{\partial H}{\partial \psi} \right|_{\mu, J} \quad \dot{\psi} = - \left. \frac{\partial H}{\partial \phi} \right|_{\mu, J} , \tag{7}$$

$$H = \mu B + \frac{1}{2} m v_{\parallel}^2 + e\Phi. \tag{8}$$

We consider an electromagnetic perturbations, $\delta\phi$, $\delta\psi$ and δB. It is immediately clear from Eq.(6) that the corresponding perturbed distribution function δf is identically zero if the equilibrium distribution function $f_0(\mu, J)$ does not depend on ψ. This fact guarantees no instability based on wave-particle interactions at $\omega \sim \omega_d$, thus no anomalous cross ψ diffusion[3]. Furthermore the electrostatic interchange instability is absent for this equilibrium[4,5].

Magnetohydrodynamic (MHD) ballooning instabilities can still be excited since $\omega_* f_0/\bar{\omega}_d = -\varepsilon \tau_b \partial \hat{f}_0/\partial J > 0$ with $\tau_b = \oint d\ell/|v_{\parallel}|$, ω_* the diamagnetic drift frequency and $f_0 = f_0(\mu, \varepsilon, \psi)$. However, the beta limit due to the MHD ballooning is shown to exceed unity [6,7]. These facts differ significantly from toroidal confinement schemes where generally $\bar{\omega}_d/\omega_* \sim a/R << 1$ while $\ell/\Delta\ell \simeq 1$. The stable plasma equilibrium in a dipole magnetic field even for $\beta >> 1$ has in fact been observed in the Jovian magnetosphere[8].

The reactor design is being performed and will be published elswhere.

REFERENCES

[1] A.HASEGAWA, Comments on Plasma Phys. Contr. Fusion 11, 147 (1987).

[2] R.J.HASTIE, J.B.TAYLOR and F.A.HAAS, Ann Phys. 41, 302 (1967).

[3] C.S.LIU, Phys. Fluids 12, 1489 (1969).

[4] B.B.KADOMTSEV, Review of Plasma Physics, Ed. by M.A.Leontovich, Consultant Bureau, New York, 1966 p.170.

[5] P.H.RUTHERFORD and E.A.FRIEMAN, Phys. Fluids, 11, 252 (1968).

[6] T.M.ANTONSEN, Jr., and Y.C.LEE, Phys. Fluids 25, 132 (1982), J.W. VAN DAM, M.N.ROSENBLUTH and Y.C.LEE, Phys. Fluids 25, 1349 (1982).

[7] L.CHEN and A HASEGAWA, to be published.

[8] N.F.NESS, M.H.ACUNA, R.P.LEPPING, L.F.BRIAGA, K.W.BEHANNON, and F.M.NEUBAUER, Science 206, 966 (1979) also, S.M.KRIMIGIS, T.P.ARMSTRONG, W.I.AXFORD, C.O.DISTROM, C.Y.FAN, G.GLOECKLER, L.J.LANZEROTTI, E.P.KIETH, R.D.ZWICKLY, J.F.CARBARY and V.C.HAMILTON, Science 206, 977 (1979).

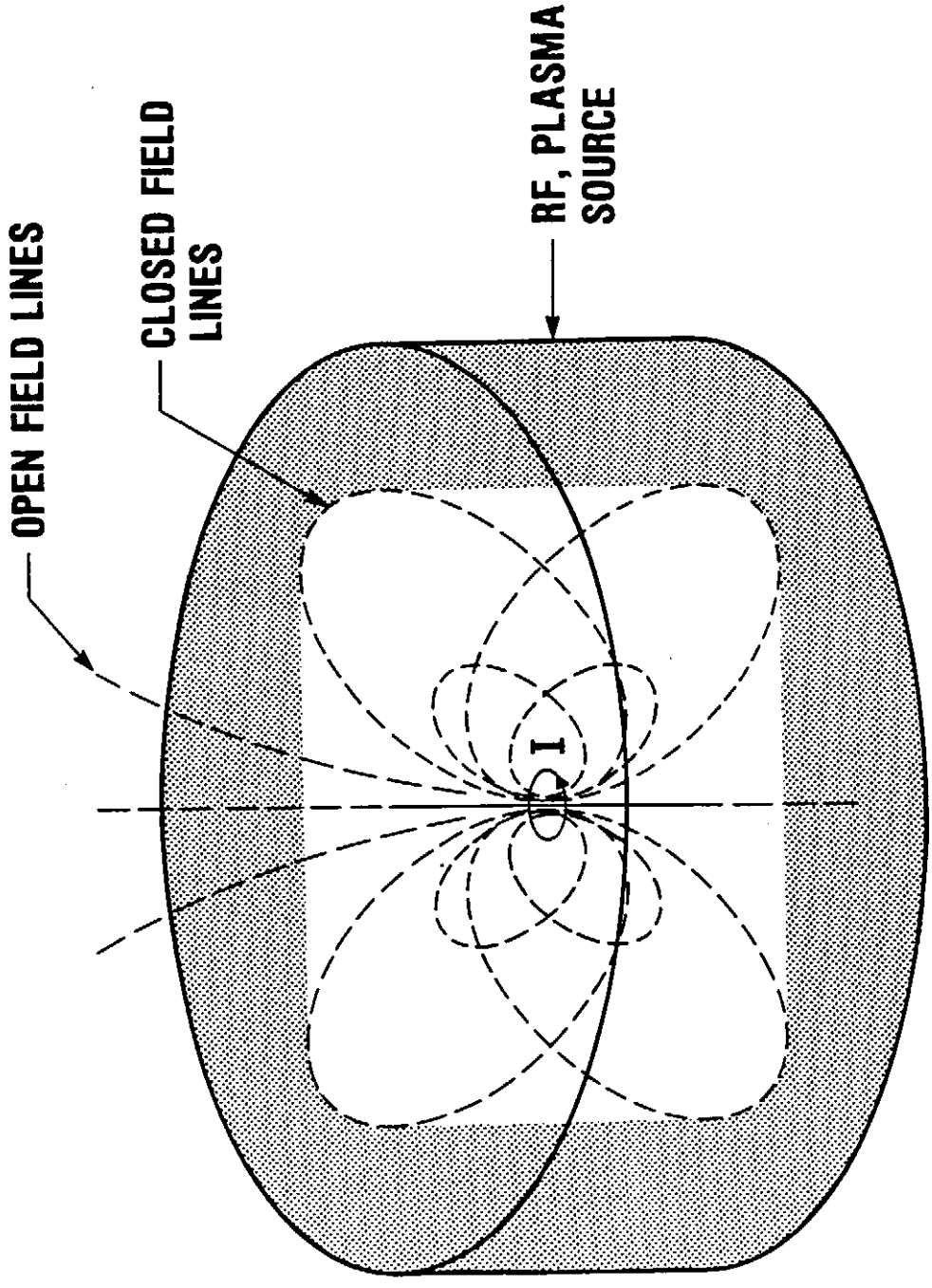
OPEN FIELD LINES
CLOSED FIELD LINES
RF, PLASMA SOURCE

Long-Time Correlations and Expansion-Rate Spectra of Chaos in Hamiltonian Systems

Takehiko HORITA, Hiroki HATA, Ryuji ISHIZAKI and Hazime MORI

Department of Physics, Kyushu University 33, Fukuoka 812

The repeated sticking of a chaotic orbit to critical tori with an inverse-power distribution of sticking times is shown to produce a universal spectrum of expansion rates Λ of nearby orbits with a linearity with zero slope for $0 < \Lambda < \Lambda^{\infty}$ (=Liapunov number), representing the intermittent switching between chaotic sea and chaos border.

Chaos has revealed its fascinating statistical scaling properties[1] in recent studies. Indeed, in order to characterize chaos, various important concepts have been proposed by generalizing statistical mechanics for dissipative and conservative (dynamical) systems.[2] In this paper, we shall discuss chaos in conservative systems from such a new viewpoint by showing results of numerical experiments for the standard map.

A typical example of two-dimensional area-preserving maps is the standard map[3]

$$X_{t+1} = \begin{pmatrix} \theta_{t+1} \\ J_{t+1} \end{pmatrix} = F(X_t) = \begin{pmatrix} \theta_t + J_{t+1} \pmod 1 \\ J_t - (K/2\pi)\sin(2\pi\theta_t) \end{pmatrix} \tag{1}$$

with a control parameter K. We take three values of parameter K; K =10.053, 6.9115, and 3.8600. These values are greater than the critical value $K_c = 0.971635406$ for the breakup of the last KAM torus,[4] so that, in the phase space (θ, J), the stochastic sea containing

the hyperbolic fixed point (θ^*, J^*) =(0.5, 0.0) spreads over the whole region of J, and a cloud of phase points initially distributed around (θ^*, J^*) exhibits a diffusive motion over the whole region of J, as shown in Fig.1. At $K = 10.053$, there are no visible tori in the time scale of the numerical experiments. At $K = 6.9115$, there are regular orbits called the accelerator modes.[5] At $K = 3.8600$, there are tori around the elliptic fixed point (0, 0). The map (1) is periodic in J with period 1 and our interest is restricted to the expansion rates of nearby orbits. Therefore, we take mod 1 also for J in (1) so that the phase space is closed between 0.5 and -0.5.

For a chaotic orbit X_t of F, let $\mu_n^{\pm}(X_0)$ be the eigenvalues of the Jacobian matrix $DF^n(X_0)$ with $|\mu_n^+|>|\mu_n^-|$, where $\mu_n^-\mu_n^+ =1$, and define the coarse-grained expansion rate

$$\Lambda_n(X_0) \equiv (1/n)\log|\mu_n^+(X_0)|. \tag{2}$$

We assume that there is a natural invariant measure of the stochastic sea containing the hyperbolic fixed point (θ^*, J^*). Then, in the limit $n \to \infty$, $\Lambda_n(X_0)$ converges to a Liapunov exponent $\Lambda^\infty > 0$ that is independent of X_0 for almost all X_0 with respect to the natural invariant measure. In Fig. 2, $\Lambda_n(X_0)$ for $K = 6.9115$ is plotted against n, which shows that $\Lambda_n(X_0)$ converges to a positive Liapunov exponent $\Lambda^\infty \simeq 1.26$, but the convergence is very slow. In order to see the slowness of the convergence, we have calculated the variance of $S_n(X_0) \equiv n\Lambda_n(X_0)$. Figure 3 shows the plot of the variance $< (S_n - n\Lambda^\infty)^2 >$ against n for $K = 6.9115$, where $< \cdots >$ denotes the long-time average

$$< G(X_0) > \equiv \lim_{N\to\infty}(1/N)\sum_{t=0}^{N-1} G(X_t). \tag{3}$$

Thus the variance turns out to grow as $< (S_n - n\Lambda^\infty)^2 > \propto n^\nu$ with $\nu \simeq 1.4$. Grassberger and Kantz[6] have shown numerical results for several values of K in a range $1 \lesssim K < 5$,

which indicate $1.15 < \nu < 1.8$. This anomalous grow is due to the repeated sticking to the accelerator mode tori. Indeed, if we take two boxes around the accelerator mode tori as shown in Fig. 1(b) and define $M_n(X_0) \equiv \sum_{t=0}^{n-1} \chi(X_t)$ where χ is the characteristic function of the two boxes, i.e., $\chi(X)$ takes 1 or 0 according as X is in one of the two boxes or not, then the variance of $M_n(X_0)$ obeys $< (M_n - < M_n >)^2 > \propto n^{\nu'}$ with $\nu' \simeq \nu \simeq 1.4$, as shown in Fig. 4.

Let τ be the duration of the sticking to the tori and $f(\tau)$ be the distribution function of τ. It is known that $f(\tau)$ exhibits a power-law decay[7),8)]

$$f(\tau) \propto \tau^{-1-\beta}, \quad (1 < \beta < 2). \tag{4}$$

Then the probability that a segment of a chaotic orbit sticks longer than n is given by

$$W(n) \equiv \int_n^\infty \tau f(\tau) d\tau / (\bar{\tau} + \bar{\tau}_c) \propto n^{-(\beta-1)} \tag{5}$$

for large n, where $\bar{\tau} = \int_1^\infty \tau f(\tau) d\tau$ and $\bar{\tau}_c$ is the average duration for staying in the chaotic sea. Since $\Lambda_n(X_0) \simeq 0$ and $M_n(X_0) = n$ around the tori, the contribution of the tori to the variances of $S_n(X_0)$ and $M_n(X_0)$ is given by $(n\Lambda^\infty)^2 W(n)$ and $(n - < M_n >)^2 W(n)$, respectively, leading to

$$< (S_n - n\Lambda^\infty)^2 > \propto n^{3-\beta}, \qquad < (M_n - < M_n >)^2 > \propto n^{3-\beta} \tag{6}$$

with $\nu = \nu' = 3 - \beta$, because $3 - \beta > 1$. Figures 3 and 4 indicate $\beta \simeq 1.6$ for the accelerator mode tori at $K = 6.9115$, leading to long-time correlations of chaos.

The probability density for $\Lambda_n(X_0)$ to take a value around Λ for given n is given by $P(\Lambda; n) \equiv < \delta(\Lambda_n(X_0) - \Lambda) >$, where $\delta(g)$ denotes the δ-function of g. The coarse-grained expansion rate $\Lambda_n(X_0)$ can also be defined in a local form by using the unit vector $\mathbf{u}_1(X_t)$

tangent to the local unstable manifold at X_t as follows:[2)]

$$\Lambda_n(X_0) \equiv (1/n) \sum_{t=0}^{n-1} \lambda_1(X_t) \tag{7}$$

where $\lambda_1(X_t) \equiv \log |DF(X_t)\mathbf{u}_1(X_t)|$. For large n, the eigenvector of $DF^n(X_0)$ with the eigenvalue $\mu_n^+(X_0)$ becomes tangent to $\mathbf{u}_1(X_0)$ due to the orbital instability, so that the two quantities defined by (2) and (7) are approximately equal to each other for large n. Furthermore, the local form (7) suggests that the Λ dependence of $P(\Lambda; n)$ scales with respect to n as[2)]

$$P(\Lambda; n) \propto \exp\{-n\psi(\Lambda)\} \tag{8}$$

for large n, where spectrum $\psi(\Lambda)$ is a concave function of Λ independent of n. Indeed, for chaotic attractors of dissipative systems, $P(\Lambda; n)$ obeys (8) and $\psi(\Lambda)$ is very useful.[2)] We expect that $\psi(\Lambda)$ is given by $\psi_n(\Lambda) \equiv -(1/n)\log\{P(\Lambda; n)/P(\Lambda^\infty; n)\}$ in the limit $n \to \infty$. Figure 5 shows $\psi_n(\Lambda)$ for n =100, 500, and 1000, where we have taken $N = 10^6$ in the long-time average (3). This indicates that the scaling (8) holds for $K = 10.053$ with $\psi(\Lambda) = \psi_\infty(\Lambda)$ which is quadratic around Λ^∞. For $K = 6.9115$ and $K = 3.8600$, $\psi_n(\Lambda)$ converges to zero for $0 < \Lambda \leq \Lambda^\infty$ in the limit $n \to \infty$, and the scaling (8) holds for $\Lambda \geq \Lambda^\infty$ with $\psi(\Lambda) = \psi_\infty(\Lambda)$. This $\psi_\infty(\Lambda)$ leads to a q-phase transition between $\Lambda = \Lambda^\infty$ and $\Lambda = 0$.[2)] $\psi_n(\Lambda)$ for $\Lambda_n(X_0)$ defined by (7) instead of (2) is shown in Fig. 5(d) with the same condition as Fig. 5(b). These two are the same except for detailed structures.

One way of justifying $\psi_\infty(\Lambda) = 0$ for $0 < \Lambda < \Lambda^\infty$ is the following. Let $\{X_0, X_1, \cdots, X_{n-1}\}$ be an orbit which stays around the tori for duration τ. Then $\Lambda_n(X_0) \simeq \{(n-\tau)/n\}\Lambda^\infty$. The probability that such orbits with $0 < \Lambda_n(X_0) \leq \Lambda < \Lambda^\infty$ appear is given by

$$\Pr\{\Lambda_n(X_0) \leq \Lambda\} \geq \int_{n(1-\Lambda/\Lambda^\infty)}^{n} \tau f(\tau) P(\Lambda^\infty; n-\tau) d\tau / (\bar{\tau} + \bar{\tau}_c) + W(n), \tag{9a}$$

$$> P(\Lambda^\infty; n)\{W(n(1-\Lambda/\Lambda^\infty)) - W(n)\} + W(n), \tag{9b}$$

$$\propto P(\Lambda^\infty; n) n^{-(\beta-1)}\{(1-\Lambda/\Lambda^\infty)^{-(\beta-1)} - 1\}. \tag{9c}$$

Therefore, $\psi_n(\Lambda) \lesssim \log n/n \to 0$ as $n \to \infty$ for $0 < \Lambda < \Lambda^\infty$.

Inserting (7) into $S_n(X_0) = n\Lambda_n(X_0)$ of (6), we obtain[2)]

$$< (S_n - n\Lambda^\infty)^2 >= nC_0 + 2\sum_{t=1}^{n-1}(n-t)C_t, \tag{10}$$

$$C_t \equiv < \hat{\lambda}_1(X_t)\hat{\lambda}_1(X_0) > \propto t^{-(\beta-1)} \quad \text{for} \quad t \gg 1, \tag{11}$$

where $\hat{\lambda}_1(X_t) \equiv \lambda_1(X_t) - \Lambda^\infty$. Thus the repeated sticking of a chaotic orbit to critical tori turns out to reduce to the long-time correlation (11). This is the second merit of the local form (7).

Let us divide the stochastic sea into two regions; one is a chaos border region encircling the tori and the other is the chaotic sea. Then the linear part of $\psi(\Lambda)$ between $\Lambda = 0$ and $\Lambda = \Lambda^\infty$ is formed by the intermittent switching motion between the chaos border region and the chaotic sea.[2)] The events that the phase points enter in the chaotic sea are considered to be the recurrent events, and the distribution of the recurrence times is given by $f(\tau)$ in (4). In the chaotic sea, the time correlations of chaotic orbits are lost so fast that Feller's theorem of recurrent events[9)] would be applicable. This states that if the integrated recurrence-time distribution $F(\tau)$ obeys $1 - F(\tau) \sim \tau^{-\beta}$, $(1 < \beta < 2)$, then the number N_n of the events which occur in the time interval n obeys

$$\Pr\{N_n \geq (n/\mu) - (b_n x)/\mu^{(\beta+1)/\beta}\} \to G_\beta(x) \quad \text{as} \quad n \to \infty, \tag{12}$$

where $1 - F(b_n) \sim 1/n$, (i.e., $b_n \propto n^{1/\beta}$), μ is the mean recurrence time, and $G_\beta(x)$ is a quasi-stable distribution of index β. This theorem states about the small-fluctuation

properties around the average of N_n. Fluctuations of $S_n(X_0) = n\Lambda_n(X_0)$ would obey a similar law. Therefore, we expect that

$$< \Theta(S_n - n\Lambda^\infty)(S_n - n\Lambda^\infty)^2 > \propto n^{2/\beta}, \quad (2/\beta < 3 - \beta), \tag{13}$$

$$\psi(\Lambda) \propto (\Lambda - \Lambda^\infty)^{\beta/(\beta-1)} \quad \text{for} \quad 0 < (\Lambda - \Lambda^\infty)/\Lambda^\infty \ll 1, \tag{14}$$

where $\Theta(x)$ is the step function, i.e., $\Theta(x) = 0$ if $x < 0$ and $\Theta(x) = 1$ otherwise. In Fig. 6, $< \Theta(S_n - n\Lambda^\infty)(S_n - n\Lambda^\infty)^2 >$ is plotted against n for $K = 6.9115$, which is consistent with $\beta \simeq 1.6$.

One of the most important problems in area-preserving maps is to determine exponent β in (4). Meiss and Ott[8] have proposed a self-similar Markov tree model. In this model, β is determined by $\sum_{j=1}^{M} w_j \varepsilon_j^{-\beta} = 1$, where $0 < w_j < 1$, $0 < \varepsilon_j < 1$ are constants characterizing the self-similarity of hierarchy of the cantori, M being the number of relevant island families, and the total area of the stochastic sea is proportional to $\sum_{k=0}^{\infty}(\sum_{j=1}^{M} w_j \varepsilon_j^{-1})^k$. Hence $\sum_{j=1}^{M} w_j \varepsilon_j^{-1} < 1$, leading to $\beta > 1$. The condition $\beta > 1$ is very important; if it is broken, then the natural invariant measure cannot be constructed. We have another example which shows $\beta > 1$. Let us consider an area-preserving map F of $S = [0,\ 1] \times [0,\ 1]$ onto itself. $F = F_1$ for $S_1 = [0,\ 1/2] \times [0,\ 1]$ is defined by $x' = x + (2x)^z/2$, $y' = y/\{1 + z(2x)^{z-1}\}$ with $1 < z < \infty$, and $F = F_2$ for $S_2 = (1/2,\ 1] \times [0,\ 1]$ is an appropriate area-preserving map of S_2 into $S - F_1(S_1)$. The region around the line $x = 0$ is considered to be the chaos border region. F becomes the baker's transformation in the limit $z \to 1$ and the identity map in the limit $z \to \infty$ with an appropriate choice of F_2. The sticking times to the line $x = 0$ are distributed as $f(\tau) \propto \tau^{-1-\beta}$ with $\beta = z/(z-1)$ for $\tau \gg 1$, because the area of $S - F_1(S_1) = F_2(S_2)$ between $x = 0$ and $x = s$ is proportional to s^z for $0 < s \ll 1$.

Note that $\beta = z/(z-1) > 1$ for any finite z, which is a consequence of the area-preserving condition. Therefore we conjecture that $\beta > 1$ is also satisfied in the standard map.

In preparing this paper, we noticed that Sepúlveda, Badii and Pollak[10] have reported a similar result to Figs. 5(b) and 5(c) with $n = 100$ for the standard map with $K = 2$. Those figures with $n = 500$, 1000 are, however, more important in the present paper.

---

1) P.Bergé, Y.Pomeau and C.Vidal, *Order within chaos* (Wiley, New York, 1984).
H.G.Schuster, *Deterministic chaos* (VCH, Weinheim, 1988).

2) H.Mori, H.Hata, T.Horita and K.Kobayashi, Prog. Theor. Phys. Supplement **No.99** (1990), and references cited therein.

3) B.V.Chirikov, Phys. Rep. **52** (1979), 263.

4) J.M.Green, J. Math. Phys. **20** (1979), 1183.

5) Y.H.Ichikawa, T.Kamimura and T.Hatori, Physica **29D** (1987), 274.

6) P.Grassberger and H.Kantz, Phys. Lett. **113A** (1985), 167.
H.Kantz and P.Grassberger, Phys. Lett. **A123** (1987), 437; J. of Phys. **A21** (1988), L127.

7) C.F.F.Karney, Physica **8D** (1983), 360.
B.V.Chirikov and D.L.Shepelyansky, Physica **13D** (1984), 395.

8) J.D.Meiss and E.Ott, Phys. Rev. Lett. **55** (1985), 2741;Physica, **20D** (1986), 387.

9) W.Feller, Trans. Am. Math. Soc. **67** (1949), 98.
X.-J.Wang, Phys. Rev. **A39** (1989), 3214.

10) M.A.Sepúlveda, R.Badii and E.Pollak, Phys. Rev. Lett. **63** (1989), 1226.

Figure captions

Fig.1 Structure of phase space for (a) $K = 10.053$, (b) $K = 6.9115$, and (c) $K = 3.8600$, where 3×10^4 points initially distributed around the hyperbolic fixed point (0.5, 0) within distance 0.01 are plotted after 40 iterations. (a) There are no visible tori. (b) In the two boxes, there are accelerator mode tori. The structure in the left box is shown in (d). (c) There are tori around (0, 0). Orbits with 15 different initial points are also shown.

Fig.2 $\Lambda_n(X_0)$ versus n for $K = 6.9115$ with $X_0 = (0.501, 0)$.

Fig.3 $< (S_n - n\Lambda^\infty)^2 >$ versus n for $K = 6.9115$. The length N in the long-time average (3) is taken to be 10^6.

Fig.4 $< (M_n - < M_n >)^2 >$ versus n for $K = 6.9115$ with $N = 10^7$.

Fig.5 Expansion-rate spectrum $\psi_n(\Lambda)$ for (a) $K = 10.053$, (b) $K = 6.9115$, (c) $K = 3.8600$, and (d) $K = 6.0115$ for three n's; $n = 100(\times)$, $500(\triangle)$, $1000(\bigcirc)$ with $N = 10^6$. $\Lambda_n(X_0)$ is defined by (2) for (a), (b), and (c). On the other hand $\Lambda_n(X_0)$ is defined by (8) for (d).

Fig.6 $< \Theta(S_n - \Lambda^\infty)(S_n - n\Lambda^\infty)^2 >$ versus n for $K = 6.9115$ with $N = 10^6$.

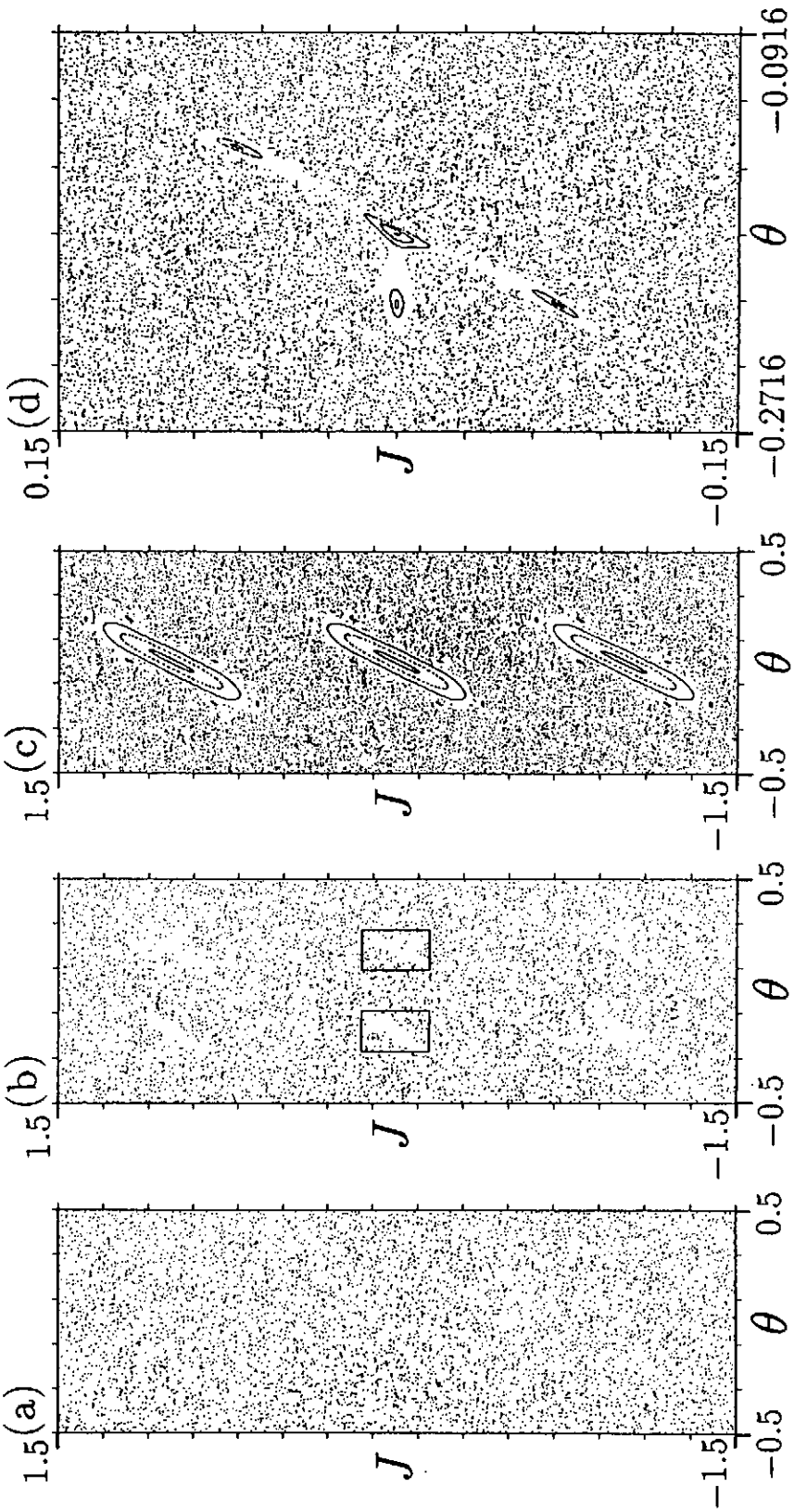
1.5
(a)
J
−1.5
−0.5
θ
0.5
1.5
(b)
J
−1.5
−0.5
θ
0.5
1.5
(c)
J
−1.5
−0.5
θ
0.5
0.15
(d)
J
−0.15
−0.2716
θ
−0.0916

Fig.1

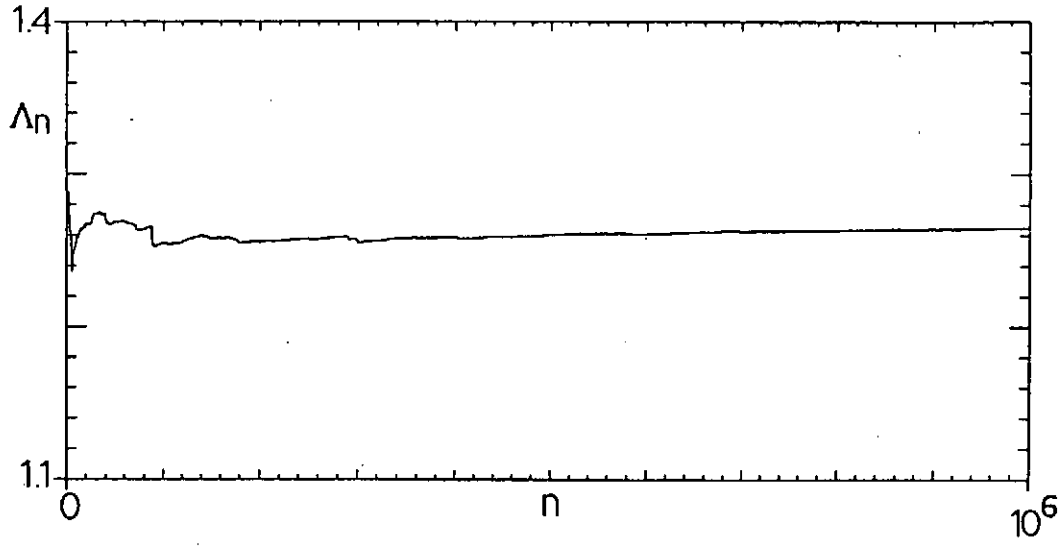
1.4
Λn
1.1
0
n
10^6

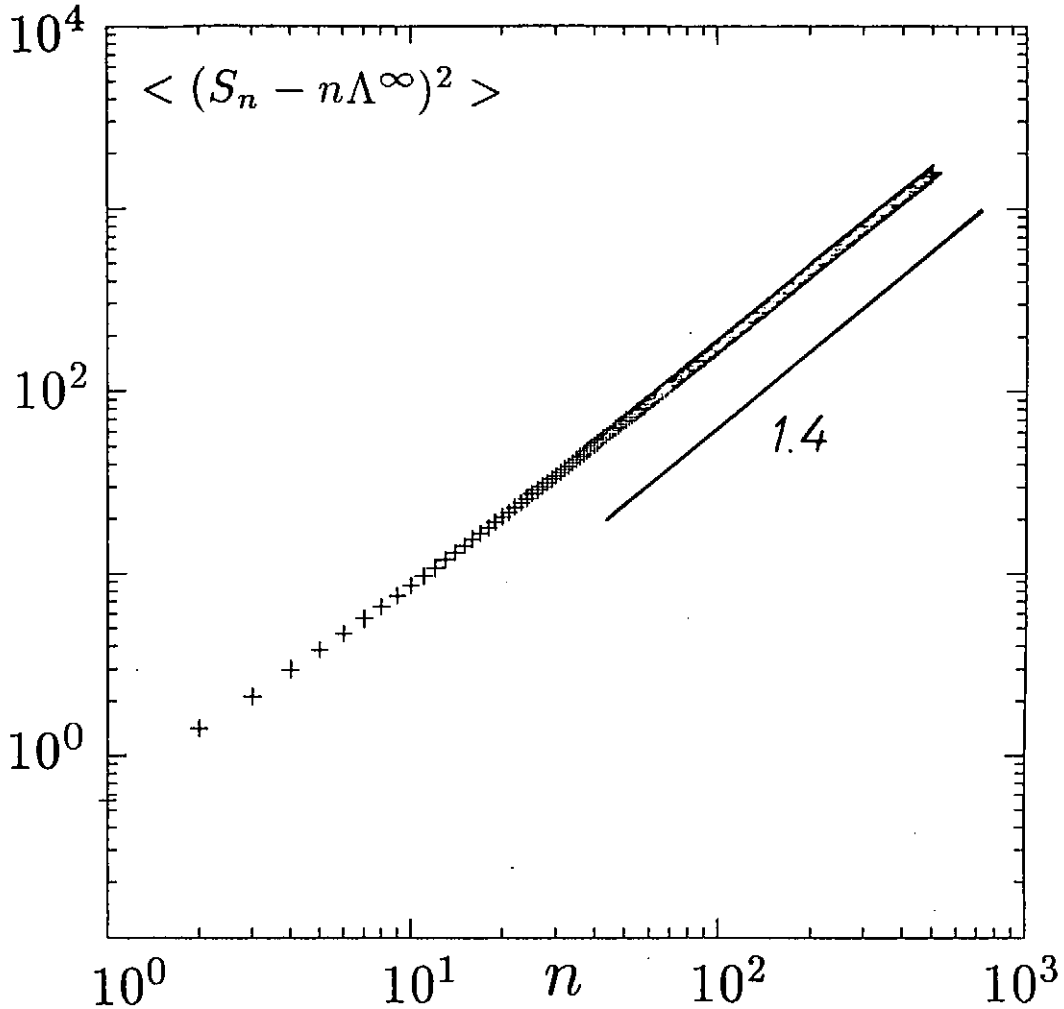

Fig.3

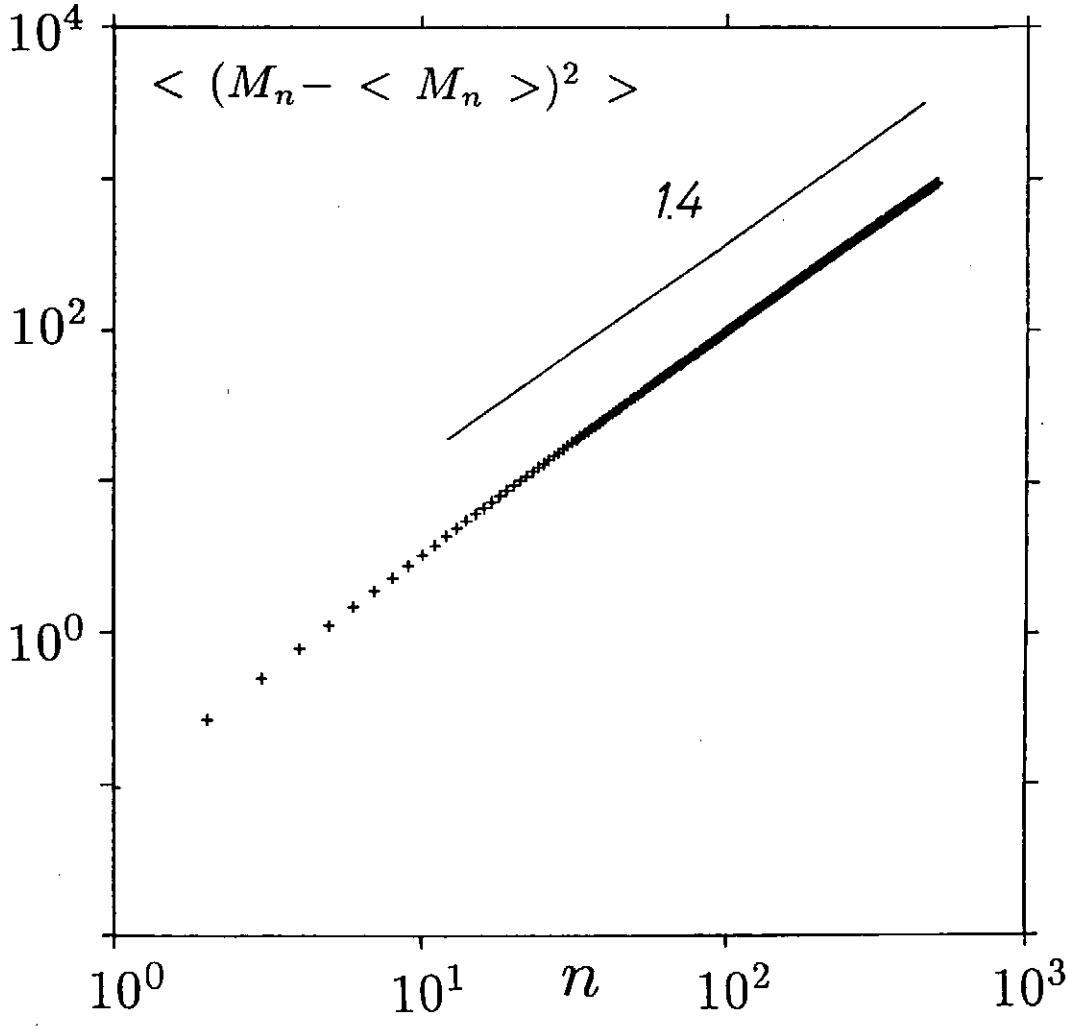

Fig.4

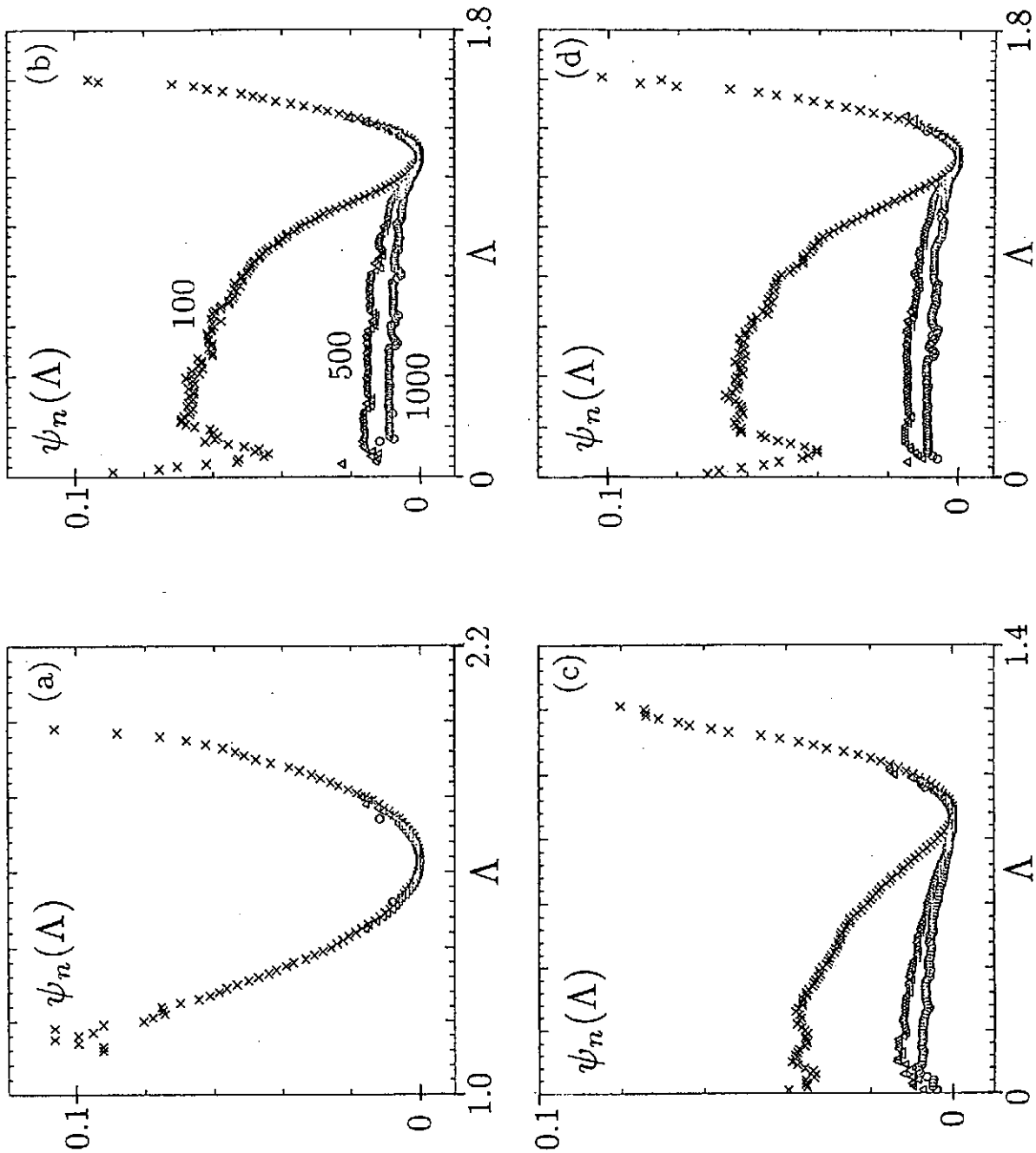

Fig.5

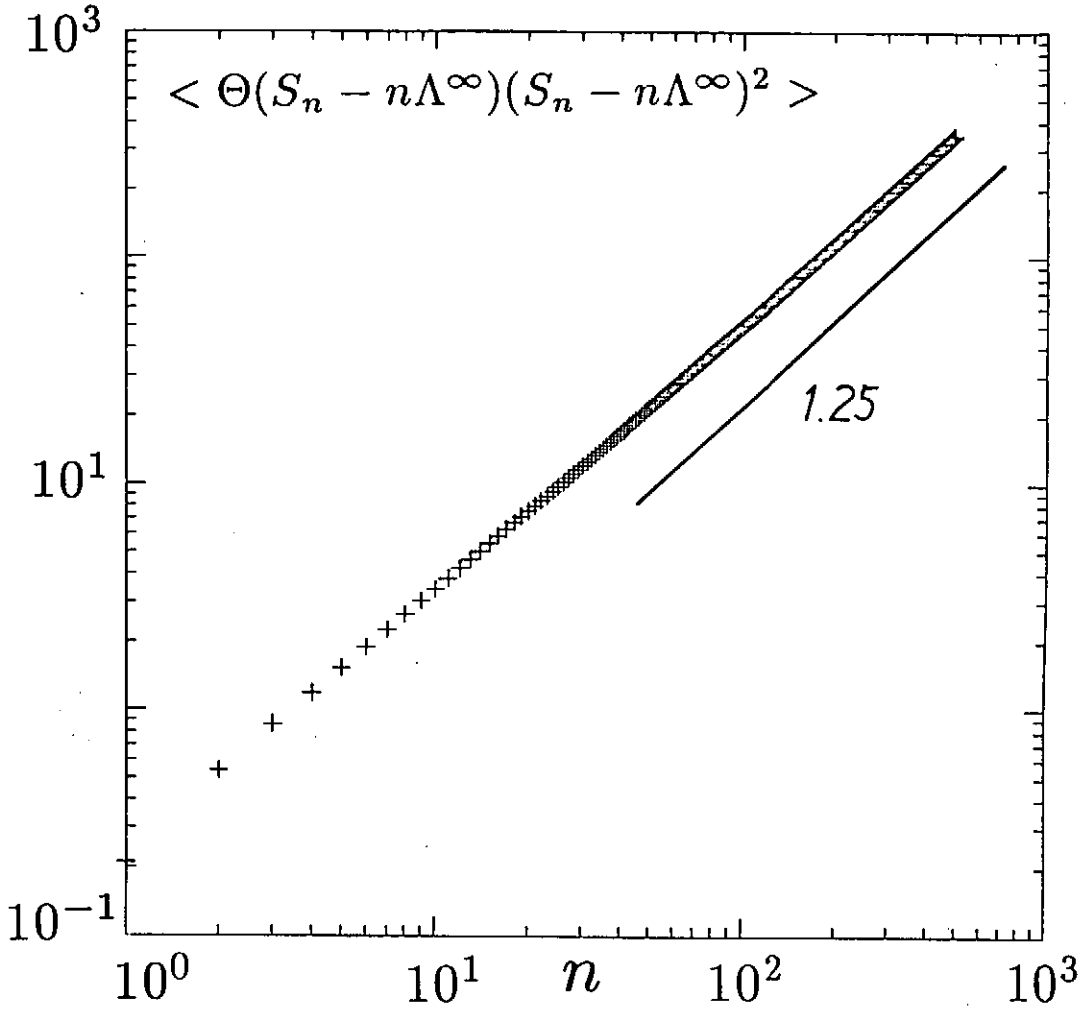
10^3
$< \Theta(S_n - n\Lambda^\infty)(S_n - n\Lambda^\infty)^2 >$
1.25
10^1
10^{-1}
10^0
10^1
n
10^2
10^3

Fig.6

CHARACTERISTICS METHOD IN DISSIPATIVE STRUCTURE THEORY

Zensho YOSHIDA
Department of Nuclear Engineering, The University of Tokyo
Hongo, Tokyo 113, JAPAN

Abstract. The characteristics method in the theory of partial differential equations has been discussed in its relation to the theory of dissipative structures. Non-characteristic Cauchy data related to the hyperbolic part of equilibrium equations characterizes intrinsic structures in the corresponding dynamical system. The concept of intrinsic structures introduced here gives a generalization of eigenfunctions. Some different examples of intrinsic structures in plasmas have been studied.

1. INTRODUCTION

The term "structure" is frequently used for many different meanings. Some of them seem to be rather "patterns" than structures. Be that as it may, structures are generally distributions of certain quantities. We may separate structures into two different classes; one is a class of "responses" of systems to external conditions, which we may call "extrinsic structures", and the other is a class of rather "intrinsic structures". Let us discuss explicit examples of structures in physics, and show the key issue of extrinsic and intrinsic structures.

A simplest example of an extrinsic structure is the distribution of temperature on a solid material, which is governed by the Poisson equation:

$$-\Delta u = f \quad \text{in } \Omega, \qquad u = 0 \quad \text{on } \partial\Omega,$$

where $\partial\Omega$ is the boundary of the domain Ω. An inhomogeneous boundary condition may be included in f by subtracting from u the extension, into the domain, of the boundary value. We obtain "the response" u to the heat distribution f by the relation

$$u = -\Delta^{-1} f.$$

An essential point is that we have the inverse Δ^{-1} of the elliptic operator Δ.

An intrinsic structure appears when we do not have a unique inverse of a governing operator. A typical example we see in quantum mechanics. The stationary quantum state is given by a Helmholtz-type equation

$$(H-\lambda)u = 0,$$

where H is the Hamiltonian. An intrinsic structure of the system is an eigenfunction that is characterized by the nonexistence of unique inverse of the operator $(H-\lambda)$. This point shows the basic difference between the extrinsic and intrinsic structures. In the next section, we give a mathematical classification of structure problems.

2. MATHEMATICAL EXPRESSION OF INTRINSIC STRUCTURES

Let us give a classification of steady-state equations for various systems from the viewpoint of partial-differential-equation (PDE) theory. Then, we will show that an intrinsic structure is characterized by Cauchy data related to the real characteristics of the hyperbolic PDE's.

A. Elliptic Systems

The Laplace and Poisson equations are the most typical steady-state PDE's. Physics examples described by this class of PDE's are electrostatic potential distributions, vector-potential distributions for static magnetic fields, steady-state stress distributions, steady-state temperature, density, and probability distributions in diffusion systems, etc. These are linear elliptic PDE's. Standard boundary-value problems are uniquely solvable, and give extrinsic structures.

B. Hyperbolic Systems

When the steady-state equations are of hyperbolic type, we should supply Cauchy data (initial data*) to integrate the equations. The Hamilton-Jacobi PDE's of classical mechanics,

$$\partial_t \phi + H(x, \partial_x \phi) = 0$$

is the most important example. The real characteristics are described by the corresponding characteristic and bi-characteristic ordinary differential equations (ODE's), viz., the Hamilton canonical ODE's

$$dx/dt = \partial_p H(x,p), \quad dp/dt = -\partial_x H(x,p).$$

*Here, the term "initial" might be confusing. It implies purely mathematical classification of integration data, and is not necessarily related to the physical time.

The Liouville equation

$$\partial_t u + \{u, H\} = 0$$

has the characteristic ODE's that is just the Hamilton canonical ODE's, so that it is an alternative expression of classical dynamics. The dependent variable u stands for the particle density in the phase space (x,p). When the Hamiltonian is temporally-homogeneous, and when we consider a uniform particle flow along each characteristics*, ∂_t drops, and the steady state is given by a nontrivial solution to the equation

$$\{u, H\} = 0.$$

The structure of this system is characterized by the Cauchy data related to the real characteristics of the equation. The system has an intrinsic structure which is determined internally by the Cauchy data.

C. Elliptic-Hyperbolic Systems

Elliptic-hyperbolic mixed systems are mostly general and interesting model equations. The equilibrium is not fully determined by external (boundary) data, but Cauchy data should be also supplied to find an equilibrium. It is usually very hard to develop a general mathematical theory for an elliptic-hyperbolic system when the characteristics is dependent to the dependent variables. The steady-state Euler equations of ideal incompressible flow is a typical example of such equilibrium problems;

$$(v,\text{grad})v + \text{grad}\, p = 0, \quad \text{div}\, v = 0.$$

Characteristic equation for this system is

$$(\text{grad}\, \psi)^2 \cdot (v,\text{grad}\, \psi)^2 = 0,$$

which says the system is two-elliptic and two-hyperbolic, and the characteristics if the flow curves themselves.

The MHD equilibrium equations

$$-(B,\text{grad})B + \text{grad}\,(\mu_0 p + B^2/2) = 0, \quad \text{div}\, B = 0$$

are also two-elliptic and two-hyperbolic PDE's. With giving Cauchy data, the system reduces to a Helmholtz-type PDE, which characterizes an intrinsic structure; see Sec. 3-B.

* When the characteristic curves open to the boundary, we consider a temporally-constant particle source.

Another important example in plasma physics is the electrostatic problem related to the ion sheath and ion acoustic solitons. When we consider collision-less ions and thermalized electrons, the system is described by the stationary Liouville equation (hyperbolic; see Sec. 2-B) coupled with the Poission equation (elliptic; see Sec. 2-A) for the electrostatic potential. Considering one dimensional problem, and assuming temporally constant ion source from the boundary that is origin of the real characteristics, we may reduce the model equations to the Bohm equation that is a nonliner Helmholtz-type equation. The intrinsic structure of the electrostatic plasma potential is discussed in the following section.

3. EXAMPLES IN PLASMA PHYSICS

A. Electrostatic Potential in Plasma

We consider a simple model of electrostatic plasmas; electrons are thermally relaxed and ions are collisionless. The model was firstly studied by Bohm[1] for the sheath potential of plasmas contacting with walls. The model is also related to the ion acoustic shock. Sagdeev[2] introduced the so-called Sagdeev potential to study oscillating solutions for the model equation. We call the model equation the Bohm equation:

$$L\psi = (1 - 2M^{-2}\psi^*)^{-1/2} - e^{\psi^*}, \tag{1}$$

where

$$\psi^* := \psi - P,$$

ψ is the electrostatic potential normalized by the thermal energy of electrons, and $L = -d^2/dx^2$ is an elliptic differential operator of one dimension. The coordinate x is normalized by the Debye length. The Bohm equation has two independent parameters; M is the Mach number defined by

$$M := [(\text{kinetic energy of ion})/(\text{thermal energy of electrons})]^{1/2},$$

and P is the potential deep inside the plasma.[3] The first and the second terms in the right-hand-side of Eq.(1) correspond to the densities of ions and electrons, respectively. Using the Sagdeev potential, we write Eq.(1) as

$$L\psi = V'(\psi^*), \tag{1'}$$

where the Sagdeev potential $V(\psi^*)$ is defined by

$$V(\psi^*) = 1 - e^{\psi^*} + M^2[1 - (1 - \frac{2}{M^2}\psi^*)^{1/2}]. \tag{2}$$

The Bohm equation is a nonlinear elliptic differential equation. We consider boundary-value problems for the equation. We set

$$\psi(0) = 0, \tag{3}$$

$$\lim_{n\to\infty} \psi(x_n) = P, \tag{4}$$

where the limit is taken for a certain sequence $\{x_n\ ;\ n=1,2,\cdots\}$ which satisfies $\lim_{n\to\infty} x_n = +\infty$. This limit is generaly dependent on the choice of the sequence. The condition (4) implies that the potential $\psi(x)$ should not deviate from the value P, but may oscillate around P. Physically P corresponds to the potential inside the plasma where the ion is originated. Therefore, the value $\psi^* = \psi - P$ is the potential difference that the ion feels. We do not consider that the ion is originated at the mathematical infinity. The weak boundary condition (4) permits a large variety of solutions for the model equation (see Refs. 4 and 5).

The Bohm equation is a nonlinear elliptic differential equation, so the solvability, the uniqueness, bifurcations of solutions, and the stabilities are subjects of mathematical considerations. When we linearize the Bohm equation, we have

$$L\psi = \alpha(\psi - P), \qquad (\alpha := M^2 - 1). \tag{5}$$

Equation (5) has different characters for $M>1$ and $M<1$ regimes. For $M>1$, Eq.(5) has a unique solution for every $P \in \mathrm{R}$:

$$\psi(x) = P\,[1 - e^{-\sqrt{\alpha}x}]. \tag{6}$$

A mathematical question is the solvability of the original nonlinear equation (1) for given P and $M>1$. Another question is the structural stability of the solution. The solution (6) for the linearized equation (5) satisfies the boundary condition (4) in a stronger sense; viz., the function asymptotically converges to P as $x \to +\infty$. Since we set a weaker condition, we may expect a wider class of solutions for the nonlinear equation. The ion-acoustic-shock solutions are given by the structural instability of the asymptotic solutions.

In the region $M<1$, the linearized equation (5) is of the Helmholtz type, and the equation has non-trivial solutions for $P=0$. This implies the possibility of bifurcation of solutions for the original nonlinear equation (1). To answer the above-mentioned questions, the Sagdeev method using a formulation of initial-value problems is useful.

Although the formulation is essentially a boundary-value problem, we may take the advantage of one-dimensional differential equations, and convert the boundary-value problem

to an initial-value problem (IVP) for an ordinary differential equation.

We consider initial values at $x = 0$;

$$\psi(0) = 0, \qquad \psi'(0) = v,$$

where v is a certain number that should be determined to meet the boundary condition (4). Using the analogy of Newton's equation (x: time, ψ: position), $V(\psi)$: potential energy, $\psi'^2/2$: kinetic energy), we may easily find v that matches the boundary condition (3). This IVP technique for solving the Bohm equation has been given by Sagdeev to find oscillating solutions.

The IVP method has an advantage in studying the structural stability for the Bohm equation. Figure 1 shows the numerically calculated Sagdeev potential. We can construct solutions by starting from x (considered to be the time) = 0 with $\psi^*(0)$ (considered to be the initial position) = $-P$ and $\psi^{*\prime}(0)$(considered to be the initial velocity) = v. The boundary condition (4) should be finally satisfied. Therefore, the curve $\psi^*(x)$ should stay around 0 in the sense of the weak convergence of the condition (4). The initial value v is chosen to satisfy this condition.

First let us consider the case of $M \geq 1$. We should set

$$v^2/2 = V(-P), \tag{7}$$

to get the asymptotic convergence of $\psi^*(x)$ to 0 at $x \to +\infty$. Figure 2(a) shows the asymptotic solution that corresponds to the Bohm sheath. The asymptotics $\psi^* = 0$, however, is top of the potential, so that the structural instability may give bifurcated solutions. When we start with a little bit larger velocity v, we get oscillations in the region of $\psi^* \geq 0$, if we may include some fluctuations to connect both solutions. The oscillating solution is the ion-acoustic shock, which has been given by Sagdeev.

Next, let us discuss the regime of $M < 1$. When $M < 1$, the position $\psi^* = 0$ is the bottom of the Sagdeev potential. Because of this structural change in the Sagdeev potential, we see a drastically different behavior of solutions. There is no asymptotic solution. Only oscillating solutions may exist. The weak boundary condition (4) retains such pathological solutions. Figure 2(b) shows a typical oscillatory solution in the $M < 1$ regime.

Figure 3 shows the solvability and classification of solutions for the Bohm equation. The Sagdeev potential is not defined in the regime $\psi^* \geq \psi^*_c := M^2/2$. The potential difference $\psi^* \geq \psi^*_c$ is large enough to stop the transit motion of ions. When ions are stopped by the potential barrier, positive charge accumulates, so that steady solutions do not exist. The no-

solution region 'C' in Fig.3 is given by the positive potential barrier. In the region 'A', the Bohm equation (1) has normal positive-ion-sheath solutions (Fig.2(a)) and ion-acoustic-shock solutions. In the region 'B', only oscillating solutions (Fig.2(b)) exist.

B. MHD Equilibrium of Plasma

The magnetohydrodynamic equilibrium equation

$$(\mathrm{rot}\, \boldsymbol{B}) \times \boldsymbol{B} = \mathrm{grad}\, p, \quad \mathrm{div}\, \boldsymbol{B} = 0$$

is a system of two-hyperbolic and two-elliptic PDE's. We should supply two of independent I-data. Physically they correspond to the distributions of the pressure and the force-free field. When we consider two-dimensional ($\partial/\partial z = 0$) problems, the magnetostatic equation reduces to the Grad-Shafranov equation:

$$L\phi = (I(\phi)^2)' + p(\phi)'$$

where L is an elliptic differential operator (Laplacian), ϕ is the flux function, $I(\phi)$ is the distribution of the z-component of the magnetic field, and $p(\phi)$ is the distribution of the pressure.

Formal analogy of the Bohm equation and the Grad-Shafranov equation is worthwhile noting. Structures are subject to the characteristic functions; for the Grad-Shafranov equation, $p(\phi)$ and $I(\phi)$, and for the Bohm equation, $V(\psi - P)$. These characteristic functions are related to the dissipative structure of the systems.

The MHD equilibrium problem is much simplified when we consider the limit of $p = 0$, viz., the force-free equilibrium. We consider three-dimensional problems. The force-free equilibrium equation

$$(\mathrm{rot}\, \boldsymbol{B}) \times \boldsymbol{B} = \mathrm{grad}\, p, \quad \mathrm{div}\, \boldsymbol{B} = 0$$

is equivalent to

$$\mathrm{rot}\, \boldsymbol{B} = \mu \boldsymbol{B}, \quad (\boldsymbol{B}, \mathrm{grad})\mu = 0,$$

where μ is a scalar function, which corresponds to the noncharacteristic Cauchy data for the present problem. Let us discuss the simplest case of $\mu =$ constant. Then, the problem reduces to an eigenvalue problem

$$\mathrm{rot}\, \boldsymbol{B} = \lambda \boldsymbol{B}. \tag{8}$$

We have the following mathematical theory for the spectral resolution of the operator rot.[6] Let Ω be a connected domain in $\mathbf{R}^3$ with smooth boundary $\partial\Omega$.

Theorem 1. *We define an operator*

$$Su = \text{rot } u,$$

$$D(S) = \{u \in H^1(\Omega) \ ; \ \text{div } u = 0, \ n \cdot u = 0, \ n \cdot \text{rot } u = 0\}.$$

Then, S is a self-adjoint operator in the space

$$L^2_\Sigma = \{u \in L^2(\Omega) \ ; \ \text{div } u = 0, n \cdot u = 0, \ \int_\Sigma n \cdot u ds = 0\},$$

where Σ is an arbitrary surface with its boundary lying on $\partial\Omega$.

Remark. The function space L^2_Σ is the orthogonal complement of the space of *irrotational fields* in Ω.

Proposition. *Operator S has a compact inverse, so that eigenfunctions of S span the space $L^2_\Sigma(\Omega)$.*

Remark. The function space

$$L^2_\sigma(\Omega) = \{u \in L^2(\Omega) \ ; \ \text{div } u = 0, \ n \cdot u = 0\}$$

is spanned by the eigenfunctions of S and the cohomology of Ω, viz.,

$$L^2_\sigma = L^2_\Sigma(\Omega) + \{u \ ; \ \text{div } u = 0, \ \text{rot } u = 0, \ n \cdot u = 0\}.$$

An interesting point of the eigenvalue problem for rot is the following theorem.

Theorem 2. *When Ω is multiply connected, the the eigenvalue problem*

$$\text{rot } u = \lambda u, \quad n \cdot u = 0$$

has nontrivial solutions for every $\lambda \in \mathbf{C}$.

This theorem shows that the simplified equilibrium equation has an intrinsic-structure solution (eigenfunction) for every complex number λ, if and only if we consider a multiply connected plasma.

4. SUMMARY

The concept of intrinsic structure gives a generalization of the eigenvalue problem, and relates elliptic-hyperbolic PDE's with Helmholtz equations through Cauchy data. We discussed two different, but mathematically analogous, problems in plasma physics; one is the electrostatic plasma potential, and the other is the magnetostatic equilibrium. Each problem reduces to a Helmholtz equation, and the corresponding eigenfunctions describe the intrinsic structure of the system.

ACKNOWLEDGMENT

The author is grateful to Prof. Y. Giga and Dr. H. Yamada for their comments and discussions. This work is partially supported by Grant-in-Aid for Scientific Research No.63050040, The Japan Ministry of Education, Science and Culture.

REFERENCES

[1] D. Bohm, in *The Characteristics of Electrical Discharges in Magnetic Fields*, Eds. A. Guthrie and R.K. Wakerling (McGraw Hill, New York, 1949) Chap.3.

[2] R.Z. Sagdeev, in *Reviews of Plasma Physics* (Consultants Bureau, New York, 1966) Vol.4, p.23.

[3] Local Mach number in the sheath region ($0 < x < 1$) is known to be greater than 1, when the normal positive ion sheath is formed and the ion is accelerated in the pre-sheath region; see T. Takizuka *et al* ., J. Nucl. Mater. **128 & 129**, 104 (1984). The Mach number we use here has a different meaning; which is defined by the velocity of ions at the potential $\psi = P$ inside the plasma.

[4] Z. Yoshida and H. Yamada, in *Proc. 13th Sapporo Symposium on Partial Differential Equation Theory*, (Hokkaido University Tech. Rep. Ser. in Math.) Ed. by Y. Kubota (1988) 21.

[5] Z. Yoshida, H. Yamada, K. Itoh and S.-I. Itoh, *Estimate of Electron Thermal Transmission in Structurally Unstable Electrostatic Potentials*, (to appear in J. Phys. Soc. Jpn.).

[6] Z. Yoshida and Y. Giga, *Remarks on Spectra of Operator rot*, Hokkaido Univ. Preprint Ser. Math. No.48, 1989, (submitted for publication).

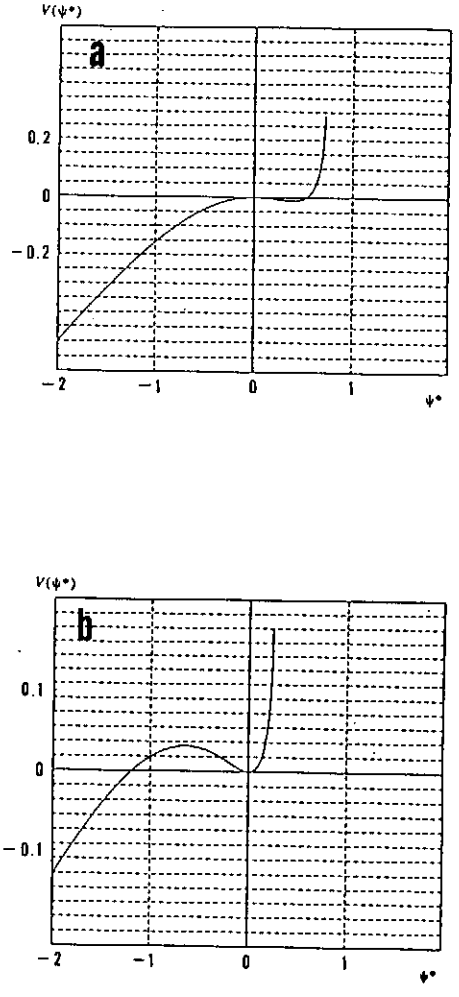

Fig.1 Sagdeev potentials for (a)M = 1.2 and (b)M = 0.7.

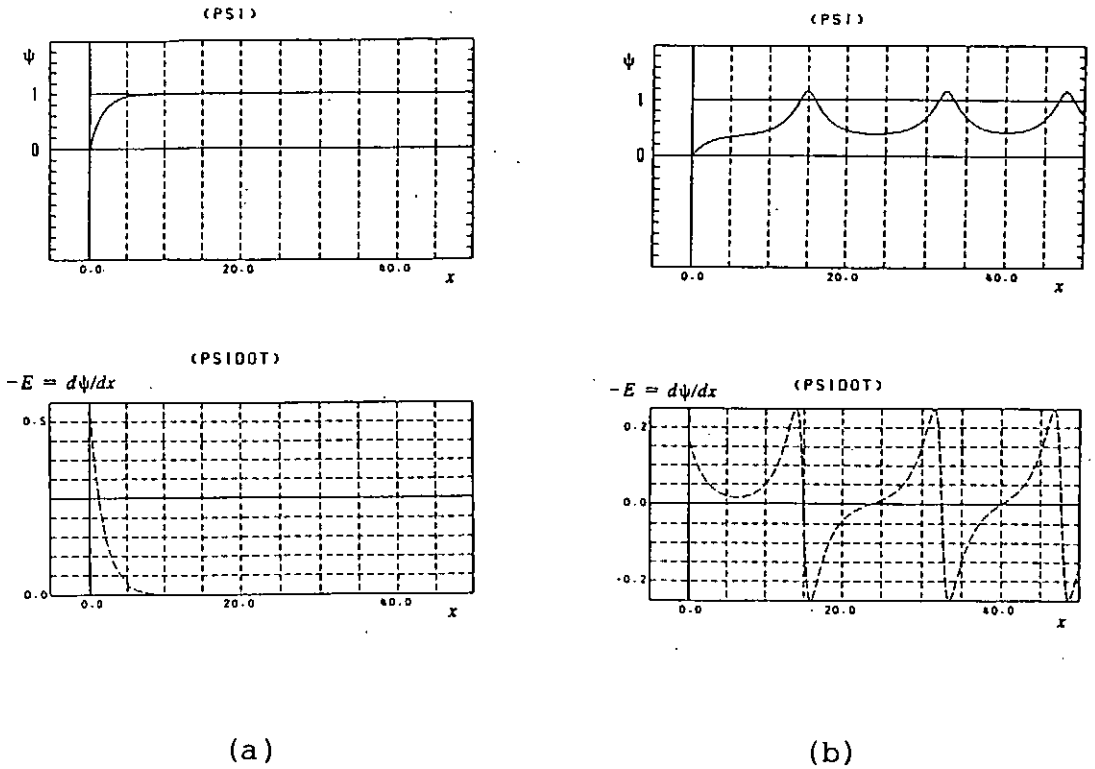

Fig.2 Solutions for the Bohm equation.
(a) Asymptotic solution for $M = 1.2$, $P = 1$.
(b) Wavy solution for $M = 0.7$, $P = 1$.

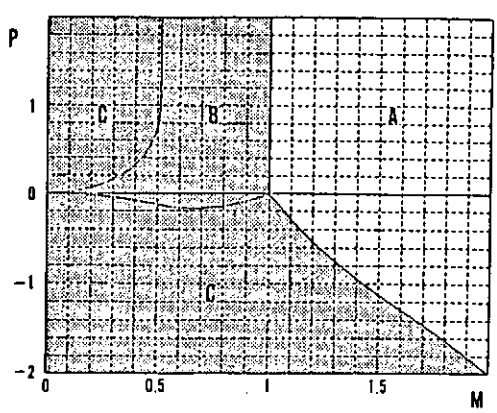

Fig.3 Solvability and classification of solutions for the Bohm equation in the M/P plane.
Region A : asymptotic solutions (Bohm-sheath solutions) and wavy solutions (ion-acoustic-shock solutions) exist.
Region B : wavy solutions exist.
Region C : no solution exists.

CHAOTIC BEHAVIOR DUE TO WAVE-WAVE INTERACTIONS IN A MODULATED ION BEAM-PLASMA SYSTEM

K. ARAKI, N. OHNO, M. SAIGOH, H. FUJIYAMA,
M. NAMBU* and H. HONJO*

Department of Electrical Engineering and Computer Science, Faculty of Engineering, Nagasaki University, 1-14 Bunkyo, Nagasaki 852, Japan

*College of General Education, Kyusyu University, Ropponmatsu, Fukuoka 810, Japan

1. Introduction

Recently, there has been a growing interest in chaos in plasma physics. However, there is very little experimental data on chaotic behavior related to a mode-mode interaction in a plasma. On the other hand, several theoretical works concerned with the conservative and dissipative system in a plasma have been reported[1].

For the plasma maser interaction[2], the model reduced the forced Lotka-Volterra equations have been studied numerically[3)4]. The model in the conservative system has already been investigated and the stochastic motion of wave energies has been found. In this paper, we show the model in the dissipative system and analyze a chaotic behavior in the plasma maser interaction.

2. Plasma maser effect

In this section, we describe the plasma maser effect which cause an energy up-conversion from a low-frequency wave to a high frequency wave. The lowest order mode-mode coupling processes in weak plasma turbulence theory[5] are composed of three parts. They

are the resonant three wave interaction[6], the nonlinear scattering (nonlinear Landau damping)[7] and the plasma maser interaction. The plasma maser interaction was formally included in standard weak turbulence theory[8)9)]. Now we assume a coherent low frequency ion sound wave in a plasma whose amplitude is small but finite. The electric field strength of a coherent ion sound wave is given by $E_1(k,\omega)\cos(\omega t-kx)$. Then we introduce a high frequency Langmuir test field with infinitesimal small amplitude. The origin of the plasma maser effect comes from the electron acceleration by the modulation electric field. A high frequency dissipative nonlinear force (F_h) cause the electron acceleration. The force per single electron reduced to the following[10]:

$$F_h(K,\Omega)=A\,\delta_{nh}(K,\Omega), \tag{1}$$

with

$$A=\frac{\pi m}{N}\left(\frac{m}{M}\right)^{\frac{1}{2}}\omega_{pe}{}^2\frac{k}{k_e{}^2}\frac{E_1(k,\omega)^2}{4\pi NT_e}\left(\frac{k_e}{k}\right)^2 . \tag{2}$$

Here, K, Ω and k, ω are the wave number and frequency for the Langmuir wave and ion sound wave, respectively. The notations m, M, N and T_e are masses for electron and ion, the number density, and the electron temperature, respectively. ω_{pe}, K_e and $E_1(k,\omega)$ are the electron plasma frequency, Debye wave number, and the amplitude of the ion sound wave. $\delta_{nh}(K,\Omega)$ is the electron high-frequency number-density perturbation due to the Langmuir wave.

For a steady ion sound wave, the growth rate of the Langmuir wave whose electric field is $\delta_{Eh}(K,\Omega)$ was obtained by several authors[11]. For the Maxwell electron distribution function without external magnetic field, the growth rate [$\gamma_{TSW}(K,\Omega)$] reduced to

$$\frac{\gamma_{TSW}(K,\Omega)}{\Omega_r}=\frac{\pi}{2}\left(\frac{m}{M}\right)^{\frac{1}{2}}\frac{K|k|}{k_e^2}\frac{E_1(k,\omega)^2}{4\pi NT_e}\left(\frac{k_e}{k}\right)^2 . \qquad (3)$$

Here, Ω_r is the real Langmuir frequency. Note that we assumed $\omega/k>0$ in deriving Eqs. (1) and (3). Accordingly, $\gamma_{TSW}(K,\Omega)>0$ for $\Omega_r/K>0$ with Maxwell electron distribution function $[\partial f_{0e}/\partial u(u=\omega/k)>0]$, the right-hand side of Eqs. (1) and (3) change their sign. Then, $\gamma_{TSW}(K,\Omega)>0$ for $\Omega_r/K<0$.

For a growing ion sound wave, an additional damping rate $[\gamma_{DP}(K,\Omega)<0]$ due to the nonresonant parametric process[12] was pointed out. The additional damping rate is

$$\frac{\gamma_{DP}(K,\Omega)}{\Omega_r}=\frac{1}{18}\left(\frac{k_e}{k}\right)^4\frac{\tilde{\nu}}{\omega_{pe}}\frac{E_1(k,\omega)^2}{4\pi NT_e}\left(\frac{k_e}{k}\right)^2 , \qquad (4)$$

where $\tilde{\nu}$ is the nonlinear growth rate of the ion sound wave. Accordingly, the effective growth rate of the Langmuir wave $[\gamma_{eff}(K,\Omega)]$ in the presence of a growing ion sound wave reduces to

$$\gamma_{eff}(K,\Omega)=\gamma_{TSW}(K,\Omega)+\gamma_{DP}(K,\Omega) . \qquad (5)$$

Thus, the estimate made in Ref. 13, Eq. (38), shows for one dimension,

$$R\equiv\frac{|\gamma_{DP}(K,\Omega)|}{\gamma_{TSW}(K,\Omega)}=\frac{1}{18}\frac{k_e(m/M)^{\frac{1}{2}}}{K}\left(\frac{k_e}{k}\right)^4\frac{\tilde{\nu}}{\nu} . \qquad (6)$$

Here, ν is the linear growth rate of the ion sound wave. Therefore, for a rapidly growing phase of an ion sound wave ($\tilde{\nu}\sim\nu$) with $K<k_e(m/M)^{\frac{1}{2}}$ and $k<<k_e$, Eq. (6) reduces to

$$R>1. \qquad (7)$$

On the other hand, we assume here that the ion sound wave is slowly growing (or damping) with $\tilde{\nu}<<\nu$, $K>k_e(m/M)^{\frac{1}{2}}$, and $k<k_e$. Then it is safe to take

$$R<1. \tag{8}$$

Throughout this paper, we assume Eq. (8), then

$$\gamma_{eff}(K,\Omega)\simeq\gamma_{TSW}(K,\Omega)>0. \tag{9}$$

3. Model equation

We assume that a coherent ion sound wave is driven by injec ting modulated cold ion beam into unmagnetized homogeneous plasma and the unperturbed electron distribution function is Maxwellian. We make a further assumption that the interaction between an ion sound wave and a Langmuir wave is caused by plasma maser effect which determines the growth and the damping rate of each one. The transport of these energies is schematically shown in Fig. 1.

For simplification, we neglect a spontaneous emsision and an additional secondary effect for nonresonant parametric interaction. Therefore, this system reduces to the following equationsof a forced Lotka-Volterra type,

$$\frac{dX}{dt}=\alpha(1+A\cos\theta)X-\beta XY-\varepsilon X^2 , \tag{10}$$

$$\frac{dY}{dt}=\gamma XY-\delta Y , \tag{11}$$

$$\frac{d\theta}{dt}=\omega_f , \tag{12}$$

where θ, X and Y are the phase of ion beam modulation, the normalized ion sound wave and the Langmuir wave energy density, respectively. In Eq. (10), $\alpha/2$ is the linear growth rate of ion sound wave driven by the cold ion beam, $\beta Y/2$ is the nonlinear damping rate of plasma maser and $\varepsilon X/2$ is the damping rate for the electron number density modification and the induced ion sound wave scattering. In Eq. (11), $\gamma X/2$ is the nonlinear growth rate of Langmuir wave by plasma maser and $\delta/2$ is the linear Landau damping rate of Langmuir wave. In Eq. (12), A and ω_f are the ion

beam modulation amplitude and frequency, respectively.

4. Numerical results

We computed Eqs. (10), (11) and (12), to obtain the temporal evolution of X ,Y and . Here, we used the typical experimental parameters : $\alpha=5.6\times10^{-5}$, $\beta=2.5\times10^{-4}$, $\gamma=5.3\times10^{-6}$, $\delta=5.4\times10^{-6}$, $\varepsilon=2.5\times10^{-5}$ and $\omega_f=3.4\ 10^{-5}$. These values are normalized by the electron plasma frequency $\omega_{pe}=8.7\times10^{8}$ red/sec.

4.1 Bifurcation to chaos

For specifying the scenario leading to chaos, we show a bifurcation diagram in Fig. 2. In this calculation, we choose the values X and Y at 500T($T=2\pi/\omega_f$:period) in the previous calculation as the initial values X(0) and Y(0), respectively. In the smaller amplitude region($A<0.13$), the system has a resonance periodic motion. With increasing A, the period-doubling bifurcation occurs at A=0.13 and then the two periodic motion appears. The system goes to chaotic state from regular motion at $A\simeq0.577$. The region $0.585<A\leqq0.6$ shows a chaotic attractor in crisis[14]. We calculate a ratio $\delta_n=(A_{n+1}-A_n)/(A_n-A_{n-1})$ for a cascade of period-doubling. This cascade obeys Feigenbaum's scenario as the calculated ratio is nearly equal to Feigenbaum constant $\delta_\infty=4.669\cdots$. Figure 3 shows Poincaré sections and power spectrum at A=0.6. In this figure, we find that the attractor is likely to the Hénon type, and that its trajectory moves irregularly in phase space because the power spectrum is broad. From the calcultion of correlation dimension, the attractor has nonintegral dimension as shown in Fig. 4, which means that the structure is fractal. Moreover, we also calculate the largest Lyapunov exponent λ_1 determining the stability of trajectory. The negative and

positive λ_1 correspond to the stable and unstable trajectory, respectively. As the value λ_1 is calulated to be 1544±11 at A=0.6 in the crisis region, it is found the present model equation has a chaotic solution.

4.2 Dependence of the system on the initial conditions

We numerically investigate the chaos in the multi-cascade region $0.48<A<0.5$. As a result of calculation for several initial conditions, the states of the coexisting regular or stochastic motion appeared it is shown in Fig. 5. As shown in Table 1, the calculated ratio δ_n for each cascade that these cascades obey Feigenbaum scenario. Furthermore, Table 2 shows calculated the largest Lyapunov exponent λ_1 for the chaotic state of each cascade. As these values are positive, it is found that the four trajectories are unstable. And also a periodic attractor coexists with the other periodic ones and a chaotic one. Figure 6 shows the basin boundary map[15]. This map was given by picking a block of initial conditions in phase space, establishing the type and number of attractors that exist, running numerical integrations for each initial condition, and plotting a different symbol for each initial condition corresponding to a distinct final steady-state attractor that the trajectory approaches. This map was first given for the forced Lotka-Volterra equations. From the reasons of the computational expense and mapping time, only a limited range of parameter values can be analyzed. In this figure, dot and blank correspond to the 2 and 6 periodic motions, respectively. It seems that the basin boundary in Fig. 6 has a fractal characteristics. The boundary appears to be formed by some Cantor set-type structure[15].

5. Conclusions

We have numerically studied the forced Lotka-Volterra equations exhibiting the plasma maser interaction and the other effects. The results are concluded as follows:

(1) Feigenbaum's period-doubling route to chaos has been observed by varying the amplitude of ion beam modulation A. Feigenbaum's number δ was calculated to be 4.756. Furthermore, it was obtained both the correlation dimension $\nu_m \simeq 2.1$ and the largest Lyapunov exponent $\lambda_1 = 1544 \pm 11$ for the strange attractor at A=0.6. These results that this attractor is fractal and its trajectory is unstable.

(2) The detailed bifurcation diagram revealed that four cascades of period-doubling to chaos($2^n, 5\times2^n, 6\times2^n, 8\times2^n$; n=0,1,2,$\cdots$) coexisted. The calculated Feigenbaum's numbers indicate that all cascade obey Feigenbaum's scenario. Furthermore, the basin boundary map was also shown.

The experimental study based on the present model are now in progress.

Acknowledgement

This work were partially supported by the Mitsubishi Foundation.

References

1) S. Qian, Y. C. Lee and H. H. Chen; Phys. Fluids B1(1), 87(1989).

2) M. Nambu; Phys. Rev. A23, 3272(1981).

3) H. Honjo and M. Nambu; J. Phys. Soc. Jpn. 55, 4160(1986).

4) H. Fujiyama, O. Hattori, S. Fukase and M. Nambu; Proceeding of International Conference on Phenomena in Ionized Gases 2, 330(1987), H. Fujiyama, S. Fukase and K. Araki; Asian Conference on Electrical Discharge, 39(1988).

5) M. Nambu; Laser and Particle Beams 1, 427(1983).

6) V. N. Oraevsky and R.Z. Sagdeev; Sov. Phys.-Tech. Phys. 7, 955(1963).

7) M. N. Rosenbluth, B. Coppi and R. N. Sudan; Ann. Phys. 55, 248(1969).

8) B. B. Kadomtsev; Plasma Turbulence (Academic, New York,1965).

9) R. C. Davidson; Methods in Nonlinear Plasma Theory (Academic, New York, 1972).

10) M. Nambu; J. Phys. Soc. Jpn. 53, 1594(1984).

11) V. N. Tsytovich, L. Stenflo and H. Wilhelmsson; Phys. Scr. 11, 251(1975), W. Rozmus, A. Offenberger and R. Fedosejevs; Phys. Fluids 26, 1071(1983), A. Hirose; Comments Plasma Phys. Controlled Fusion 8, 117(1984).

12) D. F. DuBois and D. Pesme; Phys. Fluids 27, 218(1984).

13) A. B. Mikhailovskii; Theory of Plasma Instabilities (Consultants Bureau, New York, 1974), Vol. 1, p. 68.

14) C. Grebogi, E. Ott and J. A. Yorke; Phys. Rev. Lett. 48, 1507(1982).

15) C. Pezeshki and E. H. Dowell; Physica D32, 194(1988).

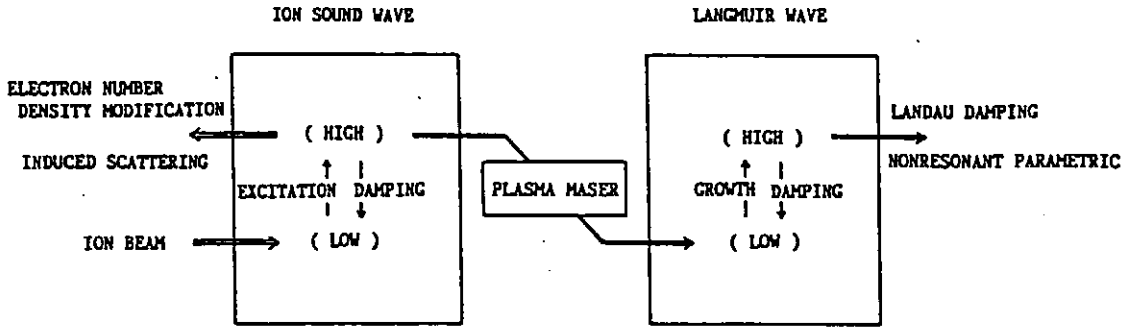

Fig. 1 Energy flow diagram for plasma maser interaction.

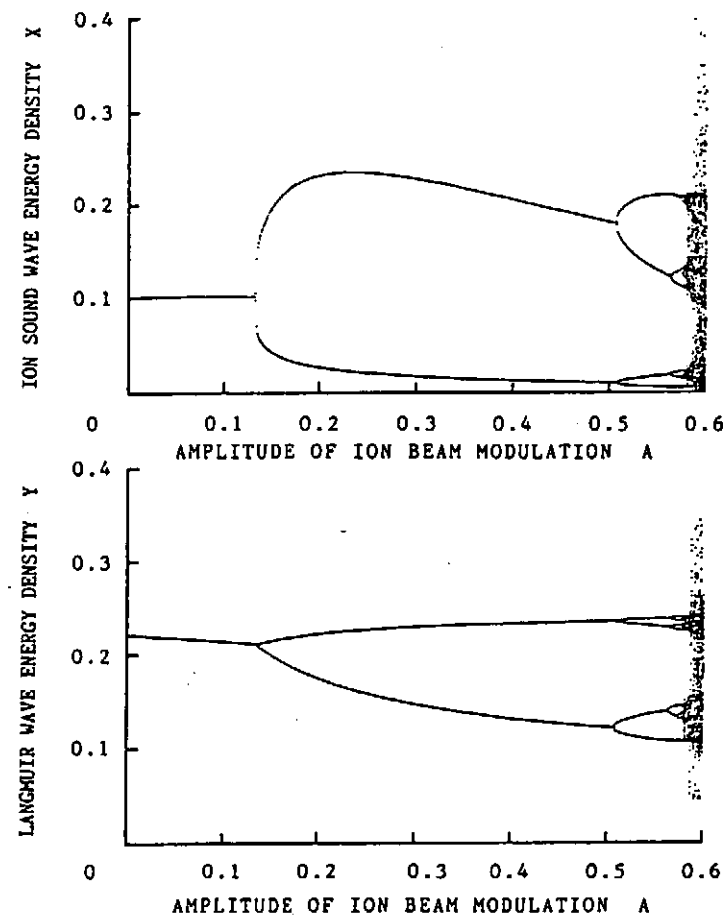

Fig. 2 Bifurcation diagram for period-doubling cascade.

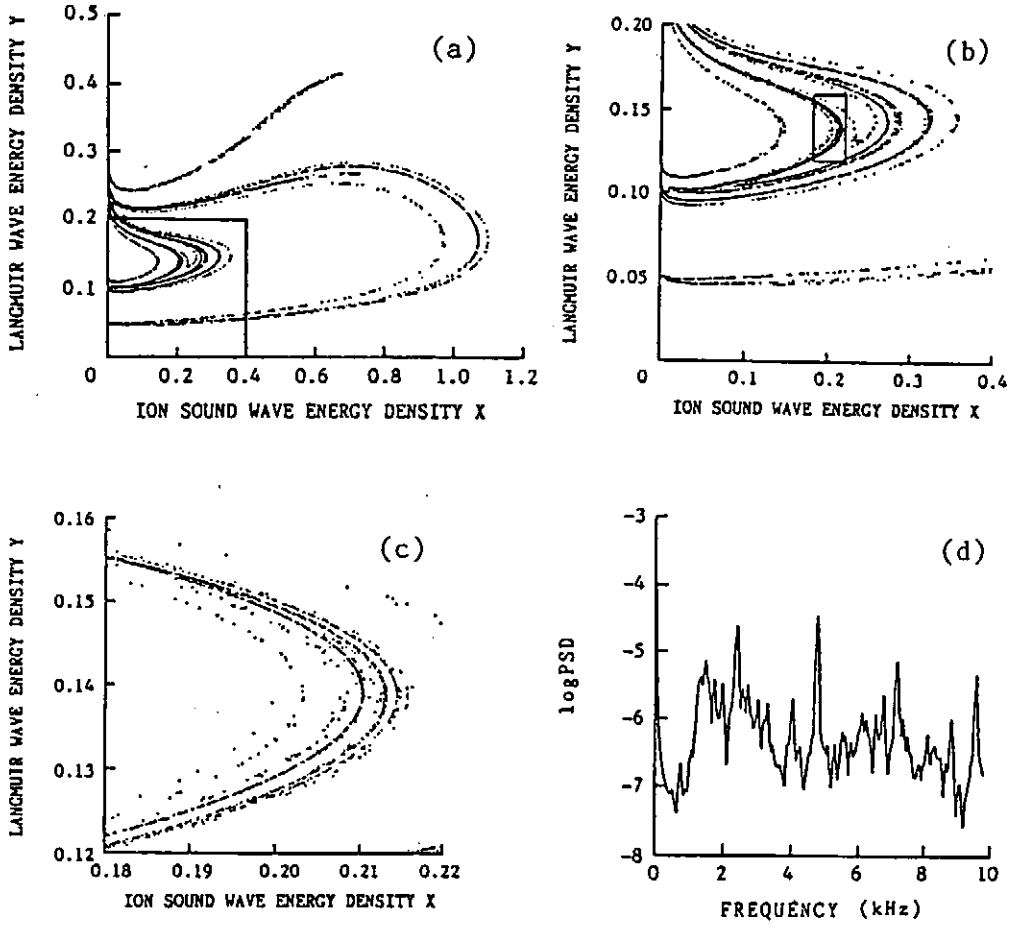

Fig. 3 Poincaré section, its enlargement and power spectral density, A = 0.6 .

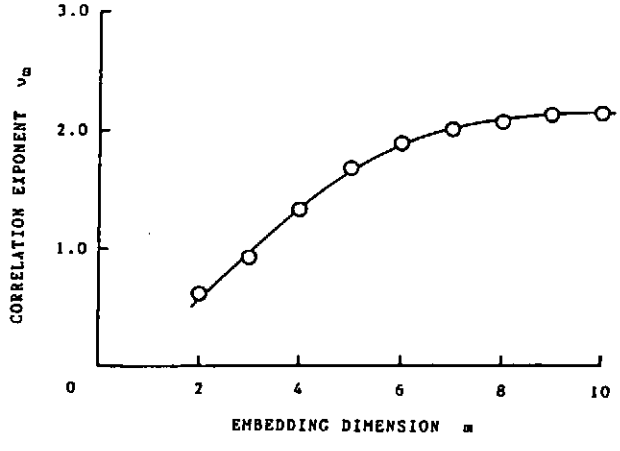

Fig. 4 The correlation exponent for the model equations, A = 0.6 .

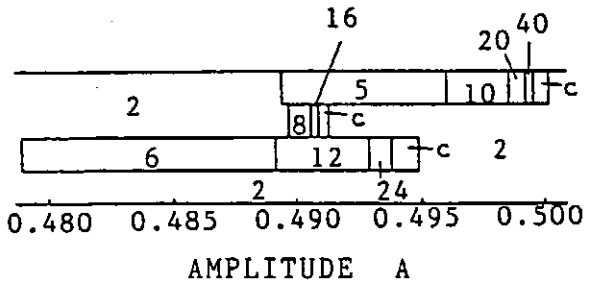

Fig. 5 Schematic bifurcation diagram in the multi-cascade region.

Table 1. Feigenbaum number for each cascade.

CASCADE	FEIGENBAUM CONSTANT
2×2^n	$\delta_5 = 4.756$
5×2^n	$\delta_2 = 4.545$
6×2^n	$\delta_2 = 4.571$
8×2^n	$\delta_2 = 4.048$

Table 2. Largest Lyapunov exponent for each strange attractor.

CASCADE	AMPLITUDE A	LARGEST LYAPUNOV EXPONENT λ_1
2×2^n	0.5850	906±16
5×2^n	0.5003	449±15
6×2^n	0.4948	438±16
8×2^n	0.4909	246±10

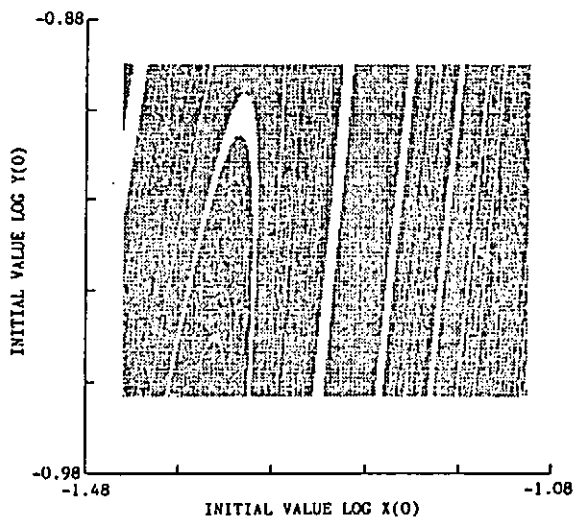

Fig. 6 Basin boundary map, A = 0.487 .

Non-adiabatic behavior of the magnetic moment in a dipole field in the presence of a low frequency electrostatic wave

Sadayoshi MURAKAMI and Tetsuya SATO
Institute for Fusion Theory
Hiroshima University, Hiroshima 730, Japan
Akira HASEGAWA
AT&T Bell Laboratories
Murray Hill, New Jersey 07974

Non-adiabatic behavior of the magnetic moment of a charged particle in a dipole magnetic field in the presence of a low frequency electrostatic wave with azimuthal component is studied both numerically and analytically. The adiabaticity can be broken due to two types of resonance, i.e., the bounce - $E \times B$ drift resonance and the wave - drift resonance.

I. INTRODUCTION

In a magnetic dipole field, high energy particles are trapped such as in the radiation belt of the earth magnetosphere. The motion of such particles consists of three periodic motions. One is a gyromotion. Next is a bounce motion along a magnetic field line and the last is a drift motion in the azimuthal direction [Fig.(1)]. We can define three adiabatic invariants[1] as actions associated with these three periodic motions: the magnetic moment μ, the action integral J of the bounce motion, and the magnetic flux Ψ sorrounded by the drift orbit of the particle. The motion of the particle can be well described in terms of these adiabatic invariants.

The particle motion in a dipole magnetic field in general has two degrees of freedom because of the conservation of azimuthal component of the canonical momentum. The two degrees of freedom can lead to the chaotic motion of the particle, which means the breakdown of the adiabatic invariants[2]. The breakdown of adiabatic invariants can lead to a drastic change of the system, e.g. , the breakdown of μ can destroy the magnetic confinement.

In the presence of an electrostatic wave, χ, the Hamiltonian can be expressed using

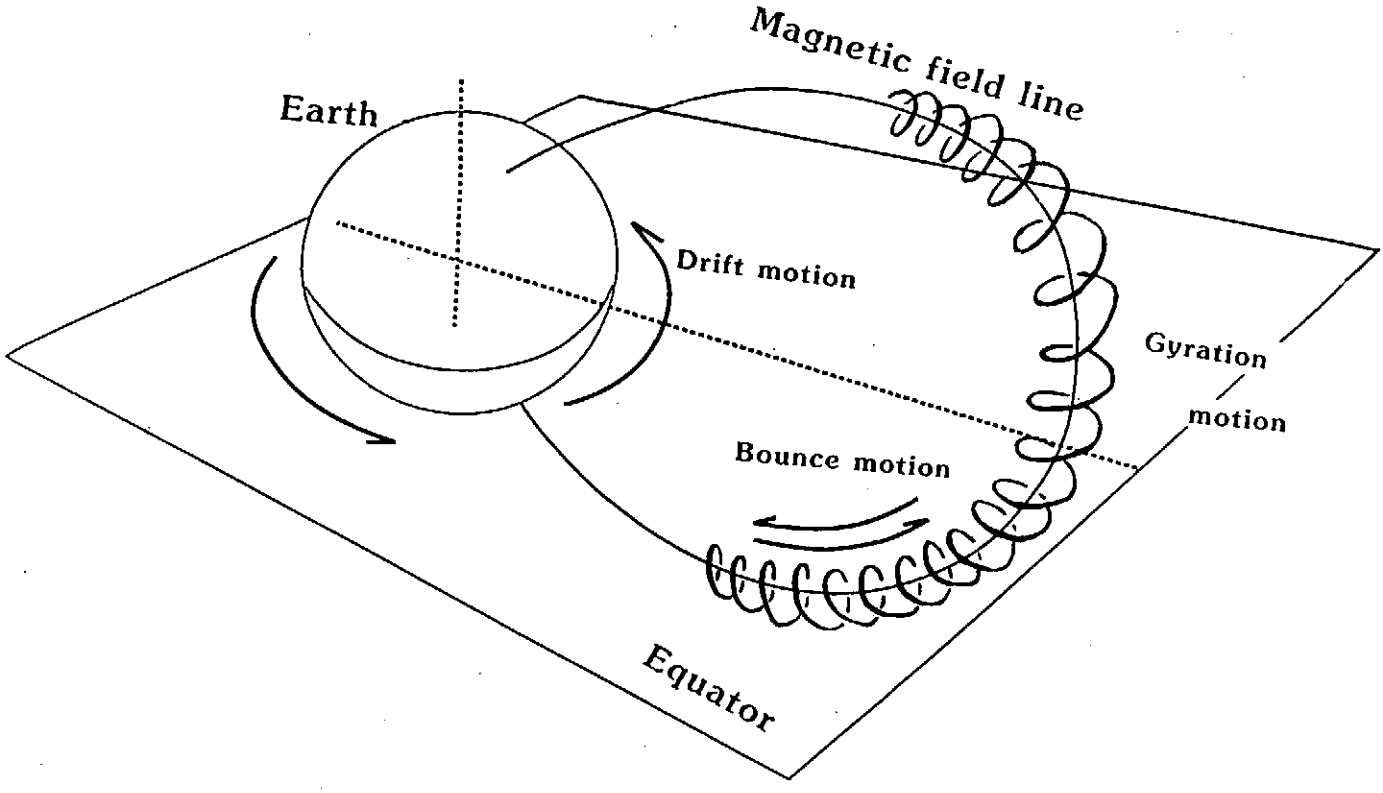

Figure 1: The motion of the particle in the earth magnetic field (a dipole field).

these adiabatic invariants as

$$H = \mu\omega_c + J\omega_b + \Psi\omega_d + q\chi + C, \tag{1}$$

where ω_c, ω_b, and ω_d are the gyrofrequency, the bounce frequency, and the drift frequency, respectively. The wave introduces additional one half degree of freedom. Under the action of an electrostatic wave, a particle oscillates in the direction perpendicular to the electric and magnetic fields due to the $E \times B$ drift motion. Even though $q\chi$ is small, the resonances between the particle motion and the wave or the $E \times B$ drift oscillation can make the nonlinear term C substantial, and the adiabaticity can be violated.

In this paper we show two kinds of resonances by which the adiabaticity of the magnetic moment is broken, and give the critical conditon for the magnetic moment conservation both in the resonant and in the nonresonant case.

The kinetic energy of the particle is taken to be sufficiently high ($\simeq MeV$ protons in the radiation belt in the earth magnetosphere). The frequency of the ambient electrostatic wave, ω, is chosen as

$$\omega_d \leq \omega \leq \omega_b. \tag{2}$$

II. THE EQUATION OF MOTION

The external magnetic field (a dipole field) is obtained in cylindrical coordinates as

$$\mathbf{B} = -B_0 \frac{1}{(r^2+z^2)^{5/2}} \{3rz\hat{\mathbf{r}} + (2z^2 - r^2)\hat{\mathbf{z}}\}, \tag{3}$$

where $\hat{\mathbf{r}}$ and $\hat{\mathbf{z}}$ are unit vectors of the respective cylindrical coordinates.

We assume that the electrostatic wave has only an azimuthal component. In cylindrical coordinates the wave potential is given by

$$\chi = \chi_0 \cos(m\phi - \omega t), \tag{4}$$

$$\mathbf{E} = -\nabla\chi = \frac{m\chi_0}{r} \sin(m\phi - \omega t)\hat{\phi}, \tag{5}$$

where m and ω are the wave mode number (positive) and the frequency, respectively.

Time, length and velocity are normalized by ω_c^{-1} ($\omega_c = qB_0/M$), L_0 and $\omega_c L_0$, respectively, and the electrostatic potential by $M\omega_c^2 L_0^2/q$, where L_0 and B_0 are the magnetic field intensity and the distance from the center of the dipole field at the initial particle position at the equator, respectively. [See Fig.(1)]

The equation of motion becomes

$$\ddot{\mathbf{r}} = \dot{\mathbf{r}} \times \mathbf{B} + \mathbf{E}. \tag{6}$$

We numerically integrate Eq.(6) by means of the 6th-order Runge-kutta method, and analyze the conservation of the magnetic moment. We numerically obtain the magnetic moment by directly integrating the vector potential $\mathbf{A}$ along the particle orbit of one gyration.

Initially, we set a particle at the equator and start with various velocities and pitch angles. Eq.(6) is integrated over the time $10000\omega_c^{-1}$, which corresponds to dozens of periods of particle drift motion. Time step, Δt, is taken to be $0.05\omega_c^{-1}$. The resultant numerical error of the particle kinetic energy is about 1.0×10^{-7} %.

III. NUMERICAL RESULTS

1. The case with no wave

First, we numerically studied the dynamic behavior of the magnetic moment without an electrostatic wave. The results of the numerical calculations for various initial conditions of the particle are shown in Fig.(2), where the vertical axis is the particle velocity, v, and the horizontal axis is the sine of the pitch angle, $\sin\theta_0$. The pitch

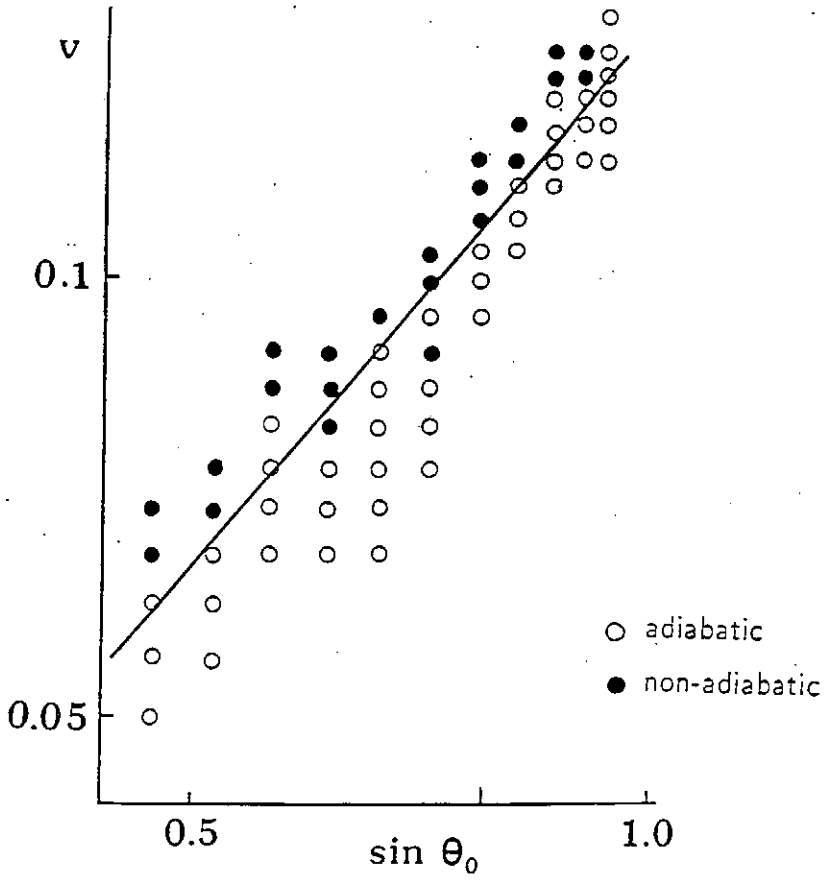

Figure 2: The numerical results of the μ conservations in terms of the velocity and the pitch angle. Open (filled) circles show the condition where μ is conserved (not conserved).

angle is defined as the angle between the velocity and the magnetic field line at the equator. The open (filled) circles show the conditions under which μ is conserved (not conserved). The area of μ conserved increases with an increase in $\sin\theta_0$.

The solid line shows the relation,

$$v = 0.12 \sin\theta_0. \tag{7}$$

Eq.(7) is rewritten in terms of the perpendicular velocity, $v_\perp$, as

$$v^2 = 0.12 v_\perp, \tag{8}$$

The relation in Eq.(8) suggests that the ratio of a centrifugal force to the Lorenz force (that is the ratio of the curvature drift of the particle to the thermal velocity) determines whether or not the adiabaticity of the magnetic moment is broken.

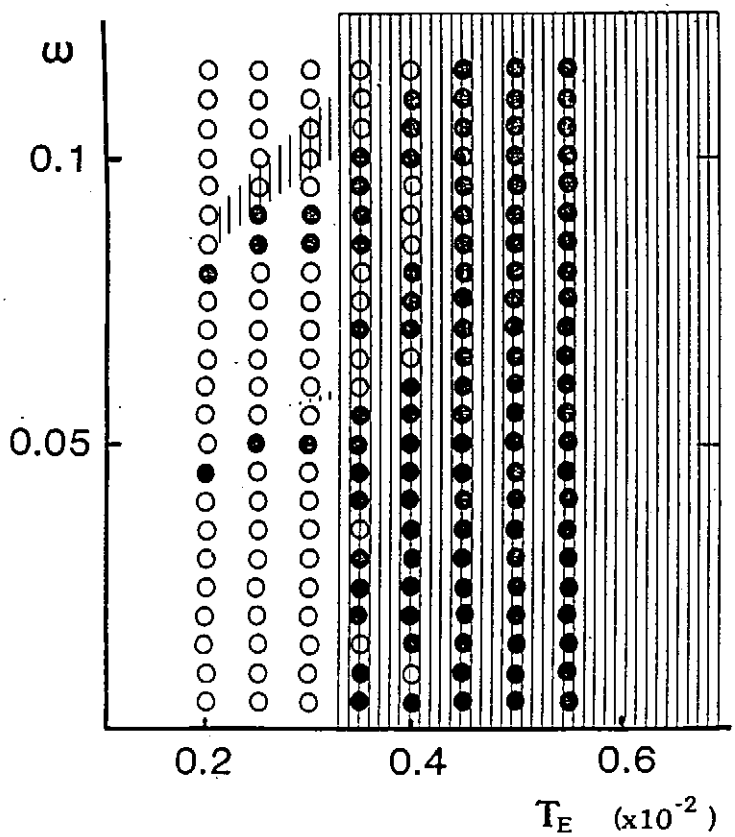

Figure 3: The numerical results of the μ conservations in terms of the kinetic energy and the wave frequency for the case of the opposite direction. The shaded regions show the analytically obtained non-adiabatic regions.

2. The case with a wave

Since the propagating direction of the wave depends on the sign of the wave frequency ω, two different cases are considered, i. e., the case where the wave propagates in the direction of the particle drift motion and the case of the opposite direction. We first study the case of the opposite direction. We have made numerical calculations under various conditions of particle kinetic energy and wave frequency. The results are shown in Fig.(3), where the wave frequency, ω, is shown in the vertical axis and the kinetic energy of the particle, $T_E = v^2/2$, is shown in the horizontal axis. Open (filled) circles show the conditions under which μ is conserved (not conserved). The amplitudes of the electrostatic wave χ_0 is 0.17×10^{-2} and other parameters are $m = 5, \theta_0 = 3\pi/10$. It is found that the non-adiabatic region where μ is not conserved extends to the lower particle energy region due to the existence of the electrostatic wave. (In the absence of the wave the adiabaticity is broken at $T_E = 5.5 \times 10^{-3}$ when $\theta = 3\pi/10$ [according to Fig.(2)]). We find two characteristic extensions of the non-adiabatic region, one which is independent of the wave frequency and the other

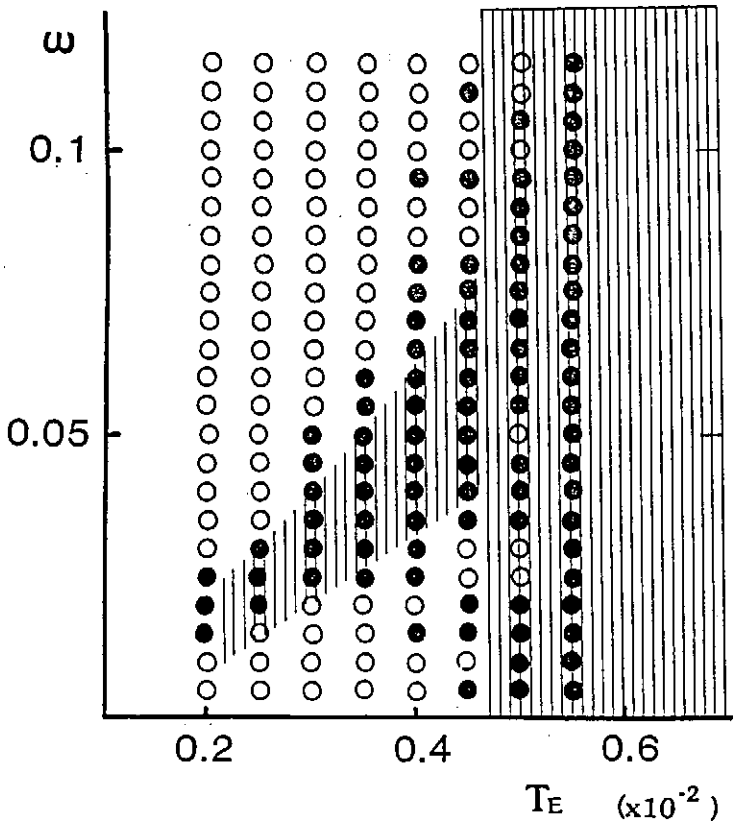

Figure 4: The numerical results of the μ conservations in terms of the kinetic energy and the wave frequency for the case of the same direction. The shaded regions show the analytically obtained non-adiabatic regions.

which has the frequency dependent spike-like structures.

Next, we consider the case when the wave propagates in the direction of the particle drift motion. The results are shown in Fig.(4) in the manner similar to Fig.(3). The amplitudes of the electrostatic wave χ_0 is 0.05×10^{-2} and other parameters are $m = 5, \theta_0 = 3\pi/10$. Compared with the previous results in Fig.(3), the spike-like structure of the non-adiabatic region becomes larger and extends futher to the lower energy region of the particle.

IV. ANALYTICAL CONSIDERATIONS

1. The cause of the non-adiabaticity

If the particle satisfy the critical condition, Eq.(8), the magnetic moment is not conserved. Otherwise, the magnetic moment is conserved. In order to study the critical condition of the adiabaticity of the magnetic moment in the presence of an electrostatic wave, we make the following assumption. When the wave frequency is comparable to the drift frequency, the mechanism of the μ breaking can still be considered as independent of the existence of the wave. Because the time scale in which the μ

adiabaticity is broken is that of the bounce motion. Hence, the critical condition of the adiabaticity of the magnetic moment in the absence of a wave, Eq.(8), will also be applicable to the case in the presence of a low frequency wave.

The critical condition, Eq.(8), suggests that a decrease of the perpendicular velocity and/or an increase of the parallel velocity cause the non-adiabaticity of the magnetic moment. The decrease of the perpendicular velocity is caused by the direct interaction between the wave and particle, because the electric field of the wave is in the azimuthal direction. While the resonant interaction leads to an increase in the parallel velocity.

2. The velocity change

A. The direct interaction case (modification of the perpendicular velocity)

We estimate the decrease of the perpendicular velocity due to the electrostatic wave during the particle gyromotion.

Since the gyrofrequency is much higher than the wave frequency, it is plausible to assume that the electric field is a constant during the gyromotion. In the constant electric field, the maximum loss of the particle kinetic energy during the gyromotion, ΔW_{max}, is given by

$$\Delta W_{max} = 2\rho q E, \tag{9}$$

where $\rho(= v_\perp/\omega_c)$ is a Larmor radius and $E(= m\chi_0/\sqrt{2})$ is the intensity of the constant electric field considered. Since the direction of the electric field is perpendicular to the magnetic field, the loss of the perpendicular kinetic energy is given by

$$\Delta W = \frac{1}{2}Mv_\perp^2 - \frac{1}{2}M(v_\perp - \Delta v_\perp)^2, \tag{10}$$

where Δv is a velocity change caused by the constant electric field. Substituting Eq.(9) into Eq.(10), we obtain the change of the perpendicular velocity

$$\Delta v_\perp = v_\perp - \sqrt{v_\perp^2 - 4qE\rho/M}. \tag{11}$$

B. The resonant case (modification of the parallel velocity)

We now estimate the increase of the parallel velocity due to the resonances by use of the guiding center Hamiltonian[3].

The guiding center Hamiltonian in the presence of an electrostatic wave is

$$H = \frac{1}{2}\rho_\parallel^2 B_0^2 + \mu B_0 + \chi_0 \cos(m\phi - \omega t), \tag{12}$$

where $\rho_{\|}(=v_{\|}/B_0)$ is the parallel gyroradius. Using the magnetic coordinate, (Ψ, Ω), the dipole magnetic field is written as

$$\mathbf{B}_0 = \nabla\Psi \times \nabla\phi = \nabla\Omega, \tag{13}$$

$$B_0 \simeq \Psi^3 + \frac{9\Omega^2}{2\Psi} - \frac{21\Omega^4}{8\Psi^3}, \tag{14}$$

where, Ψ, ϕ and $\Omega, \rho_{\|}$ are conjugate canonical variables.

Transforming to the wave frame, the Hamiltonian becomes

$$\bar{H} = \frac{1}{2}\rho_{\|}^2 B_0^2 + \mu B_0 + \chi_0 \cos\xi - \omega P_\xi, \tag{15}$$

$$\Psi = mP_\xi, \xi = m\phi - \omega t. \tag{16}$$

Expanding in the series of the ΔP ($\Delta P = P_\xi - P_0$, P_0 : the time average of P_ξ), the Hamiltonian consists of three parts

$$\bar{H} = \bar{H}_\Omega + \bar{H}_\xi + \bar{C}. \tag{17}$$

$\bar{H}_\Omega$ is the Hamiltonian of the bounce motion, $\bar{H}_\xi$ is the Hamiltonian of the $E \times B$ drift motion, and $\bar{C}$ is the coupling term of these oscillations. We first consider $\bar{H}_\Omega$ and $\bar{H}_\xi$, and study the change of the parallel velociy due to the coupling term $\bar{C}$.

Transforming to the action variables and using the Lie transfomation method[4], we find a constant of motion, $\tilde{J}_\Omega$, and the Hamiltonian of the bounce motion in terms of transformed coordinates becomes

$$\tilde{H}_\Omega = \tilde{J}_\Omega \omega_\Omega + C_1 \tilde{J}_\Omega^2 - C_2 \tilde{J}_\Omega^3. \tag{18}$$

Through this section C_n are the functions of μ, P_0, m, and ω.

Next is the Hamiltonian of the $E \times B$ motion, which is given by

$$\bar{H}_\xi = C_3 \Delta P^2 + C_4 \Delta P + \chi_0 \cos\xi, \tag{19}$$

where

$$C_4 = m\omega_d - \omega. \tag{20}$$

It is clearly understood that the wave - drift resonance occurs and ΔP becomes large when $C_4 = 0$.

a. $C_4 \neq 0$ (The bounce - $E \times B$ drift resonance)

The Hamiltonian of the $E \times B$ motion is

$$\tilde{H}_\xi = \tilde{J}_\xi \omega_\xi - 2C_3 \tilde{J}_\xi^2, \tag{21}$$

then, the coupling term $\bar{C}$ becomes

$$\bar{C} = -\frac{\chi_0 C_6}{C_4} \tilde{J}_\Omega \sum_{l=-\infty}^{\infty} \sum_{n=-\infty}^{\infty} \mathrm{J}_n(z_1)\mathrm{J}_2(z_1) \cos[(2-4n)\tilde{\theta}_\Omega \pm (1+l)\tilde{\theta}_\xi], \tag{22}$$

where Js are Bessel functions of the first kind. The change of the parallel velocity becomes outstanding when the bounce - $E \times B$ resonance

$$(2-4n)\tilde{\omega}_\Omega = (1+l)\tilde{\omega}_\xi, \tag{23}$$

is satisfied. Using the removal of resonance method[4], we obtain the maximum increase of the parallel velocity

$$\Delta v_{\parallel max} = C_8 \sqrt{\frac{rC_6\chi_0}{C_4(2C_1 r^2 - 3C_2 r^3 \hat{J}_{\Omega 0} + s^2 C_5)} \mathrm{J}_n(z_1)\mathrm{J}_l(z_2)}. \tag{24}$$

b. $C_4 = 0$ (The wave - drift resonance)

The wave-drift resonance condition is

$$m\omega_d - \omega = 0, \tag{25}$$

and the Hamiltonian of the $E \times B$ motion becomes

$$\bar{H}_\xi = C_3 \Delta P^2 + \chi_0 \cos\xi \equiv E. \tag{26}$$

$\bar{H}_\xi$ corresponds to the Hamiltonian for a pendulum. Since the $E \times B$ motion is so slow compared to the bounce motion, we can directly obtain the maximum increase of the parallel velocity by the Lie transformation method, as

$$\Delta v_{\parallel max} = \frac{4C_6}{\tilde{\omega}_\Omega} \sqrt{\frac{\chi_0}{C_3}} v_\parallel \tag{27}$$

3. The analytical results

Substituting the velocity changes, Eq.(11), Eq.(24), and Eq.(27), into the critical condition, Eq.(8), we can obtain the non-adiabatic condition in the presence of the electrostatic wave. We show the comparison of the analytical and numerical results of

the case of the opposite direction in Fig(3) and the case of the same direction in Fig(4) (the shaded regions). The frequency independent shaded regions are obtained by the direct interaction between the wave and particle. The frequency dependent shaded regions are obtained by the bounce - $E \times B$ resonance in the case of the opposite direction and the wave-drift resonance in the case of the same direction. We find good agreements in the numerical and analytical results.

V. CONCLUSION

We presented the dynamic behavior of the magnetic moment, μ, of the partilce confined in a magnetic dipole field when a low frequency electrostatic wave is present. We obtained numerically two characteristic conditions for the breakdown of μ; one which is independent of the wave frequency, and the other which forms the spike-like structure in the wave frequency - particle energy space. We showed analytically that the former is caused by the direct interaction between the particle and the electrostatic wave during the gyromotion and the latter is caused by two kinds of resonances, i.e., the bounce - $E \times B$ drift resonance and the wave - drift resonance. The unstable conditions obtained by theoretical consideration showed good agreements with those of numerical results.

REFERENCES

[1] T. G. Northrop, The Adiabatic Motion of Charged Particles, Jhon Wiley, New York, 1963.

[2] A. J. Dragt and J. M. Finn, J. Geophys. Rev., **81**(13), 2327(1976).

[3] R. B. White and M. S. Chance, Phys. Fluids, **27**(10), 2455(1984).

[4] A. J. Lichtenberg and M. A. Lieberman, Regular and Stochastic Motion, Springer-Verlag, New York-Hiderberg, 1983, pp. 63.